

Global polarization of Λ hyperons as a probe for vortical effects in A+A collisions at HADES

**Globale Polarisation der Λ Hyperonen als Nachweis für wirbelartige Effekte in A+A
Kollisionen mit HADES**

Zur Erlangung des Grades eines Doktors der Naturwissenschaften (Dr. rer. nat.)
genehmigte Dissertation von M.Sc. Frédéric Julian Kornas aus Wiesbaden
2021 — Darmstadt — D 17

1. Gutachten: Prof. Dr. Tetyana Galatyuk
2. Gutachten: Prof. Dr. Christoph Blume



TECHNISCHE
UNIVERSITÄT
DARMSTADT

Fachbereich Physik
Institut für Kernphysik
AG Galatyuk (ViP-QM)

Global polarization of Λ hyperons as a probe for vortical effects in A+A collisions at HADES
Globale Polarisation der Λ Hyperonen als Nachweis für wirbelartige Effekte in A+A Kollisionen mit
HADES

Genehmigte Dissertation von M.Sc. Frédéric Julian Kornas aus Wiesbaden

1. Gutachten: Prof. Dr. Tetyana Galatyuk
2. Gutachten: Prof. Dr. Christoph Blume

Betreuer: Dr. Ilya Selyuzhenkov

Tag der Einreichung: 29.06.2021

Tag der Prüfung: 19.07.2021

Darmstadt — D 17

Bitte zitieren Sie dieses Dokument als:

URN: urn:nbn:de:tuda-tuprints-197638

URL: <http://tuprints.ulb.tu-darmstadt.de/19763>

Dieses Dokument wird bereitgestellt von tuprints,
E-Publishing-Service der TU Darmstadt
<http://tuprints.ulb.tu-darmstadt.de>
tuprints@ulb.tu-darmstadt.de



Die Veröffentlichung steht unter folgender Creative Commons Lizenz:
Namensnennung – Keine kommerzielle Nutzung – Keine Bearbeitung 4.0 International
<http://creativecommons.org/licenses/by-nc-nd/4.0/legalcode/>

Erklärung zur Dissertation

Hiermit versichere ich, die vorliegende Dissertation ohne Hilfe Dritter nur mit den angegebenen Quellen und Hilfsmitteln angefertigt zu haben. Alle Stellen, die aus Quellen entnommen wurden, sind als solche kenntlich gemacht. Diese Arbeit hat in gleicher oder ähnlicher Form noch keiner Prüfungsbehörde vorgelegen.

Darmstadt, den 29.06.2021

(Frédéric Julian Kornas)

Abstract

In non-central heavy-ion collisions, large orbital angular momenta of the order $L \sim 10^3 \hbar$ to $L \sim 10^6 \hbar$ are generated. Due to the quantum mechanical spin orbit coupling, this might cause a spin polarization of the produced particles along the orbital angular momentum. As the system created in heavy-ion collisions is well described in the framework of relativistic hydrodynamics, the orbital angular momentum results in non-zero vorticity, classically defined as the rotation of the velocity field. Several theoretical approaches of a global polarization linked to different definitions of the relativistic vorticity tensor have been developed in the past years.

In contrast to macroscopic spin polarization effects, where the spin can be measured by applying external magnetic fields, such a direct measurement of the spin direction is not possible in heavy-ion collisions. The possibility to measure the particle spin is based on the unique feature to the weak interaction, the parity violation. This has the consequence that in weak decays, the emittance of the decay products is linked to the spin direction of the weakly decaying particle. The simplest candidate to perform such a measurement is the Λ hyperon. Through its decay $\Lambda \rightarrow p + \pi^-$ (branching ratio 63.9 %), which has two charged particles in the final state, it can be reconstructed. Due to the parity violation in this weak decay, the proton is predominantly emitted in the spin direction of the Λ hyperon. Thereby, the spin measurement is transformed into a momentum measurement which can be performed.

The orientation of the orbital angular momentum is always perpendicular to the so-called reaction plane spanned by the beam direction and the impact parameter of the collision. The reaction plane can be estimated from the event plane, which is reconstructed in a Q-vector analysis from the distribution of the spectator particles. In the laboratory frame, the event plane is fully determined by a single azimuthal angle Ψ_{EP} . Then the measure for the global polarization of the Λ hyperons can be written as $\langle \sin(\Psi_{EP} - \phi_p^*) \rangle$, while $\langle \cdot \rangle$ denotes the average over all particles and orientations of the event plane and ϕ_p^* is the azimuthal angle of the proton in the rest frame of the Λ .

In this work, the global polarization of the system using Λ hyperon polarization measurements are presented for Au+Au collisions at $\sqrt{s_{NN}} = 2.4 \text{ GeV}$ and Ag+Ag collisions at $\sqrt{s_{NN}} = 2.55 \text{ GeV}$ collision energy. The extracted signal in the Au+Au run yields $P_\Lambda[\%] = 4.609 \pm 0.966(\text{stat.}) \pm 1.220(\text{sys.})$, while for the Ag+Ag run a value of $P_\Lambda[\%] = 3.174 \pm 0.294(\text{stat.}) \pm 0.319(\text{sys.})$ has been measured. This is the highest Λ polarization ever measured in heavy-ion collisions. Our measurement continues the increasing trend measured by the STAR collaboration in the beam energy scan phase I down to $\sqrt{s_{NN}} = 7.7 \text{ GeV}$. This also constrains the energy region for the "turning point" where the polarization is supposed to decrease and yield zero at even smaller collision energies. Furthermore, the high statistics of the Ag+Ag run allowed to perform a differential analysis of the Λ polarization as a function of centrality, rapidity and transverse momentum. The results are compared to theoretical predictions based on a direct link of the Λ spin vector and thermal vorticity. The input of the velocity fields and the temperature were taken from the UrQMD transport model. The calculations are in agreement with the measured data and also reproduce the differential trends. As these calculations are based on the assumption of local thermodynamic equilibrium including the spin degrees of freedom, this sets restrictions on the equation of state in the baryon dominated energy regime with densities similar to those predicted to occur in compact stellar objects. In addition to the global polarization, which is linked to the gradients in the initial

velocity field, the azimuthal anisotropy (directed flow) is related to the initial velocity profile of the Λ has also been studied as a function of the rapidity. The slope at midrapidity has been extracted and found to be $d v_1/d y|_{y_{CM}=0} = 0.388 \pm 0.023(\text{stat.}) \pm 0.038(\text{sys.})$ in Au+Au and $d v_1/d y|_{y_{CM}=0} = 0.289 \pm 0.007(\text{stat.}) \pm 0.025(\text{sys.})$ in Ag+Ag collisions. This confirms the increasing trend of $d v_1/d y|_{y_{CM}=0}$ measured by the E895 and STAR collaborations. The results have been compared to protons within the same transverse momentum and centrality range. The slope of the Λ s is observed to be approximately $\sim 2/3$ of the proton slope in line with the measurements from E895, however, in contrast to the recent measurement from the STAR fixed target run at $\sqrt{s_{NN}} = 4.5 \text{ GeV}$, where no significant difference has been observed. This is an interesting observation and remains to be understood. This provides challenges to the theory calculations as to understand the underlying effects requires a description of both polarization and directed flow simultaneously for which the HADES measurements provide important input.

Zusammenfassung

In peripheren Schwerionenkollisionen werden große Drehimpulse erzeugt, die Größenordnungen von $L \sim 10^3 \hbar$ bis $L \sim 10^6 \hbar$ erreichen können. Durch Spin-Bahn-Wechselwirkung kann das zu einer globalen Spinpolarisation der erzeugten Teilchen entlang des Drehimpulses führen. Die in Schwerionenkollisionen erzeugte Materie kann gut durch die relativistische Hydrodynamik beschrieben werden. Im Rahmen dieser Theorie sorgen Drehimpulse für Vortizität, welche klassisch als Rotation des Geschwindigkeitsfeldes des betrachteten Systems von Teilchen definiert ist. In den letzten Jahren wurden verschiedene theoretische Ansätze entwickelt, um eine physikalische Beziehung zwischen der globalen Polarisation und dem relativistischen Vortizitätstensor zu erhalten.

Im Gegensatz zu makroskopischen Polarisationseffekten der Teilchenspins, welche über externe magnetische Felder gemessen werden können, ist dies in Schwerionenkollisionen nicht direkt möglich. Allerdings kann die Paritätsverletzung der schwachen Wechselwirkung genutzt werden, um die Spinausrichtung der Teilchen zu messen. Der naheliegendste Kandidat dafür ist das Λ Hyperon, welches im Zerfall $\Lambda \rightarrow p + \pi^-$ (Verzweigungsverhältnis 63.9 %) in zwei geladene Teilchen zerfällt. Wegen der Paritätsverletzung in diesem Zerfall wird das Proton bevorzugt in Richtung des Spins des Λ Hyperons emittiert. Dadurch wird die Messung der Spinausrichtung in eine Impulsmessung transformiert, welche mit den herkömmlichen Detektorsystemen durchgeführt werden kann.

Die Orientierung des Kollisionsdrehimpulses ist senkrecht zur sogenannten Reaktionsebene, welche durch die Strahlrichtung und den Stoßparameter der Kollision aufgepannt wird. Experimentell lässt sich die Reaktionsebene durch die Rekonstruktion der Eventebene bestimmen. Dabei werden diejenigen Teilchen verwendet, welche nicht an der Kollision teilnehmen, denn aus ihrer Verteilung kann die Eventebene mittels einer Q-Vektor Analyse berechnet werden. Im Laborsystem ist diese Ebene durch einen einzigen, azimuthalen Winkel Ψ_{EP} festgelegt. Mit diesem lässt sich die globale Polarisation der Λ Hyperonen durch die Observable $\langle \sin(\Psi_{EP} - \phi_p^*) \rangle$ bestimmen, wobei $\langle \cdot \rangle$ den Mittelwert über alle analysierten Teilchen und Orientierungen der Eventebene repräsentiert und ϕ_p^* den azimuthalen Winkel des emittierten Protons im Ruhesystem des Λ Hyperons darstellt.

In dieser Arbeit werden die Ergebnisse der globalen Polarisation der Λ Hyperonen für Au+Au und Ag+Ag Kollisionen präsentiert, erstere bei einer Kollisionsenergie von $\sqrt{s_{NN}} = 2.4 \text{ GeV}$ und letztere bei $\sqrt{s_{NN}} = 2.55 \text{ GeV}$. In den Au+Au Kollisionen wurde eine Polarisation von $P_\Lambda[\%] = 4.609 \pm 0.966(\text{stat.}) \pm 1.220(\text{sys.})$ gemessen, während die Analyse der Ag+Ag Daten eine Polarisation von $P_\Lambda[\%] = 3.174 \pm 0.294(\text{stat.}) \pm 0.319(\text{sys.})$ ergab. Das ist die größte globale Polarisation von Λ Hyperonen, die in Schwerionenkollisionen gemessen wurde. Die Ergebnisse setzen den ansteigenden Trend fort, der von der STAR Kollaboration im Beam Energy Scan Phase I bis zu einer minimalen Energie von $\sqrt{s_{NN}} = 7.7 \text{ GeV}$ gemessen wurde. Es wird erwartet, dass bei immer niedrigeren Kollisionsenergien ein Umkehrpunkt auftritt, ab dem die globale Polarisation signifikant abnimmt und schließlich verschwindet. Durch die HADES Messungen werden dafür weitere Grenzen gesetzt. Des Weiteren erlauben die Ag+Ag Daten eine differentielle Analyse der globalen Polarisation als Funktion der Rapidity, des transversalen Impulses und der Kollisionszentralität. Die Ergebnisse wurden mit theoretischen Vorhersagen verglichen, welche auf einem direkten Zusammenhang von thermaler Vortizität und dem Spin-Vierervektor der Teilchen beruhen. Dieser Zusammenhang wurde unter der Annahme eines lokalen ther-

modynamischen Gleichgewichts hergeleitet, welcher auf die Freiheitsgrade des Spins erweitert wurde. Die Anfangsbedingungen wie Geschwindigkeitsfelder und Temperaturen wurden mit dem Transportmodell UrQMD generiert. Die Vorhersagen stimmen mit den gemessenen Daten überein, was auch auf das differentielle Verhalten der globalen Polarisation der Λ Hyperonen zutrifft.

Zusätzlich zur globalen Polarisation wurde auch der direkte Fluss der Λ Hyperonen gemessen. Während erstere mit dem Gradienten des Geschwindigkeitsfeldes zusammenhängt, ist letzterer direkt vom Geschwindigkeitsfeld abhängig. Die Steigung des direkten Flusses bei Schwerpunktsrapidity wurde aus der Rapiditätsabhängigkeit bestimmt. In den Au+Au Kollisionen wurde ein Wert von $d\nu_1/dy|_{y_{CM}=0} = 0.388 \pm 0.023(\text{stat.}) \pm 0.038(\text{sys.})$ gemessen, während im Ag+Ag System die Steigung zu $d\nu_1/dy|_{y_{CM}=0} = 0.289 \pm 0.007(\text{stat.}) \pm 0.025(\text{sys.})$ bestimmt wurde. Der ansteigende Trend, der sich zu niedrigeren Energien von den Messungen der E895 und STAR Kollaborationen abzeichnete, konnte bestätigt werden. Die Ergebnisse wurden mit denen der in HADES gemessenen Protonen verglichen. Es zeigte sich, dass die Steigung der Λ Hyperonen nur etwa $\sim 2/3$ so groß ist wie die der Protonen. Das ist vergleichbar mit den früheren Messungen der E895 Kollaboration, steht jedoch im Kontrast zu den Ergebnissen der STAR Kollaboration bei $\sqrt{s_{NN}} = 4.5 \text{ GeV}$ Kollisionsenergie, wo kein signifikanter Unterschied zwischen Protonen und Λ Hyperonen beobachtet werden konnte. Der Ursprung dieser Beobachtung ist noch ungeklärt. Die präsentierten Ergebnisse liefern einen wichtigen Input zum Verständnis der zugrundeliegenden Effekte, denn die theoretischen Kalkulationen sollten in der Lage sein, gleichzeitig die Polarization als auch den direkten Fluss zu beschreiben.



Contents

1	Introduction and Motivation	17
1.1	Quantum chromodynamics and the phase diagram	19
1.2	Heavy-ion collisions	23
1.3	Collective flow in heavy-ion collisions	25
1.4	Global polarization measurement	29
1.4.1	Global polarization in heavy-ion collisions	30
1.4.2	Polarization observables	33
1.4.3	Theoretical calculations of the Λ polarization	35
1.4.4	Experimental results on the global polarization	36
1.4.5	Local vorticity and longitudinal polarization	38
1.4.6	Expectations for HADES measurements	39
2	HADES setup	45
2.1	START and VETO detector	46
2.2	Target	47
2.3	Ring Imaging Cherenkov Counter	48
2.4	Tracking System	49
2.4.1	Multiwire Drift Chambers	49
2.4.2	Magnet	50
2.5	Multiplicity Electron Trigger Array	51
2.5.1	Resistive Plate Chamber	52
2.5.2	Time-of-flight Wall	53
2.5.3	Pre-Shower Detector	54
2.6	Electromagnetic Calorimeter	55
2.7	Forward Wall Hodoscope	55
2.8	Data Acquisition and Triggering	56
3	Data Analysis Steps	58
3.1	Data samples collected by HADES	59
3.2	Track reconstruction	60
3.2.1	META matching	62
3.2.2	Momentum determination	63
3.3	Time-of-flight determination	66
3.4	Stability of the detector system	67
3.5	Event vertex reconstruction	69
3.6	Event plane reconstruction and resolution correction	70
3.7	Event and Track selection	74
3.7.1	Event selection	74
3.7.2	Centrality determination	77
3.7.3	Track selection	79
3.8	Particle identification	81

3.9	Λ hyperon reconstruction	83
3.9.1	Identification of Λ hyperon decay products	83
3.9.2	Invariant mass distribution	84
3.9.3	Background determination	86
3.9.4	Decay topology	87
3.9.5	Multilayer perceptron	91
3.9.6	Reduction of multiple counting	99
3.9.7	Reconstruction of the Λ sample	100
4	Signal extraction and implementation of flow and polarization methods	103
4.1	Determination of the Λ decay kinematics	103
4.2	$\Delta\phi$ -extraction method	104
4.3	Invariant mass fit method	110
4.4	Signal and background determination	113
4.5	Estimation of the background correlation using ϕ -rotation	114
4.6	Corrections for reconstruction efficiency	117
4.7	Correction for the radial distance asymmetry	121
4.8	Corrections due to detector occupancy	129
5	Monte-Carlo simulations	133
5.1	Event generator and setup	133
5.2	Implementation of polarization and flow to the Pluto events	135
5.3	Detector response and track reconstruction	140
5.4	Null hypothesis check	141
6	Determination of the systematic uncertainties	151
6.1	Sources of systematic uncertainties	151
6.2	Evaluation of the final systematic uncertainties	153
6.3	Evaluation of the systematic uncertainties and summary tables	157
6.3.1	Global polarization measurement in $\text{Ag}+\text{Ag}$	157
6.3.2	Global polarization measurement in $\text{Au}+\text{Au}$	171
6.3.3	Directed flow slope at midrapidity in $\text{Au}+\text{Au}$	174
6.3.4	Directed flow slope at midrapidity in $\text{Ag}+\text{Ag}$ at $\sqrt{s_{NN}} = 2.55 \text{ GeV}$	176
6.4	Hard-cut analysis	178
7	Results and discussion	181
7.1	Directed flow measurement of the Λ hyperons	181
7.2	Global polarization measurement of the Λ hyperons	185
7.3	Conclusions and outlook	191
8	Summary	194
9	Appendix	206
9.1	Natural units	206
9.2	Kinematical Quantities	206
9.3	χ^2 minimization	207

9.4	Decay Topology	208
9.5	Why the momentum of the Λ hyperon is not used in the neural network	211
9.6	Invariant mass distribution for Ag+Ag at 1.23AGeV	212
9.7	Radial distance asymmetry - Supporting material	213

List of Figures

1.1	Overview of the standard model of particle physics	18
1.2	The fundamental Feynman graphs of QCD	20
1.3	Running coupling constant and the phase-diagram of QCD	22
1.4	The different states of a heavy-ion collision from the initial to the final state	24
1.5	Sketch of two nuclei before and after a heavy-ion collision in the center-of-mass frame	25
1.6	Sketch of the collective flow in heavy-ion collisions	27
1.7	Results of the directed flow as a function of rapidity for protons and Λ s measured by STAR at $\sqrt{s_{NN}} = 4.5$ GeV	28
1.8	Results of the v_1 slope at midrapidity and the elliptic flow as a function of the beam energy	29
1.9	Sketch of the geometrical circumstances and notations for the polarization measurement	34
1.10	Distribution of the proper temperature (left) and the thermal vorticity (right) in the reaction plane perpendicular to the orbital angular momentum	35
1.11	STAR results for the global polarization measurement in Au+Au collisions as a function of the collision energy and centrality	37
1.12	Measurement of the spin alignment of K^{*0} measured for $\sqrt{s_{NN}} = 54.4$ and 200 GeV by STAR and at $\sqrt{s_{NN}} = 2.76$ GeV by ALICE as a function of the collision centrality	38
1.13	Measurement of the local polarization by STAR at $\sqrt{s_{NN}} = 200$ GeV and the hydrodynamical calculations in comparison	39
1.14	Calculation of the kinematical vorticity along the direction of the global angular momentum, energy and time dependence of the emission function of Λ and $\bar{\Lambda}$	40
1.15	Predictions of the energy dependence of the Λ polarization derived from three-fluid dynamics using different equations of state	41
1.16	Transverse momentum dependence of the Λ polarization for different impact parameters in Au+Au collisions at $\sqrt{s_{NN}} = 2.4$ GeV and Ag+Ag collisions at $\sqrt{s_{NN}} = 2.55$ GeV	43
1.17	Rapidity dependence of the Λ polarization for different impact parameters in Au+Au collisions at $\sqrt{s_{NN}} = 2.4$ GeV and Ag+Ag collisions at $\sqrt{s_{NN}} = 2.55$ GeV	43
2.1	Sketch of the GSI facility	45
2.2	Picture of the HADES detector	45
2.3	Cross section of the HADES detector	46
2.4	Pictures of the START detector strips zoomed in and mounted in position	47
2.5	Pictures of the 15-fold segmented targets used during the Au+Au and Ag+Ag beam time	48
2.6	Cross section of the RICH detector and its components	49
2.7	Schematic view of the HADES tracking system	50
2.8	Picture of the superconducting magnet	51
2.9	Magnetic field map of the superconducting magnet for different azimuthal angle	51

2.10 Pictures of the composition of a RPC cell	52
2.11 Arrangement of the resistive-plate chamber cells within one modul	53
2.12 Picture of the six sectors of the time-of-flight detector mounted in position	53
2.13 Composition of one cell of the pre-shower detector and schematic drawing of the working principle	54
2.14 Schematic view of the electromagnetic calorimeter as mounted in HADES	55
2.15 Composition of the ECAL module	55
2.16 Front view of the Forward Wall cells	56
2.17 Overview of the HADES data acquisition system	57
3.1 Schematic drawing of the data processing from pure detector hits to the production of DST files for experimental and simulated data	58
3.2 Sketch of the cluster finder process and projection of the fired wires in the track reconstruction procedure	61
3.3 Distribution of distance dx for the extrapolated Runge-Kutta tracks (see Sec. 3.2.2) to the hits in the TOF detector	63
3.4 Deflection of a charged particle in the magnetic field and the resolution of the momentum reconstruction as a function of the measured momentum for electrons	66
3.5 The mean number of charged pions on day 109 for the Au+Au beam time and the different sectors	68
3.6 The mean number of charged pions over the whole Ag+Ag@1.58AGeV beam time for the different sectors	68
3.7 Distribution of the reconstructed event vertex in Y and Z position	70
3.8 Distribution of the event plane angle before and after recentering for day 108 . .	72
3.9 Resolution of the event plane R_n as a function of the centrality	73
3.10 Event selection for all three beam times	76
3.11 Distribution of the nucleons inside the colliding Au nuclei and the comparison of cross sections as a function of the hit multiplicities with Glauber Monte-Carlo simulations	78
3.12 Track reconstruction efficiency for protons and negatively charged pions as a function of the momentum	80
3.13 Efficiency drop at the edges of the MDC	81
3.14 Distributions of velocity and energy-loss in MDC versus momentum multiplied by polarity	82
3.15 Mass distributions of the daughter particles after particle identification cuts . .	84
3.16 Invariant mass distribution after PID for experimental and simulated data . .	85
3.17 Schematic drawing of the topology of the Λ decay and its parameters	88
3.18 Distribution of the topology parameters for signal and background	90
3.19 Distribution of the topology parameters in Au+Au collisions for signal and background after pre-selection criteria applied	94
3.20 Architecture of the MLP after training for Au+Au and Ag+Ag	95
3.21 The correlation matrix for the parameters used in the MLP	96
3.22 Performance check of the MLP with the testing sample	97
3.23 Significance and signal-to-background ratio as a function of the minimum requirement applied to the discriminant for all three beam times	98

3.24 Distribution of the occurrence of the daughter tracks in the final sample of the Λ candidates before and after reduction of multiple counting	99
3.25 Distribution of the invariant mass after all cuts applied	101
4.1 Momentum distribution of the Λ hyperons before and after the transformation to its rest frame	104
4.2 Results for the Λ polarization of the $\Delta\phi$ -extraction method in Au+Au in comparison for the two method to define the amount of signal	105
4.3 Invariant mass fit to the same-event distribution for 12 bins in $\Delta\phi_p^*$ in Au+Au collisions at $\sqrt{s_{NN}} = 2.4 \text{ GeV}$	106
4.4 Fit to the invariant mass distribution after subtraction of the background using the mixed-event method for 12 bins in $\Delta\phi_p^*$ in Au+Au collisions at $\sqrt{s_{NN}} = 2.4 \text{ GeV}$	107
4.5 Polarization measurement performed with the invariant mass fit method for Au+Au collisions at $\sqrt{s_{NN}} = 2.4 \text{ GeV}$	111
4.6 Polarization measurement performed with the invariant mass fit method for Ag+Ag collisions at $\sqrt{s_{NN}} = 2.55 \text{ GeV}$	112
4.7 Polarization measurement performed with the invariant mass fit method assuming a linear shift of the whole distribution	113
4.8 ϕ distribution for the Λ decay products in Au+Au collisions at $\sqrt{s_{NN}} = 2.4 \text{ GeV}$. .	115
4.9 ϕ distribution for the Λ decay products in Ag+Ag collisions at $\sqrt{s_{NN}} = 2.55 \text{ GeV}$. .	115
4.10 ϕ_p^* distributions of the protons in the rest frame of the Λ hyperon	116
4.11 Polarization measurements after ϕ rotation according to the experimental distribution	116
4.12 Phase-space distribution for signal and background plotted from simulations . . .	118
4.13 Phase-space dependent efficiency matrices for Au+Au and Ag+Ag collisions . .	120
4.14 Efficiency matrix in rapidity and transverse momentum for the integrated polarization results in Au+Au collisions at $\sqrt{s_{NN}} = 2.4 \text{ GeV}$ and Ag+Ag collisions at $\sqrt{s_{NN}} = 2.55 \text{ GeV}$	121
4.15 Polarization extraction using the invariant mass fit method after phase-space cut and efficiency correction in Au+Au and Ag+Ag collisions	121
4.16 Distribution of the radial distance for protons to the event vertex line in comparison for experimental Au+Au collisions and UrQMD simulations with embedded Λ hyperons	123
4.17 Distribution of R'_V as a function of the topology parameter d_2 and d_3	123
4.18 Polarization measurement extracted using the invariant mass fit method and depending on the radial distance from the event vertex line in comparison for experimental data and simulations	125
4.19 Polarization in Ag+Ag at $\sqrt{s_N} = 2.55 \text{ GeV}$ extracted using the invariant mass fit method after the data has been corrected for the radial distance asymmetry in three bins	128
4.20 Polarization in Au+Au at $\sqrt{s_N} = 2.42 \text{ GeV}$ extracted using the invariant mass fit method after the data has been corrected for the radial distance asymmetry in three bins	128
4.21 Track density and occupancy correction matrix as a function of the polar and azimuthal angle in the event plane frame	129

4.22 Occupancy weights and directed flow for the Λ hyperons as a function of the rapidity in Au+Au collisions	130
4.23 Directed flow of the Λ hyperons as a function of the rapidity in Au+Au collisions at $\sqrt{s_{NN}} = 2.4$ GeV corrected for the detector occupancy	131
4.24 Measurement of the directed flow using the invariant mass fit method for different rapidity bins in Au+Au collisions at $\sqrt{s_{NN}} = 2.4$ GeV	132
4.25 Measurement of the directed flow using the invariant mass fit method for different rapidity bins in Ag+Ag collisions at $\sqrt{s_{NN}} = 2.55$ GeV	132
 5.1 Transverse mass distributions for pions, protons and Λ hyperons in comparison for simulated and experimental data	134
5.2 Two dimensional pattern of the directed and elliptic flow modeled from the experimental results of the Au+Au data for pions, protons and Λ hyperons as a function of transverse momentum and rapidity	137
5.3 Two dimensional pattern of the directed and elliptic flow from the simulated Pluto events for pions, protons and Λ hyperons as a function of transverse momentum and rapidity	139
5.4 Implementation of the polarization to the events simulated with Pluto	140
5.5 Distribution of the azimuthal angle of the proton in the rest frame of the Λ hyperon calculated from simulated Pluto events after all particle selections applied .	142
5.6 Distribution of the azimuthal angle of Λ hyperons calculated from simulated Pluto events after all particle selections applied	143
5.7 Distribution of the polarization angle calculated from simulated Pluto events after all particle selections applied	144
5.8 Distribution of the polarization angle for different input polarization implemented to Pluto events and after all particle selections applied	145
5.9 Global polarization measurement of simulated Pluto events with different amount of input polarization using the invariant mass fit method for signal extraction	146
5.10 Correlation plot of the reconstructed polarization from the invariant mass fit method for signal and background extraction as a function of the input polarization and the signal-to-background ratio	147
5.11 Background correlation in simulated Pluto events with finite input polarization without different sources of background as determined from the invariant mass fit method	147
5.12 Global polarization measurement of simulated Pluto events with an input polarization of $P_{\Lambda} = 6\%$ for a realistic multi-differential flow pattern	148
5.13 Transverse momentum and rapidity dependence of the reconstructed polarization in Pluto events with input polarization $P_{\Lambda} = 6\%$ and realistic flow pattern $v_1(p_t, y)$ and $v_2(p_t, y)$	148
5.14 Polarization measurement extracted using the invariant mass fit method and depending on the radial distance from the event vertex line in comparison for Pluto events with $P_{\Lambda} = 6\%$ with and without flow	150

6.1	Results of the extracted polarization signal for different ranges after the R-weighting has been applied and the distribution of the weights for a range of $a = 12$ mm.	155
6.2	Results of the extracted polarization signal for different ranges after the R-weighting defined only from true Λ s has been applied and the net Λ distribution as a function of the radial distance to the event vertex line	156
6.3	Measurement of the directed flow using the invariant mass fit method as a function of the radial distance asymmetry in Au+Au collisions at $\sqrt{s_{NN}} = 2.4$ GeV	157
6.4	Λ polarization in Ag+Ag collisions at $\sqrt{s_{NN}} = 2.55$ GeV depending on the individual topology parameters	158
6.5	Distribution of the net Λ counts as a function of $\Delta\phi_p^*$ in Ag+Ag collisions at $\sqrt{s_{NN}} = 2.55$ GeV	160
6.6	Systematic investigation of the $\Delta\phi$ -extraction method and the radial distance asymmetry in the Λ polarization measurement in Ag+Ag collisions at $\sqrt{s_{NN}} = 2.55$ GeV	160
6.7	Centrality dependent polarization measurement for 0 – 20% centrality	163
6.8	Centrality dependent polarization measurement for 20 – 40% centrality	164
6.9	Rapidity dependent polarization measurement in Ag+Ag collisions at $\sqrt{s_{NN}} = 2.55$ GeV	166
6.10	Invariant mass distributions in Ag+Ag collisions at $\sqrt{s_{NN}} = 2.55$ GeV for different regions of the rapidity	167
6.11	Transverse momentum dependent polarization measurement in Ag+Ag collisions at $\sqrt{s_{NN}} = 2.55$ GeV	168
6.12	Invariant mass distributions in Ag+Ag collisions at $\sqrt{s_{NN}} = 2.55$ GeV for different regions of transverse momentum	169
6.13	Systematic investigation of the $\Delta\phi$ -extraction method and the radial distance asymmetry in the Λ polarization measurement in Au+Au collisions at $\sqrt{s_{NN}} = 2.4$ GeV	172
6.14	Λ polarization in Au+Au collisions at $\sqrt{s_{NN}} = 2.4$ GeV depending on the individual topology parameters	173
6.15	Systematic investigation of the directed flow slope at midrapidity for the individual variation of the different topology parameters in Au+Au collisions at $\sqrt{s_{NN}} = 2.4$ GeV	175
6.16	Systematic investigation of the directed flow slope at midrapidity for the individual variation of the different topology parameters in Ag+Ag collisions at $\sqrt{s_{NN}} = 2.55$ GeV	177
6.17	Polarization measurement in Ag+Ag collisions at $\sqrt{s_{NN}} = 2.55$ GeV extracted from a sample determined by hard-cuts on the decay topology using the invariant mass fit method	178
6.18	Polarization measurement in Au+Au collisions at $\sqrt{s_{NN}} = 2.4$ GeV extracted from a sample determined by hard-cuts on the decay topology using the invariant mass fit method	179
7.1	Measurement of the directed flow as a function of the rapidity for Au+Au collisions at $\sqrt{s_{NN}} = 2.4$ GeV and Ag+Ag collisions at $\sqrt{s_{NN}} = 2.55$ GeV	182

7.2	Directed flow slope at midrapidity as a function of the collision energy for protons and Λ s	183
7.3	Beam energy dependence of the global polarization of the Λ hyperons	185
7.4	Centrality dependence of the global polarization of the Λ hyperons in Ag+Ag collisions at $\sqrt{s_{NN}} = 2.55$ GeV	187
7.5	Rapidity dependence of the global polarization of the Λ hyperons in Ag+Ag collisions at $\sqrt{s_{NN}} = 2.55$ GeV	189
7.6	Transverse momentum dependence of the global polarization of the Λ hyperons in Ag+Ag collisions at $\sqrt{s_{NN}} = 2.55$ GeV	190
7.7	Beam energy dependence of the global polarization of the Λ hyperons in the low energy regime in comparison to the theoretical predictions from 3-fluid hydrodynamic models	192
9.1	Comparison of the background in mixed-event versus same-event	210
9.2	Investigation of introducing the momentum of the Λ to the neural network	211
9.3	Invariant mass distribution in Ag+Ag at 1.23 AGeV for 0 – 40 % centrality	212
9.4	Polarization measurement and invariant mass distribution in Au+Au collisions for the middle range of the radial distance from the event vertex line	213
9.5	Polarization measurement and invariant mass distribution in Ag+Ag collisions for the middle range of the radial distance from the event vertex line	213
9.6	Polarization measurement and invariant mass distribution in UrQMD Au+Au collisions with embedded Λ hyperons	214
9.7	Two-dimensional distribution of the radial distance to the event vertex line with respect to different parameters	215

List of Tables

3.1	The table above shows a summary of the different beam times of HADES	60
3.2	Summary of the first order event plane resolution correction factors R_{EP} in 5 % and 10 % centrality bins	74
3.3	Hit multiplicities in the META system that define the centrality classes	79
3.4	Cut settings for the particle identification	84
3.5	Cut settings for the pre-selection according to the decay topology	93
3.6	Minimum discriminant for the final experimental data samples	98
3.7	Statistical quantities for the amount of Λ signal as found for all three beam times analyzed	102
5.1	Particle species used in the event generator Pluto with the corresponding settings	134
5.2	Percentage of the daughter combinations to a Λ candidate in the simulated Pluto events after all selection cuts have been applied	142
6.1	Summary of the systematic uncertainties in the polarization measurement for Au+Au and Ag+Ag	161
6.2	Summary of the systematic uncertainties in the polarization measurement for Ag+Ag as a function of the collision centrality	162
6.3	Summary of the systematic uncertainties in the polarization measurement for Ag+Ag as a function of the rapidity	170
6.4	Summary of the systematic uncertainties in the polarization measurement for Ag+Ag as a function of the transverse momentum	170
6.5	Summary of the systematic uncertainties in the directed flow slope at midrapidity measurement for Au+Au and Ag+Ag	176
7.1	Centrality dependent global polarization measurement of the Λ hyperons in Ag+Ag collisions at $\sqrt{s_{NN}} = 2.55 \text{ GeV}$	188
7.2	Rapidity dependent global polarization measurement of the Λ hyperons in Ag+Ag collisions at $\sqrt{s_{NN}} = 2.55 \text{ GeV}$	189
7.3	Transverse momentum dependent global polarization measurement of the Λ hyperons in Ag+Ag collisions at $\sqrt{s_{NN}} = 2.55 \text{ GeV}$	191

1 Introduction and Motivation

The idea that the matter around us is made up of small building blocks goes back to the ancient greeks. But for a long time it was a pure philosophical discussion which started to change when Sir Joseph John Thomson discovered the electron in experiments with cathode rays in 1897 [Tho97]. At that time, the atoms at the building blocks of matter have been considered positively charged objects with negatively charged electrons embedded in it. But it was until 1911 when Ernest Rutherford performed his famous scattering experiments [Rut11] and found the positively charged matter to be agglomerated in the center of the atom: the very small and very dense nucleus which was later found to consist of protons and neutrons [Cha32].

At this point in history the world of particle physics seemed to be settled. The problems were more on the theoretical side especially concerning the explanation of the binding of nuclei since the only known interaction¹ at that point was the electromagnetism, which is repulsive for protons. There have been several attempts to explain the binding, but the most promising one was the postulation of a nuclear force that excels the electric repulsion at small distances. In 1935 Hideki Yukawa published a paper [Yuk35] to explain the mechanism of nuclear force through the exchange of a new particle, in analogy to the photon exchange in the electromagnetic interaction.

In experiments with cosmic rays in 1937, Carl Anderson and Seth Neddermeyer unexpectedly found a new particle the so-called muon [And37] which was first interpreted as the Yukawa particle. However, the muon turned out to have exactly the same properties as the electron, except for the mass which was about 200 times heavier. It took ten years to dig out the second particle in the cosmic rays, just slightly heavier than the muon. This was the discovery of the pion [Lat47] which was identified to be the carrier of the strong interaction as predicted by Yukawa.

The idea born by Rutherford to investigate the structure of the matter using scattering experiments was put forward, concomitant with the developments on the technical side. From the early 1950s, several particle accelerators have been built with ever increasing amount of beam energy available. This lead to an overwhelming amount of discoveries of new particles, almost on a weekly basis. "If i could remember the names of all these particles, i'd be a botanist", was the statement from Enrico Fermi to this situation, as it is often-quoted. The comparatively simple world before the 1950s, with more or less two particles as a basis, already concerned the physicists at that time, like Paul Dirac, who was desperate to find a reason why there should be two particles and not just one. However, with this zoo of particles discovered at the different accelerators, the situation was more challenging.

This zoo of particles received ordering by the use of symmetry principles, conservation laws and the use of group theory. The latter allowed to group the particles into different multiplets and therein provided predictions for interaction cross-sections. Yet the dynamics behind the interactions remained unclear.

The situation changed with the formulation of the standard model of particle physics in the 1970s. An overview of its key ingredients is shown in Fig. 1.1. The particles can be grouped in fermions and bosons. The former are spin-1/2 particles and underly the Pauli principle and thus

¹ Of course there was also the gravitational interaction but due to the small ratio to the electromagnetic force of $F_g/F_e \approx 10^{-36}$ for two protons, the strength of gravitation is negligible with respect to other forces in elementary particle physics.

there cannot be two of them in exactly the same quantum state. The fermions are the building blocks of the matter around us.

The bosons have spin-1 and mediate the interactions, also referred to as force carriers, except for the Higgs boson, which has spin-0 and its coupling to the other particles generates their rest masses. For each of the four fundamental forces, there are mediating bosons associated. The strong interaction is mediated by the gluons and causal to confine the quarks into nucleons, the building blocks of the matter around us. It is the strongest interaction and described with the framework of quantum chromodynamics (QCD). As it is of particular interest for this study, it is discussed in more detail in Sec. 1.1.

Standard Model of Elementary Particles

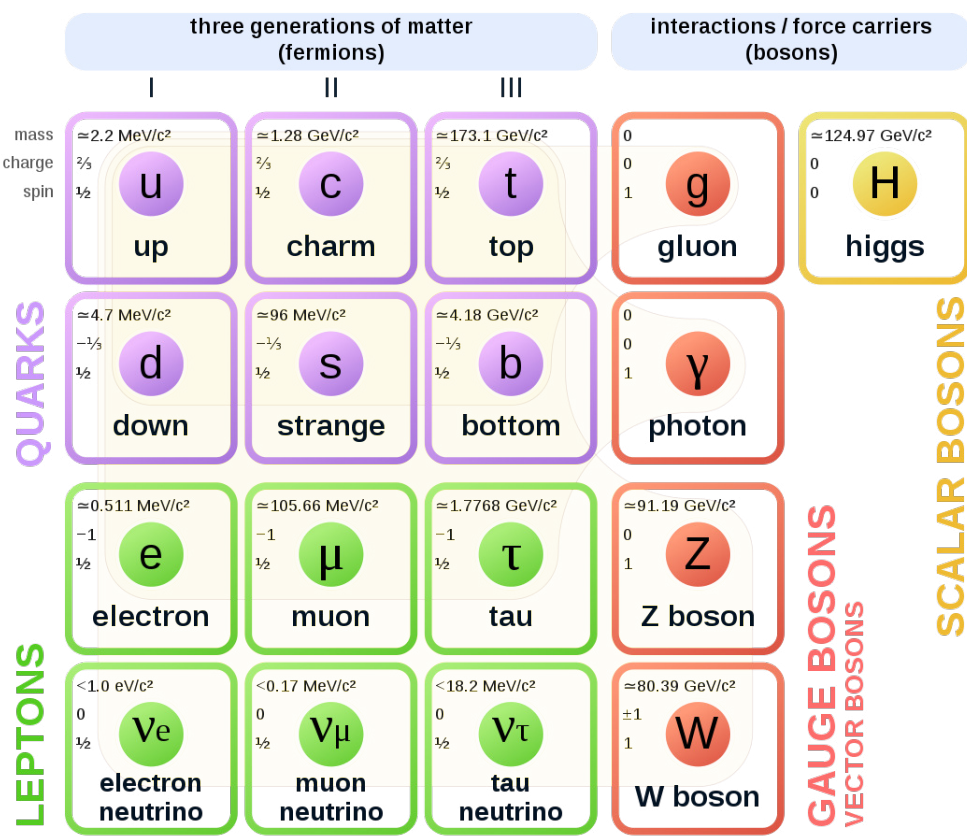


Figure 1.1: Overview of the standard model of particle physics: elementary particles can be grouped in quarks (purple), leptons (green), vector bosons (red) and scalar boson (yellow). The figure was taken (30.05.2021) from: https://commons.wikimedia.org/wiki/File:Standard_Model_of_Elementary_Particles.svg.

The next interaction, two orders of magnitude less in strength, is the electromagnetic interaction. It is mediated by the photon and only affects electrically charged particles, which excludes all neutrinos and most of the bosons, except for the W^\pm . The theory to describe the electromagnetic interaction, is called quantum electrodynamics (QED). As in other quantum field theories the Lagrangian is used to derive the equations of motion. In QED, the Lagrangian reads

$$\mathcal{L}_{\text{QED}} = -\frac{1}{4}F_{\mu\nu}F^{\mu\nu} + \sum_k \bar{\psi}_k(i\gamma^\mu(\partial_\mu - ieA_\mu) - m_k)\psi_k. \quad (1.1)$$

Here $F_{\mu\nu} = \partial_\mu A_\nu - \partial_\nu A_\mu$ is the field strength tensor and describes the free propagation of the photons being defined by the field A_μ . ψ_k is the wave function of the particle k with mass m_k , such that the second term describes the free propagation of the particles together with a term for the interaction with the photon field. The coupling strength is determined by the electric charge e .

The Lagrangian is invariant under the transformation of the wave function by multiplying with a factor $e^{ie\Phi(x)}$ while at the same time the potential has to be transformed by $A'_\mu \rightarrow A_\mu + \partial_\mu\Phi(x)$. Such a transformation is called gauge transformation and can be described in this case by the unitary group $U(1)$. Since the phase Φ depends on the space-time it is a local symmetry. The requirement of the gauge invariance leads to necessity of the photons to be massless and thus resulting in the long-range of the electromagnetic interaction.

Another force incorporated in the standard model is the weak interaction. In comparison to the electromagnetism it is about five orders of magnitude weaker and acts only on short distances. This is due to the fact that the bosons that mediate the interaction, i.e. the W^\pm and Z^0 , have large masses about ~ 100 times the mass of the proton. A unique feature of the weak interaction is the parity violation [Wu57].

Formally, the theory of the weak interaction can be described as a gauge theory in the unification with electromagnetism, known as the electro-weak interaction. From a group theory point of view, this unification can be written as $SU(2) \otimes U(1)$.

There is one more boson which is not related to one of the fundamental interactions. The Higgs boson coupled to other particles and thereby generates their rest masses [Hig64, Eng64]. It has been experimentally confirmed in 2012 by the ATLAS and CMS collaborations [Aad12] and Francois Englert and Peter Higgs received the Nobel prize in physics 2013 for their theoretical discovery.

1.1 Quantum chromodynamics and the phase diagram

In the 1970s experiments using deep-inelastic electron-proton collisions showed that the protons themselves have an internal structure. These constituents are three valence quarks, but to correctly describe the properties of the proton, a sea of fluctuating quark-antiquark pairs and gluons has to be included. The dominating force between these "partons" is the strong interaction with the corresponding charge, called "color". There are three different colors (blue, red, green), carried by the quarks, and the corresponding anti-colors, carried by the anti-quarks. They define the local symmetry of the $SU(3)$ group which represents QCD. In nature there exist only colorneutral objects, thus for the matter the combinations of qqq (baryons) and $q\bar{q}$ (mesons) are possible.

The mediator gluons carry color charge which results in a self-interaction among the gluons as shown in Fig. 1.2, where the fundamental Feynman graphs for the strong interaction are summarized. While the first two graphs can be found similar in QED as an interaction between electrons, positrons and photons, the latter two are a unique feature of the strong interaction.

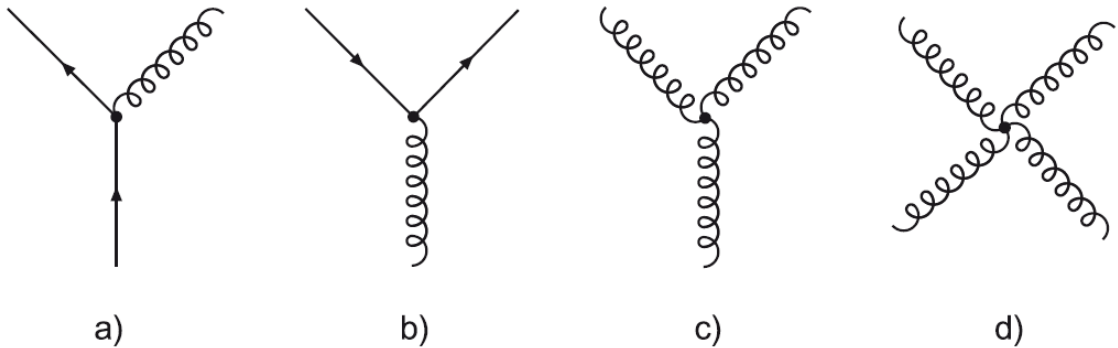


Figure 1.2: The fundamental Feynman graphs of QCD [Pov14]: a) A quark emits a gluon. b) A gluon decays into a quark-antiquark pair. c,d) Self-interaction of the gluons.

The underlying theory to describe the dynamics of the strong interaction is called quantum chromodynamics (QCD). As for the QED the Lagrangian can be written in similar fashion:

$$\mathcal{L}_{\text{QCD}} = -\frac{1}{4}G_{\mu\nu}^a G_a^{\mu\nu} + \sum_{u,d,s} \bar{q}_a (i\gamma^\mu (\partial_\mu - igA_\mu) - m)_{ab} q_b. \quad (1.2)$$

$G_{\mu\nu}^a = \partial_\mu A_\nu^a - \partial_\nu A_\mu^a + \sqrt{2}g f^{abc} A_\mu^b A_\nu^c$ is the gluon field tensor, and in comparison to QED (Eq. 1.1) it includes the self interactions among the gluons as they carry the color charge in contrast to the photons which are electrically neutral. The indices a, b, c denote the different colors and run over all eight independent gluon fields, f^{abc} are the structure constants of $SU(3)$ and g is the strong charge. The sum is performed over the quark-flavors, which usually takes into account only the up-, down- and strange-quark, since the other three (see Fig. 1.1) are much heavier. The terms after the sum correspond to the free quark propagation, the quark-quark interactions and the quark-gluon interactions, which act on the quark spinor q .

Besides the local symmetry of the QCD Lagrangian, there is also a global symmetry. The quark spinor q can be decomposed in two independent components:

$$q_L = \frac{1}{2} (1 - \gamma_5) q, \quad q_R = \frac{1}{2} (1 + \gamma_5) q, \quad (1.3)$$

while the subscripts denote the left- and right-handed components. The meaning of the decomposition can be imagined in case of a massless particle by the more descriptive quantity, the helicity. The helicity of a particle is defined as the projection of its spin direction onto the direction of the momentum. If the spin point in (opposite) the direction of the momentum, the helicity is positive (negative) which corresponds to the right (left)-handed component. However, this analogy does not work for particles with finite mass, since their helicity is not uniquely defined. This is because there is always a frame of reference, which moves faster than the particle itself, meaning that the momentum direction will be reversed while the spin is not. Thus, the helicity will flip the sign. In this case the analogy to the left- and right-handed decomposition does not work and a new quantity is introduced, the so-called chirality.

The chirality has the following relevance: when the decomposition of the quark spinor is inserted into the Lagrangian, i.e. Eq. 1.2, the Lagrangian is completely symmetric except for the

mass term, where left- and right-handed parts are mixed. Consequently, in the limit of vanishing quark masses ($m_q \rightarrow 0$), the left- and right-handed parts can be treated independently, or in other words, the QCD Lagrangian exhibits the chiral symmetry. There are two features that have to be considered. First, the mass term breaks the chiral symmetry. This is called an explicit symmetry breaking. If the quark masses are negligible in comparison to the four-momentum transfer realized in the strong interactions among them, the chiral symmetry can be considered to be realized. Therefore, the chiral symmetry is often referred to as approximate symmetry. The second feature is that the chiral symmetry is also broken spontaneously. This means that even if the Lagrangian fulfills the chiral symmetry, this is not the case for the ground state of the QCD vacuum. A measure for this is the quark-antiquark condensate $\langle \bar{q}q \rangle$, also called chiral condensate. It is defined as the expectation value of the QCD vacuum for the mixing of the left- and right-handed part according to:

$$\langle \bar{q}q \rangle = \langle 0 | \bar{q}_L q_R + \bar{q}_R q_L | 0 \rangle. \quad (1.4)$$

The value of the chiral condensate in the vacuum is about $\langle \bar{q}q \rangle_{T=0, \mu_B=0} \approx -\Lambda_{QCD}^3$. Another very important feature encoded implicitly in the QCD Lagrangian, is that the strength of the strong interaction defined by the coupling constant $\alpha_s(Q^2) \equiv g/2\pi$, depends on the momentum transfer squared Q^2 . The gluon self-interactions lead to a strong dependence on Q^2 , which is called the running coupling constant. From perturbation theory, the coupling constant can be derived [Pov14] to

$$\alpha_s(Q^2) = \frac{12\pi}{(33 - 2n_q) \cdot \ln(Q^2/\Lambda_{QCD}^2)}, \quad (1.5)$$

where $\Lambda_{QCD} \sim 200 \text{ MeV}$ is a free parameter and its magnitude is estimated from experimental data. $n_q = 3 - 6$ defined the number of flavor participating in the process and also depends on Q^2 . The heavy quarks like charm-, bottom- and top-quark only start to contribute to an interaction if their masses are $m_q < |Q|$ which only happens at very high energies.

The measurements of the strong coupling constant as a function of Q are shown in Fig. 1.3. For small momentum transfer, the strength increases strongly. Consequently, if one of the valence quarks of a nucleon is separated from the others, the binding energy will increase with the distance. At some point, the energy is large enough to generate a $q\bar{q}$ pair such that a new qqq and $q\bar{q}$ is formed from the initial proton. This effect of binding into colorneutral objects is called confinement [Wil74]. In case of a large momentum transfer, equivalent to small distances, the coupling strength decreases $\alpha_s \ll 1$ which is called asymptotic freedom and then perturbation theory can be applied. In 2004, David Gross, David Politzer and Frank Wilczek received the Nobel price in physics for the discovery of the asymptotic freedom in the strong interaction.

The behavior of the strong coupling constant has the consequence that the properties of the QCD matter strongly depend on the mean energy realized in the interaction processes among the quarks and gluons. Under normal conditions, the quarks are confined into the nucleons with a density of normal nuclear matter of $\rho_0 = 0.17 \text{ fm}^{-3}$. The matter can be characterized by the baryochemical potential μ_B which is the energy required to introduce or remove a baryon to the system and measures the imbalance of matter and anti-matter. For the normal nuclear matter the baryochemical potential is of the order of the nucleon mass, $\mu_B \sim m_N$.

When the energy density is increases for example by the compression of QCD matter, the mean

momentum transfer in the strong interactions also increases which results in a reduction of the coupling constant α_s . In the limit of very high energy density, the interactions become negligible. In such a case, the partons inside the system can move freely and one can change from the microscopic description of single particle interactions to a macroscopic picture using statistical methods and distributions. Then the energy density is linked to the temperature and baryochemical potential of the system. Depending on these two parameters, the properties of the matter can be very different and are summarized in the so-called QCD phase diagram which is shown in the right panel of Fig. 1.3.

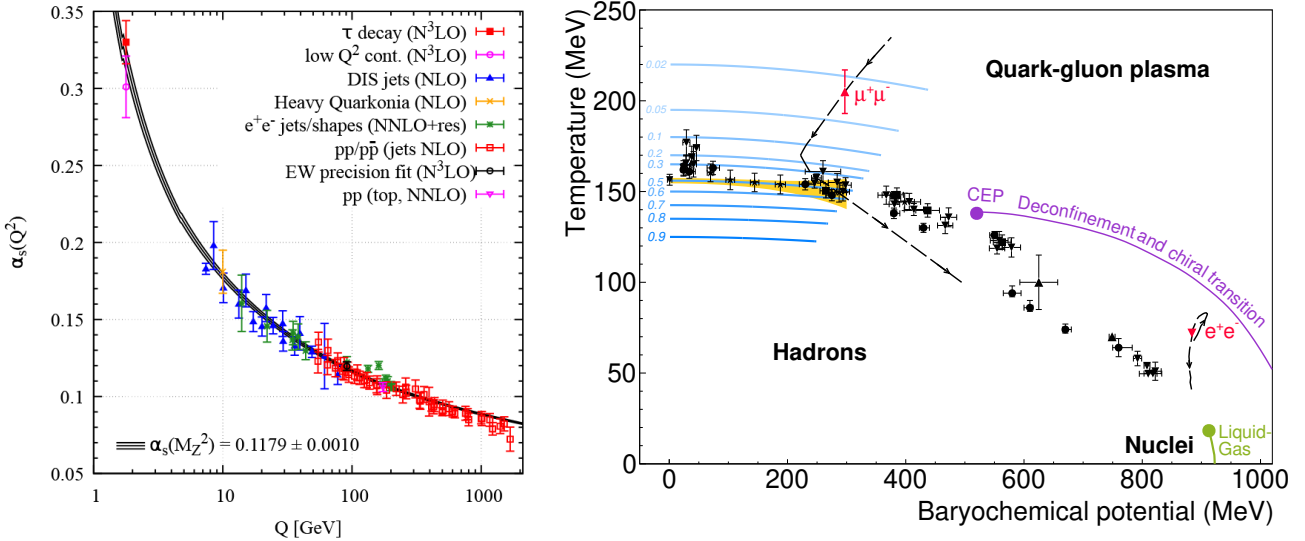


Figure 1.3: Left panel: Summary of measurements of the running coupling constant in QCD as a function of the energy scale Q [Zyl20]. Right panel: The phase diagram of QCD matter as a function of temperature T and baryochemical potential μ_B [Ada19a]. The data points represent the freeze-out conditions measured in heavy-ion collisions.

An overview over different phases can be found in [Ada12].

In the early stages of the universe, the matter was in a state of high temperature and vanishing baryochemical potential $\mu_B \sim 0$, since the amount of matter and anti-matter has been equal. The partons are asymptotically free and this state is usually called a quark-gluon plasma (QGP). In a macroscopic approach the system can be described as a bulk assuming at least local thermodynamic equilibrium. The thermodynamic properties to determine the state of matter are connected by the equation of state (EoS). The EoS at high temperature and vanishing μ_B is fundamental to describe the behaviour of the matter shortly after the Big Bang, while at low to moderate temperature and high μ_B the conditions are realized in the core of compact stellar objects [Dan01]. In this field the EoS can be constrained from the observation of neutron star merger, as has been recently measured in GW170817 [Abb17]. The core of a neutron star is expected to be dominated by nucleons packed together. This corresponds to a region of the QCD phase diagram with low temperature but high μ_B . Due to the Pauli principle, the nucleons generate a pressure that acts against the gravitational attraction. Under these conditions, it is energetically more favorable that hyperons are created. As they are not only composed of up- and down-quarks but incorporate at least one strange-quark, they are not in the same quantum state as the surrounding nucleons and thus the overall state is more compressed. This is referred to as a softening of the EoS and has the consequence of a reduction of the maximum neutron

star mass [Lon15]. Several observations seem to favor a hard EoS [Cha08, Dem10, Ant13]. This is known as the hyperon puzzle and many new developments in theory are ongoing to clarify it. To distinguish the different phases in the QCD phase diagram, a sufficient order parameter has to be defined. For the transition to the QGP, the chiral condensate is used, since it is expected to vanish, when the temperature and/or baryochemical potential increases. The transition has been found to be smooth at low μ_B [Bro90, Fod04], which is linked to a cross-over from the hadronic phase to the QGP. The theoretical calculations in this region of the phase diagram are based on Lattice QCD. Here the equations can be simulated on a discrete space-time lattice without further assumptions by effective models. However, the lattice calculations cannot be employed to describe the matter at high μ_B due to the sign problem (see [Goy17] and references therein). In this region, effective models are needed to describe the behavior of the matter. At this higher μ_B the phase transition is expected to be of first order [Sch07]. Hence a QCD critical endpoint somewhere inbetween can be expected [Ste09, Ste11].

1.2 Heavy-ion collisions

Another way to access the QCD phase diagram experimentally is to use heavy-ion collisions. This has the advantage that it takes place in the laboratory and thus parameters like the collision energy or the collision system, i.e. the ion species, can be varied. Thereby, a hot and dense medium is created which transits along a certain path of T and μ_B in time defined by the initial conditions of the collision. With increasing collision energy, an increasing amount of $q\bar{q}$ pairs is produced and the heavy-ion collisions populate along a path of decreasing μ_B and rising T . Thus, different regions of the QCD phase diagram can be probed by varying the collision energy of the heavy-ion collisions.

At ultra-relativistic heavy-ion collisions as realized at several tenths of GeV center-of mass energy and beyond, there is evidence for the formation of a state known as the quark-gluon plasma (QGP) where the quarks and gluons are no longer confined within the hadrons [Ars05, Bac05, Ada05, Adc05]. This allows to investigate how our universe evolved just few μs after the Big Bang. When the collision energy is decreased, the system gets more and more dominated by the nucleons of the colliding ions. This is closely related to the state expected to be present in compact stellar objects. Therefore, heavy-ion but also pp - and pA -collisions can be used to study of the hyperon-nucleon interactions which might help to resolve the hyperon puzzle in neutron star physics.

The experimental setup for the heavy-ion collisions is designed according to the type of colliding mode: the fixed-target or collider. In a fixed-target experiment, the beam ions are accelerated and shouted onto a stationary target. In case of a collider experiment, two beams are accelerated in opposite direction and brought to collide with each other. The latter has the advantage to achieve higher collision energies, since the center-of-mass energy for $E_{\text{Beam}} \ll m_{\text{Ion}}$ is

$$\sqrt{s} = \sqrt{2}E_{\text{Beam}} \quad (1.6)$$

while in case of a fixed target experiment under the same assumption it is given by

$$\sqrt{s} = \sqrt{2m_{\text{target}}E_{\text{beam}}}. \quad (1.7)$$

Hence in the former case the center-of-mass energy increases proportionally with the beam energy, while in the latter case it grows only with $\sqrt{E_{\text{Beam}}}$. On the other hand, the center-of-mass

frame is at rest in the laboratory for the collider mode, such that the produced particles can fly at any direction which has to be covered by the detector in order to measure the angular distributions. This is not the case for a fixed target experiment, where the center-of-mass is moving along the beam axis and thus all particles are emitted within a forward cone which allows to build much more compact detectors. In addition, much higher collision rates can be achieved. In general a heavy-ion collision undergoes several different stages sketched in Fig. 1.4. In the initial state the two ions approach each other in the center-of-mass frame and due to their relativistic velocities, the shape is Lorentz-contracted along the beam direction. When the collision starts, it is very unlikely that the two nuclei collide head-on. Instead, their centers will be shifted and the distance between the centers is defined as the impact parameter \vec{b} of the collision. Therefore, a fraction of the nucleons will not experience a collision and is called spectator. However, they are not completely unaffected since they are scattering outwards by the coulomb repulsion or inwards due to some strong interactions with the medium and also experience a fragmentation due to the demolition of the initial nuclei. The nucleons which undergo at least one inelastic collision are called participants. The number of participants is directly linked to the impact parameter of the collision, but both are not measurable in experiment. Thus relations to measurable quantities have to be established. This will be discussed in more detail in Sec. 3.7.2.

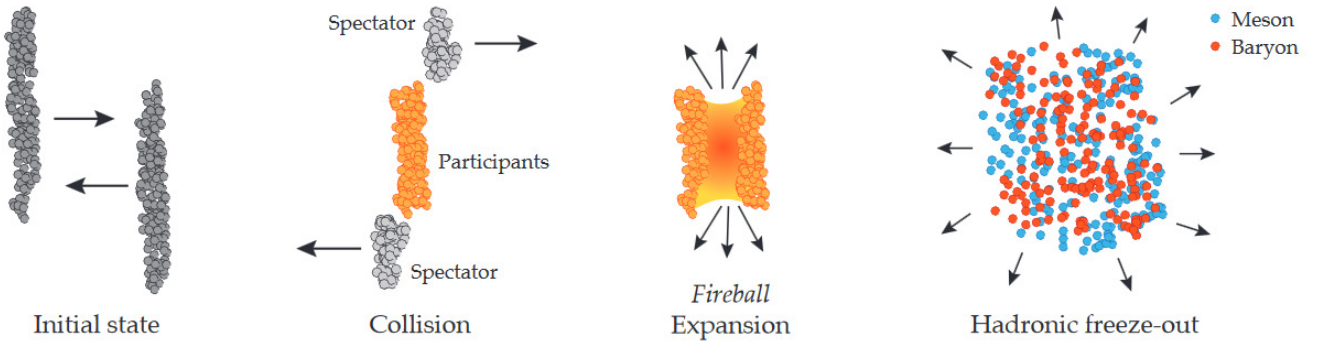


Figure 1.4: The different states of a heavy-ion collision from the initial to the final state [Kar15b].

In the center of the collision a hot and dense fireball is built which expands and undergoes several different phases. The chemical freeze-out defines the state where the production of new particles has stopped while the kinetic freeze-out specifies the end of elastic collision such that the final state is determined.

The particles produced from interactions among participants form a medium in general called fireball. Depending on the collision energy and system size, different densities and temperatures can be achieved as discussed in Sec. 1.1. At the relativistic collision energies, this hot and dense medium will expand while cooling down until the energy is not sufficient to produce new particles. This stage of the collision when the inelastic collisions stop is called chemical freeze-out. Afterwards, there are still interactions, but mostly elastic scattering processes due to electromagnetic interaction. The time when the interactions between the participants stop completely is called kinetic freeze-out and defines the final state of the collision. A typical timescale from the initial to the final state is about $t \sim 10^{-22}$ s.

The participant distribution defines the initial geometry of the collision. The overlap of the two colliding nuclei is asymmetric in the plane transverse to the beam direction which results

in an anisotropic expansion. This also holds for the longitudinal direction along the beamline. This asymmetry has the consequence of effects being driven by the initial velocity field and its gradients, i.e. the vorticity. While the former is related to the collective flow of the particles (see Sec. 1.3), the latter is related to a spin polarization (see Sec. 1.4). To measure these effects, it is useful to define a system of reference which is symmetric to the initial geometry. The symmetry plane is spanned by the beam direction and the impact parameter of the collisions and is called reaction plane. Since the laboratory frame is usually defined such that the beam direction points along the z -axis, the difference to the reaction plane is just a rotation around the z -axis and thus the reaction plane is fully determined by an azimuthal angle Ψ_{RP} . Related to the orientation of the reaction plane is the direction of the global angular momentum of the collision, which is defined as

$$\vec{L} = \vec{b} \times \vec{p}_{\text{Beam}}. \quad (1.8)$$

As the laboratory frame is defined as $\hat{p}_{\text{Beam}} = \hat{z}$ and $\hat{b} = \hat{x}$, the orbital angular momentum will point in the direction $\hat{L} = -\hat{y}$. In the left panel of Fig. 1.5 the geometry parameters and the angular momentum of the collision are sketched in the center-of-mass frame. In the right panel the situation after the collision is shown, with an outward deflection of the spectators and the expanding fireball in the center.

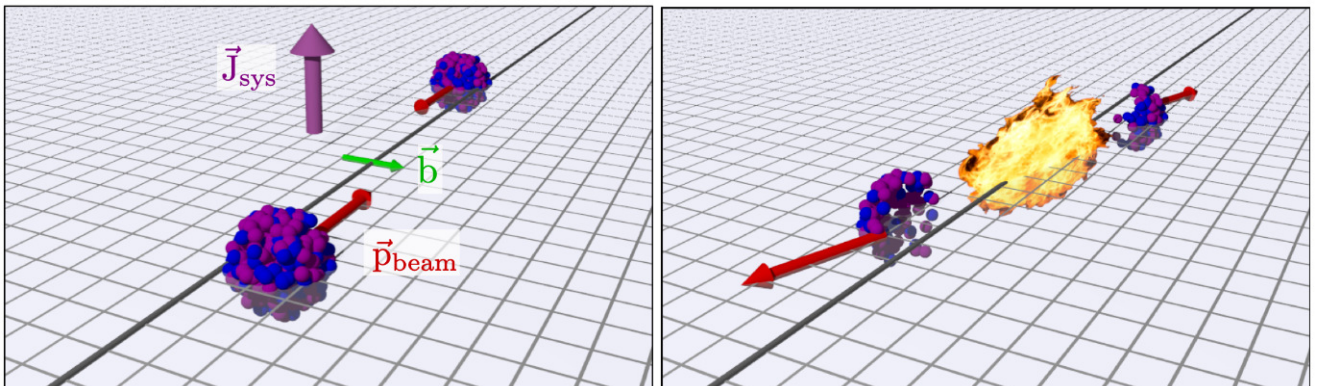


Figure 1.5: Sketch of two nuclei before and after a heavy-ion collision in the center-of-mass frame [Bec20]. The incoming beam ion with momentum \vec{p}_{Beam} collides with another ion at a certain impact parameter \vec{b} which defines the reaction plane (left). Thereby an orbital angular momentum \vec{L} (\vec{J}_{sys} in the figure) is created. After the collision the unaffected nucleons are deflected leaving behind a hot and dense medium.

1.3 Collective flow in heavy-ion collisions

The fireball created in heavy-ion collisions will expand due to the pressure gradient in the system. This will convert the spatial distributions of the participants into the final state momentum distributions. The momentum distributions in the final state will show anisotropies, due to the different geometry defined by the position of the participants including their event-by-event fluctuations. This so-called anisotropic flow is very sensitive to the early stages of the collision since the spatial anisotropies rapidly decrease with time [Vol10]. Therefore, the anisotropic flow incorporates information about the equation of state of the hot and dense medium [Dan02, Fev16].

The momentum distributions can be converted into angular distributions and related to the azimuthal angle with respect to the reaction plane. Since this angle will be often used in this work, we define it as

$$\Delta\phi = \phi - \Psi_{RP}, \quad (1.9)$$

where ϕ is the azimuthal angle for a particle in the laboratory frame. To measure the anisotropies of the azimuthal distribution, they are modulated by a Fourier series reading [Vol96, Pos98]

$$\frac{1}{N_{\text{all}}} \frac{dN}{d\Delta\phi} = \frac{1}{2\pi} \left(1 + \sum_{n=1}^{\infty} 2\nu_n \cos(n\Delta\phi) \right), \quad (1.10)$$

while the distribution has been normalized to the overall amount of particles, because

$$\int_0^{2\pi} d\Psi_{RP} \int_0^{2\pi} d\phi \frac{dN}{d\Delta\phi} = N_{\text{all}}. \quad (1.11)$$

In Eq. 1.10 the odd-terms are omitted since they are not symmetric when replacing $\Delta\phi$ by $-\Delta\phi$ and thus this would be a violation of the parity which is a globally conserved quantity. The isotropic expansion in Eq. 1.10 is referred to as radial flow. This symmetric expansion is due to the pressure gradient pointing radially outwards from the collision center. It has been shown that this expansion runs nearly isentropic [Ber81] and hence accompanies the decrease of temperature. Then the particle distributions in transverse momentum and rapidity (see Sec. 9.2 for more details) can be described by a Siemens-Rasmussen ansatz [Sie79, Sch93] assuming thermal equilibrium to extract the radial expansion velocity and the temperature of the medium. All other terms of Eq. 1.10 are determined by the flow coefficients ν_n . The components can be calculated according to

$$\nu_n = \frac{1}{N_{\text{all}}} \int_0^{2\pi} d\Psi_{RP} \int_0^{2\pi} d\phi \frac{dN}{d\Delta\phi} \cos(n\Delta\phi) \equiv \langle \cos(n\Delta\phi) \rangle. \quad (1.12)$$

In experiment there is always a finite set of particles such that the integrals turn to summations. This sets a limit on the order n up to which the flow harmonics can be extracted in experiment. Due to their importance and geometrical meaning the first three components have special names. ν_1 is called directed, ν_2 is called elliptic and ν_3 is called triangular flow.

The directed flow defines the strength of the first harmonic of the sum in Eq. 1.10. If $\nu_1 > 0$, it means that most of the particles are flying to angles $\phi \sim \Psi_{EP}$, while for $\nu_1 < 0$ it is preferably $\phi \sim \Psi_{EP} + \pi$. The magnitude of ν_1 defines the strength of this effect. The geometrical meaning can be realized when measuring the directed flow as a function of rapidity in the center-of-mass frame. Then it turned out that the directed flow is zero at midrapidity and anti-symmetric with respect to this point. As the rapidity is measured in the longitudinal direction, the dependency $\nu_1(y)$ is generated from the spectators and their interactions with the participant matter. The sign of the directed flow determines the deflection direction of the spectators: if $\nu_1 > 0$ the deflection is pointing outwards due to a repulsive effect (as depicted in Fig. 1.5) while for $\nu_1 < 0$ the deflection points inwards, accompanying an attractive force. Consequently, the directed

flow is very sensitive to the velocity field at the early stages of the collision.

As the second even modulation of the azimuthal angular distribution, the elliptic flow describes the emission pattern with respect to the reaction plane. For $v_2 > 0$, most of the particles will be emitted along $\phi \sim \Psi_{EP}$ or $\Psi_{EP} + \pi$ which is called in-plane emission. Similar, for $v_2 < 0$ the emission will be preferably out-of-plane.

Fig. 1.6 sketches the geometrical meaning of the collective flow components discussed so far. The higher order harmonics define ever finer modulations of the emission pattern and provide very precise informations about the thermodynamical properties of the medium, especially as they might differ for different particle species which can be emitted from various stages of the collision.

The flow components can also be expressed in terms of the momentum components of the particles. Then the first three components read

$$v_1 = \left\langle \frac{p_x}{p_t} \right\rangle, \quad v_2 = \left\langle \frac{p_x^2 - p_y^2}{p_t^2} \right\rangle, \quad v_3 = \left\langle \frac{p_x^3 - 3p_x p_y^2}{p_t^3} \right\rangle. \quad (1.13)$$

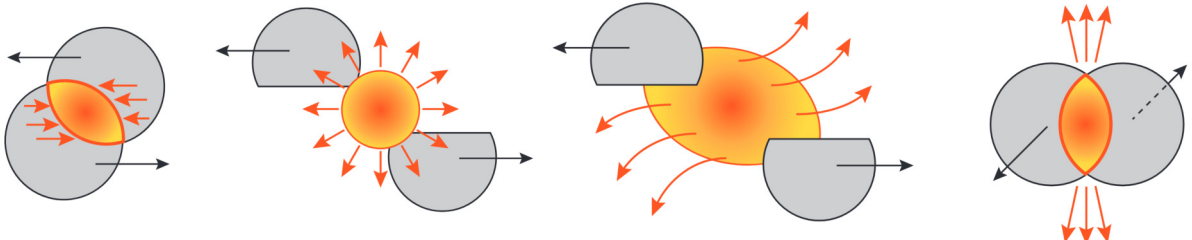


Figure 1.6: Sketch of the collective flow in heavy-ion collisions [Kar18]. From left to right: initial geometry of a non-central collisions; radial flow; directed flow; elliptic flow.

Recently, the HADES collaboration published a detailed study of the multi-differential flow pattern for protons, deuterons and tritons at Au+Au collisions at $\sqrt{s_{NN}} = 2.4 \text{ GeV}$ [Ada20a]. The same data set will be analyzed in this thesis with respect to the Λ hyperons. They are expected to be produced in collisions of e.g. the protons and thus the discussion of the flow measurements will be focussed on the comparison of these two particle species.

As discussed the geometrical meaning of the directed flow can be illustrated as a function of the rapidity. A good measure for this is to extract the slope at midrapidity, since its sign encodes the sign change of the directed flow and its magnitude is a measure for the strength of v_1 .

The first measurement of this slope for protons and Λ s goes back to the measurements performed by the E895 collaboration for $\sqrt{s_{NN}} \sim 3 - 5 \text{ GeV}$ [Liu00, Chu01]. Both particles were in qualitative agreement and showed an increasing trend of the directed flow as a function of rapidity, which indicates an outwards deflection. However, the extracted slopes have been found to be different, and could be scaled approximately by:

$$\left. \frac{d v_1}{d y_{CM}} \right|_{y_{CM}=0,\Lambda} \sim \frac{2}{3} \cdot \left. \frac{d v_1}{d y_{CM}} \right|_{y_{CM}=0,p} \quad (1.14)$$

for the lowest collision energy of $\sqrt{s_{NN}} = 2.7 \text{ GeV}$. However, the scaling decreases with increasing beam energy and at $\sqrt{s_{NN}} = 4.3$ the ratio was roughly 1/3. Recently, the STAR collaboration published their measurements for the fixed-target run at $\sqrt{s_{NN}} = 4.5 \text{ GeV}$ [Ada21]. The

directed flow as a function of rapidity is shown in Fig. 1.7 for protons and Λ s. The points for $y > 0$ have been reflected due to the anti-symmetry of v_1 . The shape can be described by a third order polynomial written as:

$$v_1(y_{CM}) = F_0 + F_1 \cdot y_{CM} + F_3 \cdot y_{CM}^3, \quad (1.15)$$

while F_1 is the slope at midrapidity. STAR found the slope of the Λ s is slightly higher than that extracted from the proton directed flow, however, this is not significant such that for both particles the results are well in agreement.

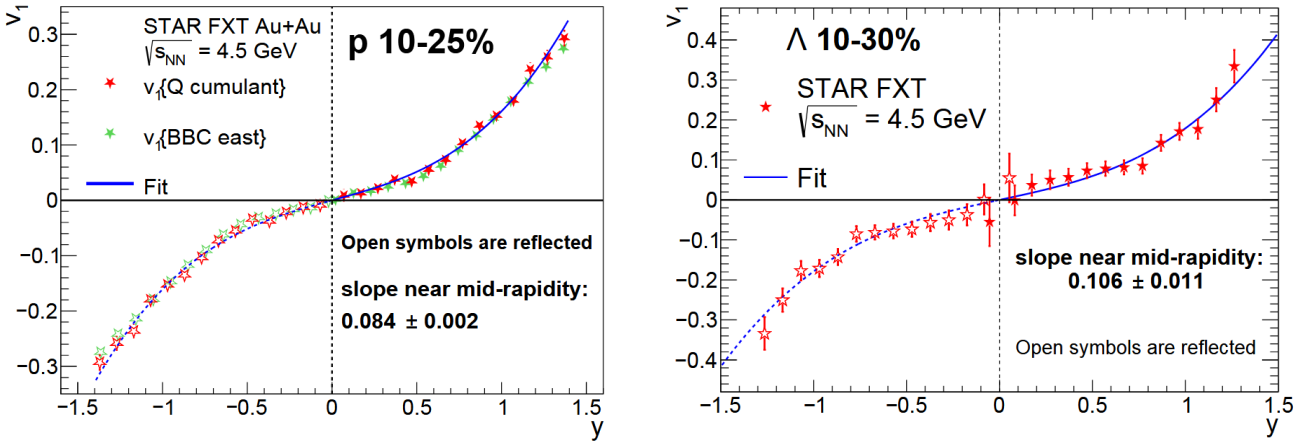


Figure 1.7: Results of the directed flow as a function of rapidity for protons (left) and Λ s (right) measured by STAR at $\sqrt{s_{NN}} = 4.5$ GeV [Ada21]. The data points measured with $y > 0$ have been reflected and the slope at midrapidity has been extracted from the fit.

This is confirmed at higher energies where the results from the STAR beam-energy scan phase I for protons [Ada14] and Λ s [Ada18b] do not show a difference within uncertainties. They are shown in the left panel of Fig. 1.8, where the slopes at midrapidity are presented as a function of the collision energy. At around $\sqrt{s_{NN}} \sim 10$ GeV a change in the sign can be noted where the deflection changes to be inwards. In the very high energy limit, the slope approaches zero what is expected since at this ultra-relativistic energies there should be no directed flow of the participants. Towards lower collision energies, the slope increases strongly. The results from the fixed-target STAR data for protons indicate a slightly higher increase as the trend measured by the E895 collaboration. However, a puzzle remains when the slopes of the protons and Λ hyperons are compared, where a significant difference is observed. This is still an open question which remains to be understood. The measurements at HADES energies of $\sqrt{s_{NN}} \sim 2$ GeV may shed some light to the behavior of the directed flow of protons in comparison to Λ s.

The collision energy dependence of the elliptic flow around midrapidity, integrated over p_t is shown in the right panel of Fig. 1.8. Above $\sqrt{s_{NN}} \sim 3 - 4$ GeV the elliptic flow is positive, which corresponds to a preferred in-plane emission of the particles. This could be expected from a simple picture that the compression of the hot and dense matter should be largest in the region of high nucleon density. At lower energies the elliptic flow becomes negative, which is not related to the fireball itself, but to the spectator particles. Due to their lower velocity, the Lorentz-contraction declines such that the expansion of the fireball is squeezed and the particle emission is forced to be out-of-plane. At even lower energies there should be a turning point

too, with FOPI measured to be around $\sqrt{s_{NN}} \sim 2 \text{ GeV}$ [And05, Rei12]. This is the energy, where the expansion of the fireball starts to dominate the motion of all the particles, including the spectators.

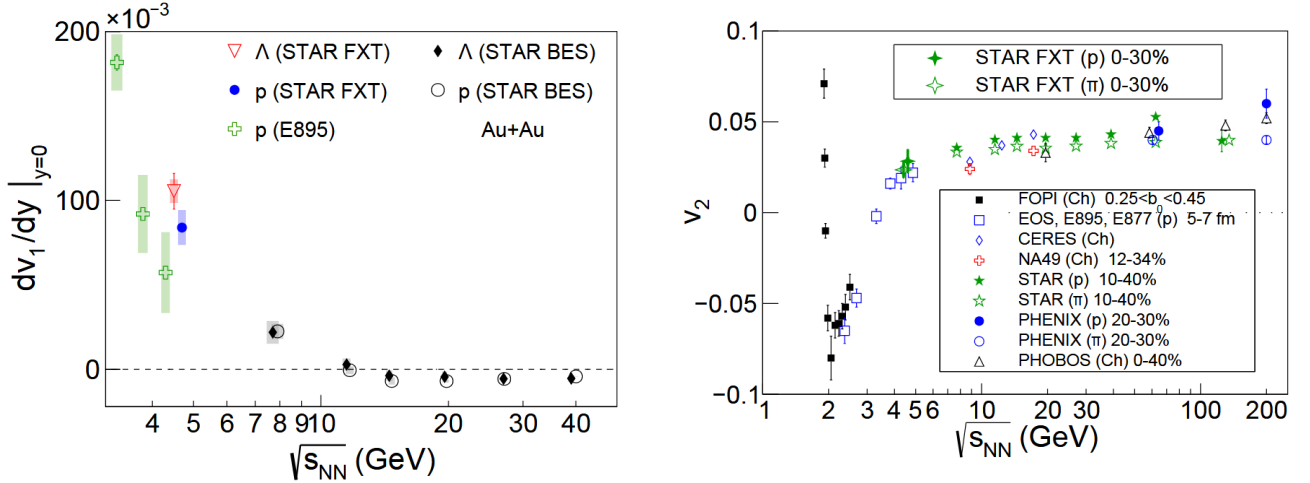


Figure 1.8: Results of the v_1 slope at midrapidity (left) and the elliptic flow (right) both as a function of the collision energy from various experiments [Ada21]. The v_1 slope for protons and Λ s from the STAR fixed-target run at $\sqrt{s_{NN}} = 4.5 \text{ GeV}$ [Ada21] and the STAR beam-energy scan [Ada14, Ada18b] are compared to the proton slopes measured by the E895 collaboration [Liu00].

1.4 Global polarization measurement

The theoretical ideas of a global polarization in heavy-ion collisions have their origin in two complementary effects which have been observed about 100 years ago. The first observation was made by the american physicist Samuel Jackson Barnett in 1915 [Bar15]. He took a cylinder of iron with zero magnetic moment. While rotating, the cylinder assembled a magnetic field and became magnetized, hence the orbital angular momentum was partly transferred to a spin polarization until thermodynamic equilibrium was reached. This is known as the Barnett effect. The second effect was observed by Albert Einstein and Wander Johannes de Haas in the same year [Ein15]. A cylindric ferromagnet started rotating when an external magnetic field built up. This is known as the Einstein-de Haas effect. In the beginning the cylinder was not magnetized and at rest, i.e. the electron spins and the orbital angular momentum are zero. If the cylinder gets magnetized by an external magnetic field (without exerting torque on the cylinder), in order to conserve the total angular momentum of zero, the cylinder has to start rotating. Hence there is a strong coupling between the spins of the particles inside a medium and its collective movement, i.e. its orbital angular momentum in case of a rigid body.

For fluids the situation is more involved. Usually the theory to describe the behavior of a fluid is hydrodynamics. The quantity to measure the bulk rotation is called vorticity $\vec{\omega}$ and defined as the rotation of the velocity field of the particles inside the medium, which is classically given by

$$\vec{\omega} = \frac{1}{2} \vec{\nabla} \times \vec{v}_{\text{fluid}}(\vec{x}). \quad (1.16)$$

There is also an experimental finding that demonstrates the relation between the vorticity and the spin polarization in liquid mercury [Tak16]. Due to the shear forces with the surrounding

pipe, the flowing mercury develops a velocity gradient. This vortical structure generates a spin current $\vec{j}^S \propto \nabla \vec{\omega}$ which could be measured through the inverse spin Hall effect as an electric field $\vec{E}_{\text{Hall}} \propto \vec{j}^S$. This showed for the first time that a polarization due to rotation can also happen in a liquid.

In all these cases, the macroscopic rotation was directly accessible and could be controlled as a variable of the experiment. The measurement of the spin polarization was also straightforward. This situation is very different in heavy-ion collisions where neither the orbital angular momentum nor the spins of the particles are directly accessible.

1.4.1 Global polarization in heavy-ion collisions

At relativistic heavy-ion collisions the system is described successfully by relativistic hydrodynamics. Especially in the description of bulk properties like the azimuthal anisotropies (flow) in the momentum distribution of the particles [Hei13], suggests that the QGP is a nearly perfect fluid. In peripheral collisions the orbital angular momentum L can be estimated in symmetric A+A collisions to be [Bec08]:

$$L \approx A\sqrt{s_{NN}} \frac{b}{2}\hbar, \quad (1.17)$$

with the atomic mass number A , the center-of-mass collision energy $\sqrt{s_{NN}}$, the impact parameter b and the reduced Planck's constant \hbar . From HADES at $\sqrt{s_{NN}} \sim 2 \text{ GeV}$ to LHC energies around $\sqrt{s_{NN}} \sim 5 \text{ TeV}$ the orbital angular momentum will be of the order $L \sim 10^3 \hbar$ up to $L \sim 10^6 \hbar$. It should be noted that even the orbital momentum increases with increasing beam energy, this might not hold for the participant medium itself, since at very high energies, most orbital momentum is carried away by the spectator particles. Still this large orbital angular momentum achieved in peripheral collisions might lead to a possible spin polarization of the particles which was first proposed in [Lia04, Vol04].

The first estimation of the global polarization was based on a spin-orbit coupling that changed the energy of the system and thus also the particle distributions. The mean polarization P for spin-1/2 particles can be calculated by counting spin-up N_\uparrow and spin-down particles N_\downarrow along the direction of polarization and it has been found to be related to the vorticity by:

$$P = \frac{N_\uparrow - N_\downarrow}{N_\uparrow + N_\downarrow} \approx \frac{\omega}{2T}, \quad (1.18)$$

where ω is the mean vorticity and T the mean temperature. From their calculations, the polarization should reach up to $P = 30\%$ at RHIC energies, i.e. $\sim 200 \text{ GeV}$ [Lia04]. However, this prediction is strongly dependent on the model of the quark-quark potential, the approximations used for small-angle scattering as well as the hadronization mechanism.

In a hydrodynamic approach the angular momentum manifests itself in the vortical structure of the system [Cse13]. A key ingredient for the formation of bulk properties is that a local thermodynamic equilibrium is achieved. This implies that the particles are well-described by the Bose-Einstein or Fermi-Dirac statistics [Bec13]:

$$f(x, p) = \frac{1}{e^{\beta(x) \cdot p - \frac{\mu_B}{T}} \pm 1}, \quad (1.19)$$

with the four momentum p , the chemical potential μ_B , the temperature T , the $+1$ corresponds to the Fermi-Dirac and the -1 to the Bose-Einstein statistics and the four-temperature $\beta(x) = (1/T)u(x)$. The latter includes the four-velocity $u(x)$ which is the four dimensional extension of the velocity field used in Eq. 1.16. The four-velocity field reproduces well the momentum spectra of the emitted hadrons which confirms the presence of local thermodynamic equilibrium in the early stages of the collision. The gradients in the temperature and four-velocity should be incorporated in the local vorticity of the system and later manifest in the spin polarization of the particles produced. Therefore, a spin potential has to be introduced to Eq. 1.19 depending on the local vorticity present in the medium. This implies that the local equilibrium is also valid for the spin degrees of freedom.

For the calculation of the final observables, the medium is usually devided into small cells for which Eq. 1.19 is applied according to the local properties. However, there are several different phases until the final particle distributions emerge. Therefore, the introduction of vorticity is not enough, more assumptions on the transfer of a possible spin polarization through the different phases of chemical and kinetical freeze-out are necessary. This requires a detailed modeling of these processes.

Under the assumption of the local thermodynamic equilibrium present from the early to the late stages of the collisions, a formula connecting the mean spin vector $S^\mu(p)$ of a spin-1/2 particle to the vorticity can be derived [Bec13]:

$$S^\mu(p) = -\frac{1}{8m} \epsilon^{\mu\nu\rho\sigma} p_\sigma \frac{\int d\Sigma_\lambda p^\lambda f_F (1-f_F) \tilde{\omega}_{\nu\rho}}{\int d\Sigma_\lambda p^\lambda f_F}, \quad (1.20)$$

where m is the mass of the particle, $\epsilon^{\mu\nu\rho\sigma}$ is the antisymmetric tensor, f_F the Fermi-Dirac distribution and the integration is performed of the 3D freeze-out hypersurface Σ_λ at constant time $t = \text{const}$, which could be replaced by $d\Sigma_\lambda p^\lambda \rightarrow dV \cdot E$ with dV being the volume to be integrated and $E = p^0$ being the energy of the spin-1/2 particle [Xie17]. The thermal vorticity:

$$\tilde{\omega}_{\mu\nu} = -\frac{1}{2} (\partial_\mu \beta_\nu - \partial_\nu \beta_\mu) \quad (1.21)$$

is the antisymmetric derivative of the four-temperature β and thus describes the gradients of the temperature and velocity fields. It has to be mentioned that in relativistic hydrodynamics, there are several possible definitions of the vorticity with prove of value in different applications. An overview can be found in [Kar21] and references therein.

Eq. 1.20 can be transformed to yield the spin polarization at a given space-time point x [Bec20]:

$$\vec{S}(x, p) \propto \frac{\gamma \hbar}{k_B T^2} \vec{v} \times \vec{\nabla} T + \frac{\gamma \hbar}{k_B T} (\vec{\omega} - (\vec{\omega} \cdot \vec{v}) \vec{v} / c^2) + \frac{\gamma \hbar}{k_B T} \vec{a} \times \vec{v} / c^2, \quad (1.22)$$

where k_B is the Boltzmann constant relating temperature and energy and \vec{a} is the acceleration. From Eq. 1.22 there are 3 contributions that can generate a spin polarization: the temperature gradient together with the particle flow (first term), the vorticity (second term) and the acceleration (third term).

To calculate a possible spin polarization according to formula 1.20, the thermal vorticity at the freeze-out hypersurface has to be determined. This involves a proper description of the hydrodynamic properties such as initial conditions, the equation of state and freeze-out conditions.

The thermal vorticity depends on the gradient of the four-velocity β , thus all calculations have to be performed in a 3+1D simulation framework. In several calculations the thermal vorticity has been found to be $\tilde{\omega}_{\mu\nu} \ll 1$ such that the relation to the mean spin can be simplified by a linear approximation. Then one results in a simpler relation for the mean spin 4-vector and the thermal vorticity given by:

$$S^\mu(x, p) = -\frac{1}{8m} \epsilon^{\mu\nu\rho\sigma} p_\nu \tilde{\omega}_{\rho\sigma}, \quad (1.23)$$

where the approximation of $(1-f_F) \approx 1$ has been used since the number density of the Λ s is very small. Eq. 1.23 defines a framework from which the polarization at the freeze-out hypersurface can be extracted from any model, that provides the four-velocity u^μ , the temperature T and the baryochemical potential μ_B .

The derivations above are only valid in local thermodynamic equilibrium which is extended to the spin degrees of freedom. The local equilibrium of the spin degrees of freedom is not trivial. To properly treat the spin dynamics one needs to introduce a spin chemical potential $\Omega_{\mu\nu} = T \omega_{\mu\nu}$, which is related to some definition of the vorticity [Bec18a, Flo19a]. This is still within ideal fluid dynamics and does not include dissipative effects. To calculate the dynamics including the spin, a set of conservation laws can be defined for a symmetric energy-momentum tensor $T^{\mu\nu} = T^{\nu\mu}$ [Flo19b] as

$$\partial_\mu T^{\mu\nu} = 0, \quad \partial_\lambda S^{\lambda,\mu\nu} = 0, \quad \partial_\mu N^\mu = 0, \quad (1.24)$$

where the first equation is the energy-momentum conservation, the second the angular momentum conservation and third is the baryon number conservation. However, this does not define the basic relations to properties like the four-temperature or the vorticity. They are not known and have to be constructed from the underlying microscopic theory which is the relativistic kinetic theory [Flo18]. It has to be applied in a quantum setup which goes back to Wigner [Wig32] who applied quantum corrections to statistical mechanics and provided a probability distribution for the whole phase-space known as the Wigner function. However, this formalism is complicated and still object of theoretical studies.

A lot of different approaches are currently developed to derive a proper theory of hydrodynamics with spin [Hat19, Shi20, Gal21, She21, Liu21]. Other attempts try to link the generation of vorticity to the axial currents which is known as the chiral vortical effect (see for example [Sor17, Pro18] and references therein).

In addition there are also completely different approaches to the final state polarization. One is the transfer of a possible polarization in the phase between the chemical and the kinetical freeze-out. The rescattering of particles might lead to a decline of the polarization. In contrast, model calculations in p+A collisions suggest an opposite effect, such that unpolarized anti-hyperons can become polarized by the final-state interactions predominantly with pions [Bar08]. Yet this effect yields vanishing polarization in case of A+A collisions [Bar11].

1.4.2 Polarization observables

As already discussed above, the system created in heavy-ion collisions carries a large orbital angular momentum which might transfer to the spin of the particles being produced. In general, a direct measurement of the particle spins is not possible. However, weak decays can be used to access the spin direction as will be outlined in the following for the Λ hyperon, but can also be applied to other hyperons like the Ξ or the Ω .

The Λ hyperon is a baryon and consists of an up-, down- and strange-quark. It is the lightest baryon containing a strange-quark and hence it can only decay via the weak interaction which can change the flavor of the quarks. The most likely decays are $\Lambda \rightarrow n + \pi^0$ (35.8 %) and $\Lambda \rightarrow p + \pi^-$ (63.9 %) [Zyl20]. The two neutral particles in the former decay are difficult to measure and hence the analysis is focussed on the latter decay into a proton and a negatively charged pion.

To conserve the angular momentum, the decay daughters can add to two different states: a p-wave ($l = 1$) and a s-wave ($l = 0$) while the latter is only allowed due to the parity violation of the weak interaction. This introduces an angular dependence to the transition amplitude which results in an angular distribution of the daughters in the rest frame of the Λ given by

$$\frac{dN}{d\Omega} = \frac{N_0}{4\pi} \left(1 + \alpha_\Lambda \vec{P} \cdot \vec{p}_p^* \right), \quad (1.25)$$

where $\alpha_\Lambda = 0.732 \pm 0.014$ [Zyl20] is the asymmetry parameter of the decay, \vec{P} is the spin polarization of the Λ and \vec{p}_p^* is the momentum of the proton in the rest frame of the Λ . The decay parameter α_Λ describes to which extend the spin orientation of the Λ is transferred to the protons direction and thus the projection of the proton direction in the rest frame of the Λ onto a particular polarization direction will reflect in the angular distribution. In case of the global polarization the polarization axis is defined by the orbital angular momentum \vec{L} . Therefore Eq. 1.25 normalized to one can be rewritten as:

$$\frac{dN}{d\cos(\theta^*)} = \frac{1}{4\pi} (1 + \alpha_\Lambda P_\Lambda \cos(\theta^*)), \quad (1.26)$$

where P_Λ is the polarization with respect to the orbital angular momentum \vec{L} and θ^* is the angle of the momentum direction of the proton to \vec{L} in the rest frame of the Λ as shown in Fig. 1.9. $\alpha_\Lambda P_\Lambda$ can also be interpreted as the slope of the angular distribution in $\cos(\theta^*)$. Thus it is possible to measure the polarization of the Λ hyperon from the angular distribution of the daughter proton. For this reason this decay is often called self-analyzing.

The global polarization can be calculated according to

$$\langle \cos\theta^* \rangle = \int \frac{dN}{d\Omega} \cos\theta^* d\Omega = \alpha_\Lambda P_\Lambda \langle \cos^2\theta^* \rangle \quad (1.27)$$

which can be transformed to get

$$P_\Lambda = \frac{\langle \cos\theta^* \rangle}{\alpha_\Lambda \langle \cos^2\theta^* \rangle} = \frac{3}{\alpha_\Lambda} \langle \cos(\theta^*) \rangle. \quad (1.28)$$

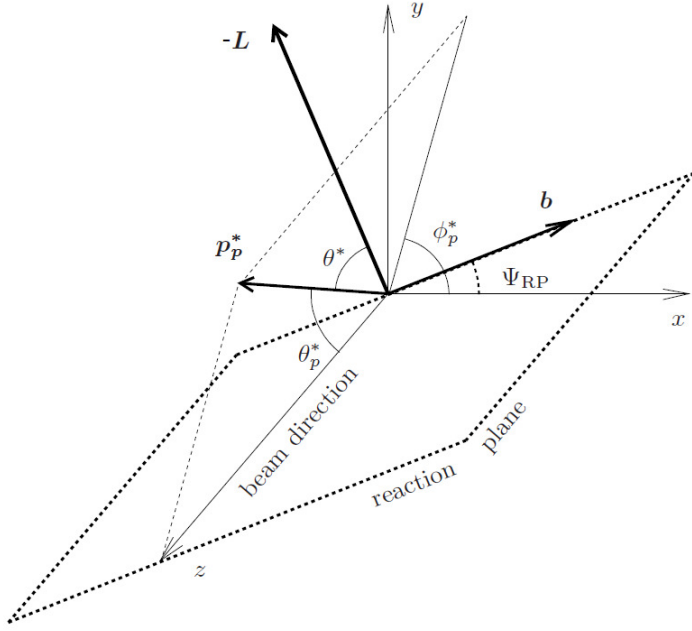


Figure 1.9: Sketch of the geometrical circumstances for the polarization measurement [Sel06].

The orbital angular momentum \vec{L} is perpendicular to the reaction plane Ψ_{RP} spanned by the beam axis (z direction) and the impact parameter \vec{b} . The momentum of the proton \vec{p}_p^* in the rest frame of the Λ hyperon is shown with all respective angles as will be used in the polarization analysis. Note the negative sign in front of \vec{L} which has been added. This is to stick to the convention of defining $\vec{L} = \vec{b} \times \vec{p}_{\text{Beam}}$.

The brackets $\langle \cdot \rangle$ denote the average over the solid angle and all possible orientations of the orbital angular momentum. The orientation of \vec{L} is perpendicular to the reaction plane of the collision. Hence Eq. 1.28 has to be transformed. The angle θ^* can be separated in the independent azimuthal ϕ_p^* and polar θ_p^* components (see Fig. 1.9) by using the trigonometric relation $\cos(\theta^*) = \sin(\theta_p^*)\sin(\Psi_{RP} - \phi_p^*)$. Assuming perfect detector acceptance the integration over the polar angle θ_p^* can be performed resulting in

$$P_\Lambda = \frac{8}{\pi \alpha_\Lambda} \langle \sin(\Psi_{RP} - \phi_p^*) \rangle. \quad (1.29)$$

It is important to mention that this equation has a similar structure as the observables for the flow analysis (see Sec. 1.3) and hence the same techniques for the analysis can be applied. The methods used to measure the polarization will be described in Sec. 4.

To measure the polarization of multi-strange particles the technique is similar. For example the decays $\Xi^- \rightarrow \Lambda + \pi^-$ (99.887%) and $\Omega^- \rightarrow \Lambda + K^-$ (67.8%) both have a Λ hyperon in the final state which decays further. Since both decays are weak the polarization is partially transferred to the Λ and then to the proton which can be measured according to Eq. 1.29. The decay parameters of $\alpha_{\Xi^-} = -0.401$ and $\alpha_{\Omega^-} = 0.0157$ [Zyl20] are smaller which makes the measurement more difficult. However, such measurements have recently been performed [Ada20c].

1.4.3 Theoretical calculations of the Λ polarization

The ansatz in Eq. 1.23 has been used in [Vit20] to calculate the polarization of Λ and $\bar{\Lambda}$ for different collision energies. These calculations have been performed in the framework of the UrQMD transport model [Bas98]. The results for the proper temperature and thermal vorticity in the plane perpendicular to the orbital angular momentum (see Sec. 1.2 the geometrical definitions) are shown in Fig. 1.10 for Au+Au collisions at $\sqrt{s_{NN}} = 7.7$ GeV, 15 fm/c after the collision time. The proper temperature peaks at the participants from the core nuclei and shows a non-trivial gradient structure towards the outer regions. The thermal vorticity shows the expected curl structure, due to the shear forces from the bypassing spectator nucleons. The maximum values are around $|\tilde{\omega}_{xz}| \leq 0.3$ which fulfills the assumption used to derive Eq. 1.23.

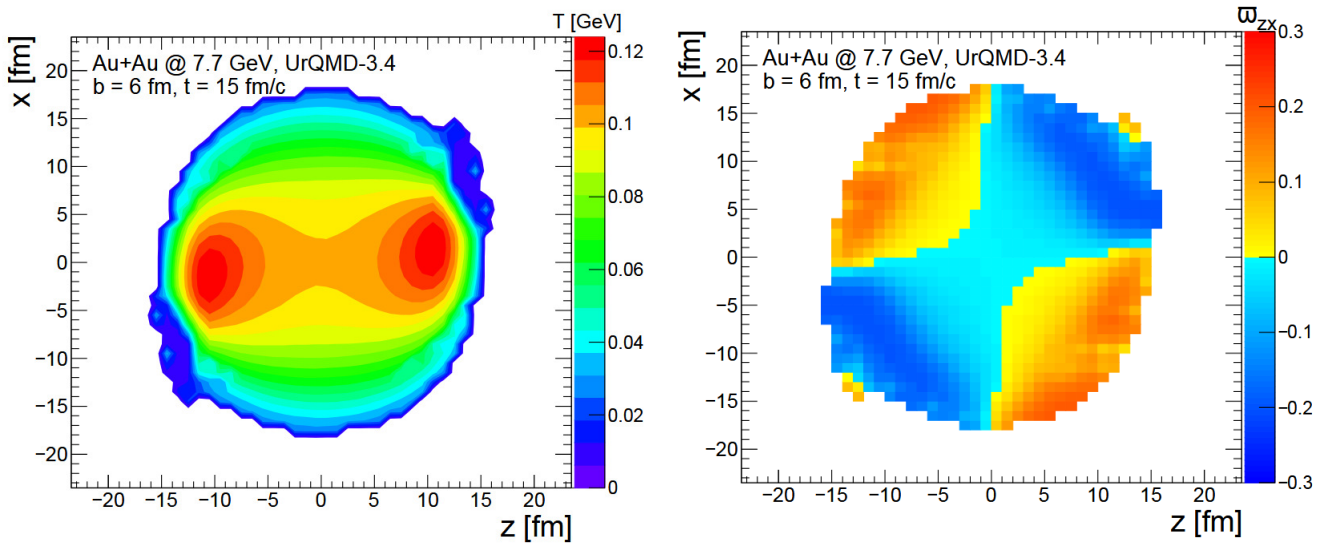


Figure 1.10: Distribution of the proper temperature (left) and the thermal vorticity (right) in the reaction plane perpendicular to the orbital angular momentum. The distributions have been calculated within the UrQMD transport model for Au+Au collisions at $\sqrt{s_{NN}} = 7.7$ GeV with an impact parameter of 6 fm and $t = 15$ fm/c after the collision time [Vit20].

The same ansatz has also been used in a hybrid approach using the UrQMD transport model [Bas98] for the early and late stages of the collision and the dissipative hydrodynamical model vHLLE [Kar15a] for the hot and dense stage of the collision. The results are shown in Fig. 1.11 and are well in agreement with the experimental data. The same can be said for the calculations performed within the AMPT model [Li17] which are also shown. For both calculations, the effect of "feed-down" has been considered to account for the polarization of primary particles decaying into a Λ hyperon like Σ^0 or Ξ . These higher lying states might be polarized themselves, however, the transfer of their polarization to the daughter particles depends strongly on the decay channel and the interaction involved. Consider example the electromagnetic decay of

$$\Sigma^0 \left(\frac{1}{2}^+ \right) \rightarrow \Lambda \left(\frac{1}{2}^+ \right) + \gamma (1^-) \quad (1.30)$$

where inside the brackets the angular momentum and parity J^P is represented. The conservation of angular momentum in this decay demands the spin of the Λ to be opposite to that of the Σ^0 .

Consequently, if Σ^0 is polarized along the global angular momentum, then the Λ hyperons will be polarized in the opposite direction and thus the overall measurement of the polarization is reduced.

1.4.4 Experimental results on the global polarization

The first measurements have been performed by the STAR collaboration in Au+Au collisions at $\sqrt{s_{NN}} = 62$ and 200 GeV center-of-mass energy [Sel06, Sel07a, Sel07b, Abe07]. The polarization was measured for Λ and $\bar{\Lambda}$ also differentially as a function of centrality, transverse momentum p_t and pseudorapidity η . No dependence within statistical uncertainty in either of these quantities has been found. Within the acceptance of the STAR detector, an upper limit for the polarization was estimated to be $|P_{\Lambda, \bar{\Lambda}}| \leq 2\%$. The results were confirmed from the analysis of strange vector mesons K_0^* and ϕ [Che07]. In contrast to the spin-1/2 particles, the vector mesons of spin 1 are expected to be aligned with the orbital angular momentum axis [Lia05]. Within uncertainties, there was no significant deviation from the results expected in case of no global polarization [Che07].

In 2017 the whole field gained new stimulation by new measurements performed by STAR [Ada17, Vol17]. During their beam energy scan phase I program, Au+Au collisions have been recorded of various center-of-mass energies ranging from $\sqrt{s_{NN}} = 7.7$ to 39 GeV. The polarization of Λ and $\bar{\Lambda}$ hyperons have been performed showing a continuous enhancement of the hyperons' polarization towards the lower beam energies to about $P_{\Lambda} \approx 2\%$ at $\sqrt{s_{NN}} = 7.7$ GeV as shown in Fig. 1.11. The effect of feed-down has been investigated and narrowed to be of the order of 10% [Kar17, Xia19, Bec19]. The two theoretical calculations in Fig. 1.11 are shown with and without feed-down corrections. Clearly, the energy dependence is decreased slightly, but within the current statistical uncertainties such an effect could not be resolved.

The polarization of $\bar{\Lambda}$ is consistently higher than the polarization of the Λ hyperons, which might indicate a possible effect of the magnetic field. In contrast to the global polarization, which is similar for particles and anti-particles, due to the magnetic moment the coupling of the particles spin to the magnetic field is opposite. Since in heavy-ion collisions, strong magnetic fields of the order $B \sim 10^{13}$ T are expected to occur, a possible difference in the spin polarization might offer the possibility of a magnetometer. However, the difference in the polarization is not significant within the precision of the measurement and there are also other possible sources which will be discussed later. Fig. 1.11 summarizes the measurements of the STAR collaboration for Λ and $\bar{\Lambda}$. At $\sqrt{s_{NN}} = 200$ GeV new results have been published and a finite polarization at the per mille level has been found [Ada18a]. The centrality dependence was also measured and shows an increasing trend with growing impact parameter as expected from Eq. 1.17. At even higher energies, ALICE measured the polarization for Λ and $\bar{\Lambda}$ in Pb+Pb collisions at $\sqrt{s_{NN}} = 2.76$ and 5.02 TeV and found it to be zero within uncertainties [Ach20].

The trend of the $\bar{\Lambda}$ hyperons indicates a larger polarization towards lower beam energies. While the polarization due to the vorticity is the same for particles and anti-particles, their coupling to the electro-magnetic field is related to the magnetic moments μ_M . These magnetic moments are opposite for particles and anti-particles and therefore the polarization might be splitted. The colliding ions provide a large number of positive charge, $Z = 79$ for a fully stripped Au-ion. The spectator protons create a magnetic field in the region of the collision medium which will be on average aligned with the orbital angular momentum and thus potentially affect the global polarization resulting in a splitting. Such an effect will increase the polarization of the anti-particles, while the polarization of the particles is reduced. Turning the argument around this

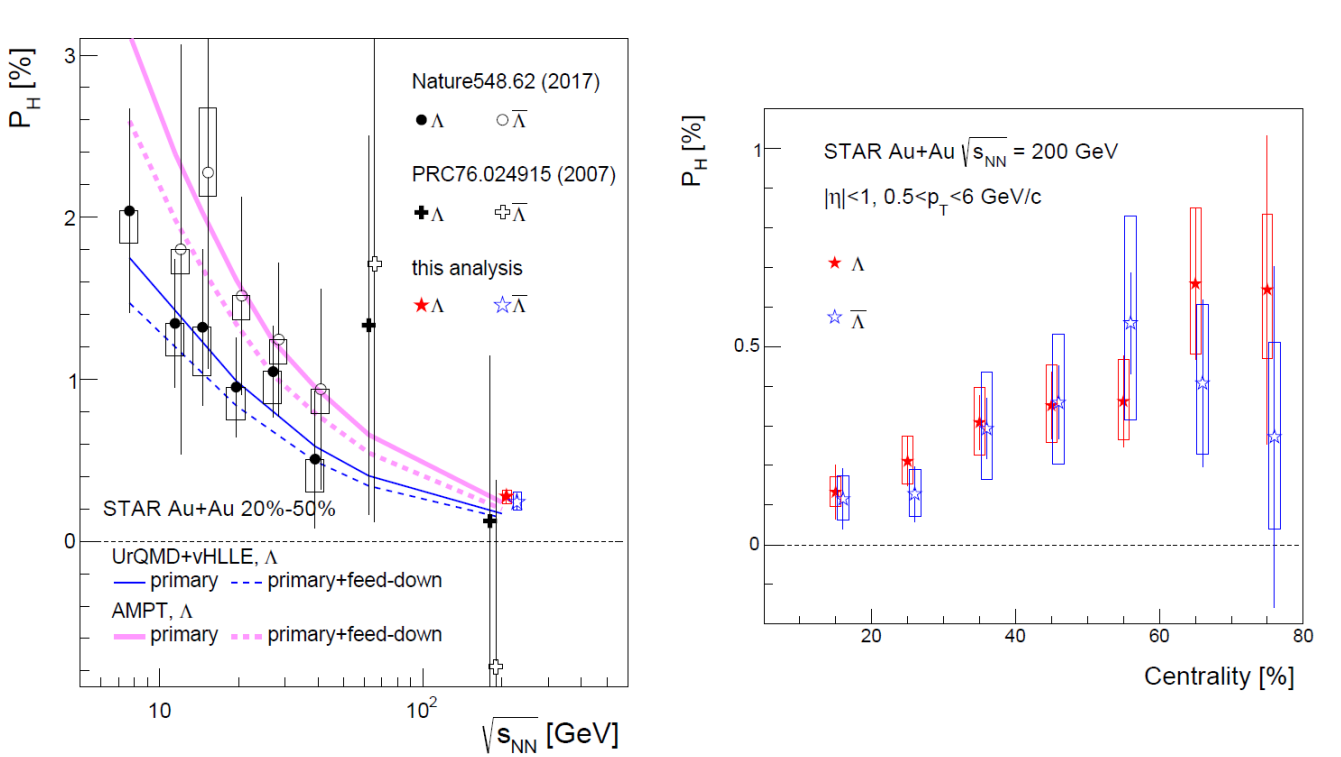


Figure 1.11: STAR results for the global polarization measurement in Au+Au collisions as a function of the collision energy for a centrality of 20 – 50% (left) and centrality dependent for $\sqrt{s_{NN}} = 200$ GeV [Ada18a]. Both Λ and $\bar{\Lambda}$ are shown. To describe the energy dependence of the Λ polarization, two model calculations based on UrQMD+vHLLE [Kar15a] and AMPT [Li17] are plotted.

could offer a possibility to actually measure the magnetic field strength in heavy-ion collisions from the splitting in the global polarization. However, there are also other explanations for a polarization splitting that have to be ruled out first. Feed-down corrections might be taken into account as they are in general different for particles and anti-particles [Bec17]. For the lower beam energies the baryons in the colliding ions play an ever important role such that a polarization splitting might originate from the fact that Λ and $\bar{\Lambda}$ are produced in different regions of the fireball as calculated in [Vit20]. According to their calculations, the difference increases with decreasing collision energy as can be seen in the right panel of Fig. 1.14. Besides the measurement of the polarization of weakly decaying particles, one can also measure the spin alignment of the vector mesons like the ϕ . The observable is the probability of the spin projection to be zero [Vol17], since for a spin-1 particle the z-component can be $S_z = -1, 0, 1$. In case of no spin alignment, the expectation for this probability is given by the spin density matrix element $\rho_{00} = 1/3$ and an alignment will reflect in a deviation from this value. The first estimations have been proposed in 2005 [Lia05] and results in

$$\rho_{00} = \frac{1}{3 + \left(\frac{\omega}{T}\right)^2}. \quad (1.31)$$

From the measurement of the Λ polarization one can estimate the vorticity and then compare the expected deviation with the experimental results. The results for K^{*0} measured at $\sqrt{s_{NN}} = 54.4$ and 200 GeV by STAR and at $\sqrt{s_{NN}} = 2.76$ GeV by ALICE are shown in Fig. 1.12 as a function of

the collision centrality defined by the mean number of participants $\langle N_{\text{part}} \rangle$. While ALICE found the $\rho_{00} \sim 1/3$ at high transverse momenta, all measurements show a clear deviation from $1/3$ for $p_t < 1.5 \text{ GeV}/c$ which is maximal at mid-central collisions. The deviation is very strong and cannot be explained solely by the vortical effects which can be estimated from the measured Λ polarization. Measurements of the ϕ meson performed by STAR indicate an opposite trend [Sin21] which brings further challenge to the understanding of the spin alignment of the vector mesons and makes the theoretical modeling even more difficult.

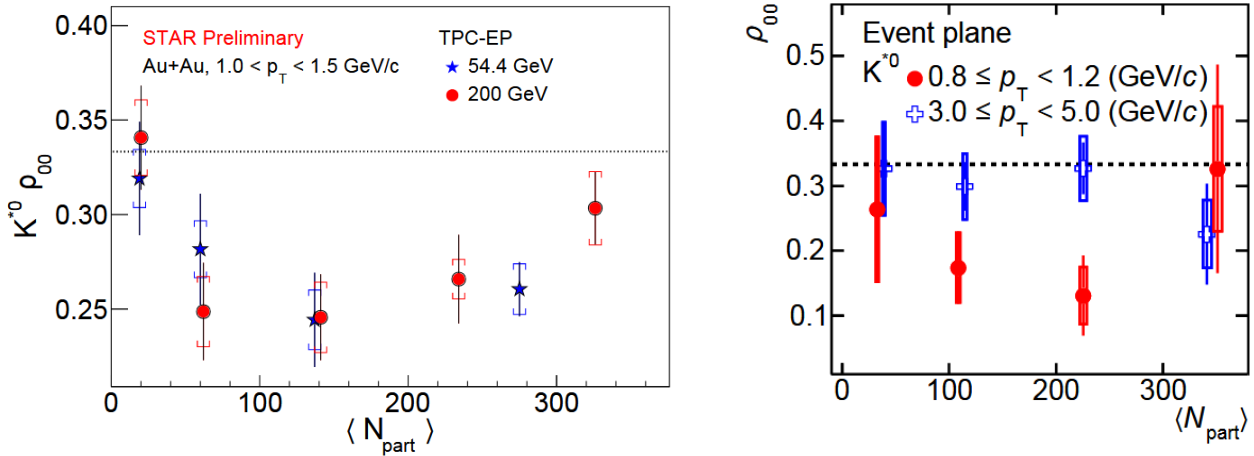


Figure 1.12: Measurement of the spin alignment of K^{*0} measured for $\sqrt{s_{NN}} = 54.4$ and 200 GeV by STAR [Sin21] (left) and at $\sqrt{s_{NN}} = 2.76 \text{ GeV}$ by ALICE [Moh21] (right) as a function of the collision centrality defined by the mean number of participants $\langle N_{\text{part}} \rangle$.

1.4.5 Local vorticity and longitudinal polarization

Using relativistic hydrodynamics and assuming local equilibrium also for the spin degrees of freedom already provides a good description of the energy dependence of the global polarization shown in the left panel of Fig. 1.11. However, it is very unlikely that a local equilibrium is guaranteed from the early stages of the collision to the freeze-out which also applies to the particle spins. While the simple picture is well in agreement with the energy dependence of the measured Λ polarization, there are also experimental results that are not described. In contrast to the rigid body, a fluid does not only rotates as a whole, but also on a local scale. Therefore, several local effects can be imagined which generate local vorticity. The most prominent effect is related to the elliptic flow. Due to the expansion of the fireball, there should be different signs of the local vorticity in the different xy -quadrants of the reaction plane frame. This can be determined by measuring the longitudinal polarization:

$$P_z = \frac{3 \langle \cos(\theta_p^*) \rangle}{\alpha_\Lambda} \quad (1.32)$$

as a function of the flow angle $\Delta\phi$. This has been done by the STAR collaboration at $\sqrt{s_{NN}} = 200 \text{ GeV}$ collision energy and the results are shown in the left panel of Fig. 1.13. The measurement is in agreement with the expectations of a elliptic flow $v_2 > 0$ which leads to a preferred in-plane emission of the particles with respect to the reaction plane. However, the calculations based on the hydrodynamic approach including the thermal vorticity and assuming

local equilibrium are shown in the right panel. The predictions in terms of the sign are exactly opposite to the experimental finding which is known as the "spin sign problem". The theoretical calculations are very consistent, independent of the model that has been used to determine T, u^μ and μ_B . Further investigations have been done using different definitions of the vorticity [Wu19] without resolving the problem. Only recent theoretical calculations found a new term in the spin polarization vector induced from thermal shear that contributes exactly opposite to the local polarization as the thermal vorticity [Fu21, Bec21], yet the studies are ongoing.

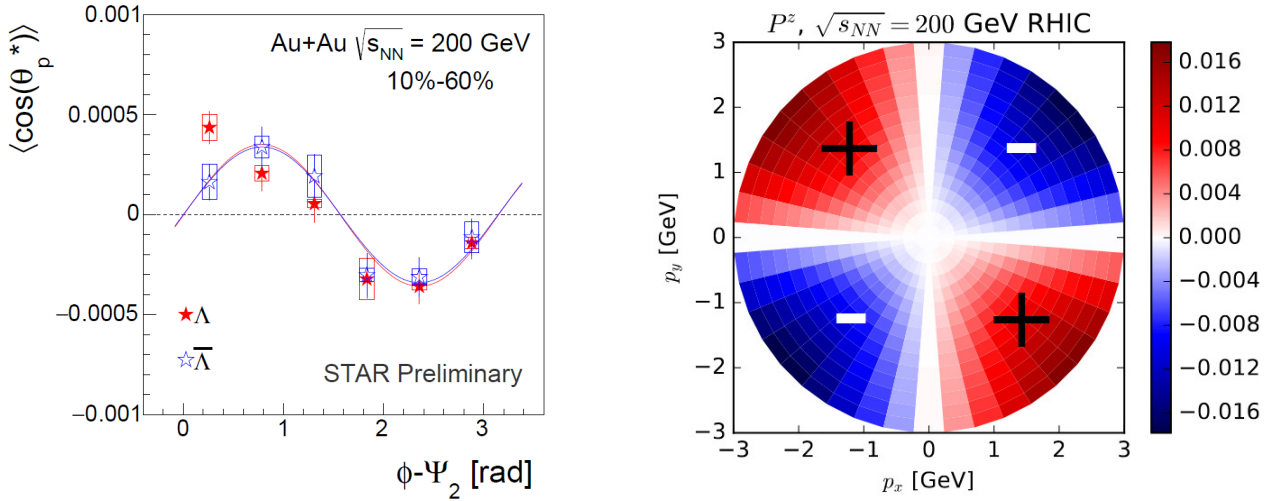


Figure 1.13: Left panel: Measurement of the longitudinal polarization as a function of the azimuthal angle with respect to the reaction plane in Au+Au collisions at $\sqrt{s_{NN}} = 200$ GeV [Nii19]. Right panel: Predictions of the longitudinal polarization in the plane transverse to the beam axis calculated from ideal hydrodynamics assuming local equilibrium [Bec18b].

1.4.6 Expectations for HADES measurements

To derive reliable predictions of the polarization pattern at lower collision energies as measured with HADES, several issues have to be addressed. In contrast to the ultra-relativistic heavy-ion collisions at RHIC or LHC, the dominating degrees of freedom are assumed to be the baryons. Thus one cannot talk about a formation of a QGP. In general, the system has a much longer lifetime thought with moderate temperature and densities. This has a lot of consequences for the theoretical approaches developed as will be discussed in the following.

A first question is related to the thermodynamic equilibrium which is required for most theoretical calculations to find a relation between vorticity and the particles' spin. Thus the application of the thermal vorticity to low energy collisions of $\sqrt{s_{NN}} \sim 2$ GeV is questionable, since the system might not reach global thermodynamic equilibrium and thus the local temperature is not well-defined. In such a case the kinematical vorticity might be a more useful concept since it does not contain the proper temperature and reads [Bec15]:

$$\omega_{\mu\nu} = \frac{1}{2}(\partial_\nu u_\mu - \partial_\mu u_\nu), \quad (1.33)$$

with $u(x)$ being the four-velocity field. In comparison to Eq. 1.21 the temperature does not appear in the calculation. This approach based on the kinematical vorticity has been followed

within the framework of the UrQMD transport model by X.-G. Deng et al. [Den20]. Their calculations have been extended down to collision energies of $\sqrt{s_{NN}} = 1.9 \text{ GeV}$ where they predict the angular momentum to be zero and consequently the global polarization should vanish. According to their study, the maximum polarization is achieved in the region between $\sqrt{s_{NN}} = 3-5 \text{ GeV}$. This is suggested by the energy dependence of the kinematical vorticity shown in the left panel of Fig. 1.14. However, as the emission of the Λ hyperons extends over a longer time period, the actual polarization may differ from the behavior of the initial vorticity. Such a study has been done by O. Vitiuk et al. [Vit20]. The emission function for Λ and $\bar{\Lambda}$ is displayed in the right panel of Fig. 1.14, showing a maximum of the emission of the Λ hyperons around $t = 10-25 \text{ fm/c}$ while the energy dependence is small.

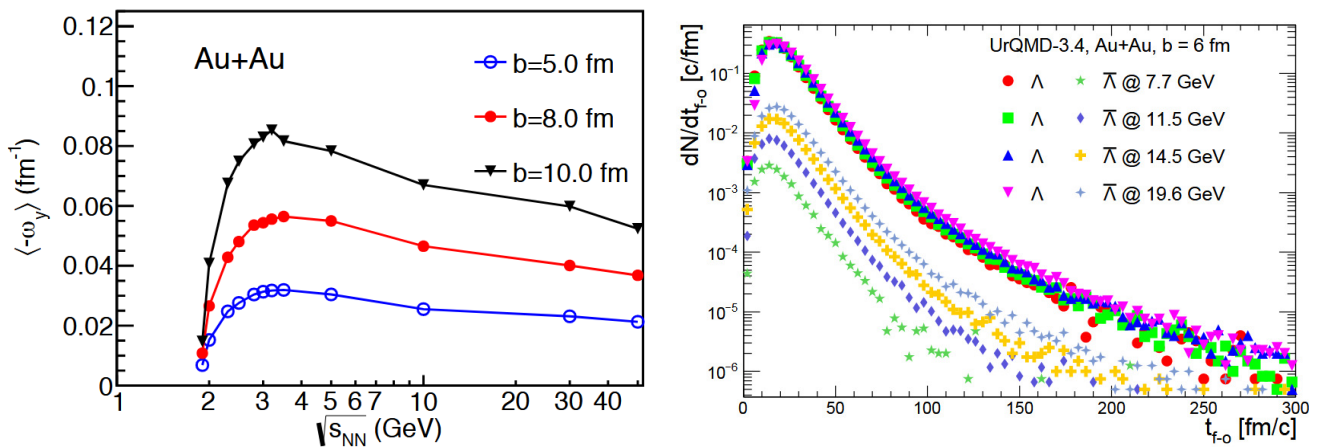


Figure 1.14: Left panel: Calculation of the kinematical vorticity along the direction of the global angular momentum [Den20]. Right panel: Energy and time dependence of the emission function of Λ and $\bar{\Lambda}$ [Vit20]. Even different assumptions have been made, both calculations have been done in the framework of UrQMD for Au+Au collisions.

Recently there have been also calculations based on the AMPT model [Lin05] which support that the maximum polarization is achieved at $\sqrt{s_{NN}} = 7.7 \text{ GeV}$ followed by a decreasing trend towards lower beam energies reaching a value of $P_{\Lambda} \sim 1\%$ for HADES energies [Lia21]. More details on the calculation can be found in [Jia16, Hua20].

Further predictions for the energy dependence between $2.4 \leq \sqrt{s_{NN}} \leq 11 \text{ GeV}$ of the Λ polarization have been made by Y.B. Ivanov [Iva21] based on a thermodynamic approach within the three-fluid dynamical model [Iva06]. In this model each of the colliding nuclei is described by hydrodynamics as baryon-rich fluids. At midrapidity, where most particles are produced, the fireball is described using different equations of state. The fireball is coupled to the surrounding fluids by the friction terms in the hydrodynamic calculations. The global thermal vorticity will then depend on thermal vorticity of the baryonic B and the fireball medium F . It is calculated as [Iva20]:

$$\langle \tilde{\omega}_{\mu\nu} \rangle = \frac{\int d^3x \left(\tilde{\omega}_{\mu\nu}^B(x, t) \epsilon_B(x, t) + \tilde{\omega}_{\mu\nu}^F(x, t) \epsilon_F(x, t) \right)}{\langle \epsilon \rangle(t)}, \quad (1.34)$$

as an average weighted by the corresponding energy densities. Starting from Eq. 1.20 the polarization of the Λ hyperons can be derived [Iva19] to yield:

$$P_\Lambda = \frac{\langle \tilde{\omega}_{xz} \rangle}{2} \left(1 + \frac{2}{3} \frac{\langle E_\Lambda \rangle - m_\Lambda}{m_\Lambda} \right). \quad (1.35)$$

The calculations of the Λ polarization have been performed for Au+Au collisions at fixed impact parameter varying from 2 – 8 fm. The results for different equations of state are shown in the left panel of Fig. 1.15. As expected the polarization grows significantly with increasing impact parameter. The energy dependence predicts an enhancement to $\sqrt{s_{NN}} \sim 3$ GeV and then seems to saturate down to the collision energies measured with HADES. In the right panel the same calculations are shown only for $b = 6$ fm. The bands indicate the effect of a symmetric rapidity cut which clearly decreases the integrated polarization. Thus the polarization is predicted to be lowest at midrapidity and increases symmetrically towards more forward/backward rapidities.

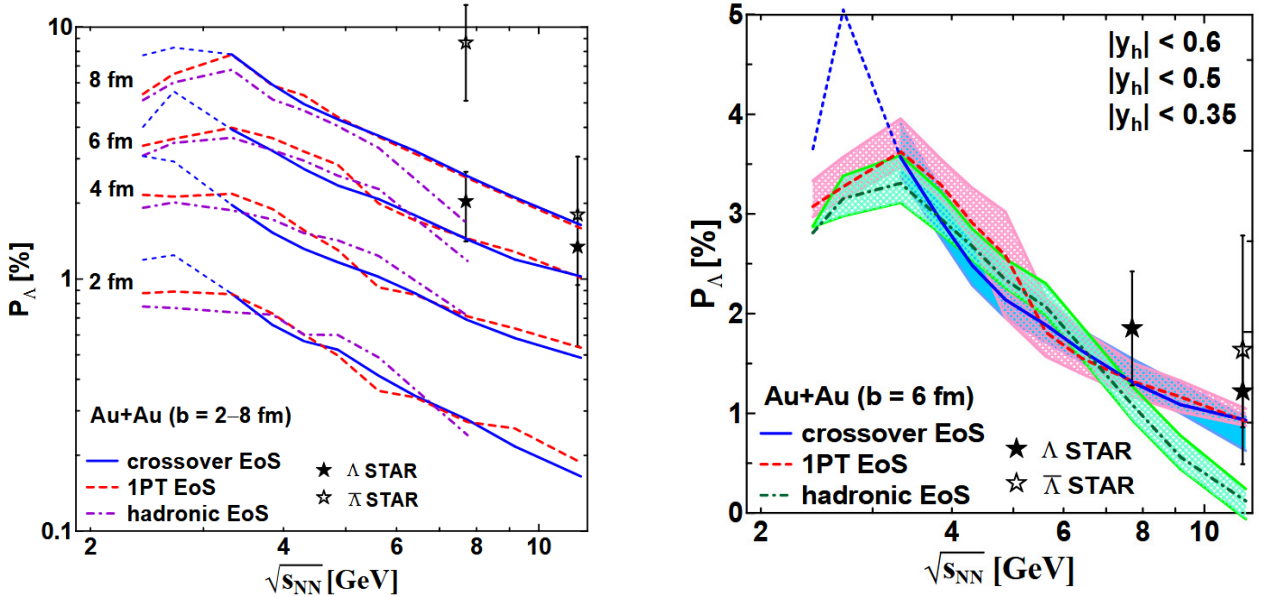


Figure 1.15: Predictions of the energy dependence of the Λ polarization derived from three-fluid dynamics using different equations of state [Iva21]. Left panel: The dependence is fragmented for different impact parameters. Right panel: The bands show the dependence on the rapidity. The upper borders corresponds to a rapidity range of $|y_{CM}| < 0.6$, the dashed line to $|y_{CM}| < 0.5$ and the lower border to $|y_{CM}| < 0.35$.

More detailed predictions for HADES measurements for both Au+Au at $\sqrt{s_{NN}} = 2.4$ GeV and Ag+Ag collisions at $\sqrt{s_{NN}} = 2.55$ GeV have been derived based on the hydrodynamical description [Vit20] discussed above. The polarization of the Λ hyperons is calculated using Eq. 1.23. The transverse momentum and rapidity dependence calculated from this ansatz are displayed in Fig. 1.16 and 1.17 respectively. Here the polarization is projected onto the y -axis, opposite to the direction of the orbital angular momentum, such that the actual polarization of the Λ hyperons is $P_\Lambda = -P_y$. Concerning the overall magnitude of the polarization, a strong enhancement towards lower beam energies is predicted. The magnitude strongly increases as the impact parameter grows, as expected by the larger angular momentum in peripheral collisions. Comparing the different systems the polarization seems to be stronger in Ag+Ag collisions, however

the results are not directly comparable since the centrality² of the collision is very different. A range of $b = 5.5 - 9$ fm in Au+Au collisions corresponds roughly to a centrality range of 10–40% while for Ag+Ag it is 20–60%. As the polarization strongly rises towards peripheral collisions³ the difference between the two collision systems can be to large extend related to this effect.

The transverse momentum dependence shows an increase towards higher momenta, which is amplified in more peripheral collisions, similar for both systems. The rapidity dependence strongly depends on the centrality. While for $b = 5.5$ fm the polarization has a minimum at midrapidity and rises slowly towards the outer regions similar as the prediction from three-fluid dynamics (see Fig. 1.15). However, as the impact parameter grows the trend changes and the maximum polarization is found at midrapidity and decreases continuously in the outer regions. There are further theoretical approaches like the kinetic quark-gluon string model [Baz18] based on the chiral vortical effect that predict a strong enhancement of the global polarization below the STAR measurements. However, their calculations have not yet been extended down to the HADES energies and thus the expectations for $\sqrt{s_{NN}} \sim 2$ GeV are unclear.

In summary, the HADES experiment provides an important tool to investigate the behavior of the polarization towards lower collision energies. As the system is dominated by the initial baryons, the approaches applied to the higher collision energies cannot be used straightforward. Recently, several calculations have been performed to predict the behavior for HADES energies, also differentially. While some models predict a strong increase of the polarization, others expect the global polarization to reach the maximum around $\sqrt{s_{NN}} \sim 3 - 5$ GeV and then drop quickly to zero. Consequently, the HADES measurements will set limits to the theoretical calculations and provide further inside to the bulk behavior of the medium.

² The centrality describes the overlap of the two colliding nuclei as a fraction of the total cross section. More details and the procedure to determine the centrality in HADES are given in Sec. 3.7.2

³ For head-on collisions, the centrality is 0% and grows the more peripheral the collision gets.

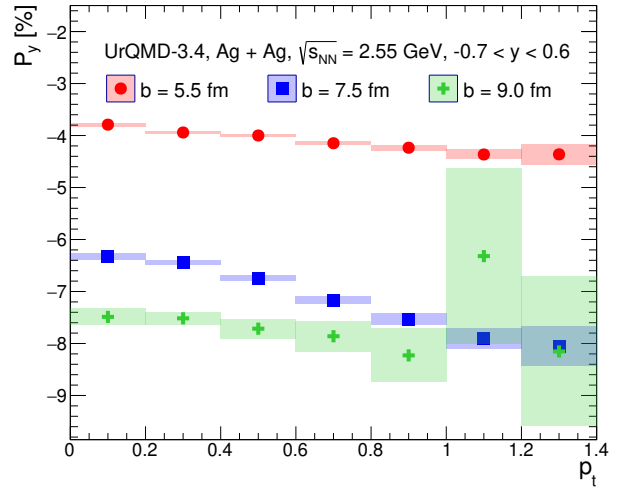
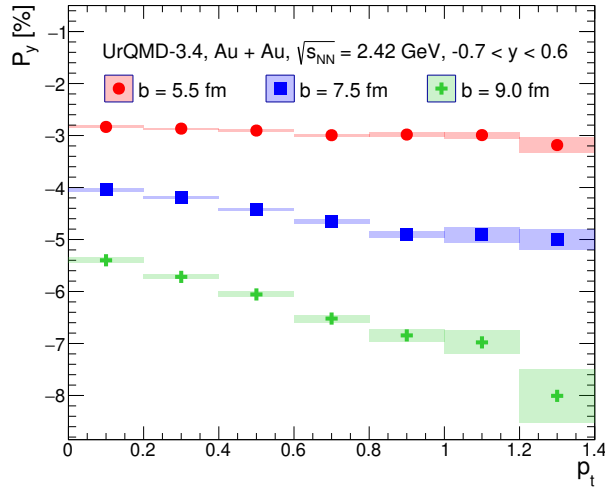


Figure 1.16: Transverse momentum dependence of the Λ polarization for different impact parameters in Au+Au collisions at $\sqrt{s_{NN}} = 2.4$ GeV (left) and Ag+Ag collisions at $\sqrt{s_{NN}} = 2.55$ GeV (right) [Vit21]. The polarization is projected onto the y -axis which is opposite to the orbital angular momentum such that the global polarization is $P_\Lambda = -P_y$. The calculation has been performed within the hydrodynamical framework described in [Vit20].

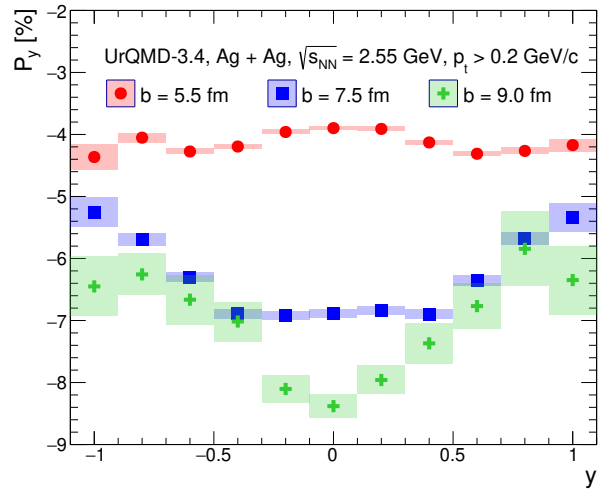
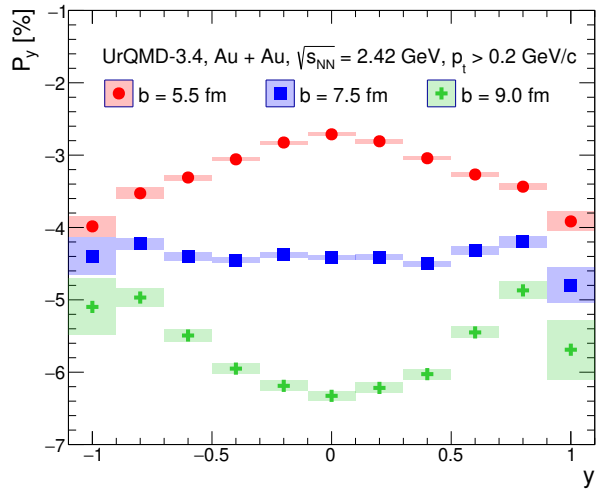


Figure 1.17: Rapidity dependence of the Λ polarization for different impact parameters in Au+Au collisions at $\sqrt{s_{NN}} = 2.4$ GeV (left) and Ag+Ag collisions at $\sqrt{s_{NN}} = 2.55$ GeV (right) [Vit21]. The polarization is projected onto the y -axis which is opposite to the orbital angular momentum such that the global polarization is $P_\Lambda = -P_y$. The calculation has been performed within the hydrodynamical framework described in [Vit20].



2 HADES setup

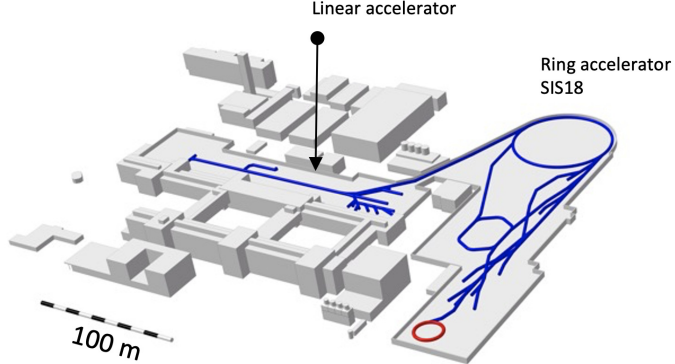


Figure 2.1: Sketch of the GSI facility. The HADES experiment is placed in the Experimental Hall II.

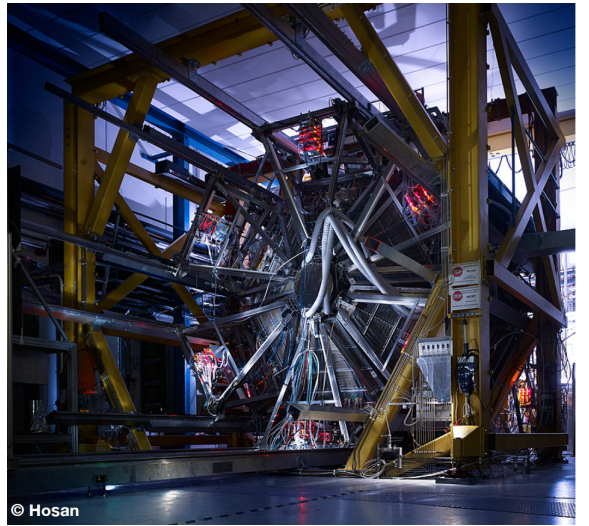


Figure 2.2: Picture of the HADES detector [Ada19a].

The first proposal for the HADES experiment goes back to the year 1994 [Sal94]. HADES is the acronym for High Acceptance DiElectron Spectrometer (see Fig. 2.2) and the experiment is located at the GSI Helmholtzzentrum für Schwerionenforschung in Darmstadt, Germany. The GSI facility (see Fig. 2.1) provides a variety of different ion beams ranging from protons to ^{197}Au or even ^{238}U with energies about a few GeV per nucleon. The beam particles are first accelerated linearly in the universal linear accelerator (UNILAC) before they enter the heavy-ion synchrotron SIS18 and are finally extracted and hit the fixed target of the HADES experiment. HADES came into first operation in October 2002. It was built to measure the in-medium modification of the light vector mesons ρ , ω and ϕ . These vector mesons are excellent probes to access the high-density phase of heavy-ion collisions although they are very rare. Because of their fast decay ($\tau \sim 10^{-24}$ s) into lepton pairs (e^+e^-) the information about the early stage of the collision can leave the fireball almost undistorted, as the leptons are not interacting strongly with the medium. However, this introduces another factor of $\sim 10^{-4}$ due to the small branching ratio of these decays. Hence a high statistics sample has to be recorded to perform a reasonable analysis.

Therefore, one of the important requirements to the spectrometer is that it should handle high trigger rates. For a detailed study of e^+e^- -pairs a high geometrical acceptance is needed too. HADES is subdivided into six identical sectors as outlined by the mount in Fig. 2.2. Each sector covers almost 60° in the azimuthal angle ϕ such that an overall acceptance of 85 % in ϕ is achieved. The coverage in the polar angle is $18^\circ \leq \theta \leq 85^\circ$ which leads to a total acceptance of about 40 % for e^+e^- -pairs with large opening angle [Aga09].

Further requirements are a low material budget in order to suppress secondary lepton pairs originating from conversion processes which are purely background. Furthermore, the multiple scattering is small which results in a better precision of the tracking.

The spectrometer consists of four Multiwire Drift Chambers (MDC) and the superconducting magnets as a tracking device. The toroidal coils produce a magnetic field inbetween the MDCs

to bend charged particles and measure their charge-to-mass ratio. The Ring Imaging CHerenkov counter (RICH) and the Pre-Shower detector are the main components for lepton identification. For the beam time in March 2019 the Pre-Shower detector has been replaced by an Electromagnetic Calorimeter (ECAL) primarily to measure photons from meson and baryon decays. For the time-of-flight (TOF) measurement a Resistive Plate Chamber (RPC) covers the inner part ($18^\circ \leq \theta \leq 45^\circ$) while the outer angles are covered by a TOF wall. The START detector is used to measure the reaction start time and together with the VETO detector allows for the discrimination of reactions without any interaction in the target. A Forward Wall (FW) placed seven meters upstream covers small polar angles and is used for event-plane reconstruction and centrality determination. A full description of all the detector components and their functionality can be found in [Aga09]. For a cross section of the arrangement of the detectors see Fig. 2.3. The following chapter is intended to provide an overview of all the relevant detector components for the analysis.

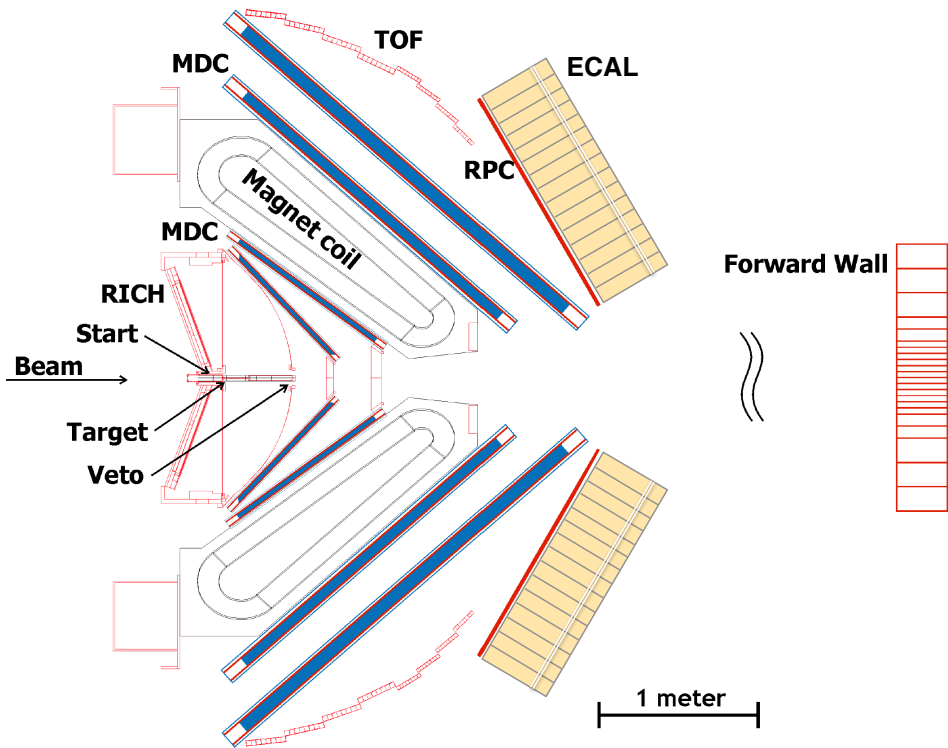


Figure 2.3: Cross section of the HADES detector showing the arrangement of the different sub-detector systems.

2.1 START and VETO detector

The first detector of HADES for the beam to pass is the START detector [Pie10] which is placed 20 mm upstream the target. It is a single-crystal Chemical Vapour Deposition (scCVD) diamond detector which has a Cr and a Au layer of 50 nm and 150 nm thickness on both sides [Pie14]. These layers are split in 16 strips with a width of $200 \mu\text{m}$ and a gap of $90 \mu\text{m}$. One is oriented in the x-, the other in the y-direction and thus allow for position measurement of the incoming beam as well as for quality and luminosity monitoring. The detector can be repositioned in order to avoid performance loss due to the radiation damage over the beam time. The spatial

extend is $50\mu\text{m}$ in thickness and 4.7 mm in x-/y-direction (see Fig. 2.4). During the Au+Au beam time the time resolution was found to be $\sim 60\text{ ps}$ while the efficiency was estimated to be 90%.

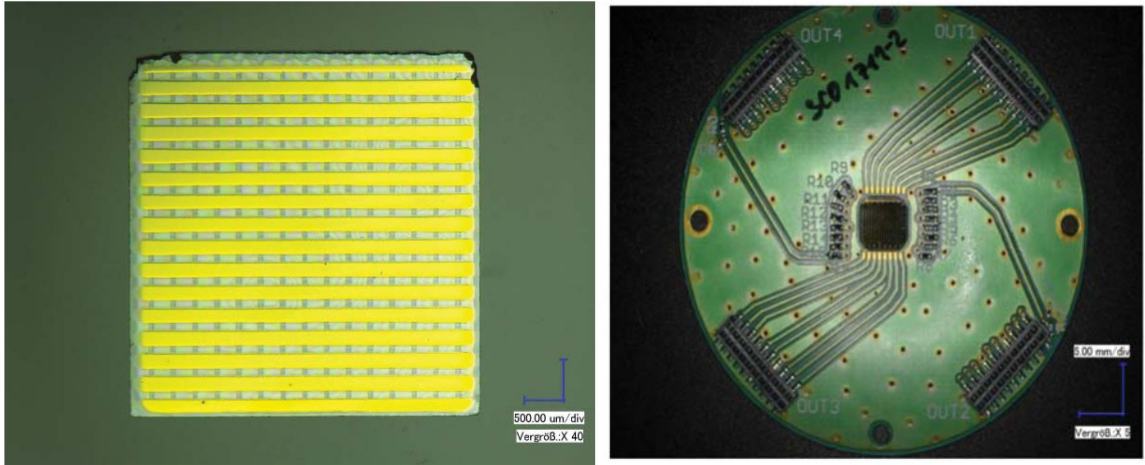


Figure 2.4: Left panel: Front view of the START detector with its 16 strips in x- and y-direction. Right panel: START detector mounted on the plate with all its connections [Pie13].

Further purpose of the START detector is the event triggering in coincidence with the TOF detector and the START time (t_0) measurement. In principle, this time t_0 is different from the actual collision time t_{coll} due to the distance to the target, but the time difference is much smaller in comparison to the time resolution of the START detector, hence it can be neglected and $t_0 = t_{coll}$.

The VETO detector is a diamond based detector as well. It is placed 70 cm downstream within the beamline and used for anti-coincidence measurement with START and TOF. The former measurement is used to reject events where no reaction took place in the target, the latter is needed to suppress pile-up or to reduce the amount of peripheral events to be written on the tape. Since VETO has an efficiency similar to START, no VETO hit does not necessarily mean that there was a reaction in the target even when a START hit has been found in the corresponding time window. More details on how the detector hits are used for event selection will be discussed in Sec. 3.7.

2.2 Target

The fixed target is mounted in the center of HADES. The target is 15-fold segmented and glued to a very thin layer ($7\mu\text{m}$) of kapton strips which are hold by a carbon tube. This arrangement of the target was implemented in order to reduce the probability of photon conversion into electron-positron pairs in the material [Kin11]. The spatial distance between two target segments is 4 mm selected to reduce significantly the probability of a photon converting in one of the next segments. For the same reason, a holder material with low atomic number has been chosen.

During the beam time in April 2012 a gold target was used. Each disk of gold used had a thickness of $25\mu\text{m}$ and a diameter of 2.2 mm . For the Ag+Ag beam time in March 2019 the thickness of the target was $42\mu\text{m}$. Both targets together with the kapton strips and the carbon tube are shown in Fig. 2.5.

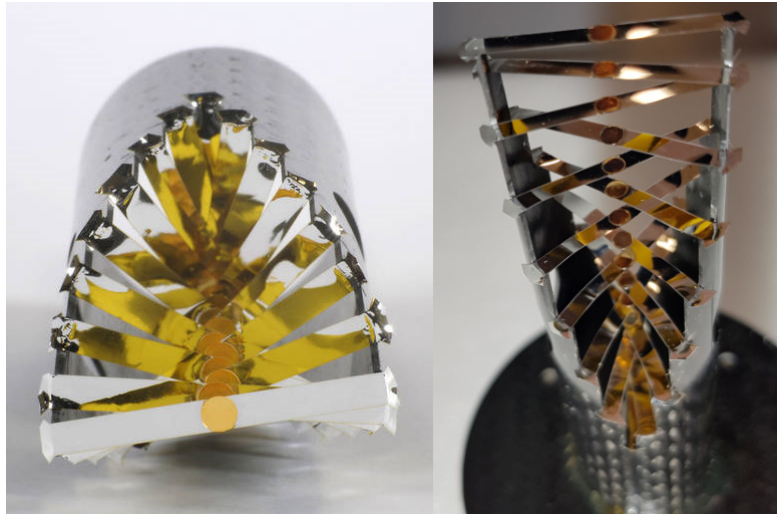


Figure 2.5: 15-fold segmented target for the beam times analyzed in this work: gold target on the left; silver target on the right.

2.3 Ring Imaging Cherenkov Counter

The RICH detector is used for electron and positron identification based on the physical effect of Cherenkov radiation which is the optical analogon to the Mach cone for acoustic noise. When a charged particle enters a medium and has a velocity v which is larger then the speed of light in this medium, then the electromagnetic pertubations in the medium will add up coherently and form a wave front which propagates as a cone. The opening angle of this cone will depend on the refraction index of the medium n , but also the velocity of the charged particle:

$$\theta_c = \arccos\left(\frac{c}{v \cdot n}\right). \quad (2.1)$$

However, the opening angle is not measured in HADES. Instead the light cone is mirrored and focussed back on a Multi-Wire Proportional Chamber (MWPC) with its photosensitive CsI cathode (see Fig. 2.6) where a ring is formed with almost constant diameter over the whole detector plane. The operation gas of the MWPC is CH_4 . It is separated from the Cherenkov gas by a CF_2 window in order to avoid mixing of the gases. The optical gas C_4F_{10} is chosen to offer a high transmission down to $\lambda = 145 \text{ nm}$. Since the C_4F_{10} threshold for a particle to emit Cherenkov light is $\gamma_{th} > 18$, this allows for a clear discrimination of electrons and positrons from all other particles. For e^+ and e^- , this threshold corresponds to a momentum of $p \sim 10 \text{ MeV}/c$ while for the next heavier particles, muons and pions, the momentum threshold is already $p \sim 2 \text{ GeV}/c$ which is far beyond the mean value at HADES energies. Hence if a ring is found in the MWPC, it is with a large probability originating from an electron or positron which makes the identification very efficient. For the $\text{Ag}+\text{Ag}$ run in 2019, the photodetector plane was replaced by photo-multipliers.

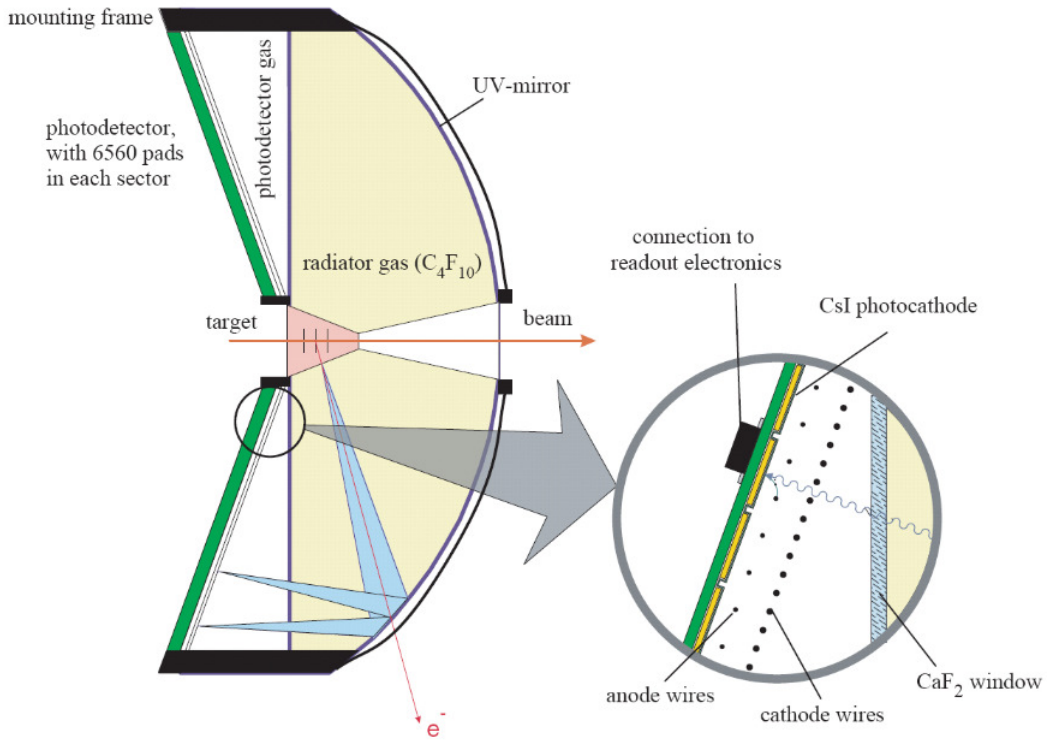


Figure 2.6: Cross section of the RICH detector and its components. The Cherenkov light is reflected by a UV-mirror and detected by a photosensitive CsI cathode.

2.4 Tracking System

The tracking system consists of four Multiwire Drift Chambers (MDC) and a superconducting magnet [Aga09, Mue04]. MDC I and MDC II are placed in front of the magnet, MDC III and MDC IV are placed behind it. This allows to construct charged particle track segments in front and behind the region of magnetic field and thus enables the reconstruction of the momentum-to-mass ratio for each track.

2.4.1 Multiwire Drift Chambers

Even they differ in size due to the geometry of the HADES spectrometer, all four MDCs are identically arranged (see Fig. 2.7). Each MDC is filled with a gas mixture: for the Ag+Ag run all MDCs are filled with 70% Argon and 30% CO₂ while for the Au+Au run this mixture was only used in MDC I, and the other chambers have been filled with 84% Argon and 16% Isobutane. Argon is used as the counting gas while the other gases are needed for quenching as an UV absorber for secondary photons. Inside this gas mixture there are six layers of wires (see right panel of Fig. 2.7). In each of these layers, there is one row of sense wires surrounded by two potential wires enclosed within two rows of cathode wires. When a charged particle travels through the chamber, it will ionize the atoms in the gas. Ionized atoms and the free electrons will then start to drift to the corresponding electrode due to the electric potential applied to the wires. Close to the sense wire the electrons will ionize further atoms leading to an avalanche which is read-out. The read-out electronics measures the time-over-threshold of the signal which can be translated into the specific energy-loss in the MDC. It also measures the drift velocity of the electron cloud which is used to deduce the minimum distance of the trajectory to the anode.

From this, the MDC is able to provide an accurate position measurement with a resolution of $60 - 100 \mu\text{m}$ in polar and $120 - 200 \mu\text{m}$ in azimuthal direction.

The six layers within one MDC are arranged in such a way that there is a 20° difference in the orientation to the next one. By this one can overlay the fired wires (wires which registered a signal) and reconstruct the hit position of a charged particle. Combining two hits in front of the magnet as well as two hits behind, one can reconstruct the full track of a particle by making use of the knowledge of the magnetic field map. The procedure is described in Sec. 3.2.

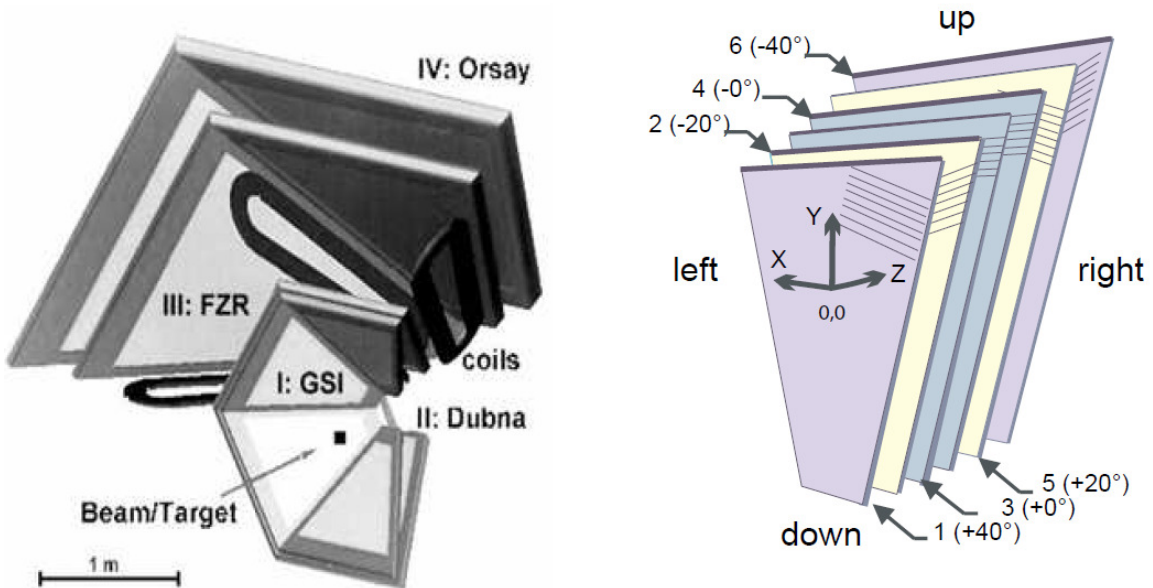


Figure 2.7: Left panel: Schematic view of the HADES tracking system. Two MDCs are placed in front and two behind the superconducting magnet. Right panel: Arrangement of the wires inside each plane of the MDC. The angle is varied such that a particle hit can be reconstructed by overlaying the fired wires from each plane. Both figures are taken from [Aga09].

2.4.2 Magnet

The IronLess Superconducting Electron magnet (ILSE) is placed in between MDC II and III. The magnet is built of six NbTi-coils which are connected by a hexagonal plate at one end and a large support ring on the other (see Fig. 2.8). The hexagonal plate has a 7° hole around the beam axis to allow the spectators to go through and reach the Forward Wall Hodoscope (Sec. 2.7). The support ring is needed to compensate for the magnetic forces acting on the coils of the order of $5 \cdot 10^4 \text{ N}$. In order to allow for the compact arrangement, it is necessary to cool the coils with He at a pressure of 2.8 bar and a temperature of 4.7 K.

The magnetic field generated by the coils has a field strength ranging from 0.8 T in the region of the drift chamber to 3.6 T inside the coils (see Fig. 2.9). Charged particles traveling through the magnetic field get a momentum kick of $0.05 - 0.1 \text{ GeV}/c$ which is enough to achieve a momentum resolution of $\sigma_p/p = 1.5 - 2 \%$. For this resolution it is also necessary to keep the magnetic field region free from material to avoid multiple scattering. The toroidal field geometry fulfills another requirement in addition, and keeps the target and the active region of the RICH relatively field free.



Figure 2.8: Picture of the superconducting magnet.

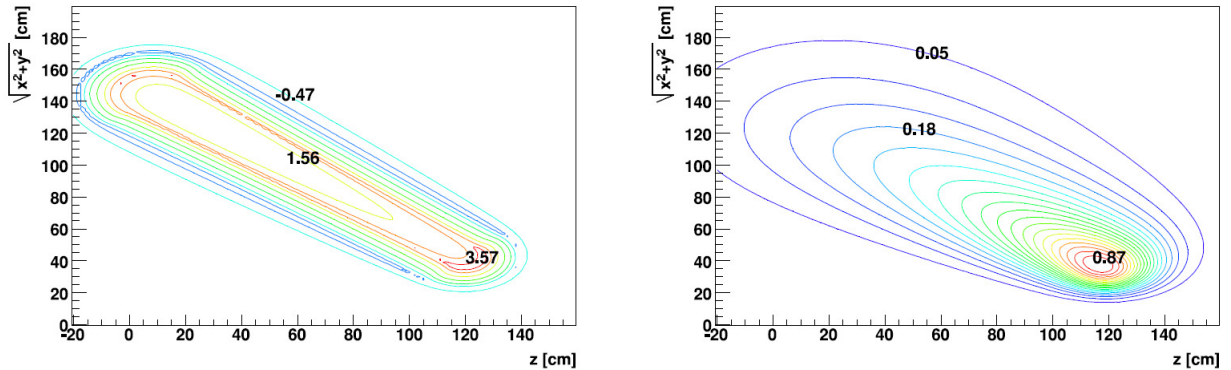


Figure 2.9: Magnetic field map as a function of position z along the beamline and the radial distance perpendicular to the beamline. Left: At azimuthal angle $\phi = 30^\circ$ (position of the coil). Right: At $\phi = 0^\circ$ (halfway between the coils).

2.5 Multiplicity Electron Trigger Array

The Multiplicity Electron Trigger Array (META) consists of three detectors and is located behind the tracking system. Like all the other components, it is composed of six sectors to fit into the HADES geometry. The innermost part of the polar angle from 18° to 45° is covered by the Resistive Plate Chamber (RPC). The main purpose of this detector is to measure the time-of-flight of the different particles in order to calculate their velocity and energy-loss (for more information see Sec. 3.8).

The same task is performed by the time-of-flight wall (TOF) for large polar angles from 44° to

88°. In addition, TOF is also used for triggering as described in Sec. 2.8.

Behind the RPC there is another detector called Pre-Shower to improve the lepton identification in the region where separation between electrons and pions is not sufficient by the RICH detector. For the Ag+Ag beam time this detector has been replaced by an Electromagnetic CALorimeter (ECAL).

2.5.1 Resistive Plate Chamber

Due to the collision geometry of a fixed target experiment, most of the produced particles will move with small polar angles. The RPC [Bel09] wall needs to be able to handle high track densities which implies a high probability of double hits. Therefore, RPC is composed of individual cells, each of them is made up of three aluminium electrodes separated by two glass plates (see Fig. 2.10). Each cell is surrounded by a kapton insulation and an aluminum shielding. The cells are filled with a $C_2H_2F_4$ and SF_6 gas mixture. This gas is ionized when a charged particle travels through the medium. Due to the high voltage applied to the cathodes up to 6 kV, the knocked-out electrons will be accelerated and cause an avalanche of further ionization leading to discharge. This signal is detected on both sides of the cell to allow for precise TOF measurement and position reconstruction along the cell.

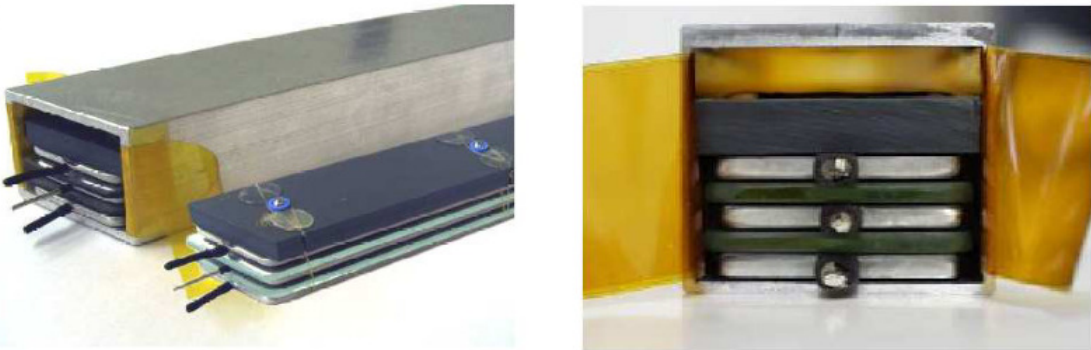


Figure 2.10: Side (left) and front view (right) of a RPC cell [Cab09]. The three aluminium electrodes (gray color) are separated by two glass plates for isolation (dark green). The bigger part on top is a plastic pressure plate surrounded by a kapton insulation foil (yellow). All is housed by an aluminium shielding.

To meet the requirements discussed above, the cells are arranged in three columns and 31 rows. Due to the trapezoidal form of the HADES detector, the innermost cells are smaller in comparison to the outer ones (see Fig. 2.11) which affects the transverse position resolution ranging from 22 mm to 42 mm. In addition, each module contains two layers to achieve a high time resolution and a granularity to handle large hit multiplicities. For the Au+Au beam time, the mean time resolution was found to be 64 ps while the overall efficiency was 97% [Kor14].

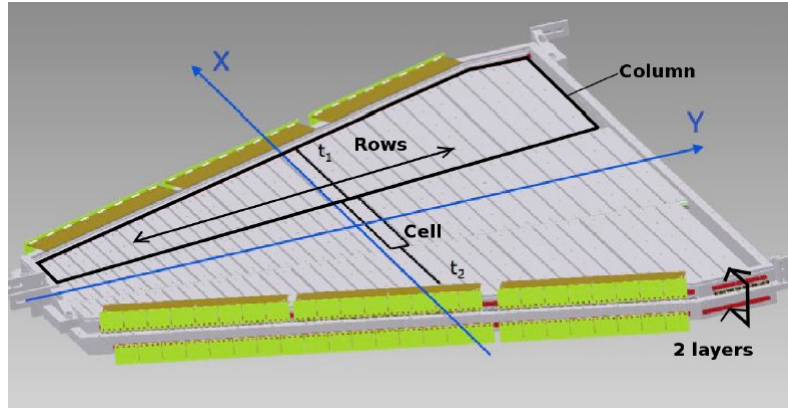


Figure 2.11: Arrangement of the RPC cells within one module [Kor14].

2.5.2 Time-of-flight Wall

Besides measuring individual particle properties like the time-of-flight or the energy-loss, the TOF wall [Ago02] is also used for event triggering (see Sec. 2.8). Hence it has to be able to determine the hit multiplicity very fast. Each sector consists of eight modules which can be seen in Fig. 2.12. Again due to this trapezoidal shape, the length of the modules vary from 1 m to 2 m. Each of these modules further consists of eight scintillator rods made up of BC408, which are plastic scintillators with a very high light output. When a charged particle travels through these scintillators, it excites the material leading to light emission. The light travels to both ends of the rod and is read-out by photomultiplier tubes (PMT). Combining the information from both PMTs, the hit position of the charged particle can be measured by making use of the time difference when the signal arrives at the PMTs. Following this approach, a precision of 2.5 cm along the rod (azimuthal direction) has been achieved while the diameter of the rods defines the spatial resolution in polar direction which is 2 cm for the innermost and 3 cm for the outermost modules. In addition, the amplitude of the signal is used to determine the energy-loss of the particle in the TOF detector.

For the Au+Au beam time, the double hit probability was $\sim 5\%$ while the time resolution was about 150 ps.

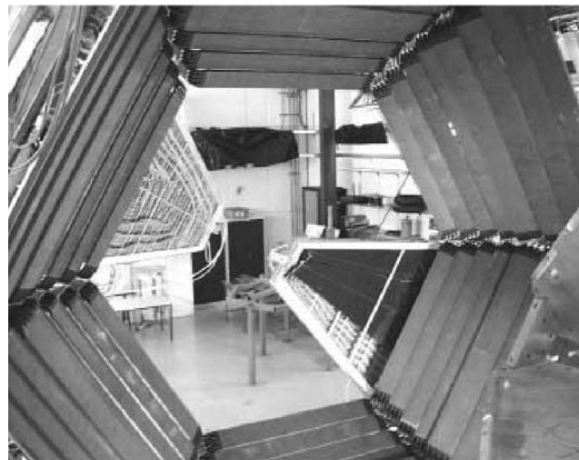


Figure 2.12: The six sectors of TOF [Ago02]. Each sector is equipped with eight modules. In addition, two sectors of the Pre-Shower detector are shown too.

2.5.3 Pre-Shower Detector

The Pre-Shower detector is used in addition to RICH to identify electrons in a momentum range of $0.2 < p [\text{GeV}/c] < 1.5$ [Bal04]. Each module is composed of three wire chambers in the HADES typical trapezoidal shape. Two of the modules can be seen in Fig. 2.12. In direction of the incoming particles, the chambers are named Pre-, Post1- and Post2-Chamber separated by two lead converter plates of thickness $2X_0$ and $1.5X_0$, where $X_0 = 0.56 \text{ cm}$ is the radiation length of lead. Each chamber consists of a read-out plane of several pads which are shown in the left panel of Fig. 2.13. Inbetween the read-out planes and the lead plates, there is an isobutane-based gas mixture therein alternating rods of anodes and cathodes (see right panel of Fig. 2.13). When a charged particle travels through the gas chambers it will ionize the medium and induce a specific amount of charge in the cathodes. The clue is the lead converter: if a light particle like an electron travels through the lead it will be slowed down while emitting photons. This effect is called Bremsstrahlung. Since these photons are very energetic they will be reconverted within the lead into electron-positron pairs and in the second lead converter the effect is multiplied several times. This phenomenon is called electromagnetic shower and is responsible for the name of the detector. For the much heavier particles like pions and so on, this effect only occurs in very rare cases, when these particles are slow enough to deposit their energy within the lead plates. Hence by integrating the charges of a particle track in 3×3 pads around the hit maximum one can distinguish electrons or positrons from all other particles, as for the former the measured charge should be higher in the Post1- and Post2-Chamber with respect to the Pre-Chamber.

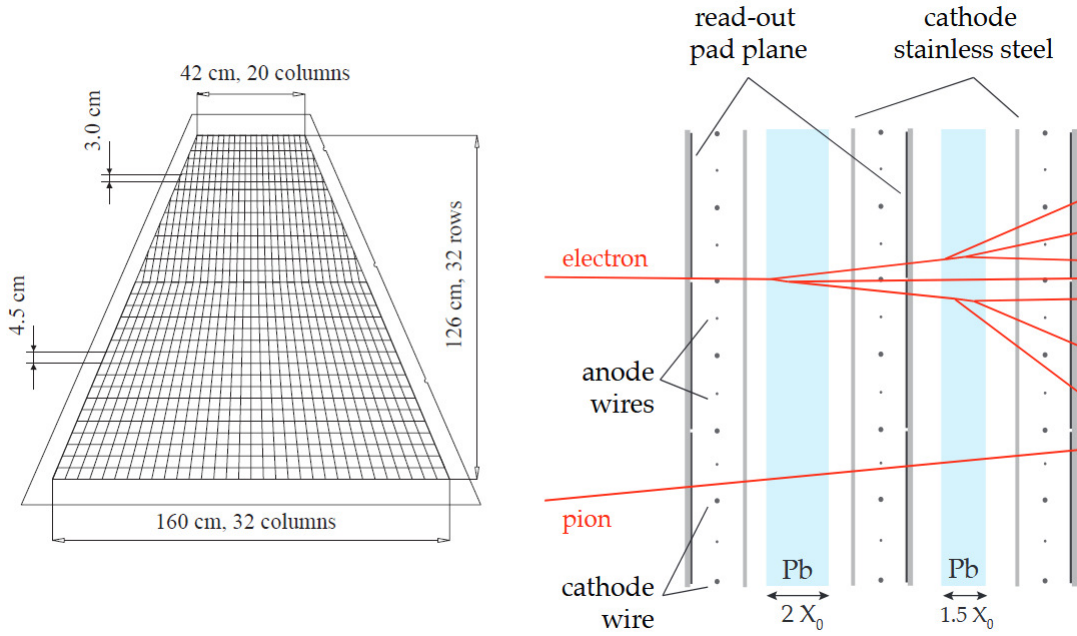


Figure 2.13: Left panel: Arrangement of the pads within one chamber of the Pre-Shower detector [Bal04]. Right panel: Side view of the Pre-Shower chambers composed of wire electrodes and read-out planes. They are separated by lead converter plates to initiate an electromagnetic shower [Kar15b].

2.6 Electromagnetic Calorimeter

The Electromagnetic Calorimeter (ECAL) has replaced the Pre-Shower detector since the beam time of March 2019 [Czy11, Svo14]. ECAL is the first detector in HADES with the possibility to measure photons. The focus is on photon pairs originating from meson decays to determine the production cross-sections. The study of the strange neutral hyperons and resonances such as the $\Lambda(1405)$ or the $\Sigma(1385)$ will also be done with ECAL in elementary as well as in heavy-ion collisions. In addition, ECAL enhances the separation power of electrons and pions with momenta $p > 400$ MeV/c.

As it is replacing the Pre-Shower detector, ECAL covers the inner part of the spectrometer of $18^\circ < \theta < 45^\circ$. ECAL consists of 163 lead glass modules per sector. The main parts of the module is a block of lead glass and the Photomultiplier tube (PMT) (see Fig. 2.15). The lead glass is used to generate electromagnetic or hadronic showers when a relativistic particle is traveling through. As for the RICH, these particles will emit Cherenkov light which is collected by the PMTs. The particle energy can be measured by making use of the proportionality to the amplitude of the signal, while the time is measured by a time-to-digital converter (TDC). With this properties at hand it is possible to identify the incoming particles and in correlation with (or without) a hit in the RPC detector especially distinguishing photons.

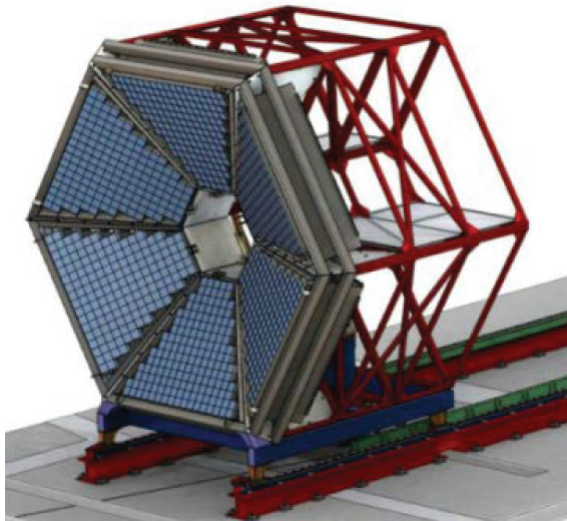


Figure 2.14: Schematic view of the HADES ECAL with all its 978 modules [Gal18].



Figure 2.15: Composition of the ECAL module: the main parts are a lead glass (upper right), the surrounding brass can (lower right), an aluminium cover (lower left) and a Photomultiplier tube (upper row, in the middle) [Svo14].

2.7 Forward Wall Hodoscope

The Forward Wall Hodoscope (FW) [And14] is placed 7 m downstream the target to measure particles at very low polar angle from $0.3^\circ < \theta < 7.3^\circ$ (see Fig. 2.16). It is part of HADES since its installation in 2007. As indicated in the figure, there are three different cell sizes: the inner cells have an active area of $4 \times 4 \text{ cm}^2$, surrounded by an array of $8 \times 8 \text{ cm}^2$ and an outer part of $16 \times 16 \text{ cm}^2$ large cells. Overall, there are 288 plastic scintillator blocks built of BC408. Their position and size is chosen to ensure a sufficient angular and spatial resolution since the track density is considerably higher towards the beam axis. The identification of particles is

done by using their time-of-flight and deposite energy in the corresponding cell. The cells have a thickness of 2.54 cm and are read-out by PMTs. The hit position is solely defined by the activated cell. For each event, the positions of all particles are combined to determine the event plane (see Sec. 3.6). Additionally, the number of hits can be used to determine the centrality of the collision. Most of the particles registered by the FW are nucleons and heavier collision fragments. For the Au+Au beam time in 2012 the time-resolution of the FW hodoscope was $\sigma = 450$ ps while the momentum resolution of protons was found to be 11 %.

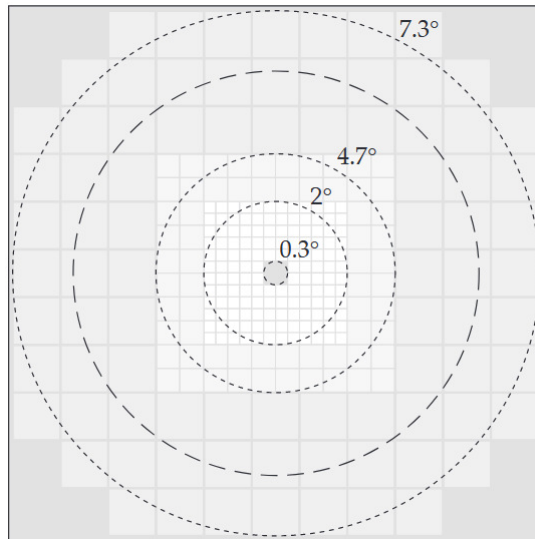


Figure 2.16: Front view of the Forward Wall cells [Kar15b]. The beam axis is perpendicular to the drawing plane in the middle of the figure. The circles denote lines of constant polar angle.

2.8 Data Acquisition and Triggering

The data acquisition system (DAQ) [Mic12] is used to collect all data from the different detectors and store it as an event. However, one has to ensure that the recorded event corresponds to a real physical reaction in the target. It is also not useful to store all detector output, as a high amount of insignificant data can already be rejected. This is especially needed for heavy-ion collisions where the interaction rates are elevated. A further reduction of the data storage can be achieved by applying a so-called Trigger.

The main component of the DAQ is the Trigger and Read-out Board (TRB) [Frö08]. For this board a special network, the TrbNet, has been developed. As shown schematically in Fig. 2.17 the input signals from all detector systems are combined. A part of these signals is used for the Central Trigger System (CTS) to pre-select events in order to reduce data storage and dead-time of the detectors. During the heavy-ion beam times a physical trigger PT2 was used which stored only events with more than five hits in the TOF detector. This corresponds to peripheral events which is not the focus of the HADES experiment. Therefore, only every eighth PT2 event was stored. The more central events are selected via the PT3 trigger with the condition of at least 20 hits in TOF.

Initially, all signals from the front-end electronics are collected by their customized end boards and propagated to separated hubs. This allows to run each detector system on an individual basis for testing but also to assign the data to the corresponding detector system in the analysis

afterwards. Then all hubs are combined with the CTS to one central hub which is connected to the so-called event builders via the Gigabit Ethernet. The event builders combine the input data to one block and finally write it to disc.

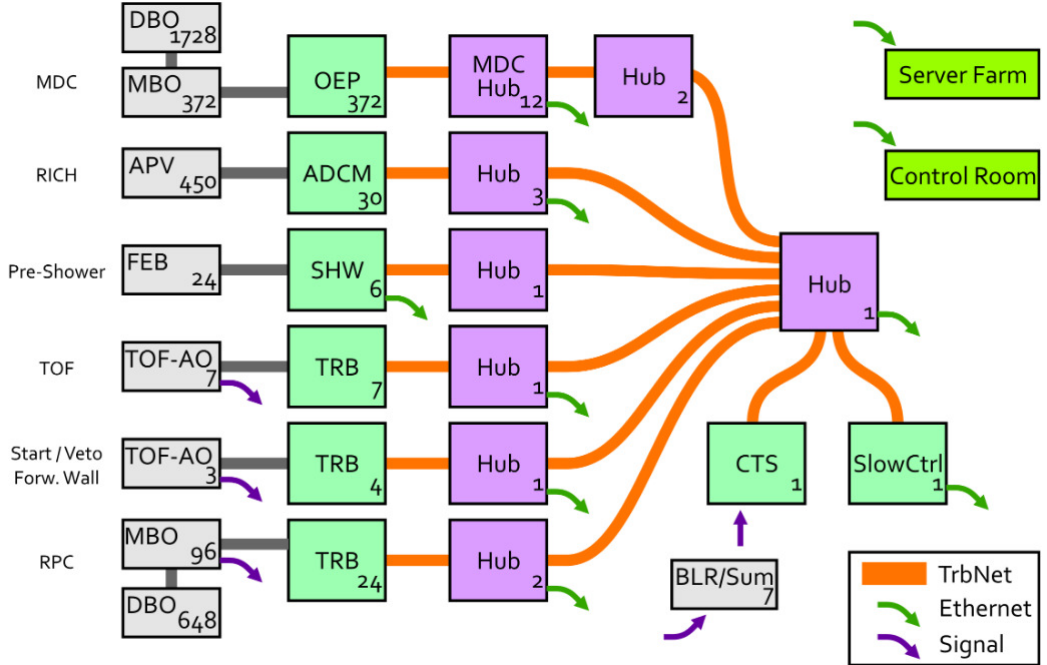


Figure 2.17: Overview of the HADES data acquisition system [Mic12]. The orange arrows illustrate the realm of the TrbNet where all the signals from the sub-detectors are processed. The central trigger system (CTS) selects only significant events in order to reduce data storage and dead time of the detectors. In the end the data is streamed to the event builders and saved to disc.

3 Data Analysis Steps

During a beam time the DAQ writes files that contain all the raw data delivered from the read-out electronics like the values from TDCs with the corresponding hardware address. These files are called Hades List Data (HLD) files but cannot be used directly for physics analysis. For further study one has to produce files that contain reconstructed tracks and physical properties such as momentum or time-of-flight. For this purpose, a summary of parameters for the tracking algorithm and the calibration of the different detectors, for example to convert ADC values to physical quantities like charges, is needed. These parameters are stored in the ORACLE database. Based on this one can produce the Data Summary Tape (DST) files which include the full track reconstruction procedure as described in Sec. 3.2.

The DST files are analyzed in the framework of the Hades sYstem for Data Reduction and Analysis (HYDRA) which is based on the ROOT software [Bru97] developed for the North Area 49 experiment at CERN (Geneva, Switzerland). ROOT was developed to provide various tools for data analysis including mathematical functions and visualization in multi-dimensional histograms. It is especially designed to deal with large amount of data and nowadays commonly used in high-energy particle physics. Furthermore there are a lot of useful extension packages for example the Toolkit for MultiVariate Analysis (TMVA) [Hoe07] which is used in this analysis.

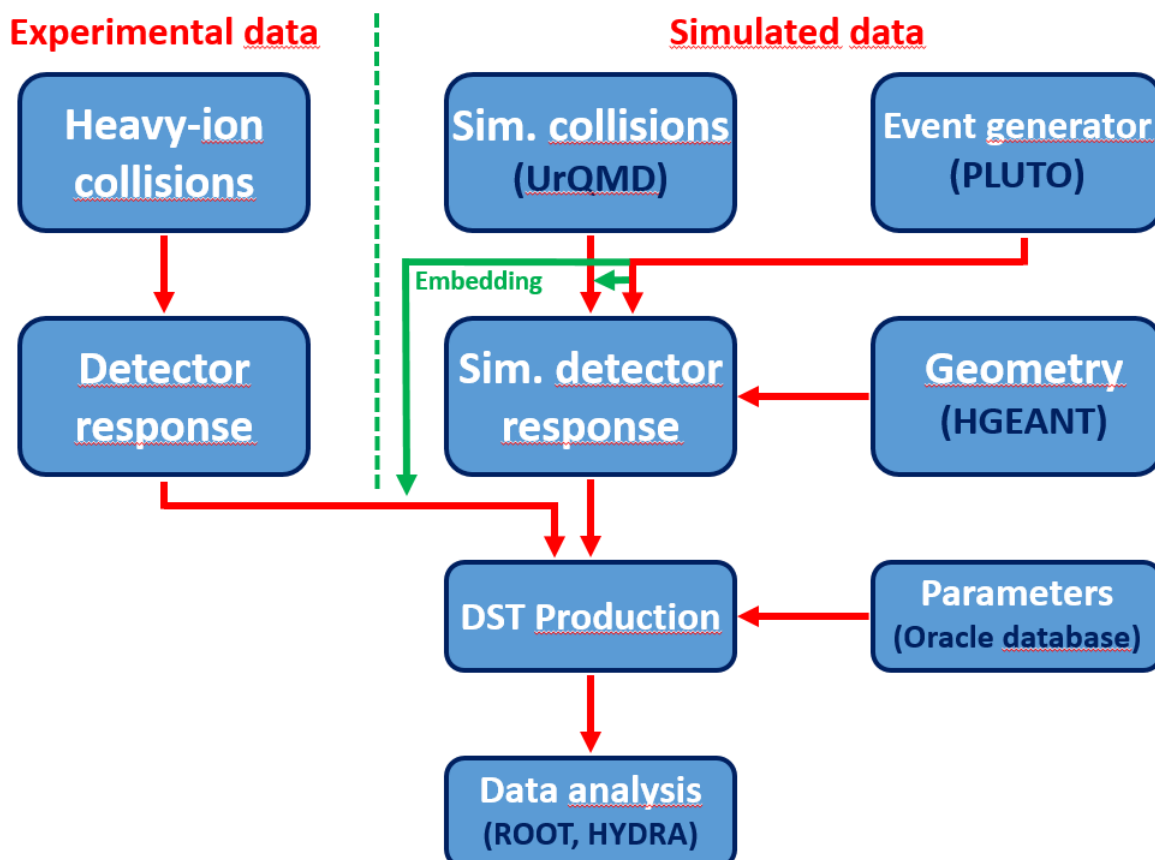


Figure 3.1: Schematic drawing of the data processing from the pure detector hits to the production of DST files. The processing for the simulated data and the embedding is shown as well.

Besides the experimental data there is also simulated data used in this analysis. This is necessary to correct the angular dependent efficiency of the detectors (see Sec. 4.6) but also for the training of the neural network to improve the selection of Λ hyperons (see Sec. 3.9). In both cases the Λ s are simulated using the Monte-Carlo event generator Pluto [Frö09] which is described in detail in Sec. 5.1. The reason is the rareness of Λ s in heavy-ion collisions of about 10^{-2} for Au+Au collisions at $\sqrt{s_{NN}} = 2.42$ GeV [Spi18] where the Λ is produced sub-threshold¹. To describe the full heavy-ion collision, transport models are used, i.e. the UrQMD model [Bas98]. Then the particles are decayed with their proper kinematics and propagated towards the detector by GEANT3 [Bru87]. The detector response is based on the HGEANT software, which includes all the HADES components including their material budget, realistic particle interaction cross sections with all material and the proper implementation of the magnetic field map. The digitizer creates an appropriate signal in each detector component along the path of each particle to match the resolution measured in the experiment.

To enhance the statistics of rare particles, one has to simulate these particles separately and embed them either to experimental or simulated data. This means that all the particle properties are merged with the full event file while usually one particle per event is embedded.

At this stage of data production, the data format is identical for both experimental and simulated data. The only difference is the additional information in the simulated files containing all the initial properties of the physical processes and particle identification code. Finally, the DST files can be produced as mentioned above. The whole process including the different options is depicted schematically in Fig. 3.1.

3.1 Data samples collected by HADES

A summary of all past beam times of HADES is given by Tab. 3.1. The focus of this analysis is to investigate a possible spin polarization measurement in peripheral heavy-ion collisions. The data samples of interest are the Au+Au data taken in 2012 as well as the Ag+Ag data taken in 2019. The Au+Au collisions were performed at a kinetic energy of the projectiles of $E_{kin} = 1.23$ AGeV while the beam intensity was about $I_{beam} = 1.5 \cdot 10^6$ ions/s. The trigger rate was 8 kHz which lead to a number of 7 billion events that have been recorded. During the Ag+Ag beam time in 2019, two beam energies were measured. The focus lied on the energy of $E_{kin} = 1.58$ AGeV corresponding to $\sqrt{s_{NN}} = 2.55$ GeV in the center-of-mass system. This energy is exactly the threshold for strangeness production in a single nucleon-nucleon collision. The Ag+Ag data was recorded over a full month without much distortion due to inactivities of detector subsystems or beam instabilities. With a higher trigger rate of around 16 kHz, 14 billion events have been recorded for data analysis.

After the first run, a second Ag+Ag run was carried out to get a sample of events directly comparable to the Au+Au data from 2012. Therefore, the same beam energy of $E_{kin} = 1.23$ AGeV has been used for three days of data taking. Due to the different beam energy, the current of the superconducting coils was adjusted from $I_{coil} = 3.2$ kA down to $I_{coil} = 2.5$ kA to match the right range of bending inside the magnetic field for the bunch of particles. The overall sample consists of 3.1 billion events.

¹ This means that in a single nucleon-nucleon collision, the energy of $\sqrt{s_{NN}} = 2.4$ GeV is not sufficient to produce a Λ hyperon for which at least $E = 2.55$ GeV is needed.

Year	System	E_{kin} [AGeV]	Events recorded [10^9]
2002	C+C	2	0.25
2004	p+p	2.2	0.44
2004	C+C	1	0.495
2005	Ar+KCl	1.76	0.925
2006	d(n)+p	1.25	0.85
2007	p+p	1.25	1.7
2007	p+p	3.5	1.18
2008	p+Nb	3.5	4.21
2012	Au+Au	1.23	7.31
2014	π^- +A	0.5 – 1.57	0.38
2014	π^- +p	0.5 – 1.57	1.23
2019	Ag+Ag	1.23	1.3
2019	Ag+Ag	1.58	14

Table 3.1: Summary of the different beam times of HADES. The corresponding beam energies, and the number of events recorded, are displayed [Kar15b]. The colored rows are the data samples which are analyzed in this framework.

3.2 Track reconstruction

The track reconstruction from the HLD files is based on the signals measured by the tracking system as described in Sec. 2.4. All charged particles traveling through the tracking system will induce a signal in the wires along their path. By overlaying the so-called fired wires within one MDC one can determine the possible hit position of the particle. Since the superconducting coils are constructed such that the magnetic field is negligible between MDC I and II as well as between MDC III and IV one can assume a straight line approximation for the inner and outer track segments. Hence two straight line segments for the inner and outer MDCs are a reasonable approximation as a first step. With the magnetic field map one can model the particle track through the magnetic field and combine the track segments to a full track but also reconstruct the momentum. This is done by a Runge-Kutta fit which takes into account the proper field map. Due to the high track density in heavy-ion collisions a lot of fake tracks can be seen, which have to be removed. In a process called META matching the full track has to be merged with the most likely hit position on the META detectors.

Since the reconstructed tracks are also involved in the determination of the event vertex, one has to take care of the off-vertex particles originating from weak decays as well. These tracks do not point to the event vertex and therefore have a worse reconstruction efficiency. For this purpose a secondary vertex finder algorithm has been introduced. All these steps will be discussed in more detail in the following.

Firstly, all fired wires are used simultaneously to be projected onto a common plane between the two inner MDCs. The plane is chosen perpendicular to the connection point of one of the 15 target segments. The one with the largest cluster size, i.e. the amount of fired wires laying on top of each other, is chosen as a first approximation of the global event vertex. This procedure is called cluster vertex finder. The vertex is fixed with respect to the beamline and the z -position is the known position of the corresponding target segment.

As a next step the cluster finder algorithm is applied to find the inner track segments. Therefore,

the fired wires are projected onto a virtual projection plane inbetween MDC I and II (see left panel of Fig. 3.2). The plane is oriented again with respect to the event vertex. By projecting the fired wires on this projection plane one finds several intersection points of the fired wires. Yet especially in case of high track densities it is likely that there are several intersection points only different by the amount of fired wires crossing. Due to that one needs to assume that not all crossings correspond to physical hits since there is also a chance of a random crossing. Hence a threshold on the amount of crossing wires is required to distinguish real tracks from fake ones. The trade-off is that a high threshold guarantees a pure track sample but with the cost of lower reconstruction efficiency. On the downside a low threshold introduces a lot of fake tracks but the reconstruction of physical tracks is much larger. Hence the threshold is set dynamically depending on the total amount of fired wires with typical values on $N_{wires} = 9$ (out of 12, since each MDC consist of 6 layers). A two-dimensional plot with one global maximum is shown in the left panel of Fig. 3.2. The straight line connecting the target position and the determined hit position results in an inner track segment.

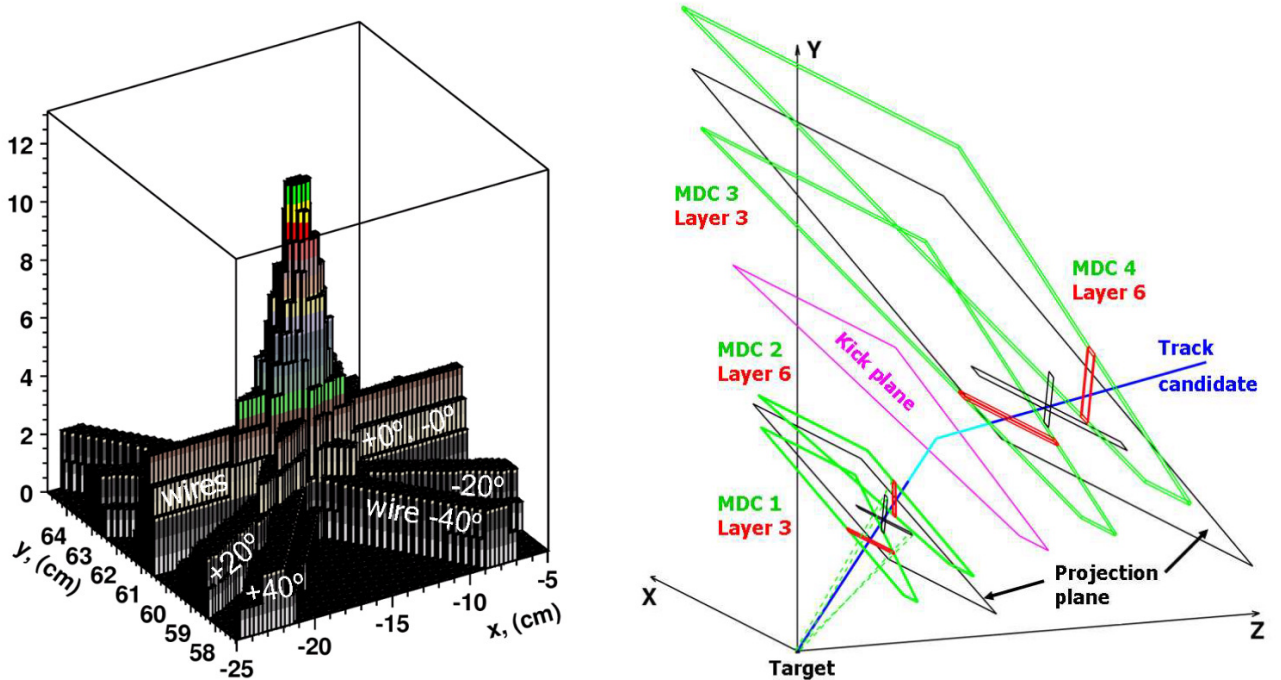


Figure 3.2: Left: Two-dimensional plots of the fired wires projected on top of each other showing a clear hit position. Right: Sketch of the cluster finder process. The fired wires of inner and outer MDCs are projected onto their particular projection planes. The target position together with the inner cluster is combined to the inner track segments. For the outer track segment the target position is replaced by the intersection point of the inner track with the kick plane [Sad07].

The procedure for the outer cluster finder is very similar. The inner track segment is extrapolated to find the intersection point with the so-called kick plane. It is placed in the region of highest magnetic field to estimate the continuous deflection of a charged particle by a single momentum kick. Then this intersection point is used as the target position for the inner cluster finder. Since there are many intersection points from various inner track segments, this procedure has to be repeated resulting in a lot of possible combinations for the outer track segment.

This sample of possible combinations contains a lot of fake tracks. These tracks consist of a fake intersection of fired wires which can be identified due to their unique features. The most obvious feature is their smaller cluster size. In addition, the corresponding amplitude of the fired wires and the number of wires contributing only to this fake cluster is much smaller. The observed effect should be higher for the inner part since the track density and therefore the random crossing of fired wires is much larger there. By analyzing these patterns and setting proper cut values the amount of fake tracks can be reduced significantly.

To improve the angular resolution of the cluster finder the measured drift time is taken into account. For the translation of the drift time to the distance of the particle track with respect to the wire the software GARFIELD is used. GARFIELD has been developed at CERN as a tool to simulate drift chambers. In case of HADES the drift cells are modeled in two dimensions resulting in a drift time depending only on one angle and the minimum distance to the wire. Then a function F [Aga09] can be defined given by

$$F = \sum_i \frac{(t_{\text{drift},i} + t_{\text{shift}} - t_{\text{TDC},i})^2}{(\Delta t_{\text{TDC},i})^2} w_i \quad (3.1)$$

where $t_{\text{drift},i}$ is the drift time from GARFIELD, shift is the calculated deviation of the drift cell from the known $x - t$ -correlation, $t_{\text{TDC},i}$ is the measured drift time with its uncertainty $\Delta t_{\text{TDC},i}$ again taken from GARFIELD and w_i are weighting constants according to the Tukey weight distribution [Rus06] to minimize the influence of outliers. The found track segments are fit to the drift times by minimizing the function F to reduce the spatial resolution by roughly a factor of ten.

For the final DST generation of Au+Au collisions a new algorithm was used to improve the reconstruction of off-vertex tracks. This secondary vertex finder loops again over all the removed wires and looks for the crossing wires with largest opening angle of more than 40° in MDC I and II. Then all the wires crossed by the straight line are considered: if the number of fired wires is higher than six, the drift time optimization process is used for this track candidate but without making use of the assumption that this track points to the event vertex. For later identification these tracks are marked with a flag as off-vertex tracks.

3.2.1 META matching

The reconstructed tracks have to be matched to the hits in the META detectors. For this purpose the track candidates (reconstructed in the MDC) are extrapolated to the META detectors to determine an intersection point. The quality χ^2_{MM} of this extrapolation can be given by the distance to a measured META hit position by

$$\chi^2_{MM} = \sqrt{\frac{dx^2}{\sigma_x^2} + \frac{dy^2}{\sigma_y^2}} \quad (3.2)$$

where dx , dy are deviations from the META hit coordinates and $\sigma_{x,y}$ the corresponding uncertainties. For the Au+Au and also the Ag+Ag beam time, dy is defined by the geometry of the META cells. Thereby, an extrapolated track is matched to a META hit, if the vertical distance has a value smaller than $dy < 4\text{ mm}$ in case of a high momentum track. Towards lower momenta

this cut value increases slightly due to multiple scattering which results in a higher offset from the measured hit position. Since the criteria in dy is fixed the META matching quality reduces to

$$\chi_{MM}^2 = \left| \frac{dx}{\sigma_x} \right| \quad (3.3)$$

which will also be the basis of the track selection in this analysis (see Sec. 3.7). The distribution of dx and χ_{MM}^2 are shown in Fig. 3.3 for minimum-, medium-, and maximum-ionizing particles. The selection is based on the measured energy-loss in the MDC and a maximum value of $\chi_{RK}^2 < 200$ is required. The distributions of dx follow a Gaussian shape. After normalization the χ_{MM}^2 distributions all agree with each other. In addition, all the distributions are well reproduced by simulations as can be seen in Fig. 3.3 by the comparison of the solid with the dashed lines. For the first estimation of a fully combined track, the best three combinations with a META matching quality $\chi_{MM}^2 < 5$ are stored.

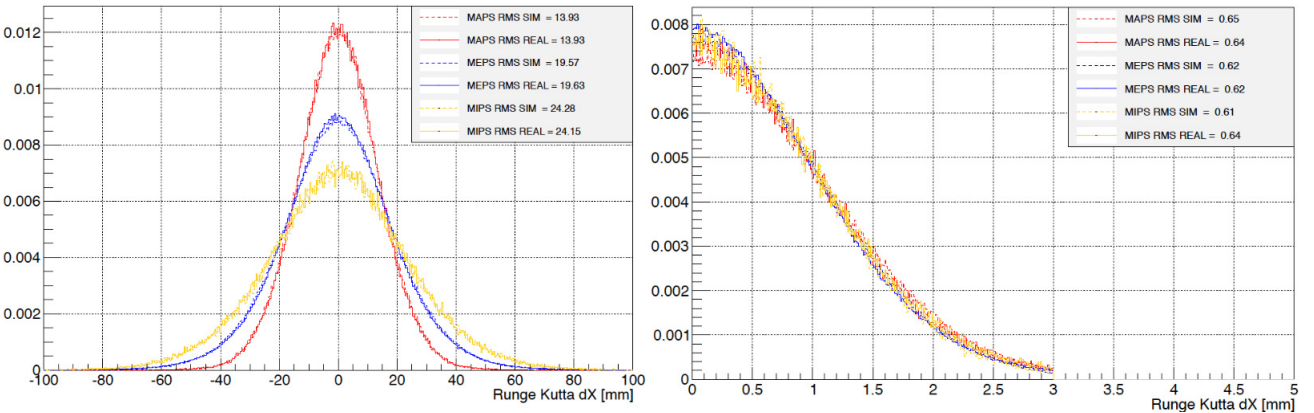


Figure 3.3: Distributions of distance dx for the extrapolated Runge-Kutta tracks to the hits in the TOF detector [Mar16]. Distinction is made between minimum- (yellow), medium- (blue) and maximum-ionizing (red) particles. Experimental data is plotted with a solid line, simulated data with a dashed one. Left panel: Distributions normalized to one. Right panel: Normalized to the calibrated σ_x .

3.2.2 Momentum determination

The determination of the particles' momentum is essential for most of the analysis in physics. In HADES three steps are used for momentum determination each of those increases the accuracy of the momentum significantly. A detailed description can be found in [Aga09] and references therein.

The first step is the "kick-plane" method. As indicated in the right panel of Fig. 3.2 it estimates the deflection of the particle in the magnetic field by a simple "kick" which only changes the direction of the trajectory. The kick of the particle is set to a virtual kick plane. Making use of simulations the inner and outer segments can be extrapolated to determine the intersection points which in total create a two-dimensional surface which is almost flat and hence called kick plane.

The force acting on a charged particle passing through a magnetic field is the Lorentz force. Besides the charge q of the particle the Lorentz force depends only on the velocity \vec{v} of the particle

and the magnetic field strength \vec{B} and acts perpendicular to both of them. In first order there is no change of the momentum, thus one can assume the incoming and outgoing momentum to have the same value, namely $|\vec{p}_{\text{in}}| = |\vec{p}_{\text{out}}| = \vec{p}$ and from the geometry the deflection angle $\Delta\theta$ (left panel of Fig. 3.4) can then be calculated by:

$$\sin\left(\frac{\Delta\theta}{2}\right) = \frac{|\Delta\vec{p}|}{2p}, \quad (3.4)$$

with $\Delta\vec{p}$ being the change in momentum. From the equation it can be seen that the deflection is assumed to take place in a static plane since there is only the polar angle θ but not the azimuthal angle ϕ involved here. For large momenta and hence small deflections we can estimate $2\sin(\Delta\theta/2) \approx \Delta\theta$ and hence the change in momentum reduces to $\Delta p = p\Delta\theta$.

A different approach is to compute the change in momentum by performing an integral over the magnetic field along the path of the particle. Using the approximation made before we can write:

$$\Delta\theta = \frac{1}{p} \int d\vec{p} = -\frac{q}{p} \int \vec{B} \times d\vec{s} = -\frac{q}{p} \int_{s_{\text{in}}}^{s_{\text{out}}} B \sin(\alpha) ds = C \frac{q}{p} (s_{\text{out}} - s_{\text{in}}). \quad (3.5)$$

In the last step, the assumption was made that the angle between the magnetic field and the trajectory α is close to 90° and hence $\sin(\alpha) \approx 1$. This is a very reasonable assumption for the HADES setup as can be seen from the field map in Fig. 2.9. The constant C actually changes with the magnetic field non-uniformities, i.e. C is different for different tracks. $s_{\text{out}} - s_{\text{in}}$ is the path length inside the magnetic field region and can be expanded by a Taylor series to

$$s_{\text{out}} - s_{\text{in}} = C_0 + C_1 \sin\left(\frac{\Delta\theta}{2}\right) + C_2 \sin^2\left(\frac{\Delta\theta}{2}\right) + \dots \quad (3.6)$$

while higher order terms can be neglected since $\Delta\theta$ is small in general. Inserting Eq. 3.6 back into 3.5, we obtain a formula for the momentum-over-charge ratio which is only dependent on the deflection angle:

$$\frac{p}{q} = \frac{1}{2} \left(\frac{C_1}{\sin(\Delta\theta/2)} + C_2 + C_3 \sin(\Delta\theta/2) \right). \quad (3.7)$$

The deflection angle is calculated for each track from its inner segment and hit point on the META detector. The three constants are determined from GEANT simulations and stored in look-up tables. They depend on the vertex and direction of each track which can be calculated straightforward. Overall the kick plane method provides a quick and robust estimation for the particle momentum. It needs only little information and can be performed with minimum computing costs. However it has only a limited resolution which ranges from 2% for tracks with low to 20% for tracks with high momentum [Aga09].

For a more precise momentum reconstruction the spline method could be used. Instead of a kick that connects two straight lines it models the trajectory inside the magnetic field by a cubic spline. This curve is able to provide smooth derivatives up to the second order which is required for a smooth interpolation between inner and outer segment. The two reconstructed segments are connected via 50 equally-spaced points in the (z,r) -plane (see big dotted points in the left

panel of Fig. 3.4). At each of this selected points the equation of motion is solved while the individual solutions have to fulfill boundary conditions up to the second order derivative. The equation of motion is given by the Lorentz force and can be written as

$$p \cdot \frac{d^2\vec{r}}{ds^2} = K \cdot q \left(\frac{d\vec{r}}{ds} \times \vec{B}(\vec{r}) \right) \quad (3.8)$$

where \vec{r} is the vector of the particle trajectory, s is the path length, p the particle momentum and K a scaling factor. For each of the 50 points the magnetic field and the spatial derivatives are calculated. This allows to integrate Eq. 3.8 numerically to achieve a result for the trajectory \vec{r} as a function of the momentum p . Then the radial distance for the determined trajectory to the spline curve is minimized in each point resulting in 50 different values for the momentum, which are averaged. A detailed description of how the calculations are executed can be found in [Win74].

In contrast to the kick plane method the spline method drops the assumption of the particle trajectory staying in one plane. For particles with negligible energy-loss, the spline method delivers a significantly improved resolution for the momentum measurement. Typical values for the momentum resolution vary from 2 to 4% for electrons as a function of the particles' momentum. For the low momentum particles, due to multiple scattering and the noticeable energy-loss, there are systematic deviations which appear in momentum but also in polar and azimuthal angle. They can be corrected using numerical simulations taking these effects into account, however, the resolution for low momentum tracks decreases (see right panel of Fig. 3.4). This is also due to the effect that their curvature is stronger so the assumption of a straight track for the inner and outer segments fades out as there is a weak magnetic field in that area as well. Yet the spline method is fast and very efficient. The results are precise enough to take as an input for the next method.

Besides the issues discussed above there is another disadvantage of the spline method: there is no quality parameter on how realistically the momentum has been reconstructed. To improve the situation the Runge-Kutta method is used. This is an iterative method with is used to solve initial value problems where the equation of motion is solved numerically. A detailed description of the method applied in HADES can be found in [Sad07].

As an input the reconstructed values from the spline method are used in combination with the vertex and direction from the fit segments. Starting from one point, the next position of the trajectory can be extrapolated. In that way the particle trajectory is reconstructed recursively. Hereby, the hit positions in each MDC plane are varied within their uncertainties to compensate the straight line approximation. The procedure is repeated up to eleven times at the cost of high computational power. It roughly takes 30% of the whole computation time during DST production. The particle trajectory is determined from the META hit back to the target which also improves the resolution of the track vertex reconstruction. From the calculated to the measured hit positions a quality parameter χ_{RK}^2 can be determined by the least square method. With this procedure the momentum of each track can be reconstructed with high accuracy and stability over the whole momentum range. As can be seen in the right panel of Fig. 3.4 the Runge-Kutta method gives the best results for the momentum resolution.

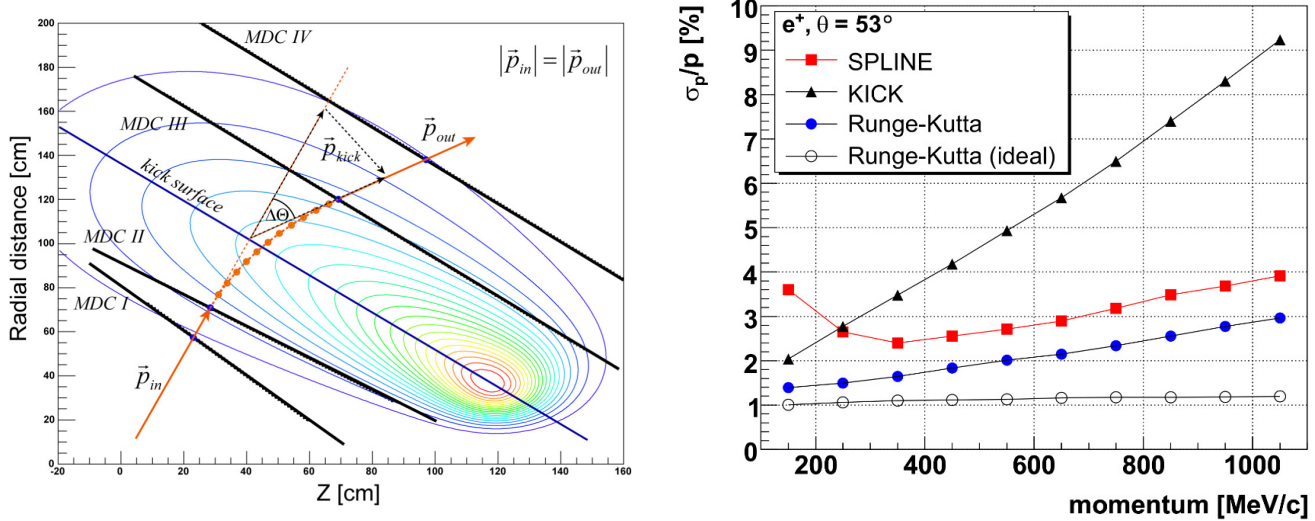


Figure 3.4: Left panel: Deflection of a charged particle trajectory inside a magnetic field [Sch08].

The approximation of the track for the kick plane method with one single momentum kick \vec{p}_{kick} as well as the interpolation of the track by the spline method (big dotted points) are shown. **Right panel:** Resolution of the momentum reconstruction as a function of the measured momentum for electrons at a polar angle of $\theta = 53^\circ$ [Sel17]. The three different methods are compared and an improvement is detectable with each step. The increase for higher momenta comes from the fact that the deflection gets smaller while the spatial resolution for the position of the tracks stays constant.

3.3 Time-of-flight determination

The measurement of the time-of-flight is done by a correlation of the signal from the START detector together with the META system. The START detector measures the absolute time t_{START} when an ion crosses the detector which is placed 20 mm in front of the target. A constant offset has to be added to the START measurement in order to take into account the time the ions need to fly to the target where the collision takes place. The time-of-flight is the difference between the time of collision and the time when a particle hits the META detectors.

When the particle passes the TOF or RPC detector it will create an electromagnetic signal which travels along the rods with a corresponding group velocity v_g . By measuring the time of the incoming signal on both sides of the rod (t_{left} and t_{right}) one can calculate the time-of-flight Δt as follows:

$$\Delta t = \frac{1}{2} \left(t_{\text{left}} + t_{\text{right}} - \frac{L}{v_g} \right) - t_{\text{START}} + t_{\text{cor.}} \quad (3.9)$$

Here L is the length of the rod and t_{cor} is the correction of the offset in the t_{START} measurement as well as for the walk corrections of the different detectors. These walk corrections are necessary since the measured signals are only registered above a certain threshold to suppress noise. Depending on the deposite charge the signal is faster or slower to cross the threshold which has to be taken into account for precise time measurement.

By using the information of a fully reconstructed track, the START time measurement is improved. Therefore the particles are pre-identified by an iterative procedure making use of their

measured momenta or specific energy-loss in the MDC both in combination with their velocities. Based on this each track is assigned to the most probable particle identification number (PID). With the physical information for all the tracks in one event the dedicated collision time t_0 is recalculated including the information of the response of the different detectors which have been studied before in Monte-Carlo simulations.

The precision of this process depends on the amount of tracks in one event, i.e. the track multiplicity, which is taken into account by the time resolution. Finally the time-of-flight for each track is recalculated according to Eq. 3.9 where t_{START} is replaced by t_0 and the offset in the correction is dropped.

3.4 Stability of the detector system

During several weeks of beam time a continuous running of all detector components cannot be guaranteed. Usually, there are several issues that occur from time to time, like problems with the high voltage drop in MDC, which takes time to be ramped up again or failures of the front-end electronics. When the DAQ has problems it needs to be restarted which leads to the loss of recording time during the time of restart. Problems can also surface with the accelerator which can result in lower beam intensities. Such problems can usually be fixed in a few minutes, however, during this time the event recording is very inefficient. These problems have to be considered in the simulations as well in order to reproduce the experimental data.

One of the quantities to quantify the stability of the detector performance is the amount of a specific particle species which should be constant over a specific time window, e.g. one run. Due to the problems described above the number of reconstructed particles will be reduced for a certain time. Looking at such a variable as a function of the sector in HADES, one can identify single sectors which were out of performance for a given time window.

For the Au+Au beam time the number of charged pions and electrons has been used [Sel17]. For the charged pions a 3σ cut around the calculated (true) value was applied to the $\beta - p$ -distribution (see Sec. 3.8) while the number of electrons is estimated by the amount of reconstructed rings in RICH. The number of charged pions is plotted for each sector in Fig. 3.5 for day 109. As can be seen all sectors perform stable, except for sector 2 which shows several drops. When the corresponding chamber of the MDC was opened after the beam time, physically broken wires were identified as an origin of the low performance of sector 2. This problem occurred during the beam time and hence sector 2 was then switched off. Overall, sector 2 was missing for most of the beam time which could affect the measurements discussed here, since without sector 2 the azimuthal range of $180^\circ \leq \phi \leq 240^\circ$ is cut from the sample. This could affect both flow and polarization observables since they depend on the azimuthal angle ϕ . This effect has been investigated and will be discussed in Sec. 4.5 and 5.4.

Despite the inactivity of sector 2 there might also occur failures in other sectors. Therefore, the average number of charged pions has been calculated for each sector and day of the beam time². If the variation in a certain run is higher than 5% from the mean value of the day, the sector is considered as not performing and excluded from this run. The results are saved in a sector file list which contains six numbers for each run, one for each sector, being either 0 (not used) or 1 (good sector). When looping over the data, this sector file list is loaded and allows

² The procedure for the electrons is similar, but for this analysis they are not used for the determination of a good sector.

a fast selection of the good sectors. The exact criteria used in this analysis are described in Sec. 3.7.

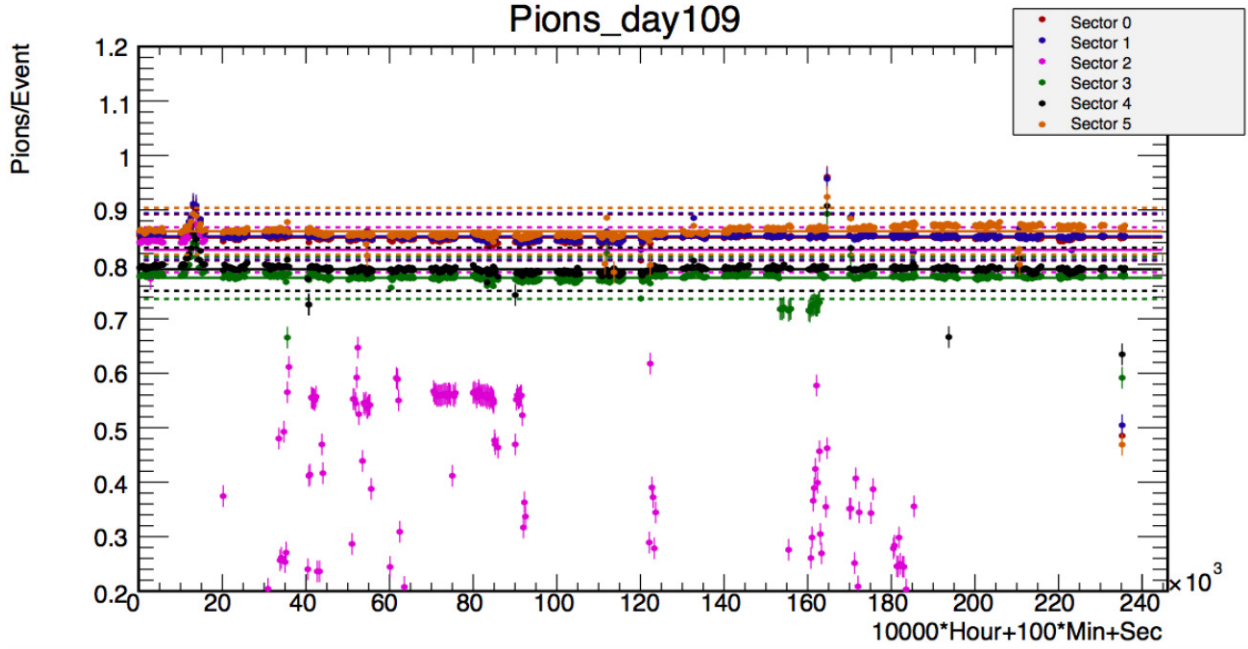


Figure 3.5: The mean number of charged pions on day 109 for the Au+Au beam time and the different sectors [Sel17]. The dotted lines indicate the range of variations in which the sectors are accepted for the analysis. The peak appearing on the left visible in all sectors is evoked by an external source, i.e. a change in the beam intensity.

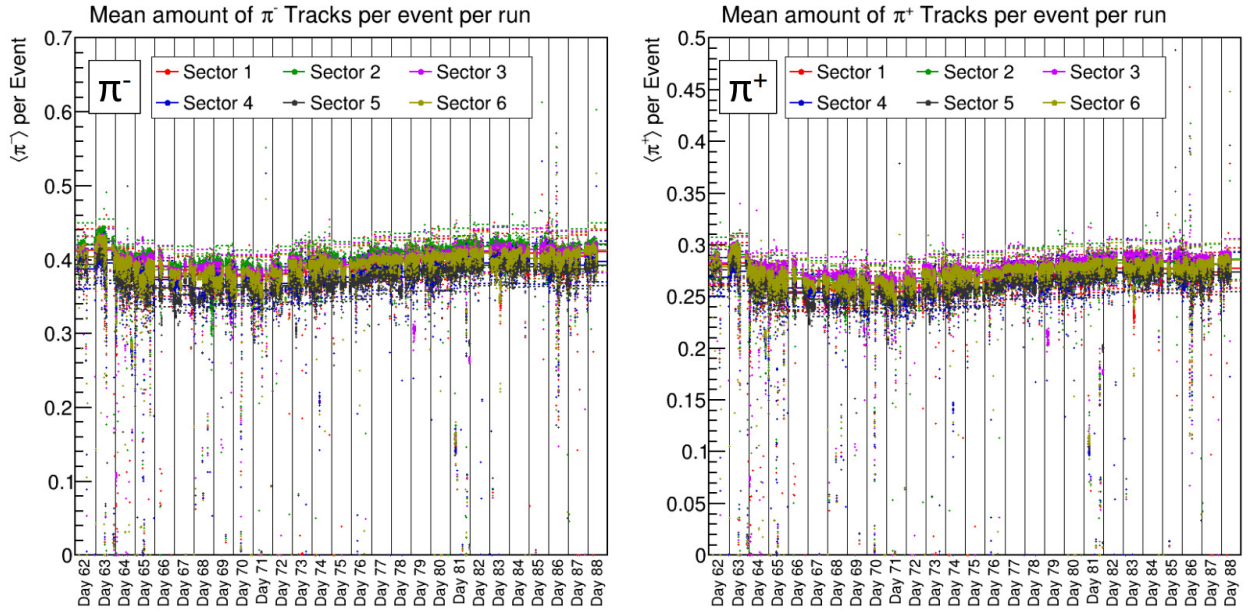


Figure 3.6: The mean number of negatively charged (left) and positively charged pions (right) for the whole Ag+Ag@1.58AGeV beam time for the different sectors [Spi20]. The dotted lines indicate the range of variations in which the sector is accepted for the analysis.

For the Ag+Ag beam time the procedure is similar. It has been adapted to the lower particle multiplicities. In addition, there is no distinction between charged pions and electrons. Instead several particles, i.e. protons, negatively and positively charged pions, electrons and positrons, are used at the same time [Spi20]. If for one of these particles the value of this run is out of the adjusted range for the daily average, the sector is removed for this run. The variations allowed are 10% for electrons and positrons and 7% for all other particles.

Fig. 3.6 shows the number of charged pions per event separated for the two charge states. Over the whole beam time, deviations from day to day are larger due to the different beam intensity and focus. Again, the dotted points indicate the threshold for each sector. For almost the whole beam time, all six sectors have been working constantly well within the defined limit.

3.5 Event vertex reconstruction

The analysis of weakly decaying particles requires a precise knowledge of the event vertex, especially to suppress the combinatorial background (see Sec. 3.9). In general, at least the target position needs to be known to calculate the correct time-of-flight for the particles. In HADES, the event vertex is reconstructed in three steps. First the clusters in the inner MDCs are projected and the target segment with the highest cluster size is chosen (see Sec. 3.2). This is already very efficient to find the segment where the collision took place. The event vertex is set to the mean target position in Z and forced on the beamline $X_{\text{Vert}} = Y_{\text{Vert}} = 0$. In the next step, the track segments of the inner MDCs are extrapolated back to the target assuming straight lines. This provides a sample of intersection points close to the beamline from which the geometrical mean position is calculated. The highest precision in the reconstruction of the event vertex is achieved using the fully reconstructed tracks from the Runge-Kutta method (see Sec. 3.2.2) instead of the inner track segments. This method is the most accurate for central collisions where the track density is high while for peripheral collisions the resolution is inferior. The distribution of the reconstructed vertex is shown in Fig. 3.7 as a function of Y and Z in the HADES laboratory frame. The vertex resolution is precise and different target segments can be separated clearly. The position of the START detector is visible at around $Z = -80$ mm. These collisions are removed by a geometrical cut on the event vertex position (see Sec. 3.7). Looking at the mean value $\langle Y_{\text{Vertex}} \rangle$ the beam is not exactly centered at zero which has to be taken into account for the event plane reconstruction procedure described in Sec. 3.6.

In the simulation, the position of the event vertex is inserted differently. In case of the UrQMD model, the Z position of the vertex is set to one of the target segment positions, with a flat probability distribution of 1/15 for each segment. Then the Z_{Vert} positions are uniformly smeared over the target thickness which is a sharp cutting edge. For X_{Vert} and Y_{Vert} a Gaussian distribution with a width $\sigma = 1$ mm is assumed with a cut-off at 1.5 mm where the target ends. Again the coordinates are chosen randomly from this distribution.

When particles are embedded either to experimental or simulated data, the particle of choice is set to the event vertex position as reconstructed in experimental data of the corresponding collision to which it is embedded.

For the Pluto simulations in Ch. 5, first a list of reconstructed event vertices from the corresponding beam time is generated. When generating particles in one event, all primaries are first set to an event vertex read from the list and then a possible decay is simulated.

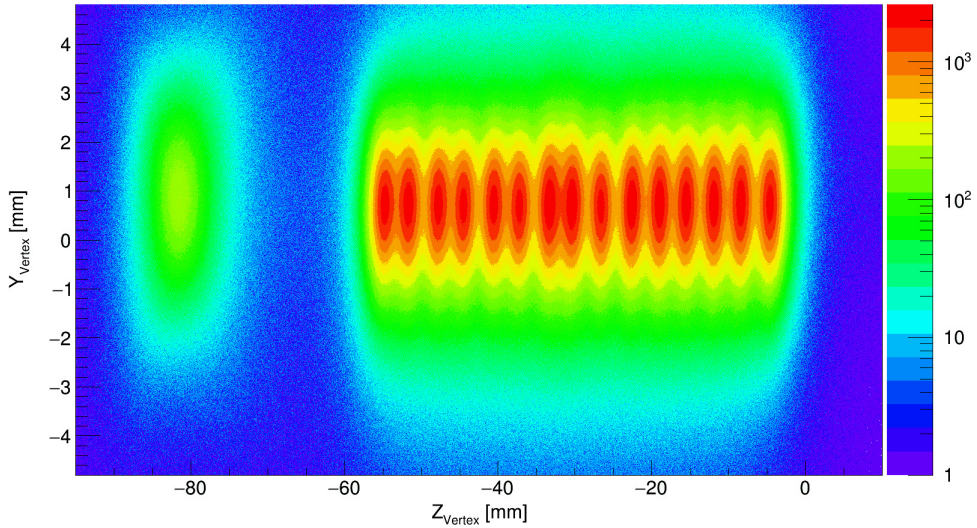


Figure 3.7: Distribution of the reconstructed event vertex in Y and Z position of the HADES laboratory frame for the Au+Au beam time. The 15 target segments can be clearly identified as well as the position of the START detector at around $Z = -80$ mm which is removed by a hard cut on Z_{Vertex} during the event selection procedure. The mean value of Y_{Vertex} is around $\langle Y_{\text{Vertex}} \rangle = 0.67$ which indicates that the beam is not exactly centered at zero.

3.6 Event plane reconstruction and resolution correction

The main observables discussed in the framework of this analysis, i.e. the flow (Sec. 1.3) and polarization observables (Sec. 1.4.2) depend on the orientation of the reaction plane (RP) in each collision (Sec. 1.2). The orientation of the RP is not known but can be estimated by the so-called Event Plane (EP). In HADES, this is done by analyzing the particles detected in the Forward Wall Hodoscope which is described in Sec. 2.7. The particles hitting the FW are mainly protons and heavier fragments with only a small deflection angle, hence they can be considered spectators in a good approximation. From the spectators, the event plane of the collision can be reconstructed using the so-called Q-vector analysis [Oll98, Pos98].

In a first step, the components of the Q-vector are calculated as an average over the hit positions X_{FW} , Y_{FW} in the FW according to:

$$Q_{n,x} = \frac{1}{N_{FW}} \sum_{i=0}^{N_{FW}} \omega X_{FW} = \sum_{i=0}^{N_{FW}} \omega \cos(n\phi_{FW}) \quad (3.10)$$

$$Q_{n,y} = \frac{1}{N_{FW}} \sum_{i=0}^{N_{FW}} \omega Y_{FW} = \sum_{i=0}^{N_{FW}} \omega \sin(n\phi_{FW}),$$

where n is the order of the Q-vector. Not all particles are taken into account here. Depending on the cell size, a minimum amount of charge deposite in the cell as well as a specific velocity window is required. While the first cut is mainly to reduce noise, the second cut is intended to reduce the participant contribution as much as possible. A typical cut window for the velocity is

$0.85 < \beta < 1.2$.

From the two components the n-th order event plane angle Ψ_{EP} can be calculated by:

$$\Psi_{EP,n} = \arctan(Q_{n,y}/Q_{n,x}), \quad (3.11)$$

while only the first order event plane ($n = 1$) angle is used in this work and $\Psi_{EP,1} = \Psi_{EP}$ will be written. The orientation of the reaction plane in the laboratory frame is completely random, however due to detector acceptance, reconstruction efficiency, contributions from participants, multiplicity fluctuations and other correlations the distribution of Ψ_{EP} is generally not flat. Therefore, several corrections have to be applied. As a first correction, weighting factors ω are introduced to Eq. 3.10. The weighting factors are calculated by analyzing the charge distribution cell-by-cell. Making use of specific energy-loss and timing cuts and comparing the first 14 charge-states, the contribution of this cell to X_{FW} and Y_{FW} is determined. This measured charge Z is then used as a weighting factor, i.e. $\omega = |Z|$ in Eq. 3.10.

Still the distributions of X_{FW} and Y_{FW} are usually not centered at zero. On a day-by-day basis, the mean values of these distributions are extracted and later on the Q-vector is shifted before the calculation of the event plane angle. This correction is usually called recentering [Pos98]. In addition to the shift of the mean position, distributions are also scaled by their corresponding width $1/\sigma_{X_{FW}}$ or $1/\sigma_{Y_{FW}}$. In Fig. 3.8 the event plane angle is shown before and after correction for different centralities on day 108 of the Au+Au beam time. The distributions are fit with a Fourier decomposition including both odd and even terms. Comparing the fit before and after correction shows that the recentering is the most important correction to be applied.

The last correction applied is the rotation of the Q-vector. This is done to correct the residual non-flatness of the Ψ_{EP} distribution. For this the distribution is fit with a Fourier decomposition up to the 8th order. Using the extracted Fourier components the distribution can be reweighted as described in the appendix of [Bar97]. The effect of the last two corrections is small compared to the recentering. However, the anisotropy of the event plane distribution is improved further. This reduces the maximum variations normalized to the mean value which are improved for the Au+Au beam time from about 5 % to less than 1 % in comparison to the previous analysis [Kor17]. Even with all the corrections applied, the reconstructed event plane has a finite resolution and may differ from the true reaction plane. For a physical correlation with the reaction plane, the value measured with respect to the event plane has a lower average than in reality. To correct this systematic effect the event plane resolution $R_{n,EP}$ is introduced. It is defined by the following equation:

$$R_{n,EP} = \langle \cos[n(\Psi_{EP,n} - \Psi_{RP})] \rangle. \quad (3.12)$$

This equation can only be used in simulation, as for experimental data the reaction plane is unknown. However, there is a method to get access to $R_{n,EP}$ also in experimental data [Oll98, Pos98]. For that, each event is randomly divided into two sub-events of equal size, indexed in the following by the letters A and B . Then the event plane is reconstructed according to the procedure described above for each sub-event separately. In an ideal case, these two event planes should be the same, i.e. $\Psi_A = \Psi_B$.

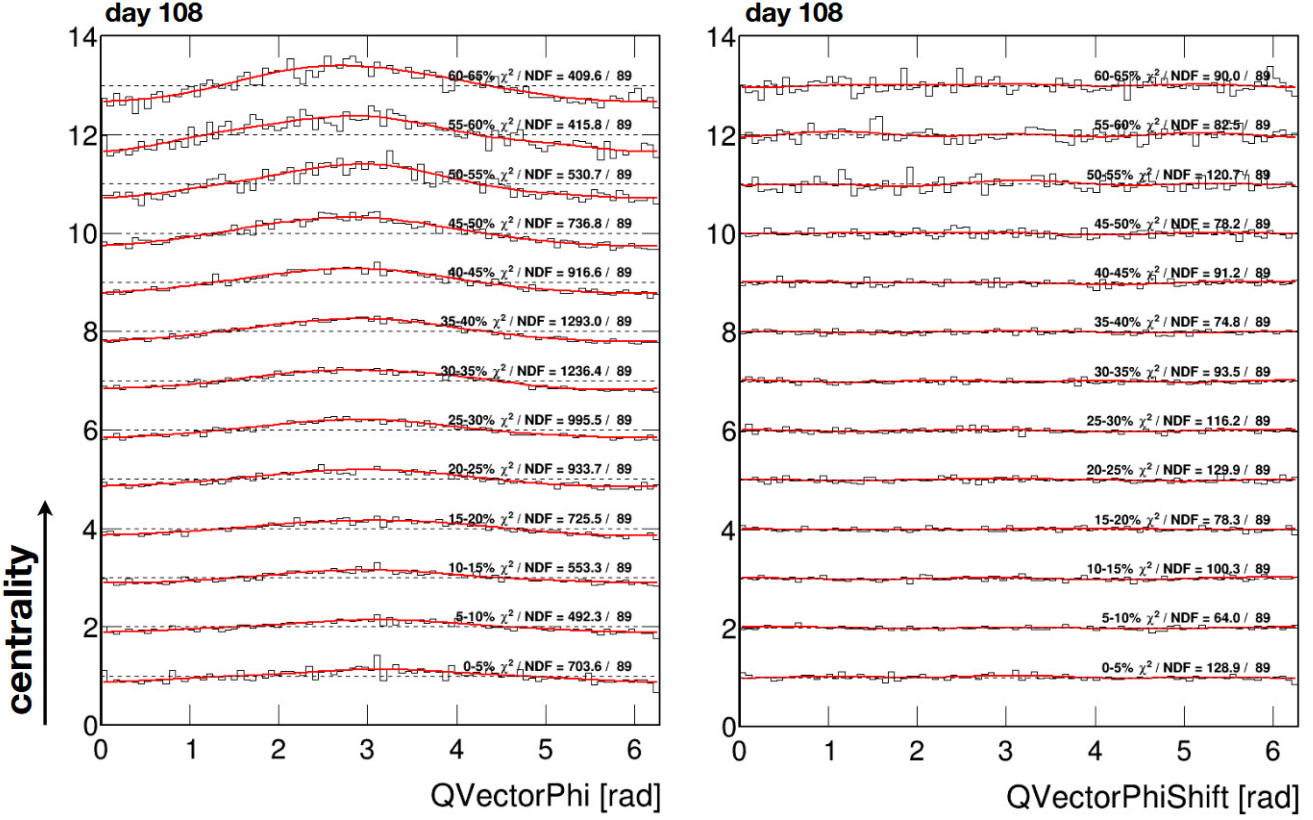


Figure 3.8: Distributions of the event plane angle for different centrality classes measured on day 108 of the Au+Au beam time [Kar18]. Left panel: Raw data. Right panel: After recentering of the Q-vector. The red curves show the Fourier decomposition as fit to the data.

In reality, one can use the difference of the two measures to estimate the resolution. From the distribution of $\Psi_{AB} = \Psi_A - \Psi_B$, a ratio r is calculated which is obtained by integrating over different parts:

$$r = \frac{\int_{-180^\circ}^{-90^\circ} d\Psi_{AB} + \int_{90^\circ}^{180^\circ} d\Psi_{AB}}{\int_{-180^\circ}^{180^\circ} d\Psi_{AB}}. \quad (3.13)$$

This procedure is applied independently for different centrality classes. Since for peripheral collisions the amount of particles hitting the FW is significantly higher than for central collisions, $R_{n,EP}$ has a strong centrality dependence. On the other hand, the event plane resolution is given by [Oll98]:

$$R_{n,EP} = \frac{\sqrt{\pi}}{2} \chi e^{-\chi^2/2} \left[I_{\frac{n-1}{2}} \left(\frac{\chi^2}{2} \right) + I_{\frac{n+1}{2}} \left(\frac{\chi^2}{2} \right) \right] \quad (3.14)$$

with I being the modified Bessel function. This equation is based on a Gaussian shape for the fluctuations of the Q-vector around its true value $\langle \vec{Q} \rangle$. This parametrizes the distribution of the Q-vector and $\Delta\Psi$ space, while the latter is the deviation of the reaction plane. Integrating first over $\Delta\Psi$ and then over the Q-vector [Oll96] results in Eq. 3.14, while a dimensionless

parameter $\chi = |\langle \vec{Q} \rangle|/\sigma$ has to be introduced. This χ has simple relation to the ratio r (eq. 3.13) given by [Oll98]:

$$r = \frac{1}{2} e^{-\chi^2/2}. \quad (3.15)$$

After calculating the ratio r from the Ψ_{AB} distribution, Eq. 3.15 is used to get the corresponding χ value. However, since two sub-events, containing only $N/2$ particles, are used for this calculation, χ has to be replaced by $\chi/\sqrt{2}$. Inserting this into Eq. 3.14, one can determine the n -th order event plane resolution for a given centrality class. The results are shown in Fig. 3.9 up to the 6-th order from 0 – 80 % centrality for 5 % and 10 % bin width. For the analysis presented here, the values are recalculated for the customized event selection and may differ. Only the first order resolution correction $R_{1,EP} = R_{EP}$ is used. As the correlation of the observables as flow and polarization with respect to the EP are always smaller than the correlations to the true RP, wherever Ψ_{RP} is replaced by Ψ_{EP} , the corresponding average is divided by R_{EP} . A detailed description of the exact application combining several centrality bins can be found in Ch. 4. The correction factors R_{EP} are summarized in Tab. 3.2. As can be seen the resulting corrections of the measured values are around 8 % for the Au+Au beam time and around 15 % for the Ag+Ag beam times where the Q-vector analysis has not yet been fully optimized. The corrections are significantly higher for the most central bins because the amount of particles reaching the FW drops dramatically and hence the resolution decreases. The main focus of the analysis is on a centrality range of 10 – 40 %.

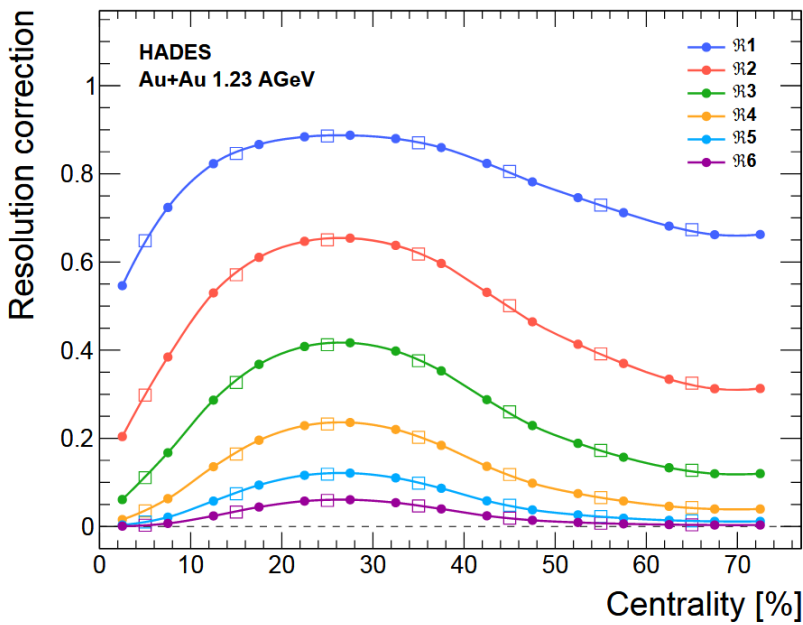


Figure 3.9: Resolution of the event plane R_n as a function of the centrality up to the sixth order [Ada20a]. Different centrality classes are indicated by the open squares for a bin width of 10 % and circles for a bin width of 5 % in centrality.

System and beam energy	Centrality range [%]							
	0 – 5	5 – 10	10 – 15	15 – 20	20 – 25	25 – 30	30 – 35	35 – 40
Au+Au at 1.23AGeV	0.6962 0.7933	0.8555	0.9173 0.9289	0.9389	0.9468 0.9476	0.9483	0.9449 0.9413	0.9368
Ag+Ag at 1.23AGeV	0.6433 0.6952	0.7342	0.8044 0.8298	0.8495	0.8722 0.8755	0.8787	0.8716 0.8624	0.8526
Ag+Ag at 1.58AGeV	0.6601 0.7298	0.7817	0.8467 0.8639	0.8777	0.8916 0.8927	0.8939	0.8857 0.8778	0.8689

Table 3.2: Summary of the first order event plane resolution correction factors R_{EP} in 5 % and 10 % centrality bins as used in this analysis.

3.7 Event and Track selection

The event selection is very important to remove unphysical events from the analysis (Sec. 3.7.1). All the information of the different detectors are combined to decide whether an event is used in the analysis or removed from the sample. In HADES, there are several conditions that are commonly used. These conditions are stored in binary flags and can be accessed during data analysis without much of computational costs.

In this analysis, we are interested in Au+Au or Ag+Ag collisions respectively, so the event sample has to be cleaned from collisions of beam ions with the START detector, the beam pipe or the target holder. The main source of background comes from collisions with carbon. Consequently, restrictions will be based on a geometrical cut on the reconstructed event vertex. Another source of background are so-called pile-up events, where more than one collision took place within a short time window. In this case, two peripheral events cannot be separated and will be assigned to one central event. In addition, there are also specific requirements for this analysis, like a certain range of impact parameter which is estimated by the collisions centrality (see Sec. 3.7.2) or that the event plane has been successfully reconstructed.

After the discussion of the event selection, the track selection will be discussed too (Sec. 3.7.3). This selection is based on track quality parameters from the Runge-Kutta method, i.e. χ^2_{RK} , or from the meta matching, i.e. χ^2_{MM} . There is also a cut applied to remove tracks that hit the edge of one of the MDC planes, since large deviations between simulated and experimental data have been observed there.

The tracks are reconstructed from an inner and outer MDC segment combined with a META hit. Especially the multiplicity of the inner track segments is large, thus several combinations to outer track segments and META hits are possible. The decision, which one of these combinations is used in the analysis, is done by a procedure called track sorting. This procedure is also described in this section. The differences in the track selection between Au+Au and Ag+Ag will be outlined.

3.7.1 Event selection

The event selection for the Au+Au beam time consists of the following flags:

- **kGoodTRIGGER:** This flag is used to only select events complying with the multiplicity trigger PT3 which corresponds to more than 20 hits in the TOF detector. In terms of centrality, this corresponds to a maximum centrality cut of 45 %, however this cut is not sharp.

- **kGoodVertexClust:** It is required that the event vertex reconstruction has been done successfully ($\chi^2_{\text{Vert}} > 0$) and by at least one track. The vertex position must be in the region of the target, i.e. $-65 \text{ mm} < Z_{\text{Vert}} < 0 \text{ mm}$ along the beamline and $R_{\text{Vert}} \leq 4 \text{ mm}$ perpendicular to it.
- **kGoodVertexCand:** Concerning the event vertex reconstruction, this flag implies the same constraints as the previous one, except that now at least two identified particles are required instead of just one track.
- **kGoodSTART:** There is at least one hit in one of the two modules of the START detector to allow for time-of-flight measurement.
- **kNoPileUpSTART:** There is only one hit cluster found in START within a time window $-5 \text{ ns} < t_{\text{START}} < 15 \text{ ns}$ around the measured START time. Hits within the cluster $\pm 0.5 \text{ ns}$ are allowed. A second collision could lead to pile-up events and wrong results in the time-of-flight determination.
- **kNoVETO:** If a START hit was found but no collision took place, the probability that this ion also generates a VETO hit is very high. Therefore, $\pm 15 \text{ ns}$ around the START time there should be no hit in the VETO detector. This is also to make sure that there was no other ion passing through which might generate some particles through a collision with completely wrong time-of-flights.
- **kGoodSTARTVETO:** Still there could be a secondary reaction spoiling the event under consideration. Hence, events are rejected if $15 \text{ ns} < t_{\text{START}} < 350 \text{ ns}$ after the START time a second START hit has been found without a corresponding VETO hit.
- **kGoodSTARTMETA:** Since the VETO has a moderate efficiency, to further reject a spoiled event, the same condition of kGoodSTARTVETO is also applied for the correlation of the second START hit to hits in the META detector system. A correlation is said to be found, if more than four META hits are found within a time window of $7 - 12 \text{ ns}$ after the second START hit.

For the Ag+Ag beam time the event selection has been improved and therefore some of the flags have been updated. To not explain everything twice, only the changes with respect to the Au+Au beam time will be summarized in the following:

- **kGoodSTART:** The condition was added, that the three fastest time-of-flights are between $5 \text{ ns} < t_{\text{TOF}} < 9 \text{ ns}$ for a track length of 2.1 m.
- **kNoSTART:** This flag replaces the old kNoPileUpSTART. It is the same condition applied for the START detector as in the flag kNoVETO.
- **kGoodSTARTVETO:** The condition to reject events with a secondary START hit without correlation to a VETO hit within $15 \text{ ns} < t_{\text{START}} < 350 \text{ ns}$ is removed. Instead the event is rejected, if the second START hit has no VETO hit $\pm 2 \text{ ns}$ around its START time $t_{\text{START},2}$.

In addition to all these requirements, there are other important criteria for the event selection that are commonly used for both beam times. As discussed in Sec. 3.4, a sector file list is used to reject sectors which were temporarily not performing properly. Especially in Au+Au where sector 2 was not operating for most of the beam time, this selection is important since for the analysis

at least 5 operating sectors are required in general. A detailed study how a non-performing sector affects the observables is discussed in Sec. 5.1.

In general a centrality range of 0 – 40 % (see Sec. 3.7.2) is analyzed with varying centrality range therein. This will be stated for the corresponding results discussed.

A last but very important criteria is that the event must have a reconstructed event plane. This is crucial since otherwise the observables could not be calculated. This has to be considered not only for the event as a whole but also for each sub-event inside the sample to determine the event plane resolution. If either of this event planes could not be reconstructed, the event is discarded. The effect of each selection to the amount of events "surviving" the corresponding cut is shown in Fig. 3.10. 40 – 50 % of all events are used in the data analysis. The effects of the individual flags cannot be read directly, since they are strongly correlated and a change in the order may also influence the percentage of events rejected by a certain condition. The overall number of events passed on to the next step of data analysis are $N_{\text{evt}} = 1.97 \cdot 10^9$ events for the Au+Au, $N_{\text{evt}} = 0.39 \cdot 10^9$ events for Ag+Ag at 1.23AGeV and $N_{\text{evt}} = 5 \cdot 10^9$ events for Ag+Ag at 1.58AGeV. The sample of Ag+Ag at 1.23AGeV is roughly 1/5 of the Au+Au sample and therefore it is tough to get reliable results especially for the polarization analysis where large statistics is crucial. A more detailed discussion is entailed in Sec. 3.9.7, after the full reconstruction chain to the final Λ sample has been applied.

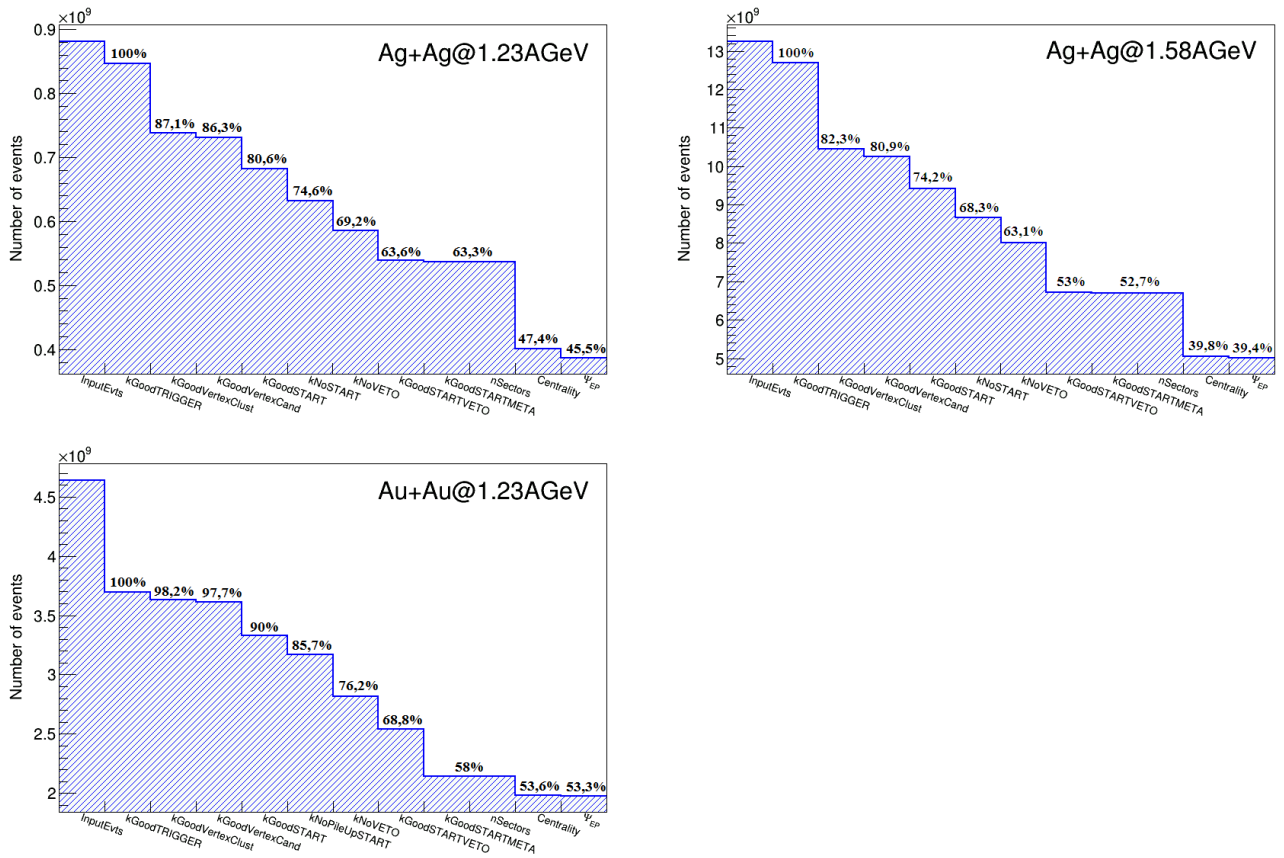


Figure 3.10: Number of events remaining after the different flags applied as described in Sec. 3.7.1. The percentages are calculated relatively to the events passing the PT3 trigger of at least 20 hits in the time-of-flight detector. Note that the amount of input events is already reduced due to instabilities in the detector subsystems as described in Sec. 3.4.

3.7.2 Centrality determination

As discussed in Ch. 1, physical observables might be very different if a heavy-ion collision is exactly head-on or if it happens to be sideways. The measure of this in theory is the impact parameter, i.e. the distance between the centers of the two colliding nuclei in the plane transverse to the beam axis. The centrality of the collision C is defined by the fraction of the total cross section σ_{AA} related to the impact parameter by the following equation [Ada18c]:

$$C = \frac{\int_0^b \frac{d\sigma}{db'} db'}{\int_0^\infty \frac{d\sigma}{db'} db'} = \frac{1}{\sigma_{AA}} \int_0^b \frac{d\sigma}{db'} db'. \quad (3.16)$$

In experiment the impact parameter or centrality cannot be accessed directly, hence a theoretical framework has to be established to relate unmeasurable quantities like the impact parameter to physical measurable quantities like charged particle or track multiplicities.

In HADES the theoretical framework used to characterize the overlap of the two colliding nuclei is the Glauber Monte-Carlo model [Mil07]. In this approach, a heavy-ion collision is treated as a superposition of independent nucleon-nucleon collisions. First, the nucleons are positioned randomly inside each nucleus with the corresponding radius $R_{\text{projectile}}$ or R_{target} respectively. The probability of the position of the nucleons is assumed to be flat in solid angle and proportional to $\rho(r)r^2$ in radial direction, where $\rho(r)$ is a two parameter Fermi distribution (see [Ada18c] for more details). Furthermore a straight track is assumed for the projectile nucleons. Two nucleons are said to collide, if the minimum distance in the transverse plane d_{\min} is smaller than the radius resulting from the inelastic nucleon-nucleon cross section:

$$d_{\min}^2 \leq \frac{\sigma_{\text{inel.}}^{NN}}{\pi}. \quad (3.17)$$

Left panel of Fig. 3.11 shows the results for the random distribution of the nucleons inside the nucleus and the estimated number of collisions for two Au ions with an impact parameter of $b = 6 \text{ fm}$. The colored nucleons schematically indicate the interactive volume of the collision. If a nucleon experiences at least one collision, it is called a participant of the collision while the rest are called spectators. The relation to physical observables is done by the assumption that the number of produced particles is on average proportional to the number of participants. Then measured particle multiplicity distributions can be used to determine the centrality of the collision referring to Eq. 3.16:

$$C \approx \frac{1}{\sigma_{AA}} \int_{N_{\text{low}}}^\infty \frac{d\sigma}{dN'} dN', \quad (3.18)$$

while N_{low} is the lower threshold for a specific centrality class. There are two options as an estimate for the number of produced particles under consideration: the amount of reconstructed tracks and the number of META hits. For this analysis, the latter one is chosen which has more contamination by background hits due to the larger amount of META hits in comparison to fully reconstructed tracks, but otherwise it is more stable against fluctuations.

The centrality classes can be directly estimated from the measured particle multiplicity distributions. However, due to the physical trigger condition discussed in Sec. 2.8 the low multiplicity

events are not recorded. The full distribution is recovered by assuming a direct relation between the mean number of participants and produced particles $\langle N_{Ch} \rangle = \mu \cdot \langle N_{part} \rangle$. To take into account particle multiplicity fluctuations, the number of charged particles per participant is described by a negative Binomial probability distribution (for details see again [Ada18c]). Then the particle distributions are sampled and by comparing them to the experimentally measured distributions all parameters can be extracted by a χ^2 -minimization procedure. The fully recovered distribution corresponds to the total cross section of the collision, hence the different centrality classes can be directly defined by specific thresholds for the charged particle multiplicities as shown in the right panel of Fig. 3.11. In this figure, the results from the Glauber Monte-Carlo simulations are shown together with the distribution of the number of hits in META for the two physical triggers. One can clearly see the drop on the lower edge of the distributions where the triggers comes in. The PT3 includes the 0 – 40% most central events, then starts to drop significantly for more peripheral events.

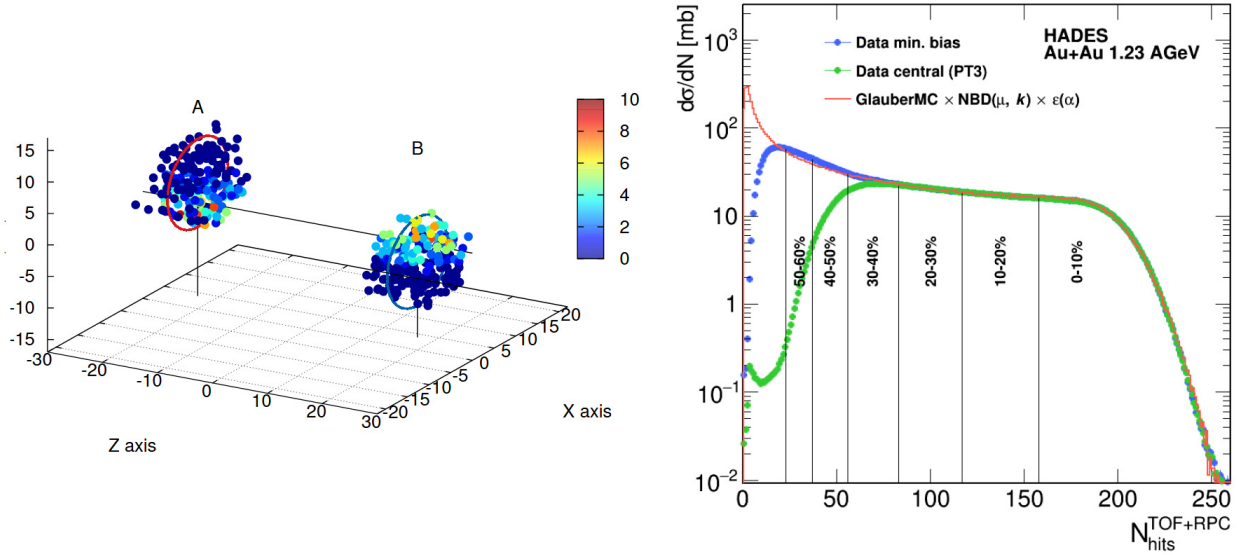


Figure 3.11: Left panel: Distribution of the nucleons inside the colliding Au nuclei for an impact parameter of $b = 6$ fm generated by the Glauber model. The colors indicate the number of collisions estimated for the single nucleons. Right panel: Cross section in Au+Au collisions as a function of the hit multiplicity in the META detector. The distributions are shown for experimental data with the two physical triggers in comparison to the results from the Glauber Monte-Carlo model. Both figures are taken from [Ada18c].

Investigations of systematic uncertainties showed that deviations related to the input parameters of the Glauber model are of the order $\sim 5\%$ while for the background contamination of the charged particle multiplicity, the influence is less than 1% [Ada18c].

The final threshold that determine the corresponding centrality classes for the different beam times are summarized in Tab. 3.3. The classes are selected according to the hit multiplicity in the TOF and RPC detector. Only events with centrality 0 – 40% are used for this analysis.

Centrality	Au+Au@1.23AGeV		Ag+Ag@1.23AGeV		Ag+Ag@1.58AGeV	
	$N_{\min}^{\text{TOF+RPC}}$	$N_{\max}^{\text{TOF+RPC}}$	$N_{\min}^{\text{TOF+RPC}}$	$N_{\max}^{\text{TOF+RPC}}$	$N_{\min}^{\text{TOF+RPC}}$	$N_{\max}^{\text{TOF+RPC}}$
0 – 5 %	180	-	102	-	116	-
5 – 10 %	157	180	90	102	101	116
10 – 15 %	136	157	79	90	89	101
15 – 20 %	117	136	68	79	77	89
20 – 25 %	99	117	58	68	66	77
25 – 30 %	82	99	49	58	57	66
30 – 35 %	68	82	41	49	48	57
35 – 40 %	55	68	34	41	41	48

Table 3.3: Threshold value for the hit multiplicity in the META system, i.e. the hits in TOF and RPC detector, to define the centrality classes of the collision for both collision systems.

3.7.3 Track selection

Every charged track consists of three parts: an inner and outer track segment and a hit in the META detector (see Sec. 3.2). Especially in heavy-ion collisions where the track densities are high, this leads to multiple combinations from which the most probable track candidate has to be chosen.

To reduce the amount of possible combinations as a first step, minimum requirements on the track quality are applied. The track candidate has to have a reconstructed momentum $p > 0$ from the Runge-Kutta procedure with $\chi_{RK}^2 < 1000$. Additionally, the inner track segment fitter must have converged, i.e. $\chi_{\text{inner}}^2 > 0$. The time-of-flight is required to be below $\Delta t < 60\text{ ns}$ while a velocity $\beta > 0$ should have been calculated³. The last requirement concerns the META matching: $\chi_{MM}^2 < 3$ and a fixed cut of $dy < 4\text{ mm}$ (see Sec. 3.2.1).

After this selection the tracks are listed according to their inner track segment, following that the combination of several inner with the same outer segment is forbidden. However, an inner segment can be combined with two outer segments either having a separate or sharing the same META hit. Then a combination of inner and outer segment could be matched to two different META hits. Another possibility would be that two different inner and outer segments are pointing to the same META hit. The amount of combinations strongly depends on the number of hits in MDC and hence on the centrality of the collision. The challenge is to select the right track from all these combinations. This is done by a procedure called track sorting. The tracks are sorted according to their reconstruction quality, i.e. by χ_{RK}^2 . The combination with the best χ_{RK}^2 is chosen and all its components are marked with the flag *kIsUsed*. Then they are removed from the list and the procedure continues for the remaining track combinations. Following this procedure, it is guaranteed that no track component is used twice in the analysis. The selection of the right track combination is crucial since it could affect both momentum and time-of-flight determination. For example when a pion track is matched to a META hit originating from a proton it leads to wrongly calculated masses and results in an increase of random background [Sch16].

In this analysis the focus is on the daughter particles of the Λ hyperon, the negatively charged pions and the protons. Simulations show, that the track reconstruction efficiency for the primary

³ If the time-of-flight is found to be $\Delta t < 0$ the velocity is set to $\beta = -1$.

particles is around 83% for pions and 89% for protons (see Fig. 3.12). As can be seen the efficiency drops significantly for low momentum tracks.

For this analysis the track selection is extended by two more conditions. First, the cut on the quality of the track reconstruction is restricted to $\chi_{RK}^2 < 400$. Second, the comparison of the number of reconstructed tracks in experimental and simulated data shows a sharp efficiency drop at the edges of the MDC planes (see Fig. 3.13). In order to not worsen the results by this systematic loss of efficiency, the corresponding areas on the edge of the MDC planes are discarded.

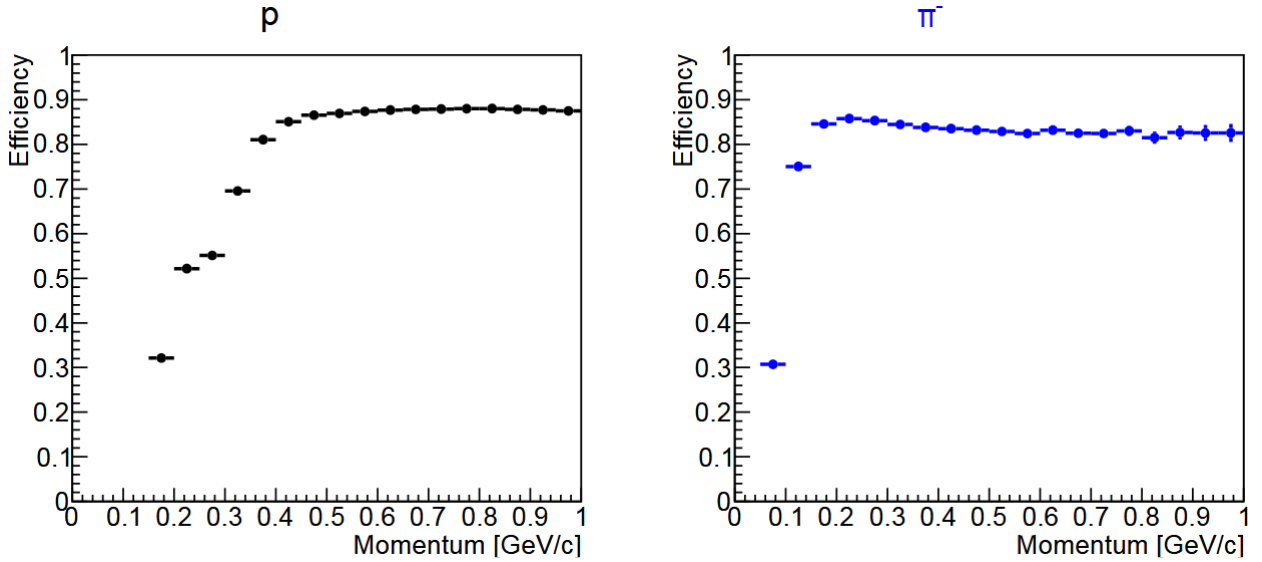


Figure 3.12: Track reconstruction efficiency for protons (left panel) and negatively charged pions (right panel) as a function of the particle momentum [Sch16].

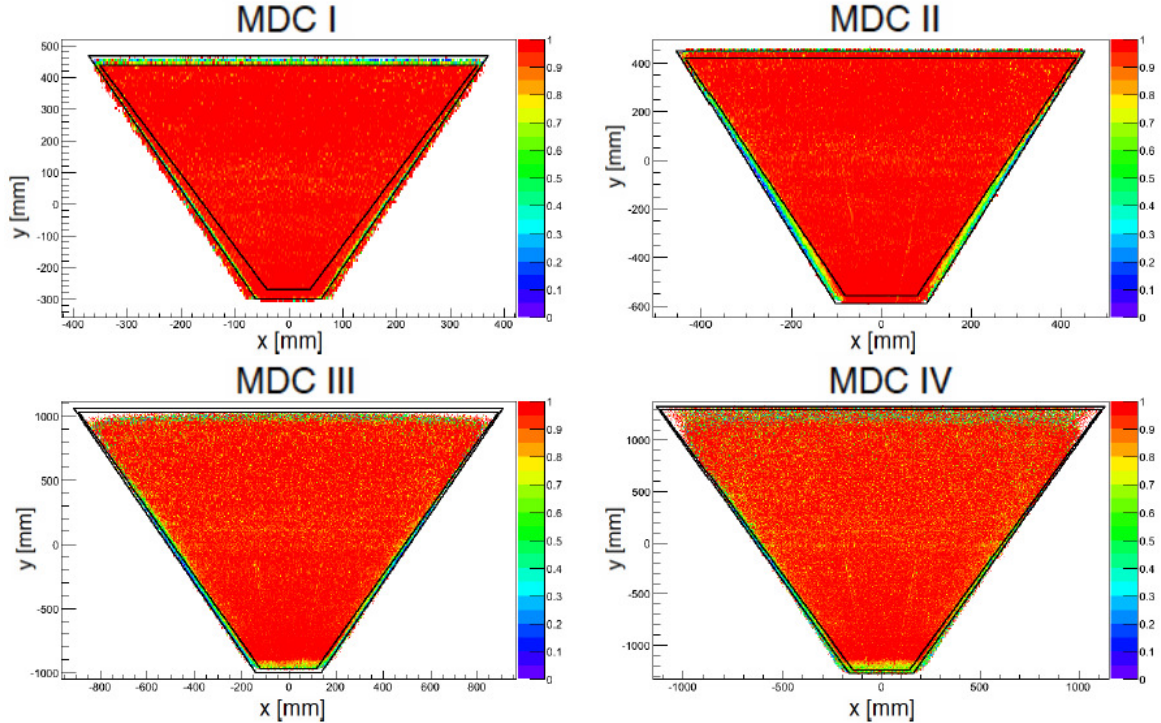


Figure 3.13: Crossing point of the track segments in x- and y-direction in experimental data divided by simulations for all four MDC planes [Mar15]. The two layers with 40° orientation are shown. Black lines define the boundaries of the regions which are removed from the analysis due to a strong drop in efficiency.

3.8 Particle identification

For the identification of a fully reconstructed track with a corresponding particle type, the reconstructed information of different detector systems have to be combined. There are two possibilities in HADES to do the particle identification, the first is based on the momentum-over-charge ratio determined by the Runge-Kutta method assigned to each track. From the bending inside the magnetic field the polarity of the track, i.e. the sign of the charge, is also determined as well as the path length Δs . Since all these information are provided by the same detector system, another information is required in addition, for particle identification. This information is delivered by the META detectors together with START, i.e. the time-of-flight of the reconstructed track. With this the velocity of the particle $\beta = v/c$ can be calculated since the path length Δs from the collision vertex to the META hit is also known:

$$\beta = \frac{\Delta s}{c \Delta t} \quad (3.19)$$

with c being the speed of light. The momentum can also be expressed in terms of the velocity from special theory of relativity it follows:

$$p = \frac{m\beta c}{\sqrt{1 - \beta^2}}. \quad (3.20)$$

This relation allows to plot the velocity versus the momentum. As can be seen from the left panel of Fig. 3.14 the different particles can be distinguished. The identification for the particle of interest can be done by fitting the corresponding peak for each momentum slice and then the selection is done via a cut of several σ around the mean value.

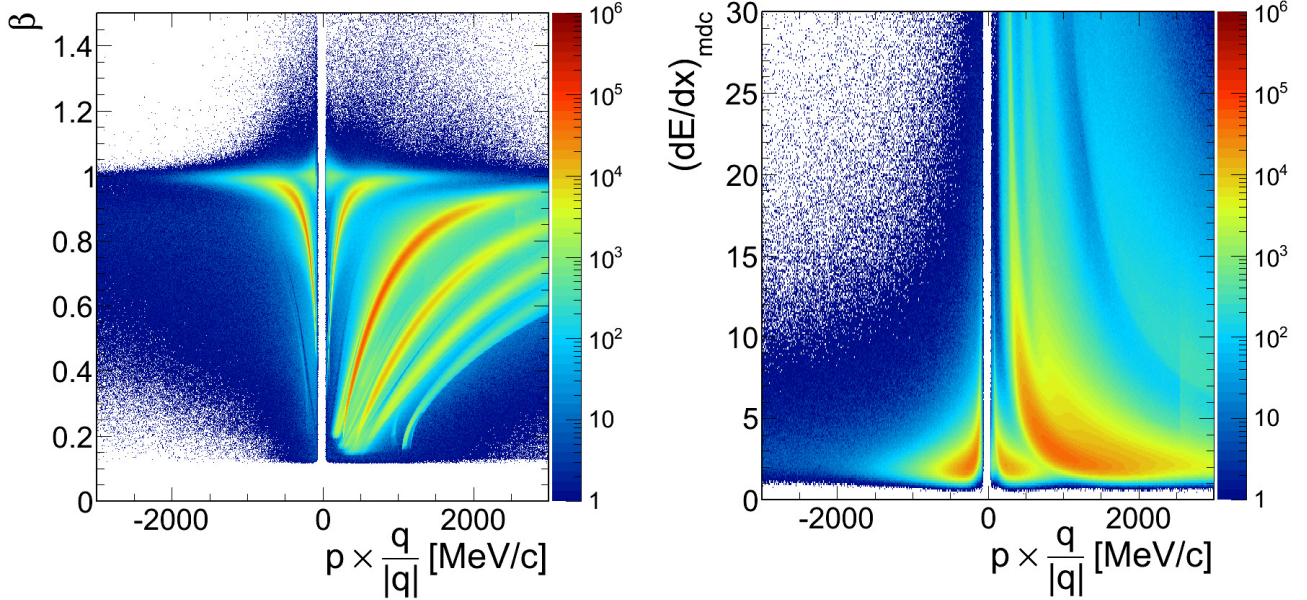


Figure 3.14: Distributions of velocity (left panel) and energy-loss in MDC (right panel) versus momentum times polarity. By the combination of these observables the tracks can be assigned to a particle species.

Another possibility is to use the energy-loss measured in the MDC or TOF. This energy-loss is linked to the velocity of the particles by the Bethe-Bloch formula:

$$-\frac{dE}{dx} = 4\pi N_A r_e^2 m_e c^2 z^2 \frac{Z}{A} \frac{1}{\beta^2} \left(\frac{1}{2} \ln \left[\frac{2m_e c^2 \beta^2 \gamma^2 W_{\max}}{I^2} \right] - \beta^2 - \frac{\delta(\beta\gamma)}{2} \right), \quad (3.21)$$

with $N_A = 6.022 \cdot 10^{23} \text{ mol}^{-1}$ being the Avogadro number, $r_e = 2.8 \text{ fm}$ and $m_e = 0.511 \text{ MeV}$ the classical radius of the electron and its mass, z the charge of the traveling particle, Z the charge of the absorber and A its atomic mass number, W_{\max} the maximum possible energy transfer to the electron in a single collision, I the mean excitation energy and $\delta(\beta\gamma)$ a correction term for the density effect. This formula describes the energy-loss of a relativistic particle when passing through a medium and interacting with the electrons via ionization and excitation as a function of the path length. It depends only on the charge and velocity of the traveling particle but not on the particles' mass which is needed for identification. Yet when plotting against the reconstructed momentum as shown in the right panel of Fig. 3.14, the different particle species get separated since the momentum is mass-dependent.

3.9 Λ hyperon reconstruction

The Λ hyperon is a weakly decaying particle. Its mean lifetime has been measured to $\tau = (2.632 \pm 0.020) \cdot 10^{-10}$ s [Zyl20]. This means that when created at the primary vertex, the Λ hyperon will travel a mean distance of $c\tau = 7.89$ cm before decaying into the final state particles. The final state or daughter particles fly through the tracking system and are both reconstructed (ideally). Since all detectors in HADES are based on electromagnetic interactions, only the decay $\Lambda \rightarrow \pi^- + p$ (branching ratio $63.9 \pm 0.5\%$) can be reconstructed, since for the other possibility, $\Lambda \rightarrow \pi^0 + n$ (branching ratio $35.8 \pm 0.5\%$) there is no device to detect neutrons in HADES yet. All other decay channels have branching ratios far below the percent level, and are therefore not considered.

In this section, the whole procedure from the identification of possible daughter particles to the final sample of Λ hyperons is described.

3.9.1 Identification of Λ hyperon decay products

The daughter particles, i.e. the negatively charged pion and the proton, can be identified by the methods described in Sec. 3.8. However, due to the long path of the mother particle, a reconstruction of the secondary vertex is essential. The momentum reconstruction and velocity calculation is based on a fully reconstructed track which is assumed to point to the primary vertex, which is not necessarily the case for secondary particles. This leads to a shift from the true velocity and momentum of the particle, hence it is not useful to cut strictly on the velocity-momentum correlation. In addition, the main identification procedure is based on the decay topology. In the first step of PID the protons and charged pions have to be identified. Then the decay topology of possible combinations is determined and used to distinguish random pairs from Λ decay products.

The pre-selection of the daughter particles is based on their calculated mass. Re-writing Eq. 3.20 leads to:

$$m^2 = p^2 \frac{1 - \beta^2}{\beta^2 c^2}, \quad (3.22)$$

from which the mass can be calculated. The pre-selection cut set applied for particle identification is summarized in Tab. 3.4. A higher momentum cut is used to remove fast particles with only a little deflection inside the magnetic field and hence low resolution for the momentum reconstruction. The restriction on the measured charge is only to select particles which have been bent in the given direction. The mass distribution after all cuts is shown for a small test sample in Fig. 3.15 for both daughter particles. While the proton peak is nearly free of background (see Fig. 3.15, right), a little contribution of negatively charged muons is visible on the left flank of the pion peak (Fig. 3.15, left). A higher value for the cut of $m_{\pi^-} > 120$ MeV/c² has been tested. While the pion sample becomes more pure, the amount of Λ hyperons is reduced. Hence, within this analysis this stronger cut on the pion mass is not considered.

Cut parameter	π^-	p
mass [MeV/c ²]	50 – 250	600 – 1250
momentum [MeV/c]	< 1000	< 2000
velocity [1/c]	< 1	< 1
charge	< 0	> 0

Table 3.4: Summary for the cut settings used to identify the daughter particles.

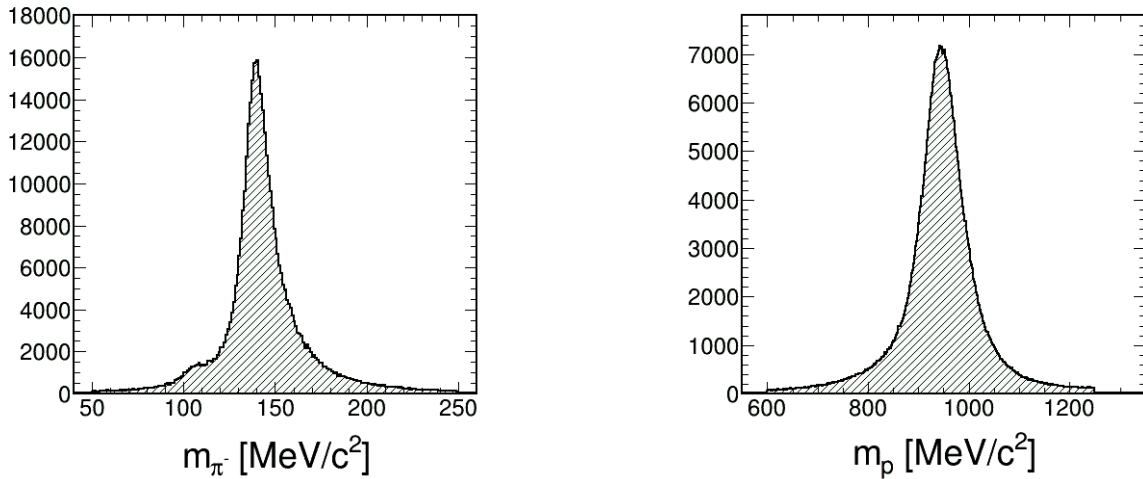


Figure 3.15: Mass distributions of the daughter particles after particle identification cuts. The figures are generated from 30.000 events for day 108 of the Au+Au beam time and plotted after pairing of π^- and p to possible Λ candidates, hence the integral of the pion mass (left panel) and the proton mass (right panel) are the same.

3.9.2 Invariant mass distribution

To decide whether a combination of two identified particles is likely to be from a Λ decay or not, the invariant mass distribution is used. The invariant mass is the mass of the system of the two (or more) final state particles and as the name suggests it is an invariant under the Lorentz-transformation, thus it does not depend on the system of reference. For the single particles, the mass m can be calculated from their energy E and momentum \vec{p} via the relativistic equation:

$$m^2 c^4 = E^2 - (\vec{p} c)^2. \quad (3.23)$$

For better visualization, we will use the so-called natural units (see Ap. 9.1) in this section. To get back the original units, the corresponding masses and momenta have to be multiplied with multiples of c according to Eq. 3.23. The invariant mass of a system of n particles is defined as:

$$M_{\text{inv}} = \sqrt{\left(\sum_{i=1}^n E_i \right)^2 - \left(\sum_{i=1}^n \vec{p}_i \right)^2}. \quad (3.24)$$

Applying this equation for the system of a negatively charged pion (index π^-) and proton (index p) and using Eq. 3.23 for the two daughter particles, we obtain the following equation:

$$M_{\text{inv}} = \sqrt{(E_{\pi^-} + E_p)^2 - (\vec{p}_{\pi^-} + \vec{p}_p)^2} \quad (3.25)$$

$$= \sqrt{m_{\pi^-}^2 + m_p^2 + 2\sqrt{m_{\pi^-}^2 + \vec{p}_{\pi^-}^2} \sqrt{m_p^2 + \vec{p}_p^2} - 2|\vec{p}_{\pi^-}||\vec{p}_p| \cos \Delta\alpha}. \quad (3.26)$$

As can be seen the invariant mass only depends on the masses, momenta of the daughter particles, and the opening angle $\Delta\alpha$ between them. If a particle candidate passes the corresponding conditions defined in Sec. 3.9.1, the nominal masses will be used in Eq. 3.26, i.e. $m_p = 938.27 \text{ MeV}$ and $m_{\pi^-} = 139.57 \text{ MeV}$ [Zyl20]. This is done in order to not propagate the uncertainties from the time-of-flight measurement further into the analysis. The momenta and the opening angle are taken from the Runge-Kutta procedure.

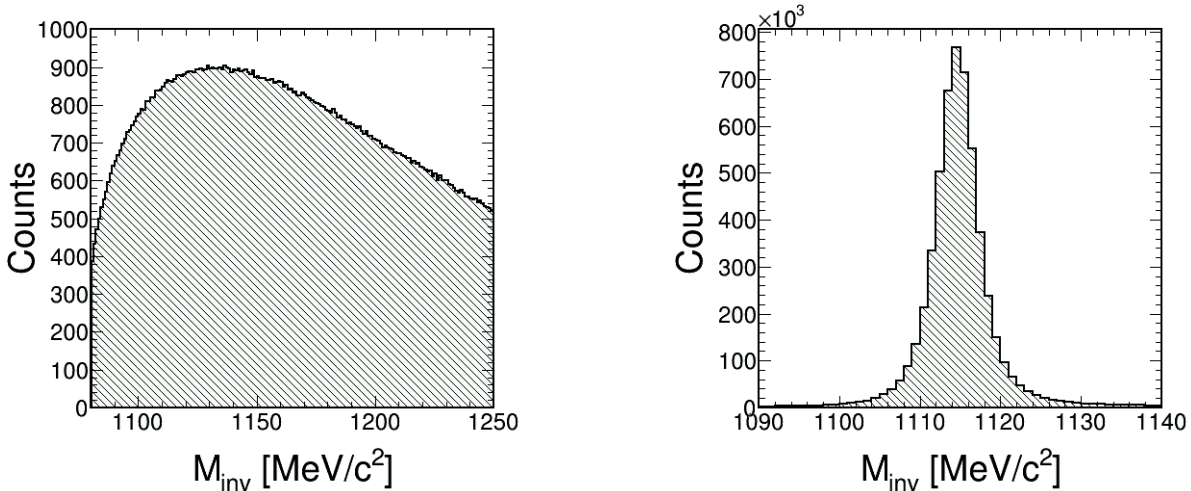


Figure 3.16: Invariant mass distribution after daughter identification. Left panel: the distribution is plotted from experimental data. No Λ peak is visible at this stage of the analysis, the combinatorial background dominates. Right panel: the same distribution is plotted for Λ hyperons generated via Pluto and embedded to UrQMD.

In the right panel of Fig. 3.16 the reconstructed invariant mass distribution for Λ hyperons which have been generated with the Pluto event generator and embedded to real data is shown. For the ideal case, when both daughter particles originate from the same Λ hyperon, a clear peak structure appears around the nominal mass of the Λ hyperon of $M_\Lambda = 1115.683 \pm 0.006 \text{ MeV}$ [Zyl20]. The measured decay width is much broader than the intrinsic width $\Gamma_\Lambda = 2.5 \cdot 10^{-6} \text{ eV}$ since it is folded with the detector resolution of the momentum reconstruction of $\sigma = o(10^6 \text{ eV})$, therefore the resolution of the Λ peak is around 0.2%.

The left panel of Fig. 3.16 shows the same distribution for experimental data. Due to the large amount of background, mainly from random combinations of π^- and p , no mass peak at the nominal Λ mass is visible. All combinations of π^- and p which do not originate from a Λ decays, are called background. Theoretically there are correlated and uncorrelated background contributions. The main source of background is random combinations of pions and protons which by chance pass all cut settings. But it is also possible that a daughter from a Λ decay

is combined with a particle not correlated to this decay. These combinations will not fulfill the energy and momentum conservation and therefore populate over the whole invariant mass range. The minimum invariant mass is set by the masses of the daughters, i.e. $m_p + m_{\pi^-} \approx 1078 \text{ MeV}$.

The correlated background is related to decays of particles, for example $\Delta^0(1232) \rightarrow p + \pi^-$, to the same final state. Due to the higher nominal mass of the Δ^0 , they are expected to populate a higher invariant mass range. However, since the lifetime of the Δ^0 is $\tau \sim 1 \text{ fm}$, the decay products p and π^- are expected to point to the primary vertex and thus being removed by topology cuts (see Sec. 3.9.4).

It is also possible that the decay products of $K_S^0 \rightarrow \pi^+ + \pi^-$ may form background pairs, i.e. when the π^+ is misidentified as a proton. Such combinations may create a second peak in the invariant mass spectrum at their nominal mass, but for the Λ there is no candidate close in the invariant mass distribution.

3.9.3 Background determination

Combinations of $\pi^- + p$ include both signal (correlated) contribution and combinatorial background (random combinations):

$$N_{\pi^- p}^{\text{TOT}} = N_{\text{Sig}} + N_{\text{BG}}. \quad (3.27)$$

Consequently, the background has to be determined and distinguished from the signal. One possibility is to exchange one of the daughter particles by its charge conjugate which is known as the **like-sign method**. Since anti-protons are extremely rare at HADES energies, for the Λ decay the only possibility would be to exchange the π^- by the π^+ . The proton and positively charged pion are very unlikely to appear in the same final state of a decay, their combinations can be considered uncorrelated. However, the acceptance for π^- and π^+ in HADES is different leading to distortions in the invariant mass spectrum and hence this method is not used.

The second method is the so-called **side-band method**. The regions besides the invariant mass peak of the signal are used. These regions are dominated by uncorrelated background and correlated contributions from other decays smeared over the spectrum are also included. To improve the performance of this method, the shape of the background is fit based on the side-bands of the distribution. This is described in detail in Sec. 3.9.7.

The third method which is also used in this analysis is the **mixed-event method**. The daughter particles are selected and combined from different events which by definition includes no physical correlations between them while succumbing the same acceptance and reconstruction effects. For this purpose, the events have to be mixed to fulfill several criteria since different event characteristics might not describe the background realistically:

- Only events from the same file are mixed (which is typically a time range of several minutes) to avoid systematics from different detector performances over the beam time.
- The events are grouped according to the number of reconstructed track candidates with a bin width of $\Delta N_{\text{track}} = 10$ resulting in 12 bins overall.
- A minimum requirement on the opening angle of $\Delta\alpha > 15^\circ$ is set, motivated by previous studies [Sch17]. For close pairs, where the opening angle between the two daughter tracks is small, the reconstruction efficiency is small in the same-event analysis compared to the mixed-event where the two tracks are independent.

Since the mixed-event method is used as an input for the neural network trained to distinguish between signal and background based on the decay topology (see Sec. 3.9.5), it is crucial that the topology parameters are reproduced well (see Fig. 9.1). To ensure this strict classification of the mixed-events, it is required to further divide the sample in classes according to the event vertex position. Concerning the z-direction, the events are grouped into 15 classes, one for each target segment. The mean positions have been fit and then the groups are chosen to be equally in size resulting in a bin width of $\Delta Z_{\text{Vertex}} = 3.577$ mm around the averaged mean position of the target. For the x- and y-direction the distributions are first shifted such that the average event vertex position matches the beam axis $(X_{\text{Vertex}}, Y_{\text{Vertex}}) = (0, 0)$. Then the events are grouped in 10 bins of equal size, resulting in 100 bins in the xy-plane.

If the mixed-event method is used to determine the background for flow or polarization observables, the events have to be classified additionally in groups of similar event plane Ψ_{EP} (see Sec. 4.4). However, for the description of the decay topology and the invariant mass distribution, this does not make any difference and thus it is not used for these quantities.

After the events are classified, the corresponding particles are mixed. It allows to generate basically an infinite amount of statistics and to reduce the statistical uncertainties in the background determination. The mixed-event distribution then has to be scaled according to the side-bands of the same-event distribution. Afterwards it can be subtracted as described in Sec. 3.9.7 and also compared to the side-band method.

3.9.4 Decay topology

The combinatorial background is dominating the distribution as shown in the left panel of Fig. 3.16. No signal is visible at this stage of the analysis. Hence further selection criteria have to be introduced to reduce the background while not affecting the signal as much. This is possible by using the topology of weak decays. Due to their longer lifetime, the mother particle travel on average a certain distance before its decay and hence produces a specific geometrical distribution. This is shown in Fig. 3.17. A detailed calculation of the topology parameters and the secondary vertex is described in Ap. 9.4. Only the geometrical meaning of these parameters is discussed in the following:

- d_1 : This is the distance of closest approach (DCA) between the mother track and the event vertex. As the Λ hyperon should have been created within the interacting volume of the collision, its track should point back to the event vertex and consequently this parameter will define an upper limit.
- d_2 : Since the two daughter particles originate from a secondary vertex, their tracks are more likely to point away from the event vertex (off-vertex tracks). This parameter returns the DCA of the **proton** track and the event vertex, which will be used as a lower limit in order to reject primary protons originating directly from the collision and to reduce combinatorial background.
- d_3 : This is the same parameter as d_2 but calculated for the **pion** track. Henceforth it will also be used as a lower limit.
- d_v : This is the distance between the secondary and the event vertex. Due to the longer lifetime of the Λ hyperon, it is expected to travel a certain distance before decaying. Hence this parameter can be used to make sure the secondary vertex is away from the event

vertex and will be used as a lower limit. This might especially reduce contributions from $\Delta^0(1232) \rightarrow p + \pi^-$ decays (strong decay), since these daughters are very likely to be created within the event vertex.

- d_t : This is the DCA between the two daughter tracks. As they should originate from the same secondary vertex, they must be rejected if the distance between them is too large (upper limit). The middle point of the DCA line connecting the two tracks is used as the **secondary vertex**.
- $\Delta\alpha$: This is the opening angle between the two daughter tracks as already used in Eq. 3.26 to calculate the invariant mass. If this angle is small, the reconstruction efficiency in MDC I and II drops significantly. The main influence is related to the background description via the mixed-event method discussed in Sec. 3.9.3 since both particles are from different events and thus their reconstruction efficiency is higher compared to close tracks in the same event. So a lower limit of $\Delta\alpha > 15^\circ$ has to be applied in both same-event and mixed-event data to fix this problem.

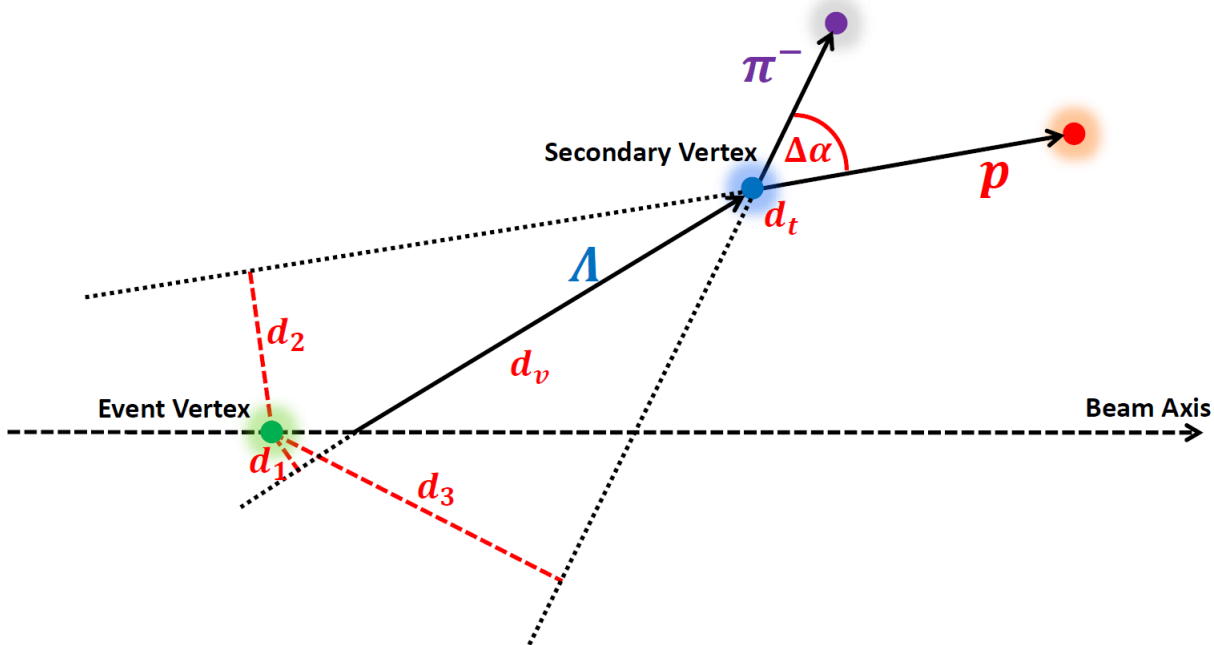


Figure 3.17: Schematic drawing of the topology of the Λ decay in two dimensions. Being produced at the event vertex, the Λ hyperon flies a certain distance and decays at the secondary vertex into π^- and p . The topology parameters to distinguish whether a combination (π^-, p) originates from a Λ hyperon are shown: DCA between mother track and event vertex (d_1), DCA between event vertex and proton respectively pion (d_2, d_3), path length of the Λ hyperon (d_v), DCA between the two daughter tracks (d_t) and the opening angle ($\Delta\alpha$).

In Fig. 3.18 the distributions of the topology parameters are shown for signal and background. The signal distributions are generated via Pluto and embedded into real events. For the determination of the background shape, the mixed-event method is used. The distributions for d_t and d_1 are very similar for signal and background, while others differ from each other especially the d_v distribution shows the largest difference. One has to mention

that the parameters are highly correlated, hence a cut on one variable may have a strong impact on all other distributions. However, this correlation is very different for signal and background which can be used to distinguish these two contributions for the same-event. In previous analysis [Sch17] the cut values of the topology parameters have been varied to find the optimum configuration in terms of signal-to-background ratio S/B and significance. The significance is defined by the signal S and the background B as:

$$\text{SIG} = \frac{S}{\sqrt{S + B}}. \quad (3.28)$$

The cut on the opening angle $\Delta\alpha > 15^\circ$ is motivated to match the reconstruction efficiency in same-event and mixed-event samples and will be kept for this analysis. The other parameters will differ from the previous analysis, since another approach is used to reconstruct the Λ hyperons with higher efficiency as described in Sec. 3.9.5.

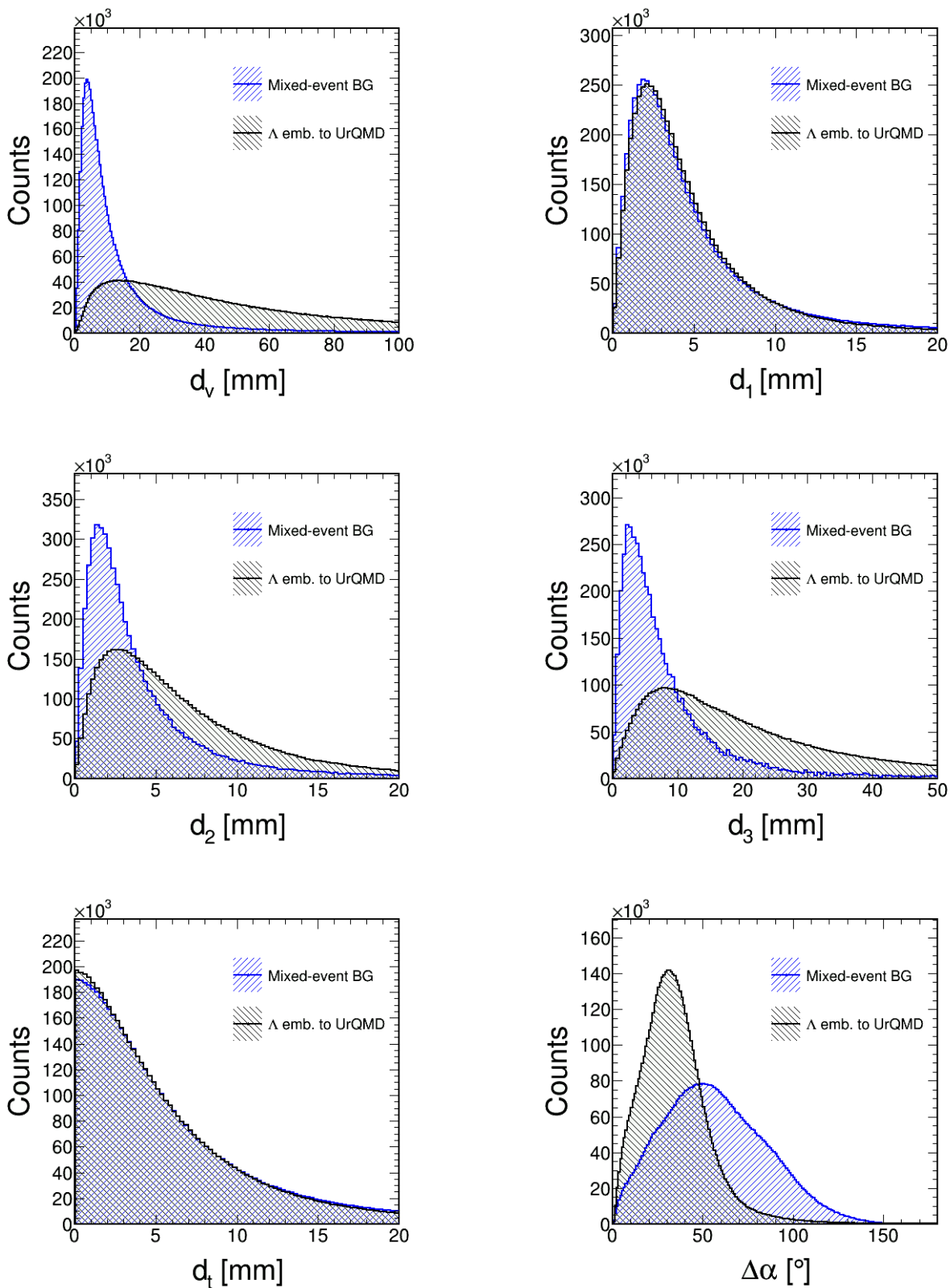


Figure 3.18: Distributions of the topology parameters in Au+Au. The signal (black) is generated using the Monte-Carlo event generator Pluto while the background (blue) is determined by the mixed-event method.

3.9.5 Multilayer perceptron

The search for a polarization signal of the Λ hyperons demands a high amount of reconstructed particles. Especially, since the Λ hyperon production is at-/sub-threshold. Therefore the yields are smaller compared to higher beam energies.

The selection of the Λ candidates is based on its decay topology which includes several parameters. A so-called hard-cut analysis can be used when the selection criteria on the topology parameter are fixed at a particular value. Yet this is not very efficient, as a pair of particles from a real Λ might be cut out only because one single parameter does not pass the cuts while others are perfectly fine. To increase the selection efficiency a neural network will be used for this purpose.

As an artificial neural network, the multilayer perceptron (MLP) as implemented in the ROOT package *Toolkit for multivariate analysis* [Hoe07] is used. The MLP was tuned to deliver a high flexibility for different applications while preserving fast calculation speed.

The MLP is used as a discriminator. Based on a set of parameters, a single decision will be made whether this set corresponds to a possible Λ candidate or not. Thereby, all correlations between the input parameters are taken into account at the same time which increases the discrimination power with respect to a default hard-cut analysis.

The MLP consists of several layers of neurons. The input layer consists of one neuron per input parameter and one bias neuron in addition. The output layer in this case consists of only one neuron, such that the network can be mathematically seen as a function $f : \mathbb{R}^N \rightarrow D$, where N is the number of input parameters and D is the discriminant returned from the output neuron. Inbetween several hidden layers with varying number of neurons can be placed. Each of these neurons gets input from all neurons from the previous layer. As a perceptron, the neurons output is only send to following layer. For each connection between a neuron i to a neuron j - again only connections from sequential layers are possible - a corresponding weight $w_{ij}^{(k)}$ is associated, while (k) accounts for the layer of neuron j . Then the overall input of neuron j is calculated according to:

$$x_j^{(k)} = \text{Act} \left(w_{0j}^k + \sum_{i=1}^{N_{\text{Neurons}}^{(k-1)}} w_{ij}^{(k)} x_i^{(k-1)} \right), \quad (3.29)$$

while $x_i^{(k-1)}$ is the output value from the previous layer $(k-1)$ and the sum is performed over all neurons in this layer. The bias neuron has a fixed output value of $x_0 \equiv 1$. The bias neuron is implemented to guarantee the convergence of the optimization procedure. For a fixed discriminant D the network defines a $(N-1)$ -dimensional hypersurface in the space spanned by all input parameters and the bias neuron shifts the surface with respect to zero such that the minimization stability is ensured. $\text{Act}(x)$ is the activation function of the neuron which maps the overall input to a value in the intervall $[0, 1]$. During this analysis, the activation function is a sigmoid given by:

$$\text{Act}(x) = \frac{1}{1 + e^{-x}}. \quad (3.30)$$

The activation function will not be applied for the output layer. Besides the structure of the network, the MLP is solely defined by the weights $w_{ij}^{(k)}$. To find the right setting of weights for

a certain application the network has to be trained. In a sense, training or learning is nothing more than adjusting the weights via a minimization procedure. In this case, the neural network will be used to distinguish between signal and background. In an ideal case, for a set of input parameters from the signal, the network should return 1, while the return value is 0 in case of background. The network starts with random values for the weights. Then training samples, one for signal and one for background, are used to calculate the output of the network. Knowing that the result should be either 1 or 0, the weights can be adjusted by a procedure called back-propagation. Therefore, an error function which depends on the input parameters and all weights is defined as:

$$E(\vec{x}_1, \dots, \vec{x}_{N_{\text{Training}}} | \vec{w}) = \sum_{a=1}^{N_{\text{Training}}} E_a(\vec{x}_a | \vec{w}) = \sum_{a=1}^{N_{\text{Training}}} \frac{1}{2} (D_{\text{ideal}} - D_a)^2. \quad (3.31)$$

N_{Training} is the number of events in the training sample, D_{ideal} is the ideal output value for the event, and D_a the calculated value. Based on the difference of all training events, the weights are updated according to the gradient of E in the w -space by:

$$\vec{w}^{(l+1)} = \vec{w}^{(l)} - \eta \vec{\nabla}_{\vec{w}} E, \quad (3.32)$$

with $l + 1$ being the training cycle meaning one loop over the training sample and η being the learning rate. If the learning rate is too large, the weights will change significantly from cycle to cycle and might not converge. If the rate is chosen too small, the training speed is very slow and a lot of cycles or a large amount of data is needed. In both cases, the result of the network might not be very efficient, hence η has to be chosen properly. For this purpose the default value defined by the TMVA package of $\eta = 0.02$ is used. As shown in previous analysis [Spi18] the structure of the neural network has only little influence on the results. However, the performance could be improved by increasing the amount of training cycles and the number of neurons in the hidden layers. A compromise has been made with respect to reasonable training times and complexity. Two hidden layers were set up consisting of $N + 2$ and N neurons, N being again the number of input parameters. The training cycles have been set to 1500.

For this analysis, the main purpose of the MLP is to distinguish random combinations of identified π^- , p from the correlated Λ decay products. Therefore, the decay topology parameter will be used as input variable for the network, i.e. d_1, d_2, d_3, d_ν and d_t (see Sec. 3.9.4). The opening angle $\Delta\alpha$ is not used as it is associated to different reconstruction efficiencies between same-event and mixed-event data as discussed above. Another parameter not used is the momentum of the Λ hyperon. Even this would improve the background suppression further, it also introduces a strong phase-space dependence of the selection which is dangerous for the extraction of the final results. More details can be found in Ap. 9.5.

Due to the strict daughter particle selection, there are more misidentified particles in the sample, especially the μ^- peak classified as π^- as can be seen by the small peak on the left of the pion mass peak in Fig. 3.15. Investigations showed that the discrimination between signal and background could be improved by additionally using the calculated masses m_p and m_{π^-} as input parameters. This lead to a final set of 7 input parameters for the MLP. Another issue was related to a pre-selection of the training samples in order to increase the efficiency of the discrimination. The aim is not to use any hard-cuts on the decay topology and instead let the neural network

take all correlations into account which are then used in the discrimination process to distinguish signal from background. However, as it has been discussed in the first use of an MLP for Λ selection in Au+Au [Spi18] in comparison to hard-cut analysis [Sch17], pre-cuts on the decay topology highly increase the performance of the MLP. Since most Λ hyperons still decay very close to the primary vertex they are hard to distinguish from random combinations of primary p and π^- , especially since the difference in correlations of the topology parameters is smeared by the spatial resolution of the tracking system. Therefore, a pre-selection according to the decay topology parameters is done before the MLP is trained. The summary of the minimum requirements is summarized in Tab. 3.5 and compared to the final hard-cut analysis used in [Sch17]. Starting from these values, the thresholds for the decay topology parameters have been lowered in steps and then the performance of the MLP has been compared. It has been seen that the cut on d_v is one of the most important cuts for the discrimination of signal and background. Even when the threshold of $d_v > 50$ mm already cuts more than half of the sample (compare to Fig. 3.18), this cut could not be lowered further without significant loss in discrimination power.

Topology parameter	Hard-cut analysis [Sch17]	This analysis
d_v	> 65 mm	> 50 mm
d_1	< 5 mm	< 12 mm
d_2	> 8 mm	> 5 mm
d_3	> 24 mm	> 15 mm
d_t	< 6 mm	< 10 mm
$\Delta\alpha$	$> 15^\circ$	$> 15^\circ$

Table 3.5: Thresholds for the decay topology parameters as used in this analysis. In comparison to the hard-cut analysis, the thresholds are much lower as the final selection is based on an artificial neural network. An explanation of the topology parameters can be found in Sec. 3.9.4.

The topology parameters for signal and background following the selection mentioned above are shown in Fig. 3.19. As can be seen when compared to Fig. 3.18, the differences in the shapes of the two samples are much stronger, especially for d_1 and d_t , which will support the neural network to improve discrimination. Furthermore, the mass distribution of the negatively charged pions, the background has a second peak at around $m = 105$ MeV/c² which corresponds to the muon mass peak. This contamination is significant, however, since the network will be trained on the masses too, it will learn to distinguish muons from pions.

Making use of this pre-selection, the MLP can be trained to distinguish background with similar characteristics from true Λ decays. To train the neural network, two training samples - one for signal and one for background - are needed which describe both in the same-event experimental data as close as possible. As a modeling of the signal, the Λ hyperons are generated using the Monte-Carlo event generator Pluto. The Λ hyperons are assumed to be created from a thermal source with temperature $T = 100$ MeV and radial expansion velocity $\beta_r = 0.34$. For a realistic reconstruction efficiency the Λ hyperons are embedded into real events. To assure a high statistics sample, an acceptance filter is applied prior, such that only both daughter particles of the Λ hyperon reaching the detector and having at least the chance to be reconstructed, are used for embedding. The simulation of the detector response and reconstruction efficiency is done by HGEANT. Finally, one Λ hyperon per event is embedded to the real event.

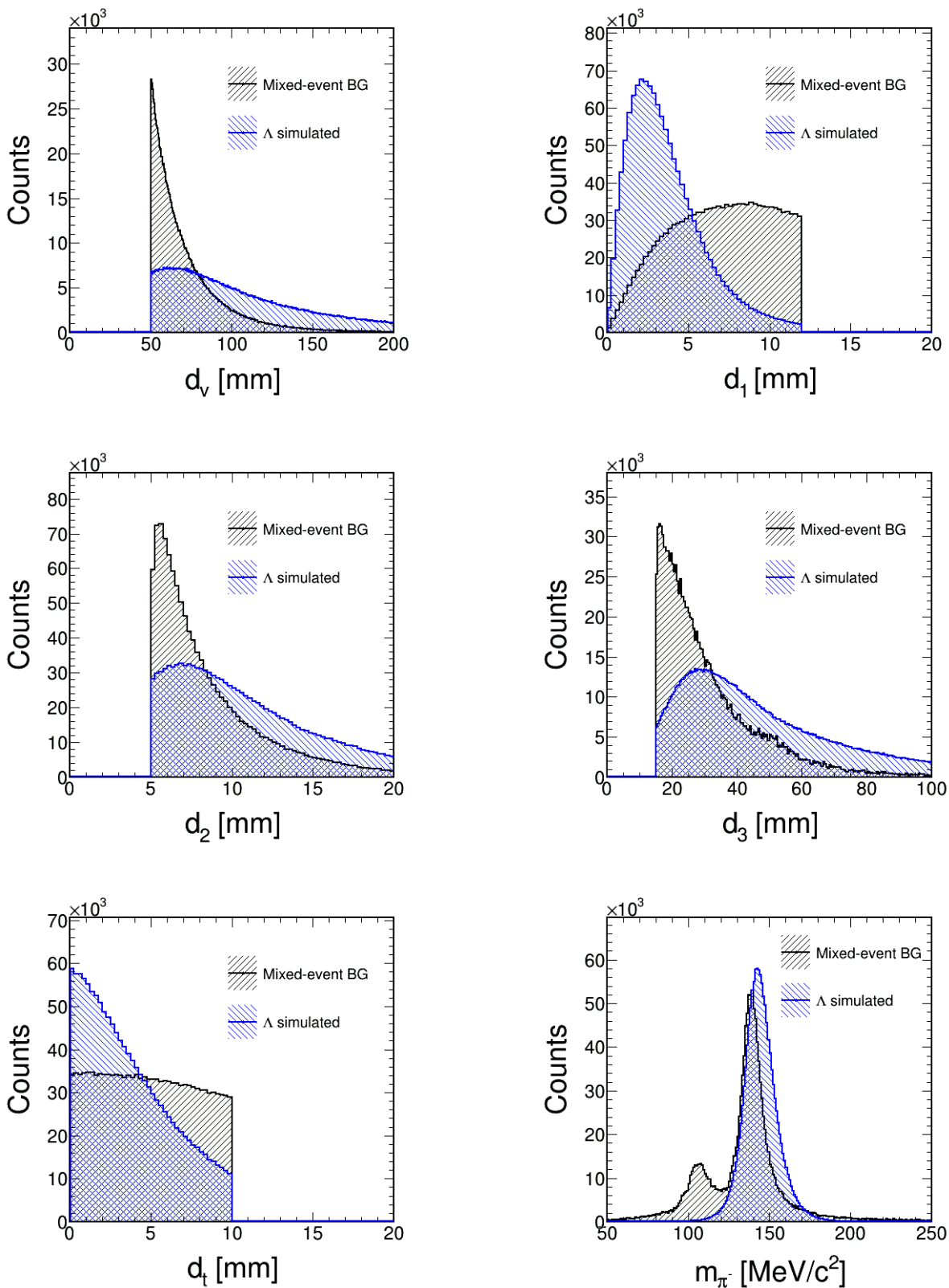


Figure 3.19: Distributions of the topology parameters in Au+Au collisions after pre-selection criteria applied. The signal (black) is generated using the Monte-Carlo event generator Pluto and can be clearly distinguished from the background (blue) which is determined by the mixed-event method. The results without pre-selection are shown in Fig. 3.18.

Since the mixed-event background by definition contains only combinatorial background, it is used for training of the MLP, because physical correlations do not appear in this sample but kinematical distributions of the particles are as realistic as possible. As can be seen from Fig. 9.1 in the appendix, the distributions of the topology parameter from the same-event are excellently reproduced by the mixed-event background.

$5 \cdot 10^5$ simulated events for Au+Au and $2.5 \cdot 10^6$ for Ag+Ag (at 1.58AGeV) have been used, splitted in half for training and testing of the MLP. These numbers are set by the statistics which have been simulated. The number of background events have been adjusted to an equal amount, to not train the network specifically on signal or background. After all weights are determined, the TMVA package provides a number of tools to control the performance of the training procedure. Fig. 3.20 displays the architecture of the neural network as it was used. The input parameters on the left are connected to the neurons of the first hidden layer and in the end one single output value is returned. The thickness and color of the connections between two neurons indicate how large the corresponding weight is. Since in the beginning, the weights are initialized randomly, the neurons from the first hidden layer on are not necessary the same for two trained network. This can be seen when comparing the results for Au+Au on the left with the one from Ag+Ag on the right. However, the structure in both cases is similar, see for example the strongest connections from the input to the first hidden layer, where for both the strongest weights are connecting d_2 and the bias neuron with one neuron of the next layer.

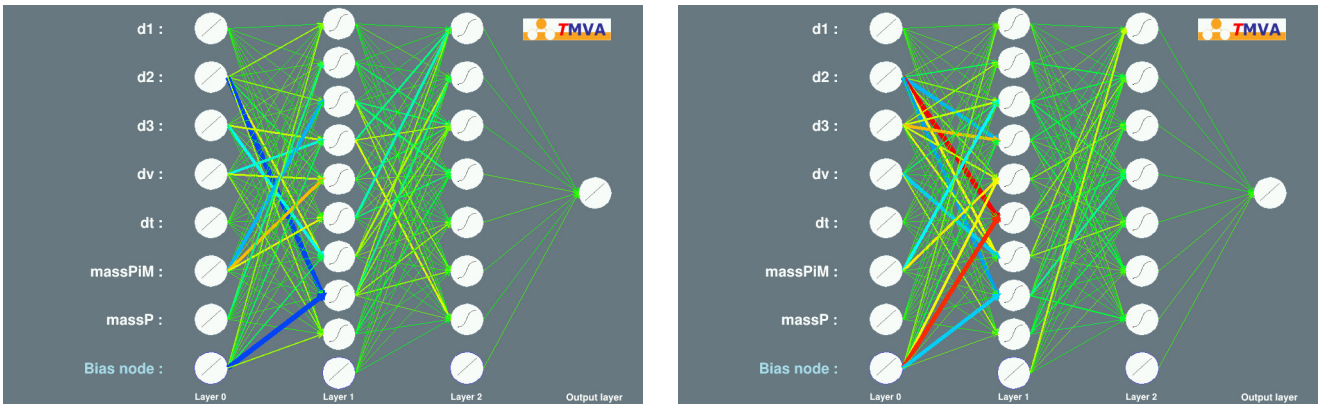


Figure 3.20: Architecture of the MLP after training for Au+Au (left) and Ag+Ag (1.58AGeV, right). The network consists of an input and two hidden layers which varying number of neurons and returns one final output value. The thickness and color of the connections between neurons indicate how strong the corresponding weights are. The figure has been produced using the TMVA package [Hoe07].

In Fig. 3.21 the correlation matrix for all the parameters used for the MLP is displayed for signal and background separately. The diagonal elements are the correlations of the parameters with themselves and hence they are always 100 %. For the background, most of the parameters do not show any correlation between them, there is only a $\approx 50\%$ correlation between d_v and d_3 . For the simulated Λ hyperons, this correlation is much stronger ($\approx 80\%$). In addition, there are also strong correlations between d_v , d_2 and d_3 and a small correlation of d_1 and d_t . This illustrates the advantage of an MLP for such a discrimination problem since all these correlations can be taken into account at the same time. Even if parameters like the masses do not show strong correlation to the decay topology, they can still be important to improve the selection power by being differently distributed for signal and background as shown in Fig. 3.19.

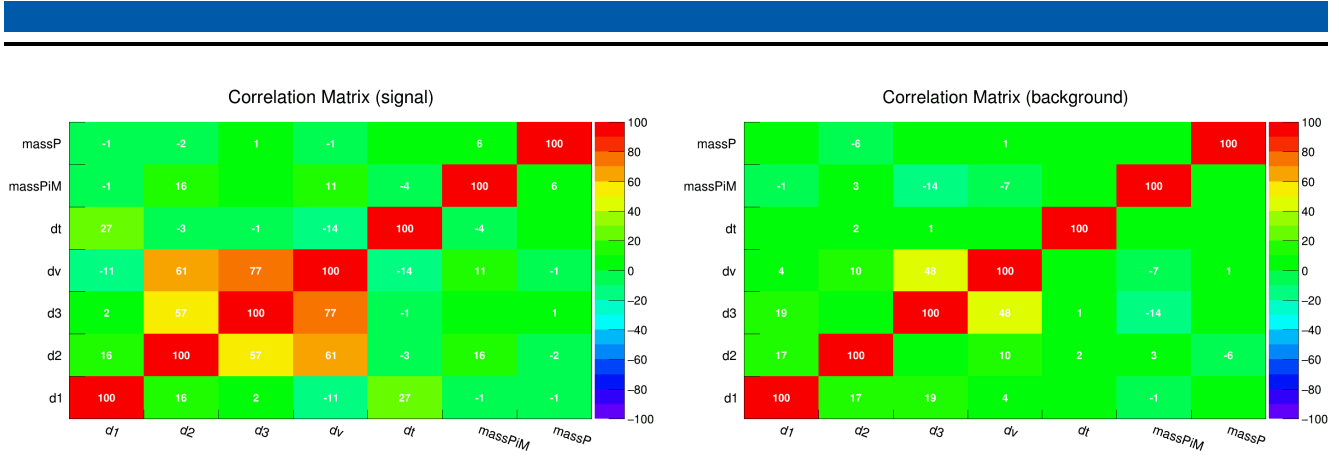


Figure 3.21: The correlation matrix for the parameters used in the MLP for signal (left) and background (right) as calculated from the testing samples. The diagonal entries are the correlations of the parameters with themselves and hence have to be 100%. The figure has been produced using the TMVA package [Hoe07].

To check the performance of the MLP on the training sample, one can plot the distribution of the MLP output, i.e. the discriminant, for the testing samples. This has been done in the left panel of Fig. 3.22. Clearly, the distribution of the background peaks at the ideal value of $D = 0$ while for the signal the peak is at $D = 1$. This shows that the network training was successful. Since the discrimination is never perfect, both distributions have long tails and consequently there will always be background classified as signal and vice versa. However, this contamination in the testing sample is very small. The right panel of Fig. 3.22 shows several different statistical parameters as a function of a minimum discriminant cut value D_{\min} . To bring these distributions closer to the situation of the real experiment (here for the Au+Au data), the amount of background is enhanced by a factor of 20 to match the measured Λ production rate of $5 \cdot 10^{-2}$ per event [Spi18].

The solid blue and red lines show the cut efficiency for signal and background respectively. Without a cut on D , the efficiency is $\epsilon = 1$ for both samples. Increasing the minimum discriminant, the background is cut more strictly than the signal which can be seen by the sharp drop of the red solid line from 0 to 0.2. Enhancing the cut further, at some point the background only decreases slowly, however, the reduction of the signal becomes more and more important. This must be considered in order to find the optimum cut value for the discriminant D . Regarding the purity of the sample, the distribution grows monotonically with increasing discriminant. This means that the sample gets cleaner with a strict D -cut. However, for the type of analysis here, there are methods to measure signal and background contributions but a high amount of statistics is required. Hence, it is not useful, to aim at the purest Λ sample.

A statistical quantity taking both purity and statistics into account is the significance. It is shown as the green solid line in the right panel of Fig. 3.22. As can be seen, the distribution rises to some maximum value (at around $D = 0.9$) and then drops down to zero if the sample gets minuscule. It follows that to find the optimum cut value for the discriminant, the significance will be used. One has to mention, that the distribution of the significance strongly depends on the signal-to-background ratio. In addition, the distributions shown here are generated from the testing sample which includes pure combinatorial background and simulated Λ s. This might not fully reproduce the situation in experimental data, especially since the signal-to-background ratios for the different beam times differ. In addition, there are also other sources of correlated

background which are not known to the MLP since they are not included in the mixed-event sample.

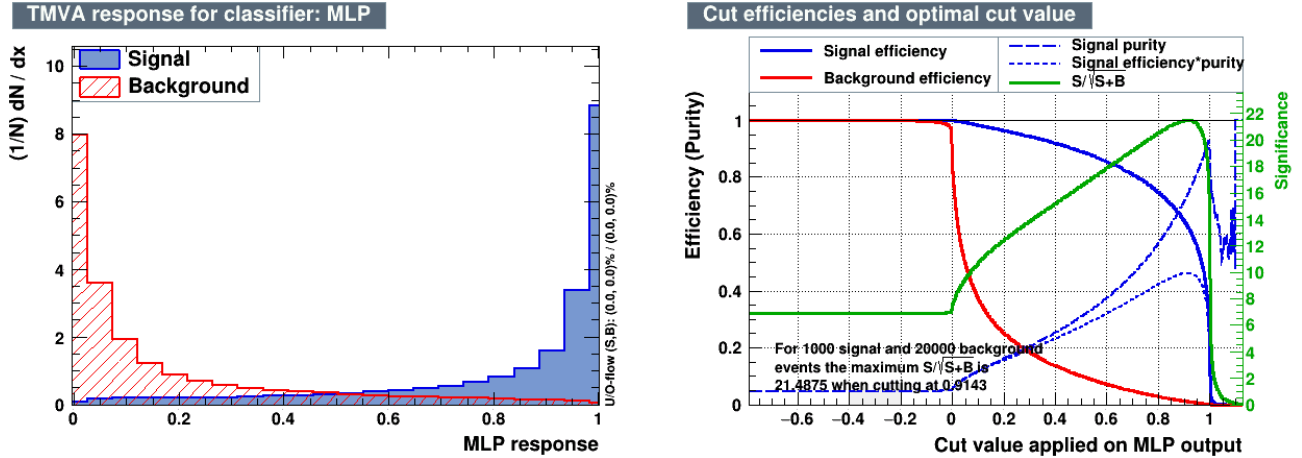


Figure 3.22: Left panel: Normalized distributions of signal and background as a function of the discriminant (MLP response). As required, the background mostly peaks at 0 while the signal is situated at 1. Right panel: Several distributions of significance, purity, signal and background efficiency as a function of the discriminant for a more realistic signal-to-background ratio of 1 : 20. Both figures have been produced using the TMVA package [Hoe07].

To decide which minimum requirement for the discriminant will be used, similar plots of statistical quantities have been produced for the experimental data. From the response of the MLP, it is expected that the optimum cut value will be somewhere between $D = 0.5$ and $D = 1$. The lower limit is very helpful in order to determine the actual signal in the sample. Taking only the stage of the pre-selection according to the decay topology - corresponding to a cut of $D = 0$ - there is no Λ peak visible in the invariant mass distribution⁴. Hence the amount of signal cannot be determined. Starting from a minimum value of $D = 0.5$, the Λ peak can be fit as described in detail in Sec. 3.9.7. The amount of signal and background in the sample can then be determined and based upon this all the statistical quantities are calculated. The same can be done with a slightly higher cut value, for example $D = 0.505$. Increasing the discriminant in these small steps up to a minimum cut of $D = 1$, all the statistical quality parameters can be plotted as a function of the discriminant. Fig. 3.23 shows the significance as well as signal-to-background ratios as they vary with different requirements for the discriminant. While the signal-to-background ratio always improves with increasing D , the significance enhances until a certain value and then starts to drop as the amount of signal rejected gets larger⁵. This trend is the same for all beam times, however, the maximum significance is achieved at different positions. It is very dependent on the production rate of the Λ and the amount of background, which is expected to be larger in Au+Au than in Ag+Ag reactions due to the higher amount of nucleons involved in the collision. When comparing the two samples of the same beam energy, the significance

⁴ For such investigations a minimum cut of $D = -10$ is used, since negative output values from the MLP are possible in reality.

⁵ The very last bins around $D_{\min} = 1$ behave different. This is due to the fact that here most of the Λ hyperons are cut out and for the Ag+Ag sample at 1.23 AGeV, the amount of entries are small in general, thus the points are jumping up and down due to variations in the background determination.

is generally larger for Au+Au, the signal-to-background ratio in contrast is larger in Ag+Ag. It has to be mentioned that simulated data of Λ hyperons embedded to Ag+Ag at 1.23AGeV are not available at the moment, thus the neural network trained for the higher beam energy was used to generate these plots.

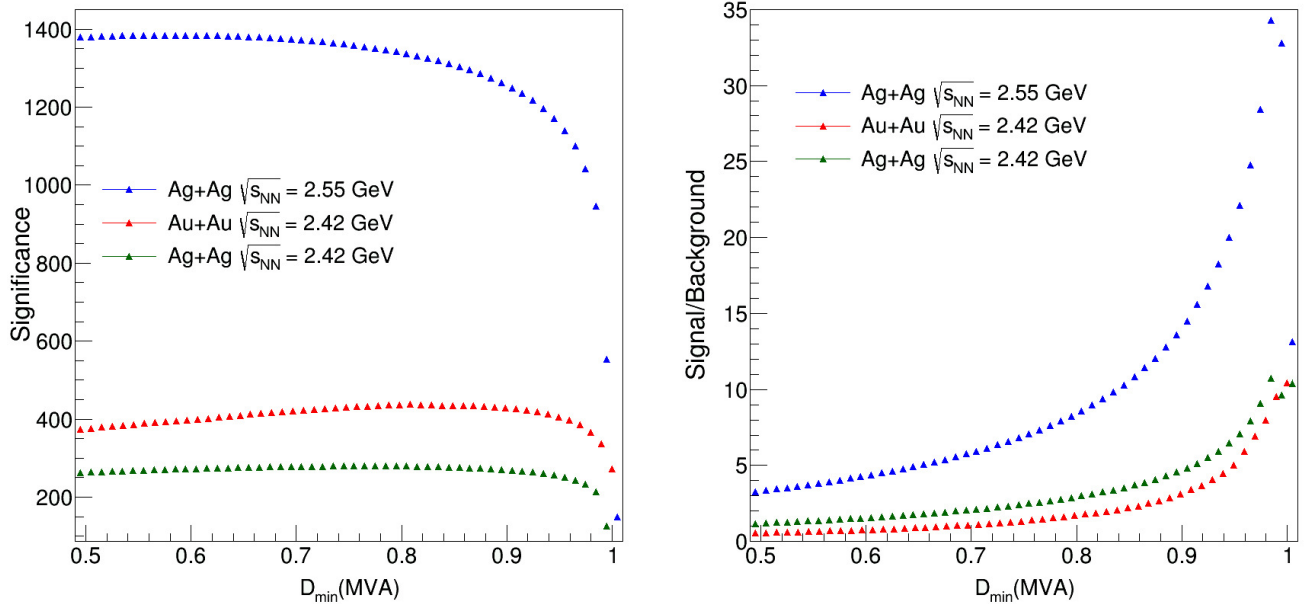


Figure 3.23: Significance (left panel) and signal-to-background ratio (right panel) as a function of the minimum requirement applied to the discriminant for all three beam times. The larger amount of Λ hyperons produced at the threshold is reflected in the higher energy Ag+Ag sample, as the significance and signal-to-background are much higher compared to the other two beam times.

The cut value of the discriminant has been chosen to hit the sample with the largest significance. This is a trade-off between having a clean sample of Λ hyperons but also making sure that the statistics is high enough to perform the analysis. It is also not necessary to go for the purest sample, since the methods used for flow and polarization analysis include a way to describe and subtract the background behavior for these quantities as described in detail in Ch. 4. The minimum requirements for the discriminant for the different beam times are summarized in Tab. 3.6. They will be used in the following for the all calculations based on the corresponding set of experimental data. If any change will be made, this will be mentioned specifically.

Cut parameter	Au+Au@1.23AGeV	Ag+Ag@1.58AGeV	Ag+Ag@1.23AGeV
D_{\min}	0.81	0.58	0.77

Table 3.6: Minimum discriminant as used for the different experimental data samples. These values are determined from the experimental data and hit the maximum value of significance for all beam times separately.

3.9.6 Reduction of multiple counting

The pairing of the identified daughters within one event to a possible Λ candidate does not exclude the possibility of multiple counting. Due to the sheer amount of protons, it is likely that one pion is combined with several protons which are all stored as a possible Λ candidate. This is not a realistic situation since a particle cannot appear in more than one Λ hyperon.

Consequently, a decision has to be made which of the combinations will be used in the analysis. This is done after all the selections and cuts are applied. For the two identified daughter candidates, the occurrence of the same particle is displayed in the left panel of Fig. 3.24. As expected, the same pion appears up to six times in the final sample. The proton appears only up to two times. Overall, the effect is at the percent level, however, the multiple counting will be avoided by an additional step in the analysis procedure.

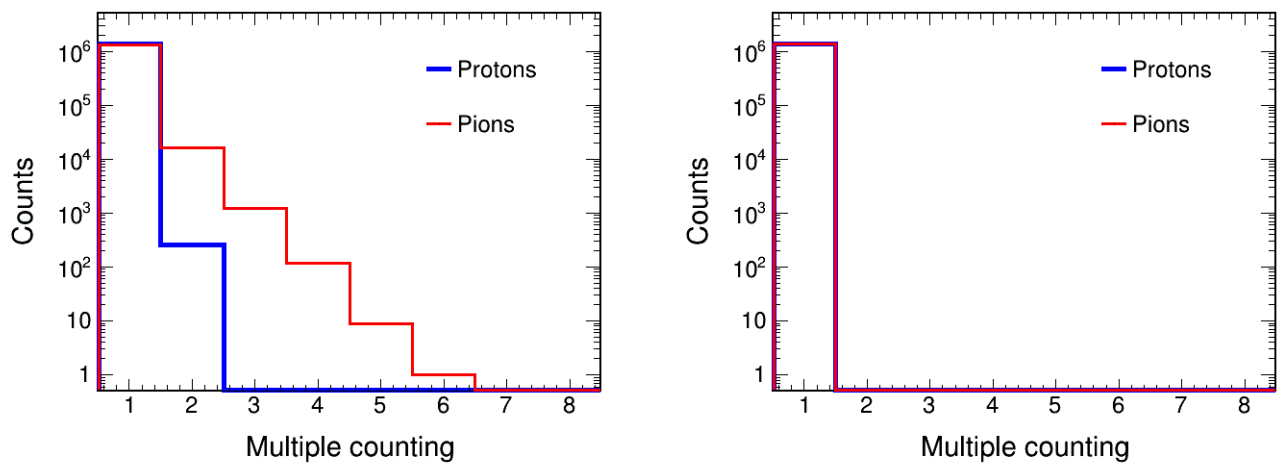


Figure 3.24: Distribution of the occurrence of the daughter tracks in the final sample of the Λ candidates before (left) and after reduction of multiple counting (right).

For the choice of the best pair within an event, all Λ candidates that share the same daughter track are compared in terms of their invariant mass. For each combination, the difference to the nominal Λ mass is calculated and the pair with the smallest difference is handed to the analysis, while the others are removed from the sample. An option has been implemented to change the decision to be based on the discriminant instead of the invariant mass. In this regard, only the pair with the highest discriminant is used in the analysis. This option will be used in the systematic studies described in Sec. 6.

It is also possible, that one pion is combined with two protons, while one of the protons is combined with another pion too. In this case, if, for example, a decision is made on the pion to pick the combination with the double counted proton, this will then influence the availability of this particular proton in other Λ candidates. Hence, an ordering is needed which of the tracks is considered first. The multiple counting mostly affects the pion candidate and hence it is considered first. This can be changed by an option such that the order is switched to check for a possible influence on the observables. After the first iteration and selection of the best pair, only the remaining pairs are checked for multiple counting of the second daughter and the selection procedure is applied again. In the right panel of Fig. 3.24 the occurrence of each track in the

final sample is counted after the procedure has been applied. The multiple counting disappears such that each particle track is only used once.

3.9.7 Reconstruction of the Λ sample

After application of all the cuts described above, the remaining sample still consists of both signal and background combinations. Their different contributions can be distinguished by looking to the invariant mass distribution. The distribution shows a clear peak around the nominal mass of the Λ hyperon at $M_\Lambda = 1115.683 \pm 0.006$ MeV [Zyl20] lying on top of a second shape which can be attributed to the background (see Fig. 3.25). To determine the amount of Λ hyperons in the sample, the background shape has to be estimated. This has been done by two different methods which are compared afterwards.

First, the mixed-event method is used. This pure combinatorial background can be generated with very high statistics. For this purpose, only the days of the beam time with fully operational detector systems are used to generate the background. Then the background shape must be scaled down to the side-bands of the same-event distribution to match the overall amount of background in experimental data. Although the mixed-event background sample is very large and therefore the statistical uncertainties and bin-to-bin fluctuations are supposed to be small, the mixed-event background has been fit to ensure a smooth distribution. The best function to describe the shape properly without including too many fit parameters has been the Landau function. The Landau function is defined as

$$L(x) = \frac{L_0}{2\pi i} \int_{c-i\infty}^{c+i\infty} e^{s \cdot \ln(s) + x \cdot s} ds, \quad (3.33)$$

where $s = (x - L_1)/L_2$ includes two additional parameters that are fit. L_0 determines the heights of the distribution and c is an arbitrary positive real number, such that the integral is performed only along the imaginary axis (or any positive parallel axis). After fitting the Landau function to the mixed-event background this function is subtracted from the same-event distribution. The result can be seen in Fig. 3.25 illustrated by the black points which show a continuous decrease beneath the peak. The signal peak is wider due to its intrinsic mass resolution related to the limited lifetime of the Λ hyperon and a second contribution originating from the multiple scattering of the daughter particles. Hence a single Gaussian distribution is not enough to describe the signal shape well, a second Gaussian function has to be introduced. However, this second Gaussian function is also centered at the same mean value which reduces the number of fit parameters by one. Finally, the signal peak is fit with the double Gaussian function:

$$G_{SG}(x) = \frac{A_1}{\sqrt{2\pi}\sigma_1} \exp\left(-\frac{(x-\mu)^2}{2\sigma_1^2}\right) + \frac{A_2}{\sqrt{2\pi}\sigma_2} \exp\left(-\frac{(x-\mu)^2}{2\sigma_2^2}\right), \quad (3.34)$$

with μ being the mean position, A_1, A_2 the peak areas and σ_1, σ_2 the corresponding widths of the Gaussian distributions. The number of Λ hyperons can then be calculated by summing up the two peak areas $N_\Lambda = A_1 + A_2$ or by integrating the function $G_{SG}(x)$ in a reasonable range. To calculate quantities like signal-to-background ratio or significance the range has to be restricted to not integrate the whole background far away from the nominal Λ mass. Typically, a 2σ -range is used for these calculations. The integration range is determined by the combined width of the distribution, defined by the single widths weighted with the corresponding peak fraction:

$$\sigma = \frac{A_1}{A_1 + A_2} \sigma_1 + \frac{A_2}{A_1 + A_2} \sigma_2. \quad (3.35)$$

The second method is to take only the same-event mass distribution and fit directly the combined function of Landau (Eq. 3.33) and a double Gaussian function (Eq. 3.34) as

$$F_{All}(x) = L(x) + G_{SG}(x). \quad (3.36)$$

This function has eight free parameters which have to be adjusted. By this fit the signal and background is fit simultaneously. For an adequate background fit, the range has to be extended to regions away from the peak. Initial parameters for the fit function have to be set to make the procedure stable. Therefore, as a first step the background is fit only at the side-bands. Afterwards it is subtracted and the remaining signal peak is fit with the defined double Gaussian function. The resulting parameters are used as starting values for the global fit.

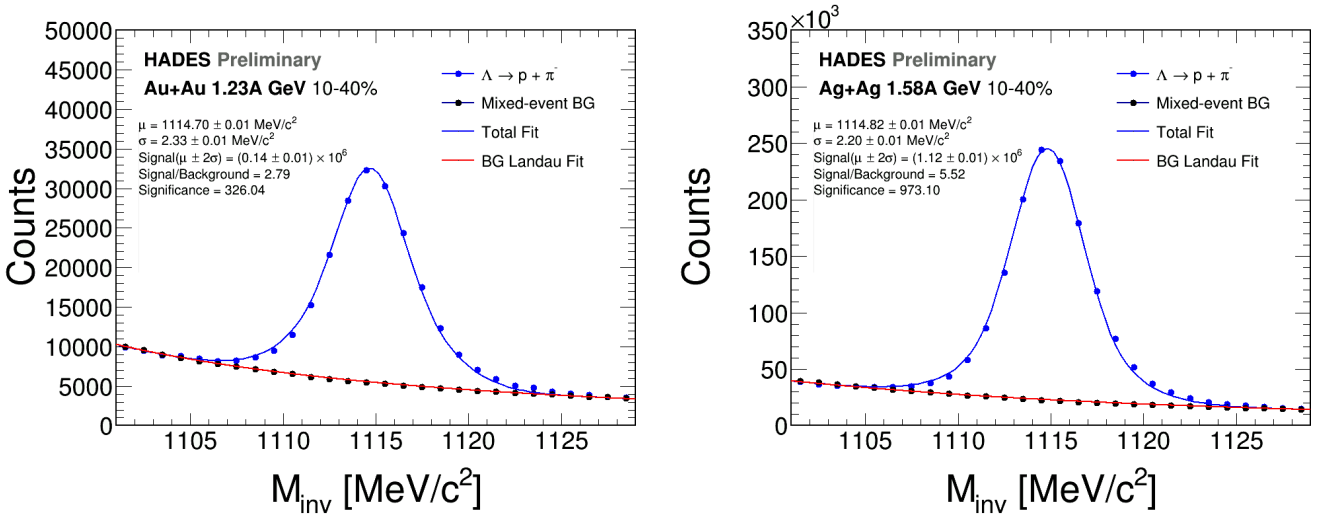


Figure 3.25: Final distribution of the invariant mass after the full selection chain. The result is shown for 10 – 40 % centrality which is the most common centrality range used for the polarization analysis. The sample for Ag+Ag at 1.58A GeV (right panel) has roughly 10 times more entries as have been recorded for the Au+Au beam time (left panel).

Centrality	Au+Au@1.23 AGeV			Ag+Ag@1.23 AGeV			Ag+Ag@1.58 AGeV		
	$N_\Lambda/10^4$	SIG	S/B	$N_\Lambda/10^4$	SIG	S/B	$N_\Lambda/10^5$	SIG	S/B
0 – 10 %	8.48 ± 0.05	228	1.57	2.96 ± 0.02	149	3.08	7.83 ± 0.01	794	4.11
10 – 20 %	6.52 ± 0.04	213	2.31	2.33 ± 0.02	135	3.44	5.16 ± 0.01	657	5.12
20 – 30 %	5.18 ± 0.03	197	2.99	1.54 ± 0.02	109	3.29	3.61 ± 0.01	555	5.87
30 – 40 %	2.95 ± 0.03	150	3.27	0.94 ± 0.01	82	2.56	2.42 ± 0.01	455	5.91
0 – 40 %	23.1 ± 0.07	398	2.16	7.69 ± 0.04	242	3.25	19.0 ± 0.1	1255	4.86

Table 3.7: Summary of the statistics of the Λ signal as calculated from the invariant mass distribution. The numbers are also given in 10% centrality bins. As can be seen, the sample gets cleaner for more peripheral bins, however the amount of Λ hyperons produced decreases as the significance.

Fig. 3.25 shows the final results for Au+Au and Ag+Ag at 1.58 AGeV in the 10 – 40 % centrality bin which is most commonly used in this analysis. A similar figure for the Ag+Ag at 1.23 AGeV beam time can be found in Ap. 9.6. Signal and background are determined by integrating the peak or the background fit in a 2σ range around the mean value. Here the uncertainty is assumed to be purely of statistical nature, hence it is \sqrt{N} where $N = S + B$ is the number of counts. For example the uncertainty for the signal can then be calculated using Gaussian error propagation which results in

$$\Delta S = \sqrt{N + B} = \sqrt{S + 2B}, \quad (3.37)$$

where the assumption of \sqrt{N} holds also in case of the pure background sample. Having determined signal and background, statistical quantities like the significance and the signal-to-background ratio can be calculated as has also been done for Fig. 3.23.

These parameters and the amount of Λ hyperons for all three beam times and different centrality ranges are summarized in Tab. 3.7. Note that the sample of Ag+Ag at 1.58 AGeV has a factor of ten more statistics than the other two. Taking the 10% centrality classes, one observes most of the Λ s to be produced in central collisions, where the highest amount of energy for particle production is available in the fireball as the number of participants is larger [Ada19b]. Unfortunately, this particular bin is not so much of interest for the polarization (and also for flow analysis), since the polarization in central events is expected to be zero (see Sec. 1.4). In addition, as the reaction plane is determined from the spectators which are pretty rare in most central collisions, this centrality class has to be treated very carefully and has the lowest event plane resolution. This means that almost 1/3 of the overall statistics are not used in this analysis.

In general, the significance decreases towards peripheral events while the purity or signal-to-background ratio increases since the amount of combinatorial background is much smaller in peripheral collisions.

The Ag+Ag at 1.58 AGeV sample has a high amount of statistics and will allow for a precise measurement of a possible polarization as discussed in the following chapters. In case of the other two samples, it might be needed to lower the cut on the discriminant to allow more statistics, despite higher background is introduced at the same time. All this details and the methods used for this analysis will be explained in Sec. 4.

4 Signal extraction and implementation of flow and polarization methods

As discussed in the previous chapter, the Λ hyperon candidates are reconstructed by combining their identified daughters, i.e. the negatively charged pion and the proton. However, this is not sufficient as there are a lot of random combinations even after all cuts have been applied. The aim of this analysis is to extract observables for the Λ signal only and consequently methods have to be used to subtract the remaining background contribution.

For this purpose, the invariant mass distribution is used to determine the amount of signal and background. Since it is never possible to judge on an event-by-event basis whether a combination corresponds to an actual Λ hyperon or to the background, signal and background contributions to the final observables cannot be distinguished directly. Nevertheless, there are methods to separate the final observables from the background contribution and thus reconstruct the signal value. The first method will be called $\Delta\phi$ -extraction method¹ [Pos98] and is described in Sec. 4.2. The second method which will be used for reporting the final measurement results is the *invariant mass fit method* [Ada13, Bor04] described in Sec. 4.3.

4.1 Determination of the Λ decay kinematics

Before the methods can be applied, all the necessary quantities must be determined. In case of the flow analysis, the momentum of each Λ hyperon can be calculated from the reconstructed daughters by $\vec{p}_\Lambda = \vec{p}_p + \vec{p}_{\pi^-}$. Since the momentum also determines the direction of the Λ hyperon, one can directly calculate the azimuthal angle ϕ_Λ in the laboratory frame of HADES. Subtracting the event plane angle in the corresponding event, results in the flow angle $\Delta\phi_\Lambda = \phi_\Lambda - \Psi_{EP}$ which is converted to the interval $[0, 2\pi]$.

For the polarization analysis the situation is more complicated. To measure a possible polarization of the Λ hyperons, the momentum of the proton in the rest frame of the Λ hyperon as in Eq. 1.25 is needed. Since the speed of the Λ hyperon, β_Λ , is close to the speed of light c , the Lorentz transformation from the laboratory to the Λ 's rest frame has to be performed.

For the Lorentz transformation the velocity of the Λ hyperon is used as input. Since only the quantities along the direction of the transformation undergo the Lorentz-contraction, the velocity vector must be used. One can calculate the velocity from the momentum \vec{p}_Λ and energy E_Λ of the Λ hyperon which are both determined from the daughter particles. Then the velocity is given by:

$$\vec{\beta}_\Lambda = \frac{\vec{p}_\Lambda}{E_\Lambda}. \quad (4.1)$$

Then the transformation to the rest frame of the Λ hyperon can be performed. The particle of interest is the proton whose energy E_p and momentum \vec{p}_p have to be transformed in the manner mentioned previously. The new values of these quantities in the rest frame of the Λ hyperon will be marked with an superscript ** . The full transformation can be written as:

¹ In literature this method is often referred to as *event plane method* but since the event plane is used in both methods the name is changed for better differentiation.

$$\vec{p}_p^* = \vec{p}_p + \frac{\gamma_\Lambda - 1}{\beta_\Lambda^2} (\vec{\beta}_\Lambda \cdot \vec{p}_p) \vec{\beta}_\Lambda - \gamma_\Lambda E_p \vec{\beta}_\Lambda \quad (4.2)$$

$$E_p^* = \gamma_\Lambda (E_p - \vec{\beta}_\Lambda \cdot \vec{p}_p), \quad (4.3)$$

where γ_Λ is the typical γ -factor calculated from the velocity of the Λ hyperon. From Eq. 4.2, one can see that the change of the proton momentum, given by the last two terms, only happens in the direction of $\vec{\beta}_\Lambda$. To validate the software implementation, this transformation is also applied to the Λ hyperon itself by replacing $(E_p, \vec{p}_p) \rightarrow (E_\Lambda, \vec{p}_\Lambda)$ in the equations given above. In its rest frame, the Λ hyperon is not moving and hence its momentum should be $\vec{p}_\Lambda = \vec{0}$ after transformation. As can be seen in Fig. 4.1 it proves to be true - the momentum distribution of simulated Λ hyperons is shown before and after the transformation where the the distribution is completely zero.

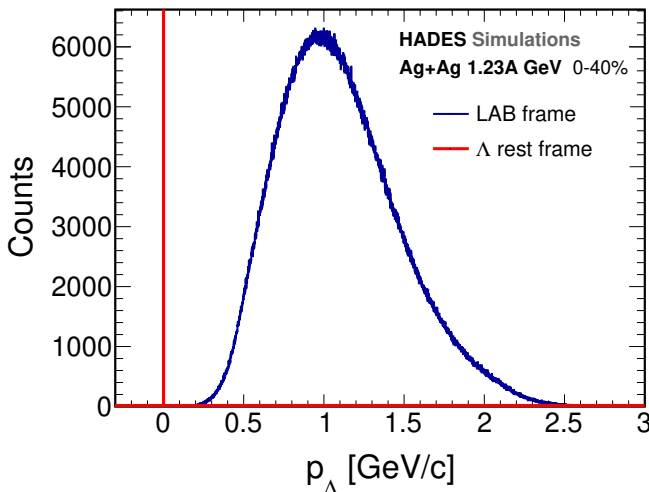


Figure 4.1: Momentum distribution of the Λ hyperons before (blue curve) and after (red curve) the transformation to its rest frame. Simulated Λ hyperons embedded to UrQMD in Au+Au collisions are shown. As a proof of principle, the Λ 's momentum is zero after the transformation.

Then the azimuthal angle ϕ_p^* can be calculated from the momentum direction in the same way as the azimuthal angle of the Λ hyperon above. Afterwards, this angle is subtracted from the event plane angle for each Λ candidate in each event, resulting in $\Delta\phi_p^* = \Psi_{EP} - \phi_p^*$ which is again converted to the interval $[0, 2\pi]$.

Finally, the methods can be applied to extract the observables of interest. The methods will be explained predominantly for the polarization analysis, but the application for the flow extraction is similar. Differences will be mentioned at the corresponding places in the text.

4.2 $\Delta\phi$ -extraction method

The $\Delta\phi$ -extraction method has been established over the years for the analysis of particle flow [Pos98]. Here the anisotropies in the azimuthal angular distribution are determined. For the

most apparent particles as protons and charged pions, the particle selection can reach purities up to 99% and thus the background contribution to the results is negligible. This allows to directly analyze the azimuthal angular distributions for these particles.

However, for other particle species, especially for unstable candidates that can only be reconstructed from their decay products, the background contribution is not negligible. As explained in Sec. 3.9.7, the amount of Λ hyperons in the sample can be determined from the invariant mass distribution. It can also be plotted in distinct bins of the polarization angle $\Delta\phi_p^*$ as shown in Fig. 4.4 for the Au+Au data. Twelve equally-spaced bins in $\Delta\phi_p^*$ have been chosen each covering a range of 30°.

To avoid systematic shifts of the invariant mass fit from bin-to-bin, the mean position and the width of the Λ peak are taken from the integrated fit and fixed for the individual fits. This means that only the areas of the two Gaussian functions are free fit parameters. The same applies to the background shape, where only the entirety in the Landau fit is taken as a free parameter. Concluding, the fit has only three parameters that have to be adjusted to the data which results in more stable results for the signal determination.

From the individual fits, the amount of signal can be determined as a function of the azimuthal angle $\Delta\phi_p^*$. The result is shown in Fig. 4.2 for two different options to determine the background, i.e. by a direct fit to the same-event data or by the mixed-event method. The distributions contain only true Λ hyperons and thus the background contribution is removed completely. In case of an isotropic emission, this distribution is expected to be flat, meaning that in each direction the amount of emitted particles is the same. However, in general the distribution is not flat due to various effects which have to be corrected for.

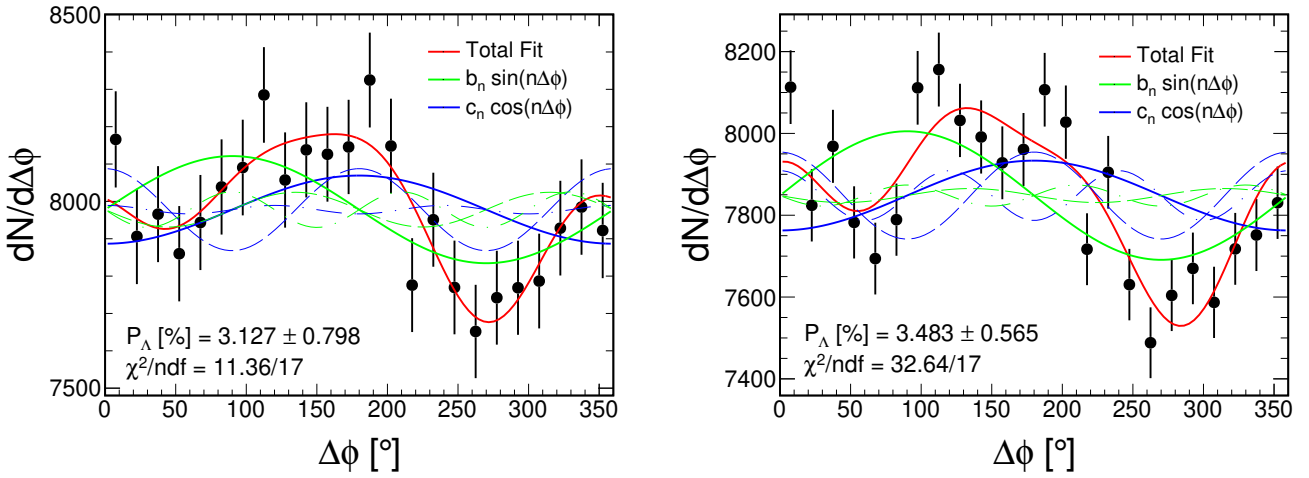


Figure 4.2: Results for the Λ polarization of the $\Delta\phi$ -extraction method in Au+Au in comparison for the two methods to define the amount of signal: the invariant mass fits to the same-event data (left) and the background determination via the mixed-event method (right). The red curves show the overall fit of the Fourier expansion up to the third order. The green curves display the odd and the blue curves the even components. The solid curves represent the first, the dashed line the second and the dashed-dotted curves the third order components.

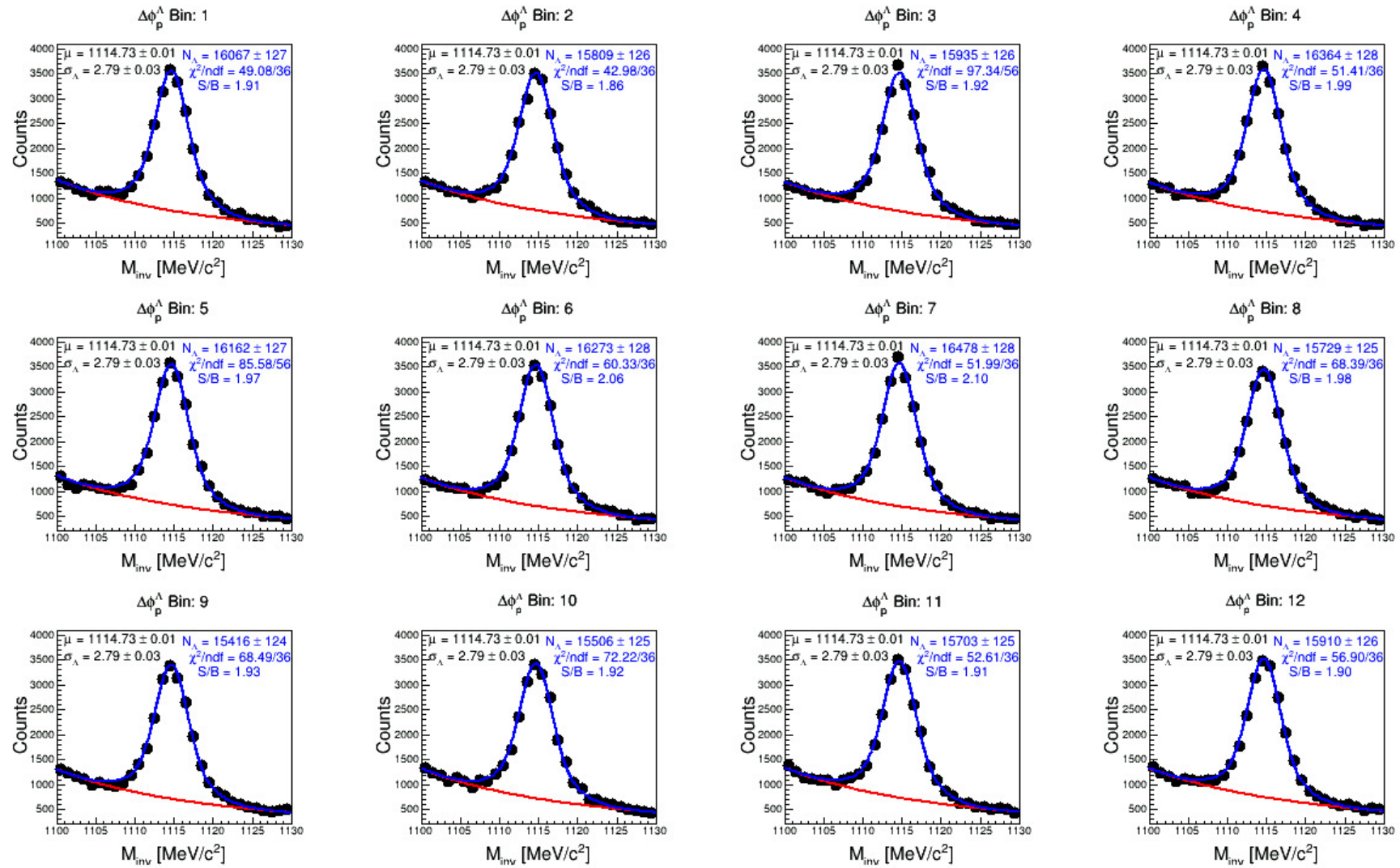


Figure 4.3: Invariant mass fit to the same-event distribution for 12 bins in $\Delta\phi_p^*$ in Au+Au collisions at $\sqrt{s_{NN}} = 2.4$ GeV. The shape is fit with a double Gaussian function to describe the signal yield and a Landau function for the background. All parameters, besides the two areas of the Gaussian functions and the heights of the Landau function, have been fixed to get stable results and lower bin-to-bin fluctuations from the fit.

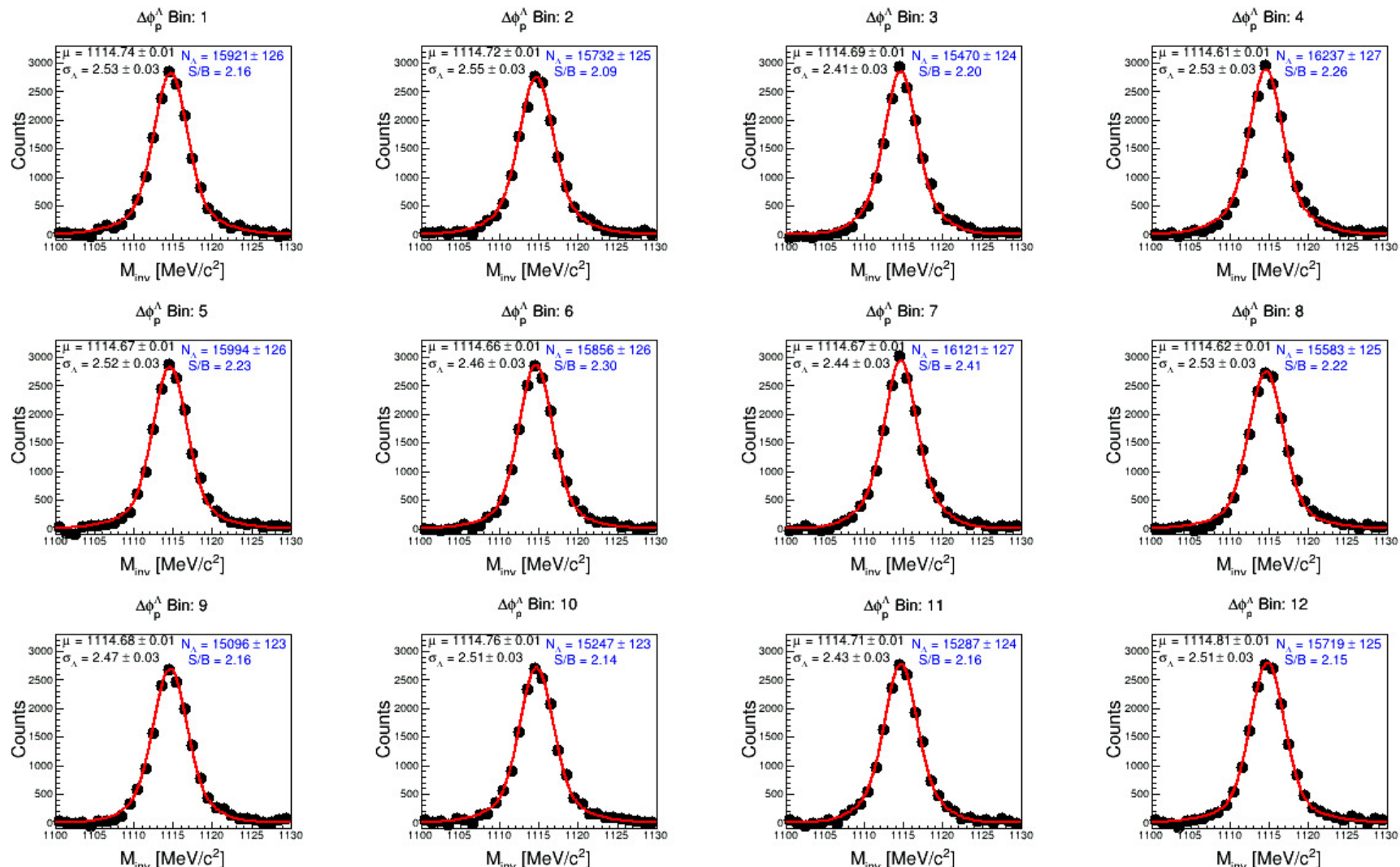


Figure 4.4: Fit to the invariant mass distribution after subtraction of the background using the mixed-event method for 12 bins in $\Delta\phi_p^*$ in Au+Au collisions at $\sqrt{s_{NN}} = 2.4 \text{ GeV}$. The shape is fit with a double Gaussian function to describe the signal yield.

To measure the possible anisotropies, the distribution is fit with a Fourier series as

$$\frac{dN}{d\Delta\phi_p^*} = \frac{N_0}{2\pi} \left[1 + 2b_1 \sin(\Delta\phi_p^*) + 2c_1 \cos(\Delta\phi_p^*) + 2b_2 \sin(2\Delta\phi_p^*) + 2c_2 \cos(2\Delta\phi_p^*) + \dots \right], \quad (4.4)$$

where $b_n = \langle \sin(n\Delta\phi_p^*) \rangle$ are the odd and $c_n = \langle \cos(n\Delta\phi_p^*) \rangle$ are the even terms of the distribution. A global polarization of the Λ hyperons will contribute to the first odd component b_1 . The strength of this component can be seen by the green solid curve in Fig. 4.2. A possible polarization of the Λ hyperons with respect to the total angular momentum can then be calculated according to

$$P_\Lambda = \frac{8}{\pi\alpha_\Lambda R_{EP}} \frac{b_1}{R_{EP}}, \quad (4.5)$$

while its statistical uncertainty is given by

$$\Delta P_\Lambda = \left| \frac{8}{\pi\alpha_\Lambda R_{EP}} \Delta b_1 \right| \quad (4.6)$$

and thus being solely defined from the fit by Δb_1 . The results must be corrected for the event plane resolution (see Sec. 3.6). The uncertainty in the determination of the event plane resolution is taken into account as a systematic uncertainty which also applies for the uncertainty related to the decay parameter α_Λ (see Ch. 6).

For the flow analysis, the procedure is exactly the same, one just has to exchange the polarization angle $\Delta\phi_p^*$ by the flow angle $\Delta\phi_\Lambda = \phi_\Lambda - \Psi_{EP}$. Furthermore, the different components of the Fourier analysis given by

$$\frac{dN}{d\Delta\phi_\Lambda} = \frac{N_0}{2\pi} \left[1 + 2a_1 \sin(\Delta\phi_\Lambda) + 2v_1 \cos(\Delta\phi_\Lambda) + 2a_2 \sin(2\Delta\phi_\Lambda) + 2v_2 \cos(2\Delta\phi_\Lambda) + \dots \right]. \quad (4.7)$$

are named differently. Here $a_n = \langle \sin(n\Delta\phi_\Lambda) \rangle$ are the odd components which should all be zero within errors and thus they are usually dropped from the fit such that only the even terms $v_n = \langle \sin(n\Delta\phi_\Lambda) \rangle$ are used. For the flow analysis the even components are of interest and hence the final observables will be calculated as

$$v_n = \frac{v_n^{obs}}{R_{EP}} \quad (4.8)$$

to again account for the finite resolution of the event plane reconstruction. These components have also geometrical meaning and are named v_1 being the directed, v_2 the elliptic, and v_3 the triangular flow. Applying this procedure allows to reconstruct the flow and polarization signal for the Λ hyperons. A clear advantage of this method is that the amount of signal and background can be determined from the invariant mass distribution in a clean way which allows to subtract the background directly.

Nonetheless, there can be bin-to-bin fluctuations from the invariant mass fit, influencing the final result. This can be controlled by fixing most of the fit parameters as explained above but

also by determining the signal in a distinct range, i.e. 2σ around the mean value. Since both these parameters are fixed, the range is exactly the same in all $\Delta\phi$ -bins. The advantage of not integrating the whole function is to reduce the effect of small variations in the background shape, which would accumulate over a large range in the invariant mass. Still there are remaining variations from bin to bin which can be seen, e.g. in the third and seventh bin of Fig. 4.4 where the fit does not hit the highest point of the invariant mass. Such small deviations might lead to fluctuations from bin to bin not related to any physical phenomena. To understand how the fluctuations influence the extracted parameters, two methods for the background fit in the invariant mass distribution are used: the same-event fit to the side-bands and the mixed-event technique. Within the statistical limitations of the overall signal, the number of bins is also varied. This gives a good handle on the statistical fluctuations on the final results. More details will be discussed in Ch. 6.

To exactly determine the Fourier components, the fit functions 4.4 and 4.7 have to be applied up to an infinite order which is not possible in reality due to the finite amount of bins. Introducing higher order components to the fit will have less and less influence on the first and second components, however, this is only true for a reasonable amount of bins. Otherwise, the higher order components will start to fit the bin-to-bin fluctuations, which can also be the case if the signal to be extracted is small. This should be avoided since it is not any physical effect but just an issue of finite amount of bins. For the measurement of the first and second order components, it is enough to fit up to the third order $n = 3$. All these different components are plotted in Fig. 4.2. Another issue of this method is the application of the event plane resolution correction R_{EP} . The most accurate application requires another decomposition of signal and background in narrow centrality bins which is difficult for the polarization analysis as it requires excessive statistics. The correct result for the component b_1 is received when the value is first corrected for R_{EP} and then averaged as:

$$b_1^{\text{true}} = \left\langle \frac{b_1^{\text{obs}}}{R_{EP}} \right\rangle. \quad (4.9)$$

Yet this is difficult to implement for the $\Delta\phi$ -extraction method since it would require infinitely narrow centrality bins. Hence the event plane resolution correction is applied in the end as an average weight in 10% centrality bins, taking into account the corresponding particle multiplicities of each bin. It follows that this average has to be recalculated for instance when a specific region of the phase-space is analyzed. Finally, the resulting b_1^{final} is calculated as:

$$b_1^{\text{final}} = \langle b_1^{\text{obs}} \rangle \left\langle \frac{1}{R_{EP}} \right\rangle \neq \left\langle \frac{b_1^{\text{obs}}}{R_{EP}} \right\rangle = b_1^{\text{true}}. \quad (4.10)$$

This leads to a systematically higher value of the reconstructed b_1^{final} than the true value b_1^{true} . A detailed discussion to apply the event plane resolution correction and the derivation of Eq. 4.10 can be found in [Mas16].

Similar issues appear for each possible correction that should be applied to the data. This can only be done within a finite bin setting and hence the weighting numbers have to be averaged in a suitable way. This introduces a systematic bias which might distort the extracted signal. Based on the mentioned reasons, this method will only be used for comparison to the results obtained

from the invariant mass fit method (see Sec. 4.3). The differences will enter the systematic uncertainties described in Ch. 6.

4.3 Invariant mass fit method

The method which is used to report the final measurement results is the *invariant mass fit method* [Ada13, Bor04]. In contrast to the $\Delta\phi$ -extraction method, there will be no distinction between signal and background at first. The components of interest are calculated directly as a function of the invariant mass as $\langle \sin(\Delta\phi_p^*) \rangle_{\text{TOT}}(M_{\text{inv}})$ for the polarization measurement and $\langle \cos(\Delta\phi_\Lambda) \rangle_{\text{TOT}}(M_{\text{inv}})$ for the flow measurement. The brackets $\langle \cdot \rangle$ denote the average of all particles in all events and the index "TOT" denotes that no distinction between signal and background is made and both enter the calculation. Both signal and background entering to the total value but their contribution varies with the invariant mass. The weight of the signal and background contribution can be determined from the invariant mass distribution itself by calculating the signal and background fraction in each bin of the invariant mass. Then the total distribution can be written as follows (similar for the flow coefficients):

$$\langle \sin(\Delta\phi_p^*) \rangle_{\text{TOT}}(M_{\text{inv}}) = f(M_{\text{inv}}) \langle \sin(\Delta\phi_p^*) \rangle_{\text{Sig}} + (1 - f(M_{\text{inv}})) \langle \sin(\Delta\phi_p^*) \rangle_{\text{BG}}(M_{\text{inv}}), \quad (4.11)$$

where $f(M_{\text{inv}})$ is the signal fraction and hence $1 - f(M_{\text{inv}})$ the corresponding background fraction. Both are determined based on the fit to the invariant mass distribution. The signal contribution $\langle \sin(\Delta\phi_p^*) \rangle_{\text{Sig}}$ is assumed to be constant and therefore not changing as a function of the invariant mass. The shape of the background contribution $\langle \sin(\Delta\phi_p^*) \rangle_{\text{BG}}$ is not known and has to be adjusted to the measured results. For this analysis, a reasonable assumption is a linear shape of the background as a function of the invariant mass and thus the background is set to:

$$\langle \sin(\Delta\phi_p^*) \rangle_{\text{BG}}(M_{\text{inv}}) = \alpha + \beta M_{\text{inv}}, \quad (4.12)$$

while α and β are fit parameters. If the slope is consistent with zero, the fit function is modified by setting $\beta = 0$ to reduce the number of fit parameters and thereby decreasing the statistical uncertainty of the result. This would correspond to the assumption of a constant background correlation as a function of the invariant mass. Finally, the difference between the two assumptions for the background shape is considered as a systematic uncertainty in Ch. 6.

Inserting the linear background assumption into Eq. 4.11, the distribution $\langle \sin(\Delta\phi_p^*) \rangle_{\text{TOT}}(M_{\text{inv}})$ can be fit with two or three free parameters, one or two of the parameters for the background fit together with the actual signal contribution which is of interest. It is necessary to perform the fit in a wider range of the invariant mass such that the background contribution can be fixed from the side-bands where the signal fraction is negligible $f(M_{\text{inv}}) \approx 0$. Hence, in order to precisely fit the background, it might be needed to change the cut setting such that the sample analyzed is larger, even if this reduces the overall purity.

The calculation of the actual polarization can directly be calculated from the fit using:

$$P_\Lambda = \frac{8}{\pi\alpha_\Lambda} \langle \sin(\Delta\phi_p^*) \rangle_{\text{Sig}}, \quad (4.13)$$

while the statistical uncertainty is calculated by:

$$\Delta P_\Lambda = \left| \frac{8}{\pi \alpha_\Lambda} \Delta(\langle \sin(\Delta\phi_p^*) \rangle_{\text{Sig}}) \right| \quad (4.14)$$

while again it is solely defined from the fit. In comparison to Eq. 4.5, the event plane resolution does not appear. It is already taken into account when $\langle \sin(\Delta\phi_p^*) \rangle_{\text{TOT}} (M_{\text{inv}})$ is calculated where every entry is weighted by the inverse of the corresponding event plane resolution via:

$$\langle \sin(\Delta\phi_p^*) \rangle_{\text{TOT}}^{\text{true}} = \left\langle \frac{\langle \sin(\Delta\phi_p^*) \rangle_{\text{TOT}}^{\text{obs}}}{R_{EP}} \right\rangle. \quad (4.15)$$

As it is the most appropriate way to apply the correction (compare to Eq. 4.9 and 4.10), the only limitation arises from the finite centrality bins which are used to determine R_{EP} . As a good compromise, the 5% centrality bins are used to determine the event plane resolution. The values are summarized in Tab. 3.2. A clear advantage of this method is that the decomposition in $\Delta\phi$ must not be applied. Consequently, this method is suitable especially if the statistics is a limiting factor of the analysis.

The results of the method are shown in Fig. 4.5 for the Au+Au system at $\sqrt{s_{NN}} = 2.4 \text{ GeV}$ and in Fig. 4.6 for the Ag+Ag system at $\sqrt{s_{NN}} = 2.55 \text{ GeV}$. In the panels on the left hand side, the distribution of $\langle \sin(\Delta\phi_p^*) \rangle_{\text{TOT}}$ defined in Eq. 4.11 is plotted as a function of the invariant mass. They are fit with the function described above which takes the signal and background fractions into account that are displayed in the panels on the right hand side. Clearly, the signal fraction peaks at the nominal mass of the Λ hyperon while being close to zero at around 10 – 15 MeV away from the peak. The distributions outside the peak region are needed to fix the background shape. As can be seen from the panels on the left hand side of Fig. 4.5 and 4.6, a linear shape for the background is necessary as the background is not zero and for the Ag+Ag sample a non-zero slope β is observed.

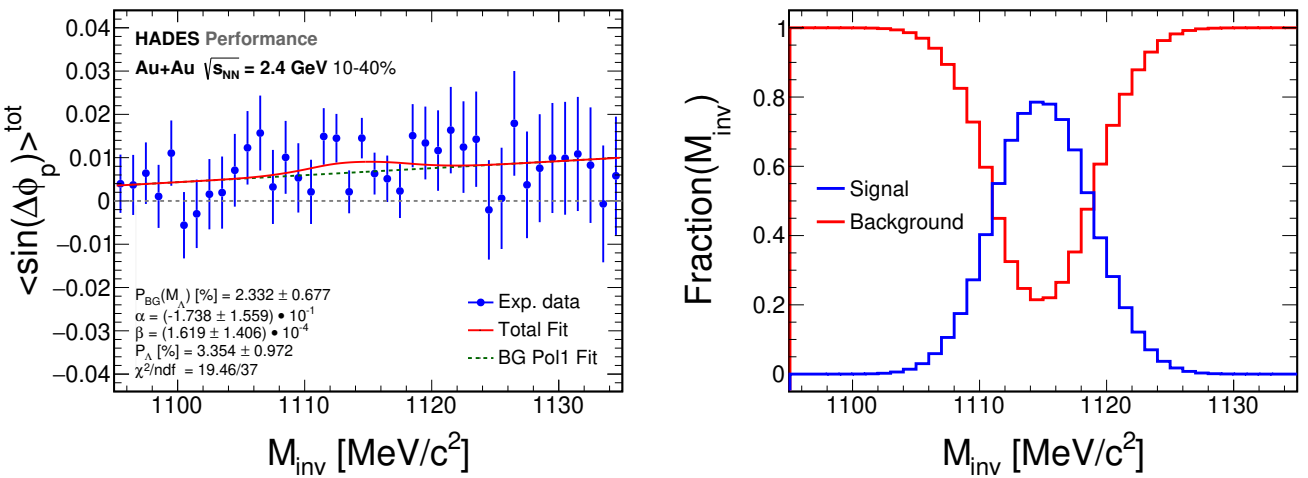


Figure 4.5: Polarization measurement performed with the invariant mass fit method for Au+Au collisions at $\sqrt{s_{NN}} = 2.4 \text{ GeV}$. Left: The total distribution is fit with a linear background shape (dashed line) and a constant signal. Right: The signal and background fractions as a function of the invariant mass.

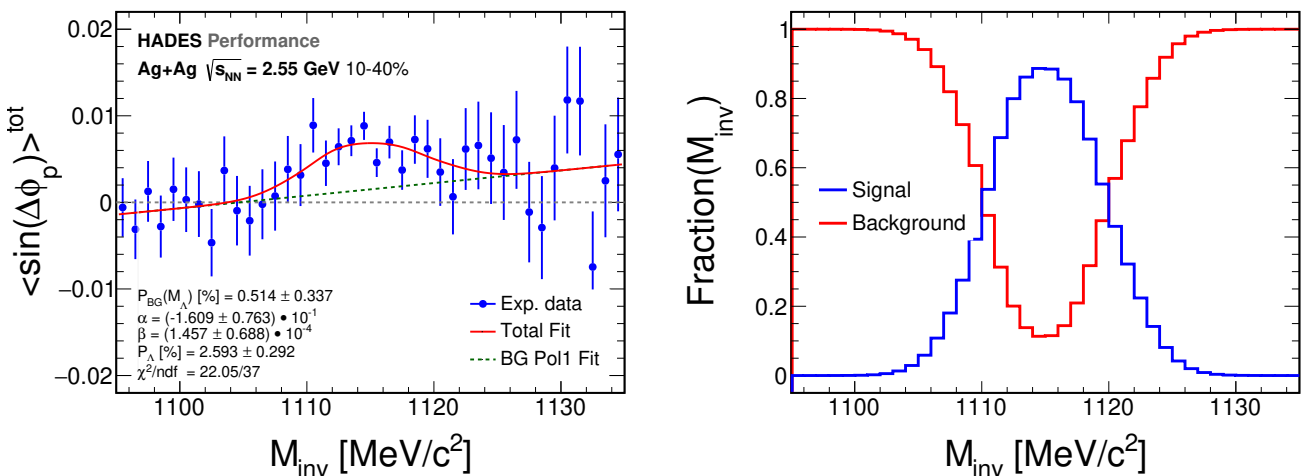


Figure 4.6: Polarization measurement performed with the invariant mass fit method for Ag+Ag collisions at $\sqrt{s_{NN}} = 2.55$ GeV. Left: The total distribution is fit with a linear background shape (dashed line) and a constant signal. Right: The signal and background fractions as a function of the invariant mass.

The polarization measurement for the Λ hyperons with its statistical uncertainty is extracted according to Eq. 4.13 and 4.14. To compare the fit background correlation to the extracted signal, the polarization analysis is also performed for the background at the Λ peak position from the invariant mass distribution $M_\Lambda \pm \Delta M_\Lambda$ as:

$$P_{\text{BG}} = \frac{8}{\pi\alpha_\Lambda} (\alpha + \beta M_\Lambda). \quad (4.16)$$

The statistical uncertainty is then calculated by taking into account all the uncertainties from the parameters and hence results in:

$$\Delta P_{\text{BG}} = \frac{8}{\pi\alpha_\Lambda} \sqrt{(M_\Lambda \Delta \beta)^2 + (\Delta \alpha)^2 + (\beta \Delta M_\Lambda)^2 + 2M_\Lambda \text{cov}(\alpha, \beta)}. \quad (4.17)$$

The term $2M_\Lambda \text{cov}(\alpha, \beta)$ of this calculation is very important, as the two parameters of the linear background fit are strongly correlated and cannot be varied separately. Therefore, the two terms for their single variations ($(M_\Lambda \Delta \beta)^2$ and $(\Delta \alpha)^2$ above) have to be corrected for the covariance $\text{cov}(\alpha, \beta)$ which results in a negative value and thus reduces the contribution to the overall uncertainty of the correlation measurement for the background. In case the background is assumed to be constant, Eq. 4.17 is changed by inserting $\Delta \beta = \Delta M_\Lambda = \text{cov}(\alpha, \beta) = 0$. Overall, this method achieves conclusive results and will be used for the flow and polarization analysis. It allows to deal with limited amount of statistics and for a multi-differential measurement of the global polarization. Furthermore, corrections can be applied on an event-by-event basis by weighting the corresponding entry when filling the histogram of $\langle \sin(\Delta\phi_p^*) \rangle_{\text{TOT}}(M_{\text{inv}})$ or $\langle \cos(\Delta\phi_\Lambda) \rangle_{\text{TOT}}(M_{\text{inv}})$ respectively. Thus the systematic distortions by phase-space or multiplicity integrated corrections can be reduced significantly.

4.4 Signal and background determination

The results without any corrections (raw results) for the polarization measurement are shown in Fig. 4.5 and 4.6. The smaller uncertainties in the Ag+Ag sample reflect the larger event statistics available for the analysis. In both cases, a non-zero polarization of the Λ hyperons is extracted from the fit. Especially for the Au+Au data, this background correlation is prominent over the full invariant mass range. The strength is as strong as the signal itself, as can be seen in the calculated background polarization at the nominal Λ mass. For the Au+Au case, a clear signal peak structure is not visible, making it difficult to judge whether the extracted signal is really related to a polarization of the Λ hyperons or to a non-zero polarization of the background.

At this stage, it cannot be ruled out that a systematic effect may introduce a correlation to both signal and background in a similar way, resulting in a shift of the $\langle \sin(\Delta\phi_p^*) \rangle_{\text{TOT}}(M_{\text{inv}})$ to higher values. If this were the case, one would have to subtract this contribution before the fit is applied, in order to extract the true signal present in the distribution. Since the extraction of the pure background contribution $\langle \sin(\Delta\phi_p^*) \rangle_{\text{BG}}$ is not of particular interest, the subtraction can be performed directly by rewriting the fit function in Eq. 4.11 to:

$$\langle \sin(\Delta\phi_p^*) \rangle_{\text{TOT}}(M_{\text{inv}}) = f(M_{\text{inv}}) \langle \sin(\Delta\phi_p^*) \rangle_{\text{Sig}} + \langle \sin(\Delta\phi_p^*) \rangle_{\text{BGshift}}. \quad (4.18)$$

Here the background correlation $\langle \sin(\Delta\phi_p^*) \rangle_{\text{BGshift}}$ is set to be linear over the whole invariant mass range and incorporates a possible polarization of the combinatorial background. The variation of the signal extraction using a constant background correlation for the fit is included to the systematic uncertainties (see Ch. 6). As it is not scaled down with the decreasing background fraction in the region of the Λ invariant mass peak, this means that this background shift can be assumed to be also present for the true Λ hyperons. Following up this assumption,

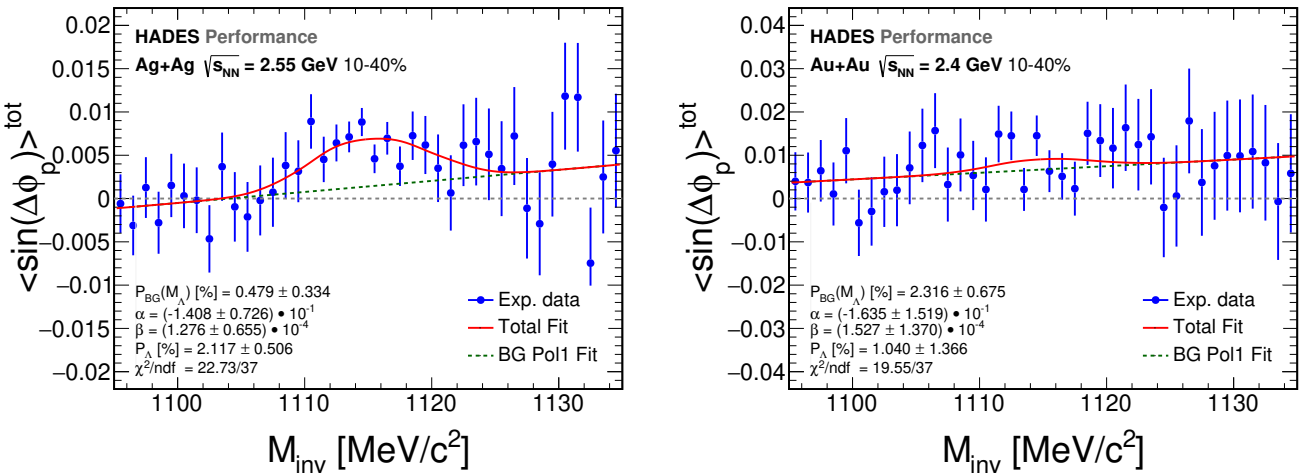


Figure 4.7: Polarization measurement performed with the invariant mass fit method assuming a linear shift of the whole distribution. The total distribution is fit with a linear background shape (dashed line) and a constant signal which scales with the signal fraction (see Eq. 4.18). The experimental data from Ag+Ag collisions (left panel) and Au+Au collisions (right panel).

the true polarization of the signal must be present on top of the shifted background and follow the shape of $f(M_{\text{inv}})$.

In Fig. 4.7 the experimental data is fit with the reworked function in Eq. 4.18. As can be seen in comparison to Fig. 4.5 and 4.6, the values of the extracted background contribution are consistent and do not change within errors (compare P_{BG} , α , β). However, this is not the case for the extracted signal value. For the Ag+Ag system, the polarization of the Λ hyperons is reduced by $\Delta P = -0.476\%$ but due to the clear peak structure a significant polarization signal still remains. This differs for the Au+Au system where the polarization is changed from above 3% to be consistent with zero.

This shows the importance of determining the origin of the background correlation. It is necessary to understand why a non-zero background correlation is present in the global polarization measurement. Even if the source of the background correlation is not fully understood, it is important to check if this is changing the extraction of the signal values and if so, to quantify the influence in order to reconstruct the true value for the polarization of the Λ hyperons.

4.5 Estimation of the background correlation using ϕ -rotation

One of the main concerns for the Au+Au run is the fact that the track reconstruction in sector 2 was not possible due to the inactive drift chamber for most of the beam time. Since the aim of this analysis is to extract observables that depend on the azimuthal distribution of the particles in general, the area which is excluded from the sample of $180^\circ \leq \phi \leq 240^\circ$ might have an impact on the final results which has to be examined.

The azimuthal angular distributions after the selection of all Λ candidates are shown for both daughter particles (p and π^-) in the Au+Au run in Fig. 4.8. The missing sector can be clearly identified since the particle multiplicity in that region is significantly reduced compared to the other sectors. Considering that for this analysis a proton and pion are paired to form a Λ candidate, the removal of a specific sector also bears on the neighboring sectors as can be seen in Fig. 4.8, especially for the proton distribution at around $\phi = 170^\circ$ and $\phi = 250^\circ$. The only sector which is not affected is sector 5 ($0^\circ \leq \phi \leq 60^\circ$) opposite to sector 2.

Besides this inactive sector, there are also small variations in the particle yields from sector to sector. These variations are visible in the azimuthal distributions for the Ag+Ag collisions at $\sqrt{s_{NN}} = 2.55 \text{ GeV}$ too, as shown in Fig. 4.9. However, they should be compensated when the azimuthal distributions are correlated to the event plane as its orientation is not correlated to the laboratory frame.

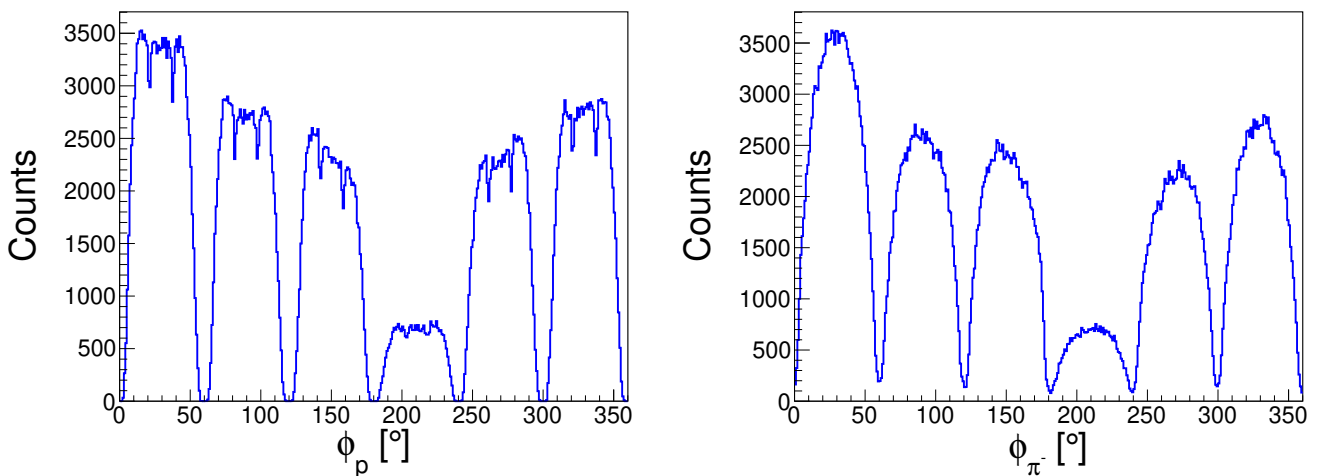


Figure 4.8: ϕ distribution for the Λ decay products in Au+Au collisions at $\sqrt{s_{NN}} = 2.4$ GeV: the protons are shown in the left panel, while the pions are plotted in the right panel. One can clearly identify the sector which was absent for most of the beam time by the reduced amount of particles.

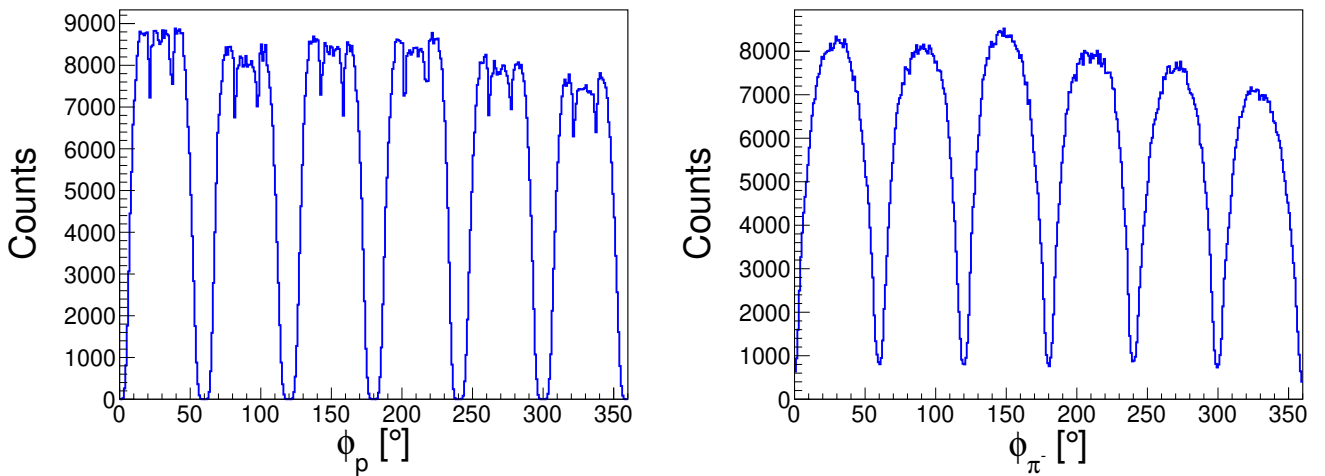


Figure 4.9: ϕ distribution for the Λ decay products in Ag+Ag collisions at $\sqrt{s_{NN}} = 2.55$ GeV: the protons are shown in the left panel, while the pions are plotted in the right panel.

After the proton has been boosted to the rest frame of the Λ hyperon according to Eq. 4.2, the azimuthal angular distributions are smeared out. However, as can be seen from Fig. 4.10, for both samples the structure of the different sectors is clearly visible. Hence it has to be investigated if this anisotropy in the ϕ angle does influence the final polarization measurement, which also manifests itself in an asymmetry in the azimuthal distribution of $\Delta\phi_p^*$. The shape in Fig. 4.10 is a result of the missing acceptance (MDC frames) between the sector but also due to different detector efficiencies and especially for the inactive sector in the Au+Au run. However, even in the Ag+Ag case these asymmetries are significant, although all six sectors were available.

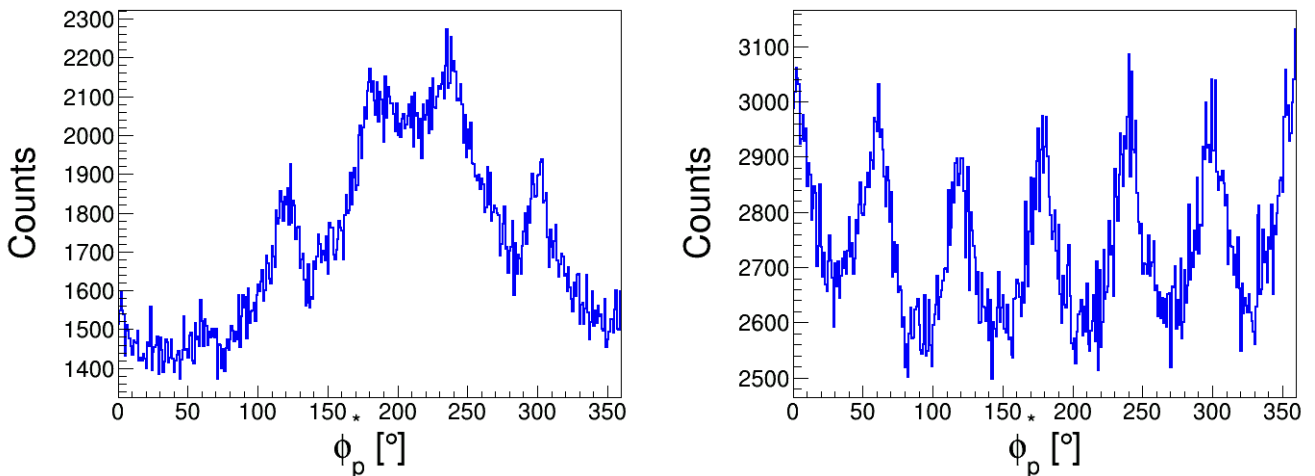


Figure 4.10: ϕ_p^* distributions of the protons in the rest frame of the Λ hyperon for Au+Au collisions at $\sqrt{s_{NN}} = 2.4$ GeV (left) and Ag+Ag collisions at $\sqrt{s_{NN}} = 2.55$ GeV (right). Even after the Lorentz boost has been performed there are still remaining structures present, especially the missing sector for most of the Au+Au beam time introduces a strong asymmetry in the distribution.

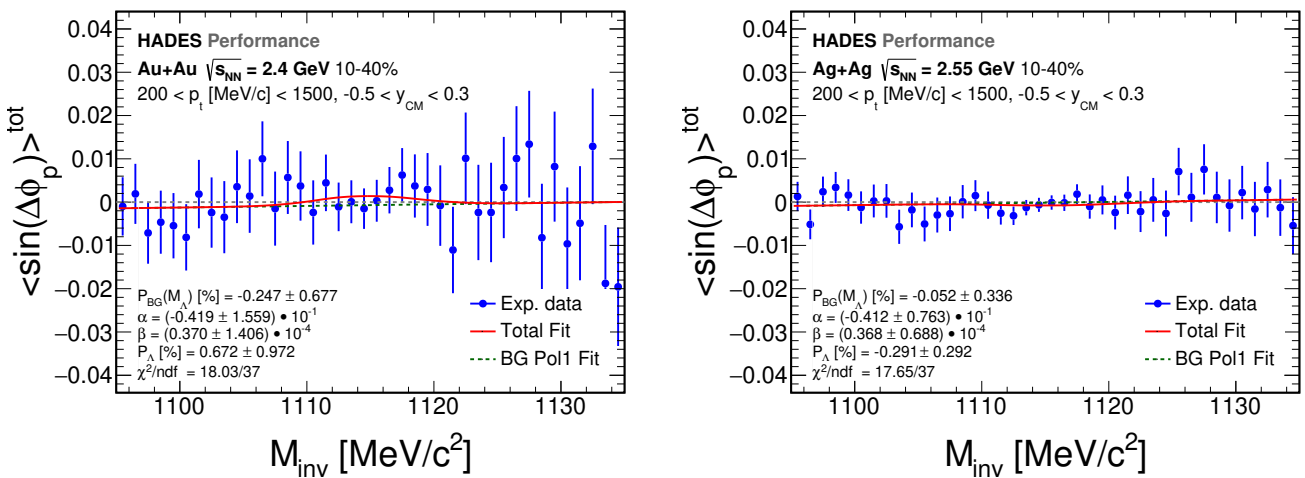


Figure 4.11: Polarization measurements after ϕ rotation according to the experimental distribution for Au+Au collisions at $\sqrt{s_{NN}} = 2.4$ GeV (left) and Ag+Ag collisions at $\sqrt{s_{NN}} = 2.55$ GeV (right). Both signal and background contributions fully disappear and the results are consistent with zero.

To reweight the distribution and force it to be flat is not an option, since a possible signal could already be reflected in the shape of the ϕ_p^* distribution. In general, this is expected to be a small effect due to the random orientation of the event plane with respect to the detector.

Another possibility to investigate the influence of the azimuthal shape is the *ϕ rotation method* which is commonly used for background determination. Here the ϕ angle of each particle is rotated randomly in order to destroy all physical correlations. If the ϕ_p^* angle is rotated

randomly, using Fig. 4.10 as a probability distribution for this transformation, the shape in ϕ_p^* will be kept while the physical correlations of the particles are destroyed. Thus we can study only the effect of the detector acceptance. The results are displayed in Fig. 4.11. All the data points are fluctuating around zero. The signal and background correlations disappear and are consistent with zero. Therefore the pure detector acceptance reflected by the shape of the ϕ_p^* distribution is not able to introduce a non-zero correlation in $\langle \sin(\Delta\phi_p^*) \rangle_{\text{TOT}}$. Otherwise, there would have been a clear non-zero correlation present in Fig. 4.11. However, this does not exclude a possible correlation of some physical effect which is coupled to the detector acceptance and finally influences the measurement. Hence this investigation can only be seen as a first step, to exclude a pure detector effect but more detailed investigations are needed in order to make the polarization measurement most precise. To disentangle such correlations is not trivial in the experimental data, therefore Monte-Carlo simulations will be used as described in Ch. 5.

4.6 Corrections for reconstruction efficiency

From all the Λ hyperons that are produced in the heavy-ion collisions, only a certain percentage will have both daughter particles reaching the active volume of the detector. This is defined as the geometrical acceptance and reduces the amount of Λ hyperons that can be detected. If one wants to get the number of Λ hyperons being produced in the collisions, this has to be taken into account via acceptance correction. The acceptance correction is realised based on simulations. Yet it is not clear how the acceptance influences the measurement of the polarization and thus further studies as described in Ch. 5 are necessary.

Not all particles that reach the detector (accepted) are reconstructed. This can be traced back to several reasons. For example the amount of charge deposited in one of the detector subsystems might not be enough to generate a hit such that a full track could not be reconstructed. Hence, particles are lost. This is particularly influencing the reconstruction of particles which decay to two or more particles. If one of the decay particles is not reconstructed, there is no possibility to reconstruct the original signal while the combinatorial background is increased. To take these effects into account the data is usually corrected to match the finite detector reconstruction efficiency. This includes all the selection criteria applied (event and particle selection, cuts on the decay topology etc.), since typically the amount of Λ hyperons in acceptance N_{InAcc} is compared to the amount of reconstructed Λ hyperons in the final sample N_{Reco} . Hence the acceptance a and the reconstruction efficiency ϵ can be defined as:

$$a = \frac{N_{\text{InAcc}}}{N_{4\pi}}; \quad \epsilon = \frac{N_{\text{Reco}}}{N_{\text{InAcc}}}. \quad (4.19)$$

The efficiency depends on the phase-space as well as on the centrality of the collision due to the larger amount of particles hitting the detector in central collisions. For the Λ hyperon, the efficiency lies between 5 – 15 % depending on the phase-space region. On the edges of the measured phase-space, defined by the acceptance, it even gets smaller. Hence the correction factors, i.e. $1/\epsilon$, can reach large values. This might be problematic if single bins are strongly overweighted and influence the overall distributions under observation.

The flow and polarization components are averaged as a function of the invariant mass to extract the signal. While the azimuthal anisotropic flow is of the order $\sim 10^{-1} – 10^{-2}$ for directed and elliptic flow, the polarization effect is one order of magnitude smaller, 10^{-3} . Especially for such small signals, single bins have statistical fluctuations and will fluctuate from zero. When

the average of many particles and events is performed, these fluctuations cancel to a certain precision which depends on the overall statistics. However, if such a strongly fluctuating bin is weighted with an efficiency correction factor of 20 or more, the deviation from zero is strongly amplified. Thus the average value is strongly distorted by these fluctuations and as a result the bin-to-bin variations are strong, which is only a systematic uncertainty introduced by the method.

To avoid such issues, one can make use of the fact that the flow and polarization components are averaged observables and not absolute numbers. Hence the absolute weighting is not of a primary importance, but the relative one. Consequently, one can scale the efficiency distribution to the average efficiency, such that the weighting factors scatter around one and on average no correction is applied. By this only the relative difference are corrected and large bin fluctuations are avoided. This is sufficient since an overall loss of Λ candidates equally distributed in space will only reduce the statistical significance but have no influence on the final value of the observable. However, if, due to physical effects, the polarization is not constant over the full phase-space, a phase-space dependent reconstruction efficiency will prefer a certain region more than others and thus the integrated value is systematically shifted. To properly take into account this effect, weighting with relative efficiency is necessary.

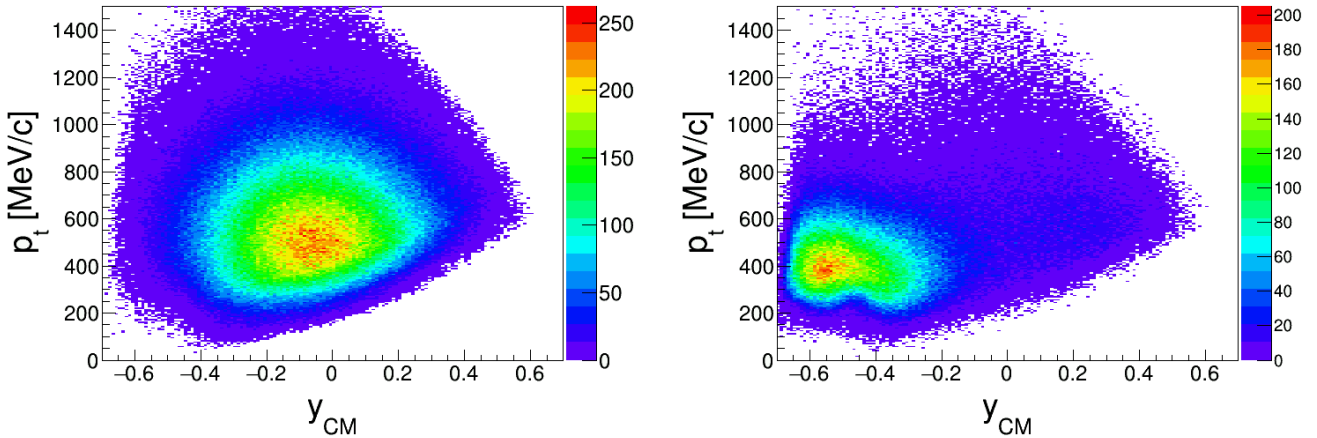


Figure 4.12: Phase-space distribution for signal (true Λ hyperons, left panel) and background (only primary p and π^- , right panel) shown for simulated Λ hyperons embedded to UrQMD Au+Au collisions. Different regions of the phase-space are populated from signal and background.

The efficiency correction will be applied as a function of the phase-space, i.e. $\epsilon = \epsilon(\theta, \phi)$. Fig. 4.12 shows the phase-space distribution for true Λ hyperons (left panel) and pure background, consisting only of primary protons and pions (right panel). Both distributions have been calculated from Λ hyperons simulated with the Pluto event generator and embedded to UrQMD Au+Au collisions. The results are shown after all selection criteria have been applied, however, the cut on the MVA is not used here. As can be seen, signal and background populate the same region in p_t and different region in y . The Λ hyperons are mainly detected at backward rapidity and moderate transverse momenta from $300 - 700$ MeV/c. The boundaries of the distribution are defined by the geometrical acceptance. The background is focussed at backward rapidities $y_{CM} < -0.3$ but also at the low to moderate p_t range of $200 - 600$ MeV/c. It has a distribution

which goes beneath the main phase-space region of the Λ hyperons. All in all this makes the signal-to-background ratio strongly dependent on the phase-space region. While at the backward rapidity the distribution is dominated by background, it is exactly opposite at forward rapidities where the signal dominates.

The efficiencies are calculated from Λ hyperons embedded to experimental data. To determine the amount of Λ hyperons inside the detector acceptance, for each of the daughter particles six fired wires in each of the four MDCs, together with a hit in META system, are required. If these conditions are fulfilled the Λ hyperon is considered to be in acceptance. Similarly, the Λ candidates are defined to be successfully reconstructed if they pass all selection criteria that are used in the experimental data. Then the amount of accepted Λ hyperons, $N_{\text{Acc}}(p_t, y)$, and the amount of reconstructed Λ hyperons, $N_{\text{Reco}}(p_t, y)$ are counted for each phase-space bin separately. The corresponding efficiencies are calculated according to Eq. 4.20 by dividing the two distributions. A minimum requirement of $N_{\text{Acc}} > 30$ has been used to remove bins at the edges of the distribution with large statistical fluctuations. Then the mean efficiency $\bar{\epsilon}$ is calculated by:

$$\bar{\epsilon} = \frac{\int dy \int dp_t \frac{dN_{\text{Reco}}}{dy dp_t} \epsilon(p_t, y)}{\int dy \int dp_t \frac{dN_{\text{Reco}}}{dy dp_t}}, \quad (4.20)$$

while the integration is performed over the particular phase-space region which is analyzed. In the next step, the efficiency map, i.e. $\epsilon(p_t, y)$, is divided by the mean efficiency to result in the final efficiencies $\epsilon'(p_t, y) = \epsilon(p_t, y)/\bar{\epsilon}$. Thereby, it is guaranteed that the average correction is $\epsilon = 1$ and that only the relative efficiency differences in the phase-space are corrected. A further requirement of $\epsilon'(p_t, y) > 0.3$ is used to remove areas of low efficiencies. Due to the finite binning, there can still be fluctuations, especially in the outer regions of the phase-space. They reflect by sharp transitions from one bin to the neighbouring one. These fluctuations propagates to the final results which introduces unnecessary systematics. This can be avoided if the efficiency matrix is smoothed, a procedure which adjusts the efficiencies by taking into account the neighboring bins. For this purpose the Savitzky-Golay filter [Sav64] is used. This is a polynomial regression and its degree depends on the amount of data points used for flattening. A clear advantage of this method is that local minima or maxima are not cut from the distribution and therefore the local structure is conserved partially. It turned out that the smoothest results can be achieved when the flattening is done in a box of 9×9 bins around the bin to which the flattening procedure is applied. For sure this has some limitations at the edges of the distribution.

The efficiency matrices which will be used to correct the data for detector reconstruction losses and the selection of the Λ candidates are shown in Fig. 4.13. The highest efficiency is achieved in the backward rapidity, high transverse momentum area where only few particles hit the detector. This can be seen by taking a look at the same phase-space region in the number distribution shown in Fig. 4.12. At the center-of-gravity of the Λ hyperons the efficiency is slightly above one and drops significantly towards the edges of the distribution which are defined from the requirement $\epsilon'(p_t, y) > 0.3$. This also cuts a lot in the region where the background is dominating.

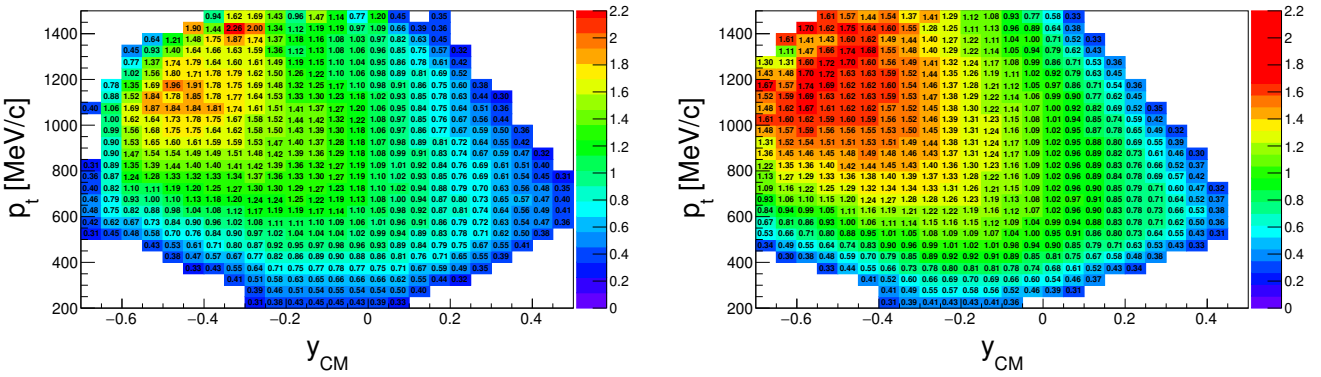


Figure 4.13: Phase-space dependent efficiency matrices for Au+Au (left panel) and Ag+Ag (right panel) collisions. The efficiencies have been calculated using simulated Λ hyperons embedded to experimental data. The efficiencies have been further rescaled to the mean efficiency and smoothed by making use of the Savitzky-Golay filter [Sav64]. A minimum requirement of $\epsilon > 0.3$ is applied to remove areas of very low efficiency.

Motivated by the distribution of the efficiencies, a minimum cut on the transverse momentum of $p_t > 200$ MeV/c is applied. The effect of this cut is negligible, however, regions of low efficiency and also little coverage in rapidity are removed. In principle, the aim is to cut out an area of the phase-space, which is symmetric to all directions and is not affected by the limit of acceptance. As can be seen in Fig. 4.13, the bin from $p_t = 200 - 400$ MeV/c is affected as the coverage of rapidity is very limited. Since the signal could be potentially depending on the phase-space region, this might introduce an effect from the acceptance which should be avoided. Nonetheless, a stronger cut on the transverse momentum like $p_t > 400$ MeV/c already heavily cuts into the main distribution of the Λ hyperons (compare to the left panel of Fig. 4.12) and is not suitable. Following the same train of argumentation, the rapidity range is restricted to $-0.7 < y_{CM} < 0.3$. The remaining phase-space bin is well in the acceptance of the HADES detector and therefore all regions can be corrected for the finite reconstruction efficiency.

For the integrated result of the polarization measurement, the phase-space bin is further restricted in rapidity to $-0.5 < y_{CM} < 0.3$. This has been motivated from the fact that the rapidity range of $-0.7 < y_{CM} < -0.5$ is dominated by background while the amount of reconstructed Λ hyperons is small. This combinatorial background shows fluctuations under the variations of the selection criteria beyond the fluctuations of the signal and consequently enhances the systematic uncertainty of the polarization measurement (see Ch. 6). Thus the removal of this rapidity range reduces the systematic uncertainties without influencing much the statistical significance of the polarization measurement.

The updated efficiency matrices according to Eq. 4.20 for both data sets are shown in Fig. 4.14. The efficiency maps are smooth over the whole phase-space and the acceptance effects are reduced as much as possible without removing too much of the statistics. In Fig. 4.15 the results from the invariant mass fit method are also updated to serve as a reference to the following investigations. The main effect of the phase-space cut is related to the backward rapidity, especially $-0.7 < y_{CM} < -0.5$ which is removed.

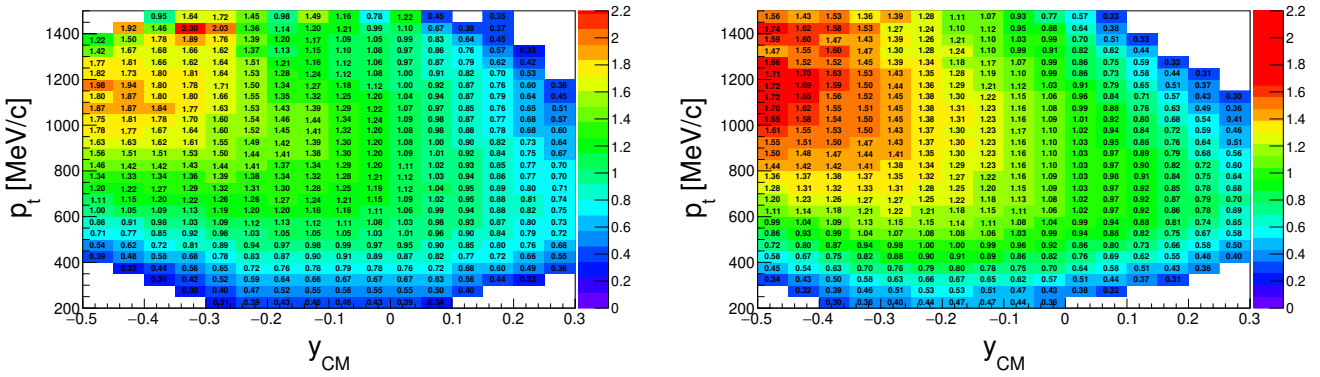


Figure 4.14: Efficiency matrix in rapidity and transverse momentum for the integrated polarization results in $\text{Au}+\text{Au}$ collisions at $\sqrt{s_{\text{NN}}} = 2.4$ GeV (left) and $\text{Ag}+\text{Ag}$ collisions at $\sqrt{s_{\text{NN}}} = 2.55$ GeV (right).

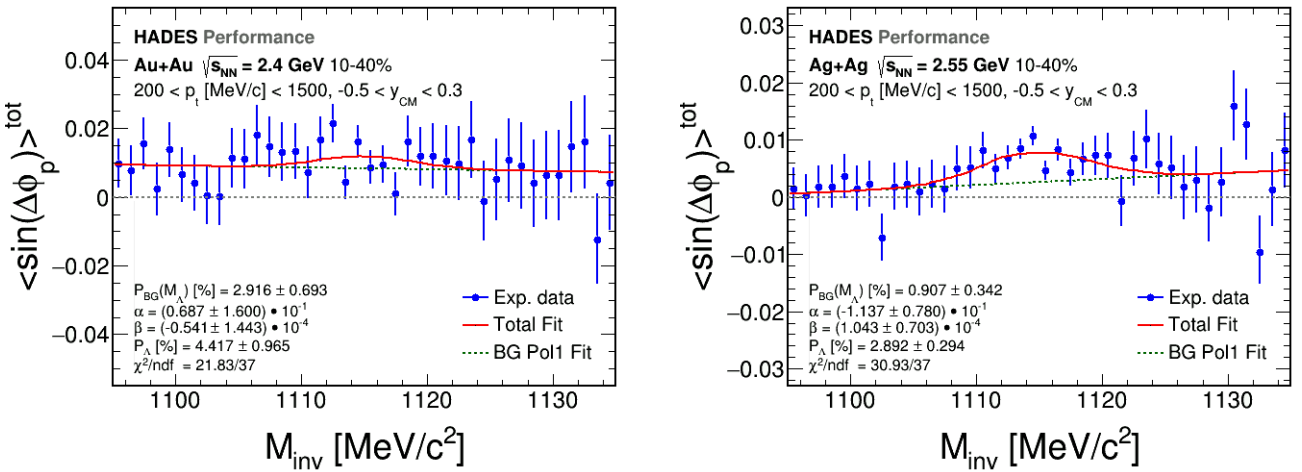


Figure 4.15: Polarization extraction using the invariant mass fit method after phase-space cut and efficiency correction in $\text{Au}+\text{Au}$ and $\text{Ag}+\text{Ag}$ collisions.

4.7 Correction for the radial distance asymmetry

The calculation of the topology parameters (see Sec. 3.9.4 and 9.4) involves the track parametrization as used by the track reconstruction algorithm. The proper description of the track involves a direction \vec{d}_{track} , which can be given by an azimuthal and polar angle and a base \vec{b}_{track} , which is given in cylindrical coordinates. The former is normalized to one. For the latter this requires a position along the beam axis z , the azimuthal angle ϕ and a radial distance R . This radial distance is the minimum distance of the reconstructed track to the beam axis. It can be determined from Eq. 9.16 resulting in:

$$R = |\vec{d}_{\text{track}} \times (\vec{b}_{\text{track}} - \vec{x}_{\text{ref}})|, \quad (4.21)$$

where \vec{x}_{ref} is a reference point to which the distance of the straight line is measured. The minimum distance to the beam axis will be in the perpendicular (x, y) -plane, thus the reference point will have only its z -components being non-zero, while the other two components are zero by definition. Eq. 4.21 can then be written as:

$$R = \left| \begin{pmatrix} d_x \\ d_y \\ d_z \end{pmatrix} \times \left[\begin{pmatrix} x_{\text{track}} \\ y_{\text{track}} \\ z_{\text{track}} \end{pmatrix} - \begin{pmatrix} 0 \\ 0 \\ z_{\text{ref}} \end{pmatrix} \right] \right| = \left| \begin{pmatrix} d_y(z_{\text{track}} - z_{\text{ref}}) - y_{\text{track}} d_z \\ x_{\text{track}} d_z - d_x(z_{\text{track}} - z_{\text{ref}}) \\ y_{\text{track}} d_x - x_{\text{track}} d_y \end{pmatrix} \right|. \quad (4.22)$$

Since the minimum distance is calculated to a line, it will be in the plane perpendicular to the beam axis and only the z -component will be used. This results in a short expression, which can be used to calculate the minimum distance for any given point on the particle track:

$$R = y_{\text{track}} d_x - x_{\text{track}} d_y. \quad (4.23)$$

As can be seen the absolute value is not taken, which means that R carries a sign. It is an inherent property for each reconstructed track and therefore also used in the calculations of all the decay topology parameters.

The radial distance can also be calculated to any other straight line parallel to the beam axis, specified by two components x_{shift} and y_{shift} . Inserting this in Eq. 4.21 and considering again only the z -component, which gives the distance in the xy -plane, one gets:

$$R'(x_{\text{shift}}, y_{\text{shift}}) = y_{\text{track}} d_x - x_{\text{track}} d_y + x_{\text{shift}} d_y - y_{\text{shift}} d_x. \quad (4.24)$$

Taking into account that the components of the direction can be written in terms of the azimuthal angle, i.e. $d_x = \cos(\phi)$ and $d_y = \sin(\phi)$, R' is given by:

$$R'(x_{\text{shift}}, y_{\text{shift}}) = R + x_{\text{shift}} \sin(\phi) - y_{\text{shift}} \cos(\phi). \quad (4.25)$$

A suitable reference is the event vertex position. For each of the reconstructed proton and pion tracks, the radial distance to the current event vertex line is calculated by inserting the coordinates X_{Vertex} and Y_{Vertex} in Eq. 4.25. If the incoming beam is aligned with the z -axis, the distribution of $R'(X_{\text{Vertex}}, Y_{\text{Vertex}}) = R'_V$ should be symmetric around zero. This distribution is shown for the proton candidates in Fig. 4.16 for experimental and simulated data in comparison, once with the default cut setting and once without the DCA cut on the daughter tracks, i.e. $d_2 > 0$ and $d_3 > 0$. Since these cuts remove tracks which pass a spherical volume around the event vertex with radius d_2 or d_3 , this will also reflect in the distribution of R'_V which can be seen in the right panel by the sharp drop of the distribution at $d_2 = \pm 5$ mm. However, there are still some entries within the d_2 cut range. These tracks pass the topology cuts as they are far away from the event vertex, but at the same time close to the event vertex line to generate entries with $R'_V < \pm 5$ mm.

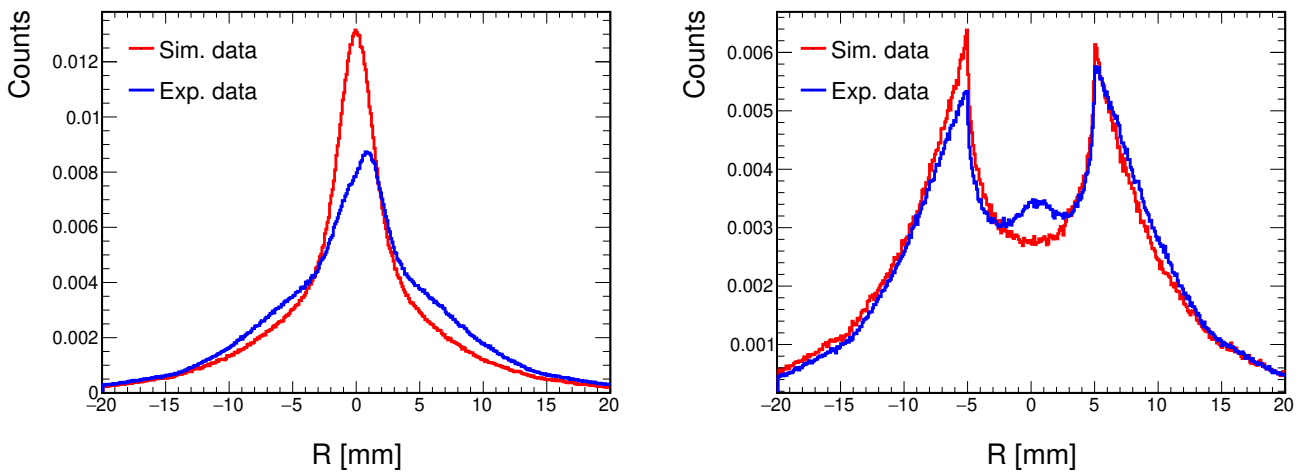


Figure 4.16: Distribution of the radial distance for protons to the event vertex line in comparison for experimental Au+Au collisions and UrQMD simulations with embedded Λ hyperons. The distributions are compared without discriminant cut and an additional invariant mass cut of $1110 \leq M_{\text{inv}}[\text{MeV}/c^2] \leq 1120$ to match the signal region. In comparison to the complete topology cut setting (right), the d_2 and d_3 cut have been removed (left panel) since they are strongly correlated to R'_V .

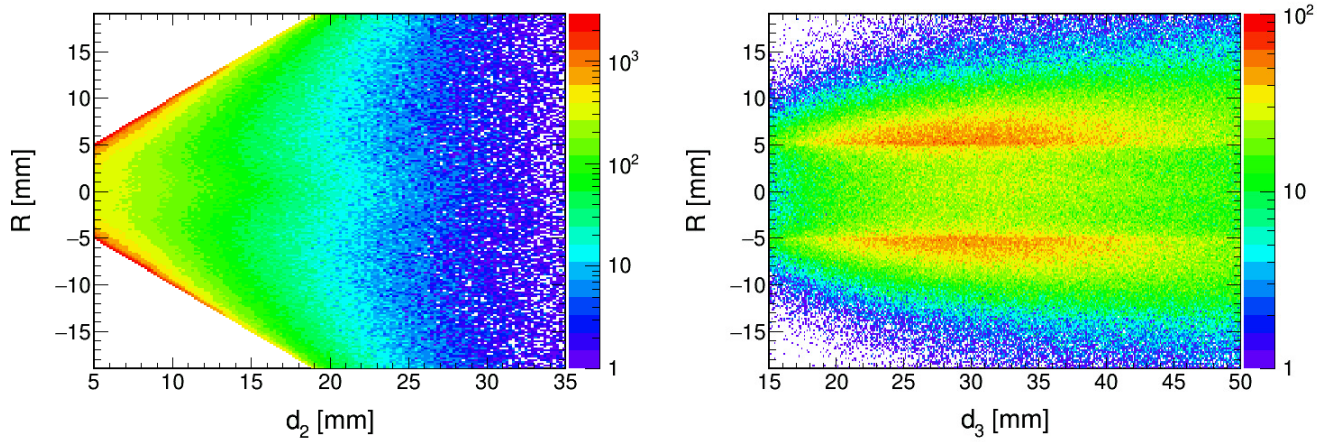


Figure 4.17: Distribution of R'_V as a function of the topology parameter d_2 (left) and d_3 (right) for $1110 \leq M_{\text{inv}}[\text{MeV}/c^2] \leq 1120$ to match the signal region. The current value of d_2 restricts the maximum value for R'_V . The minimum requirement of $d_2 > 5 \text{ mm}$ reflects in the sharp edge for $R'_V = \pm 5 \text{ mm}$ constantly as a function of d_3 .

Besides statistical fluctuations, the simulated data confirms the expectations of the symmetry with respect to the event vertex line for both cut settings. In the left panel of Fig. 4.16 the experimental data shows a double peak structure, while the main peak is shifted slightly to positive values of R'_V . Below the double peak there seems to be another broad structure which generates the middle peak after applying the symmetric d_2 cut displayed in the right panel. The shifted peaks lead to an asymmetry such that the positive side is weighted more than the nega-

tive part of R'_V , which is not reproduced in the simulations.

Fig. 4.17 shows the distribution of R'_V as a function of the topology parameters d_2 and d_3 . Since R'_V is calculated for the proton track, this reflects in the clear correlation to d_2 , which restricts the maximum value possible for R'_V . This means that the observed asymmetry in R'_V might depend on the cut value of d_2 which has to be taken into account for the systematic uncertainties (see Sec. 6.2). The cut setting of $d_2 > 5$ mm generated a loss in the region of $-5 \leq R[\text{mm}] \leq 5$ which reflects in the d_3 distribution by the sharp edge as plotted in the right panel. In principle, the correlation to other parameters is expected to be negligible, which means that the shape of R'_V should be constant for any value of the parameter. This is indeed confirmed as shown in Fig. 9.7 in the appendix. For the d_3 distribution shown here the situation is similar. However, due to the correlation of the proton and pion track, as they are combined to a possible Λ candidate, the asymmetry might also vary to some extend as a function of d_3 .

To check for a potential influence on the polarization observables, the data can be analyzed for the different values of R'_V . The sample is divided into 3 regions with $R'_V < -3$ mm, $R'_V > 3$ mm and the range inbetween. The results of the invariant mass fit method for the former two are shown in Fig. 4.18 for experimental and simulated Au+Au collisions and experimental Ag+Ag collisions. A very strong correlation to both signal and background is observed in the experimental data. The background correlation shows a very strong and opposite shape for positive and negative values of R'_V . Yet for the signal, there is a very clear peak in all cases, opposite in sign for the different regions of R'_V . The extracted values are very large, of the order of $P_\Lambda \sim 10\%$ which is one order of magnitude larger than the integrated result.

The dependence itself could be corrected for, although it would be good to get a better understanding of the exact origin, but the asymmetry with respect to R'_V can have an influence on the polarization measurement when the full distribution is integrated. Due to this asymmetry, one side of the R'_V distribution is weighted more than the other and thus the resulting correlations in $\langle \sin(\Delta\phi_p^*) \rangle_{\text{TOT}}$ might be artificial due to this finding. The effect, primarily on the signal extraction, needs to be quantified and a proper way to correct the experimental data has to be developed.

Accordingly, the middle region of $-3 \text{ mm} \leq R'_V \leq 3 \text{ mm}$ has been studied. The observable $\langle \sin(\Delta\phi_p^*) \rangle_{\text{TOT}}$ shows a flat distribution in terms of the background correlation (see Fig. 9.4 and 9.5) and a significant positive result for the signal. However, the overall statistics is very poor and also the signal-to-background ratio is very small which can be seen in the invariant mass distributions.

The UrQMD simulations with embedded Λ hyperons also show the similar trend of the background correlation as a function of the invariant mass. The slope is lower in comparison to the experimental data. Concerning the signal, there is a slight offset from zero, but clearly in the invariant mass region where the Λ hyperons are dominating, the observable tends to zero away from the general trend of the background. This is also expected since in UrQMD there is no polarization of the Λ hyperons and indeed the integrated result confirms the zero measurement (see Fig. 9.6). Nevertheless, the pattern of the signal with respect to the background correlation is exactly opposite to the experimental data. This suggests that the effect in the latter is coupled to some true polarization signal and not an artificial generation of a signal value. A more detailed simulation study using polarized Λ hyperons and multi-differential flow indeed confirm this statement as discussed in detail in Sec. 5.

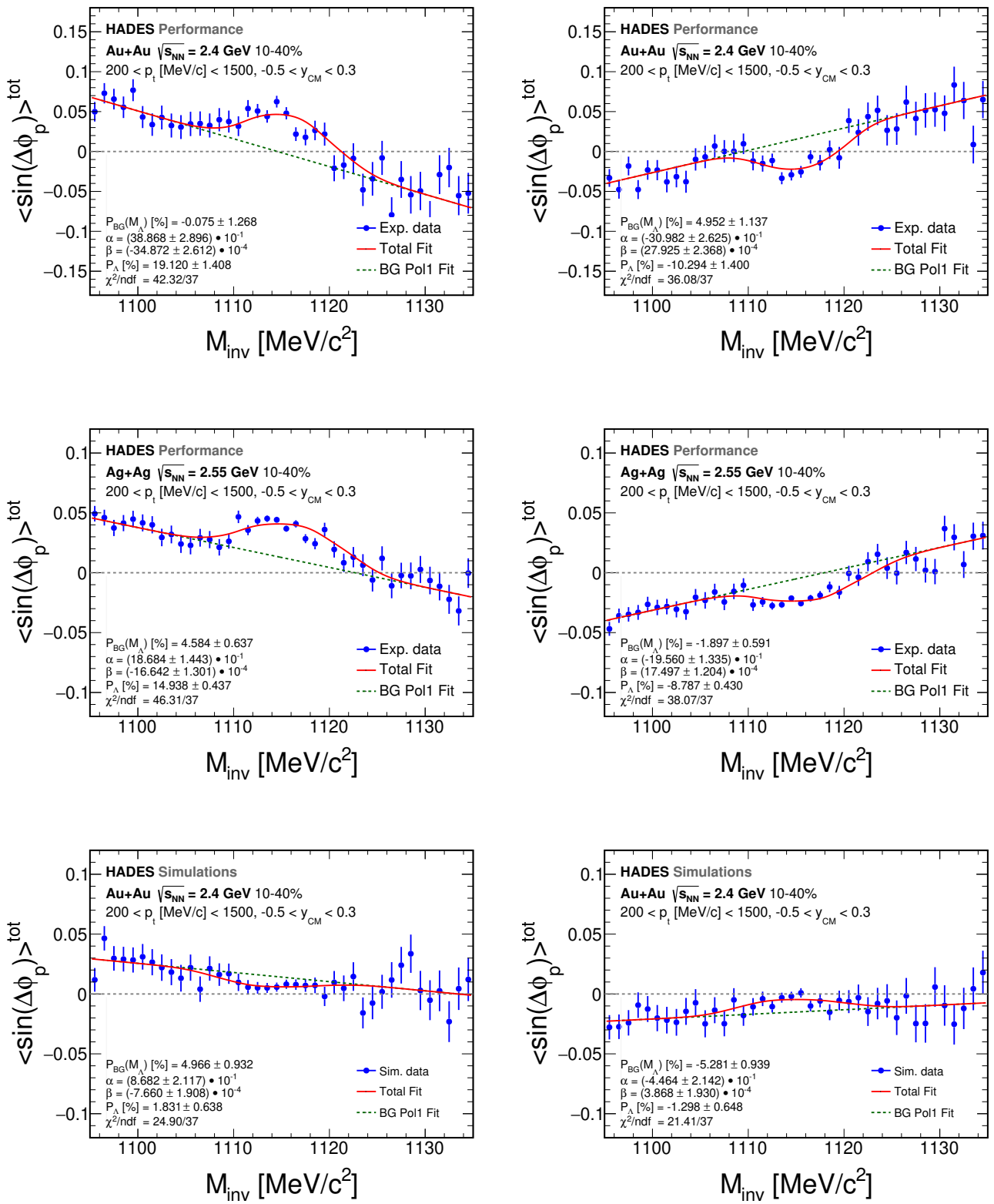


Figure 4.18: Polarization measurement extracted using the invariant mass fit method and depending on the radial distance from the event vertex line of $R'_V < -3 \text{ mm}$ (left column) and $R'_V > 3 \text{ mm}$ (right column). Different data sets are analyzed: experimental Au+Au collisions (upper row), experimental Ag+Ag collisions (middle row) and simulated Au+Au collisions using the UrQMD model with embedded Λ hyperons (lower row).

The study of this effect in the simulation can be used to get a qualitative understanding, but to extract realistic correction factors for the experimental data is difficult. This is because there are several parameters involved that determine the effect, i.e. the behavior and strength of the multi-differential flow of the particles and the phase-space dependence of the polarization which has not been measured at HADES energies so far. Consequently, the only way to correct for the radial distance asymmetry (RDA) is to derive an experimental data driven approach. This approach will be discussed using as an example the Ag+Ag at $\sqrt{s_{NN}} = 2.55$ GeV data sample, since it provides the largest statistics and besides larger fluctuations, no qualitative difference has been found in comparison to the Au+Au data, to which the same checks have been done. One way to correct for the asymmetry would be to use the R'_V distribution in the narrow invariant mass range of $1110 \leq M_{\text{inv}}[\text{MeV}/c^2] \leq 1120$ and calculate weights such that the distribution is flat after correction. As for the efficiency correction, it is important to make sure that the weighting procedure only accounts for relative differences and therefore the weights $w(R'_V)$ should fulfill the following relation:

$$\int_{-a}^{+a} N(R'_V) w(R'_V) dR'_V = \int_{-a}^{+a} N(R'_V) dR'_V, \quad (4.26)$$

while a is the symmetric range to which the procedure is applied. To calculate the weights that fulfill Eq. 4.26, the distribution of R'_V needs to be scaled down within the defined range such that its center-of-gravity is at unity. Thus the scaling factor reads:

$$s_{\text{Down}} = \frac{\int_{-a}^{+a} N(R'_V) dR'_V}{N_{\text{Bins}}|_{-a}^{+a}}. \quad (4.27)$$

Then the weights can be defined as:

$$w(R'_V) = \frac{s_{\text{Down}}}{N(R'_V)}. \quad (4.28)$$

It can be easily tested that these weights indeed fulfill Eq. 4.26. It is necessary to define a finite range a for the calculation, due to the large tails of the distribution of R'_V (see Fig. 4.16). It turns out that reasonable weights scattering around unity can be achieved for a range of roughly $a \leq 15$ mm. There should be also a lower boundary to not cut strongly into the distribution. It has been estimated to be $a \geq 7$ mm.

According to this procedure, the weights can be calculated within a fixed range and then the invariant mass fit method can be applied. The results of the extracted signal for different ranges are discussed in detail in Sec. 6.2 where the stability of this procedure is demonstrated.

In principle, the asymmetry only reflects in the shoulder of the peak, which is enhanced for positive values of R'_V due to an overall shift of the distribution. Therefore, the approach to correct the RDA is to divide the distribution in three bins, for example of $R'_V < -3$ mm, $-3 \text{ mm} \leq R'_V \leq 3$ mm and $R'_V > 3$ mm as used for the polarization dependency study in Fig. 4.18. Since the middle part has a flat shape of the background correlation, it will not be weighted and the weight is fixed to: $w_{-3 \leq R'_V \leq 3} \equiv 1$. Then the other parts can be weighted such that afterwards their integral is identical. This results in the following equation:

$$w_x = \frac{N_{R'_V < -3}^{\text{Sig}} + N_{R'_V > 3}^{\text{Sig}}}{2N_x^{\text{Sig}}} \quad (4.29)$$

while x can be either $R'_V < -3$ or $R'_V > 3$. The amount of signal N^{Sig} can be determined from the invariant mass distribution also for smaller subsamples as in the differential analysis.

The effect of this correction is shown in Fig. 4.19. The weights that are applied to the data are $w_{R'_V < -3} = 1.028$ and $w_{R'_V > 3} = 0.973$. Thus the asymmetry is about $\sim 3\%$. Looking to the extracted polarization, the correction returns a value consistent with the previous attempts and the overall effects enhances the signal again by $\Delta P_{\Lambda} \sim 0.4\%$. This observation also does not change when the boundaries to define the three bins are changed, such that $a = 4$ or 5 mm. This is an important result, since the weights grasp at a fixed value of R'_V and might in principle produce a boundary effect. Yet this effect is not significant and can be neglected.

In summary, the overall effect of the correction is stable against changes of the procedure how the corrections are applied. The same study has been repeated for the Au+Au data and the same conclusions can be drawn. The results for the three bin weighting is displayed in Fig. 4.20. The weights in the Au+Au run have been determined to: $w_{R'_V < -3} = 1.015364$ and $w_{R'_V > 3} = 0.985094$. The correction is lower as in the Ag+Ag run and accounts to $< 2\%$. The effect on the polarization measurement is again an enhancement of the extracted signal, and consistently to the smaller weights, the shift is about $\Delta P_{\Lambda} \sim 0.2\%$ (compare to Fig. 4.15).

Due to the stability with respect of the correction procedure and the fact that the three bin weighting sustains the complete data set since no further cut is introduced, it will be used as a default in the following. Especially for the differential analysis, it will prove of value as the weights have to be updated for each differential bin to account for potential correlation related to the RDA. Another advantage is that the results can be interpreted consistently as the same correction procedure is used. More details and the estimation of the systematic uncertainty introduced by the radial distance asymmetry correction will be discussed in Sec. 6.

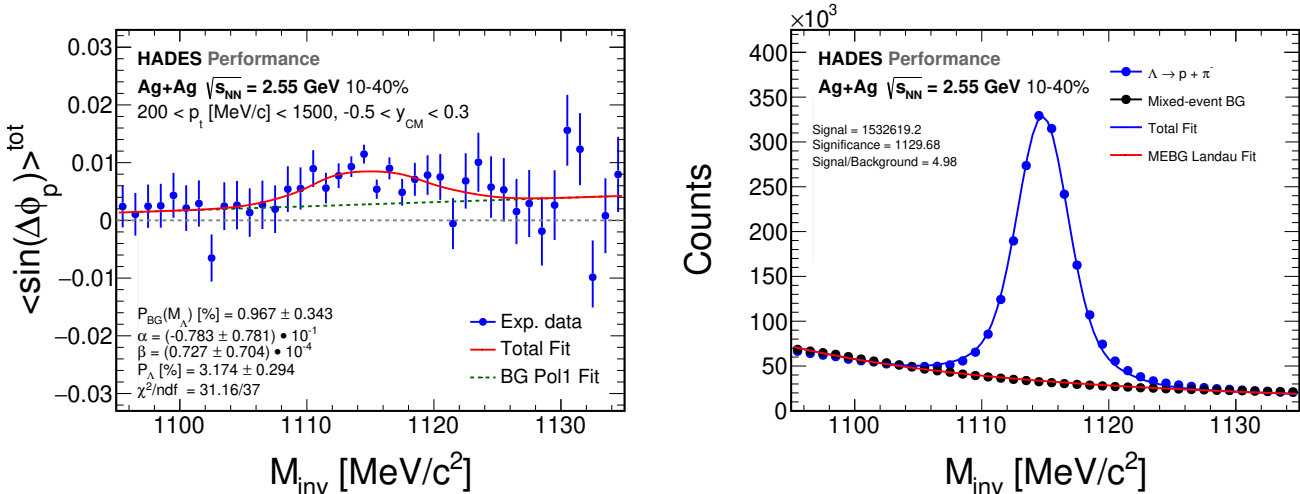


Figure 4.19: Polarization in Ag+Ag at $\sqrt{s_N} = 2.55$ GeV extracted using the invariant mass fit method after the data has been corrected for the radial distance asymmetry (left panel). The weights have been calculated from the invariant mass distribution relying only on the net Λ counts in three bins of $R'_V < -3$ mm, -3 mm $\leq R'_V \leq 3$ mm and $R'_V > 3$ mm. The weights are calculated such that the integral of the first and third bin are equal after correction while the second interval remains unchanged. The corresponding invariant mass distribution is shown too (right panel).

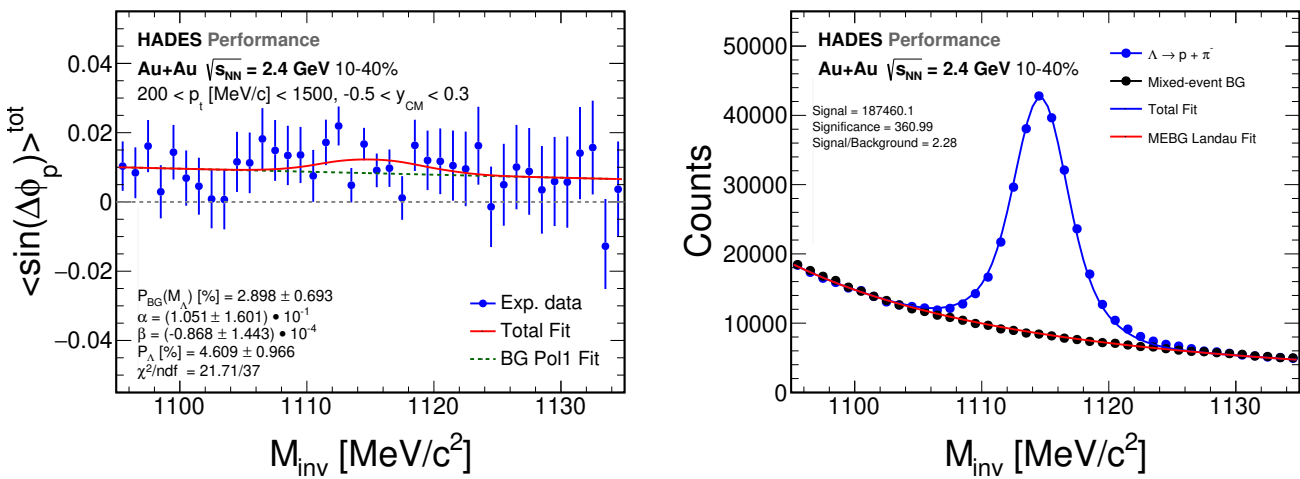


Figure 4.20: Polarization in Au+Au at $\sqrt{s_N} = 2.42$ GeV extracted using the invariant mass fit method after the data has been corrected for the radial distance asymmetry (left panel). The weights have been calculated from the invariant mass distribution relying only on the net Λ counts in three bins of $R'_V < -3$ mm, -3 mm $\leq R'_V \leq 3$ mm and $R'_V > 3$ mm. The weights are calculated such that the integral of the first and third bin are equal after correction while the second interval remains unchanged. The corresponding invariant mass distribution is shown too (right panel).

4.8 Corrections due to detector occupancy

Another correction which needs to be taken into account is the loss of efficiency due to the strongly varying track densities in different regions of the detector called occupancy correction. This correction was motivated by a study of the directed flow of protons and pions which showed a small off-set from zero at mid-rapidity and furthermore an asymmetry when backward and forward rapidities² are compared. To correct for these unphysical asymmetries a method based on the detector occupancy has been proposed [Tlu17]. Since the occupancy depends strongly on the centrality of the collision but also on the track position in the detector, it has been applied to four centrality classes and depends on the polar angle θ as well as the azimuthal angle $\phi - \Psi_{EP}$. The track density distribution is shown in the left panel of Fig. 4.21. As a function of θ , the shape is approximately linear. Thus, the shape of the occupancy correction is assumed to be linear too and the correction is defined as:

$$\epsilon(N_{\text{track}}) = \epsilon_0(1 - k \cdot N_{\text{track}}) \quad (4.30)$$

where N_{track} is the amount of tracks in a given $(\theta, \phi - \Psi_{EP})$ -bin. ϵ_0 is determined using simulations and set to $\epsilon_0 = 0.98$. The constant k is flexible and has been adjusted in a way that the directed flow of the pions vanishes at mid-rapidity, i.e. $v_{1,\pi}|_{y_{CM}=0} = 0$. The efficiency loss due to occupancy can be calculated in the angular space which is shown in the right panel of Fig. 4.21. This procedure has been performed for negatively and positively charged pions as well as for protons in 10% centrality bins from 0 – 40%. The corrections have been applied to the experimental data in Au+Au showing a clear improvement of the backward-forward anti-symmetry for all the particle species [Kor17].

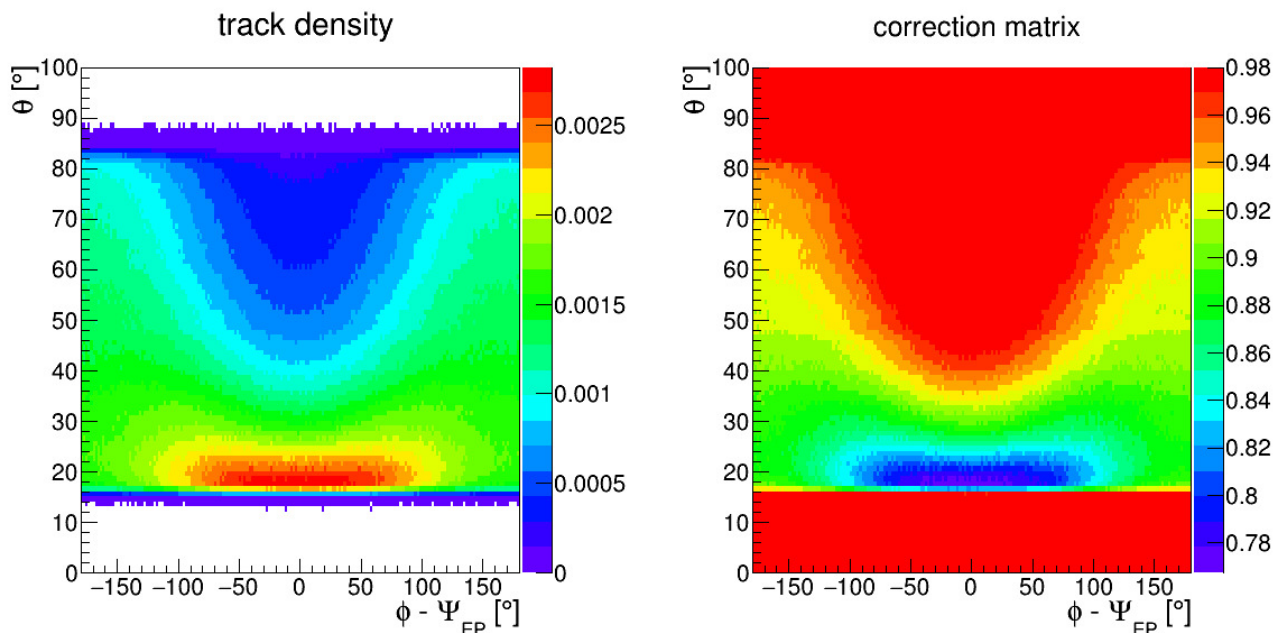


Figure 4.21: Track density (left) and occupancy correction matrix (right) as a function of the polar θ and azimuthal angle $\phi - \Psi_{EP}$ in the event plane frame for protons in Au+Au collisions normalized to one event [Tlu17].

² The symmetry of the collision demands that the directed flow is anti-symmetric with respect to mid-rapidity, such that $v_1(y) = -v_1(-y)$.

To apply similar corrections to the Λ hyperons is not so straightforward, as the Λ hyperon itself does not hit the detector, but its daughter particles do. However, the single particle corrections for protons and negatively charged pions can be used. The overall correction can further be defined as the multiplication of the two single particle weights, i.e. $\epsilon_{\Lambda} = \epsilon_p \cdot \epsilon_{\pi^-}$. The resulting weights $w_{\Lambda} = 1/\epsilon_{\Lambda}$ are displayed in the left panel of Fig. 4.22. The distribution of weights calculated in 10% centrality bins show several structures which may introduce systematics to the results. Since the Λ production has a strong centrality dependence, a finer binning of 2% in centrality has been interpolated. Therefore, the 10% occupancy matrices are interpolated by the function:

$$f(x) = 1 - \frac{k_1}{(x - k_2)^2} \quad (4.31)$$

which turned out to be the most proper description of the centrality dependence with two free parameters k_1 and k_2 to be adjusted. The fit has been performed individually for each $(\theta, \phi - \Psi_{EP})$ -bin and the results are stored for 2% steps in the centrality. The resulting weights are represented by the red curve in the left panel of Fig. 4.22. The distribution shows a continuous behavior while the center-of-gravity is shifted to higher values, i.e. the average weights are higher.

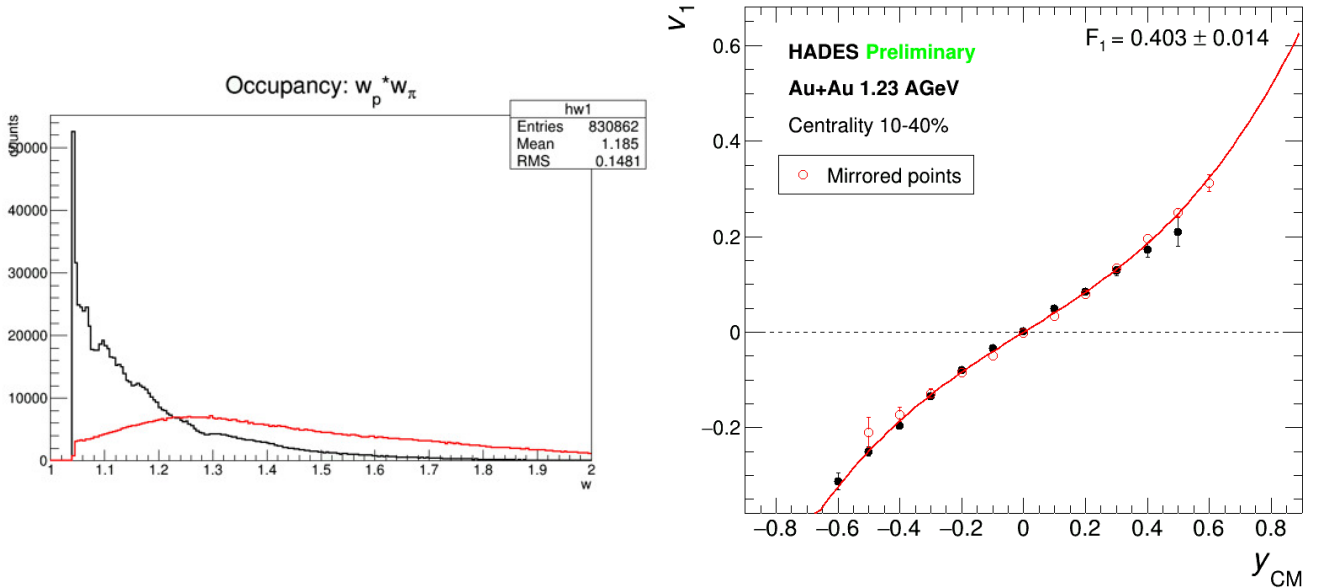


Figure 4.22: Left panel: Occupancy weights for the Λ candidate for 10% centrality bins (black curve) and interpolated in 2% centrality (red curve). The interpolation is necessary to get a continuous correction factor. Right panel: Directed flow of the Λ hyperons as a function of the rapidity for 10–40% centrality in Au+Au collisions at $\sqrt{s_{NN}} = 2.4$ GeV. Reflected points are shown to demonstrate the agreement for the backward-forward rapidity regions.

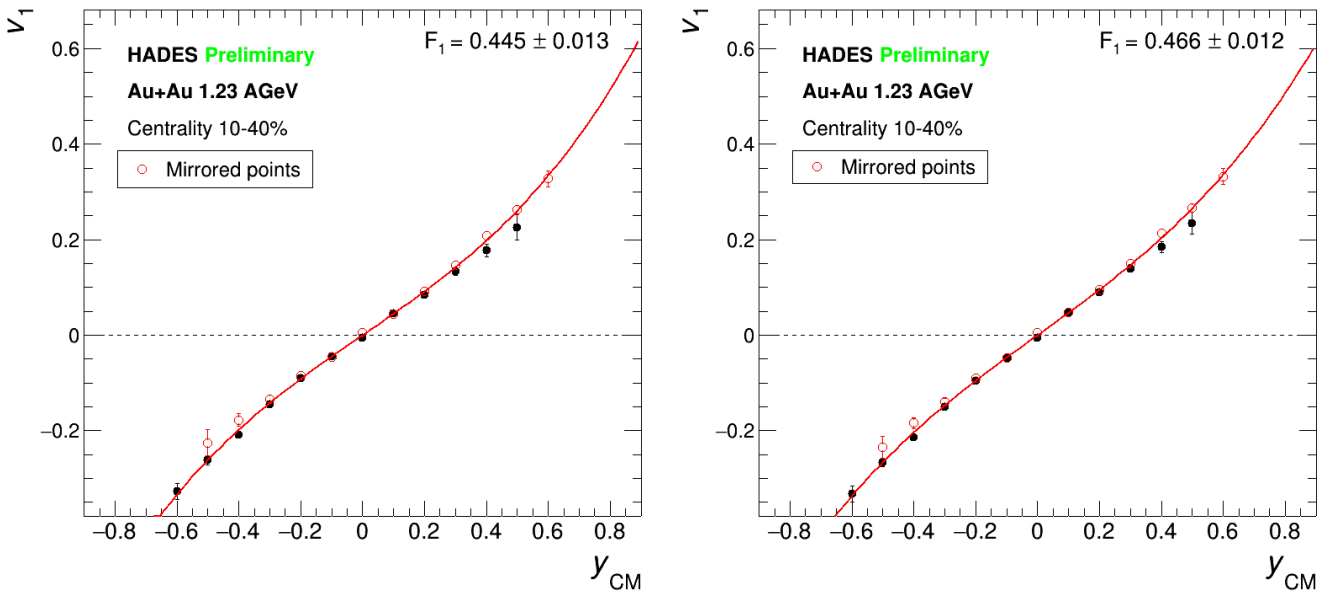


Figure 4.23: Directed flow of the Λ hyperons as a function of the rapidity for $10 - 40\%$ centrality in Au+Au collisions at $\sqrt{s_{NN}} = 2.4\text{ GeV}$. Reflected points are shown too, to demonstrate the agreement for the backward-forward rapidity regions. The results have been corrected for the occupancy in 10% centrality bins (left panel) and in 2% centrality bins (right panel).

The right panel of Fig. 4.22 displays the uncorrected results for the directed flow of the Λ hyperons in Au+Au collisions as a function of rapidity. The reflected points are shown to demonstrate the anti-symmetry of v_1 as a function of rapidity. The shape has been fit with a third order polynomial function while the quadratic component is fixed to be zero as in Eq. 1.15. Within statistical uncertainties, the directed flow is consistent with zero at midrapidity, i.e. $F_0 = 0.001 \pm 0.003$. Already without occupancy corrections applied, the shape is anti-symmetric and within statistical errors the directed flow vanishes at mid-rapidity.

In Fig. 4.23, the same data is shown but now the occupancy correction factors are used to reweight the distribution. As a result, the data point at mid-rapidity is shifted away from zero by $\Delta v_1|_{y_{CM}=0} = 0.007$ which is significant within the statistical uncertainty of the measurement. As these corrections have been introduced to force the directed flow at mid-rapidity to zero³, this does not work out for the Λ hyperon as a composite particle. Moreover, the slope at mid-rapidity, i.e. F_1 in the figures above, is enhanced by roughly 15%, which is more than introduced by other corrections and excels most systematic uncertainties (see Ch. 6). In comparison to the uncorrected result, there is also no improvement with respect to the backward-forward asymmetry. In Fig. 4.24, the results of the invariant mass fit method are shown for two rapidity bins symmetric with respect to midrapidity, without occupancy corrections applied. Although the background behaves quantitatively different, the extracted signal of v_1 confirms the anti-symmetry as the absolute values are consistent within uncertainties and have opposite sign. The situation is similar for the Ag+Ag sample as shown in Fig. 4.25, although the extracted signal of v_1 is slightly different. Due to these findings the correction does not really improve the situation of anti-symmetry and off-set at $y_{CM} = 0$, it will not be used in further analysis to not introduce a systematic bias.

³ For sure this only concerns protons and pions for which this correction has been settled.

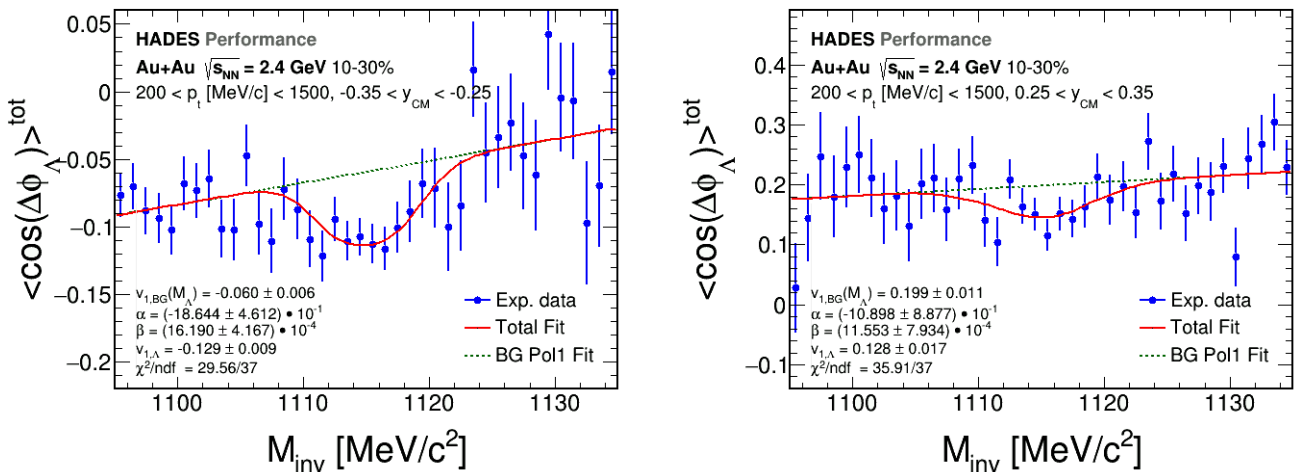


Figure 4.24: Measurement of the directed flow using the invariant mass fit method for different rapidity bins in Au+Au collisions at $\sqrt{s_{NN}} = 2.4$ GeV. The rapidity ranges are symmetric with respect to midrapidity, i.e. $-0.35 < y_{CM} < -0.25$ (left) and $0.25 < y_{CM} < 0.35$ (right). The extracted values confirm the expected anti-symmetry of v_1 as a function of rapidity.

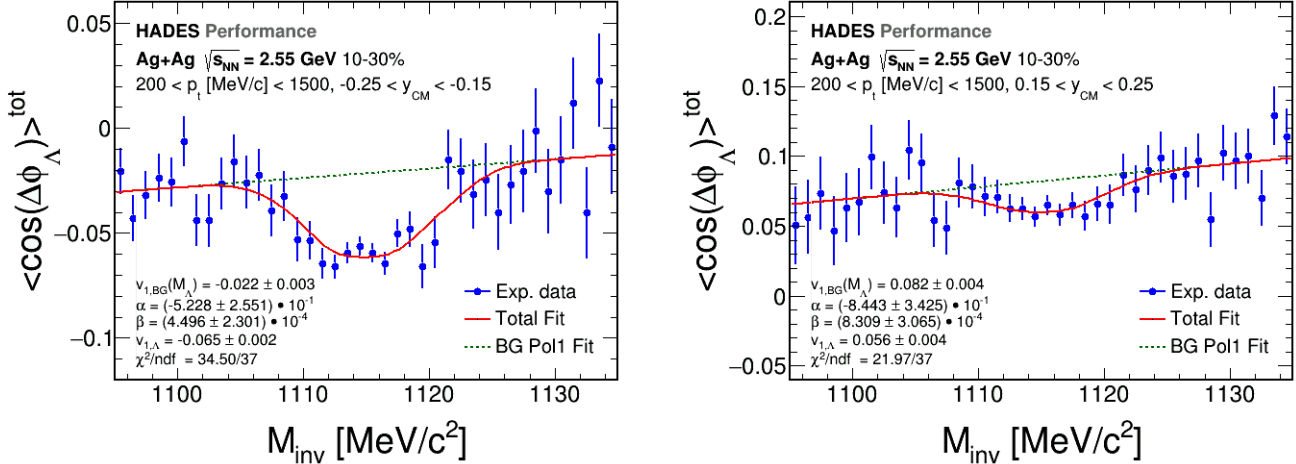


Figure 4.25: Measurement of the directed flow using the invariant mass fit method for different rapidity bins in Ag+Ag collisions at $\sqrt{s_{NN}} = 2.55$ GeV. The rapidity ranges are symmetric with respect to midrapidity, i.e. $-0.25 < y_{CM} < -0.15$ (left) and $0.15 < y_{CM} < 0.25$ (right). The extracted values confirm the expected anti-symmetry of v_1 as a function of rapidity.

5 Monte-Carlo simulations

For the precise measurement of the global polarization of the Λ hyperons, it is important to understand the effect of other physical correlations and detector acceptance in simulations where the amount of polarization can be set by the user. For this purpose the Monte-Carlo event generator Pluto is used [Frö09]. As a simulation framework based on C++, it is developed to generate low-energy heavy-ion collisions. It contains a library of particles together with their physical properties according to the PDG, such as the mass, decay channels, branching ratios, lifetimes, etc. The particles are assumed to be produced from a thermal source in order to generate realistic momentum and also angular distributions.

For the study of the polarization measurement the events are set up to contain the Λ hyperons of interest but also the most important background source, i.e. pions and protons. The properties are set to cope the situation as close as possible to the experimental data, as described in detail in Sec. 5.1. Then the events are produced with a varying amount of polarization together with a realistic flow pattern for all particles as described in Sec. 5.2. Having set all the properties of the particles, the data is handed to HGEANT to simulate a realistic detector response and finally reconstruct the full tracks from the simulated hit position as described in Sec. 5.3. Sec. 5.4 will summarize the simulated results and conclusions that could be drawn from the study.

5.1 Event generator and setup

To generate a heavy-ion collision in Pluto, a special particle called fireball is introduced for each particle species. It contains properties of the collision as the beam energy but also properties inherent to the particles themselves. From these sources the particles can be generated without being restricted by energy and momentum conservation as it would be the case for a fully simulated heavy-ion collision. The fireball is initialized with the temperatures T_1 and T_2 at which the particles are generated while the corresponding fractions are set by a parameter f . Afterwards, the total energy of the particle is randomly generated from a Siemens-Rasmussen distribution [Sie79] given by

$$\frac{dN}{dE} \propto \sqrt{E^2 - m^2} E \left\{ f e^{-\gamma_r E/T_1} \left[\left(\gamma_r + \frac{T_1}{E} \right) \frac{\sinh(\beta_r \gamma_r \sqrt{E^2 - m^2}/T_1)}{\beta_r \gamma_r \sqrt{E^2 - m^2}/T_1} - \frac{T_1}{E} \cosh(\beta_r \gamma_r \sqrt{E^2 - m^2}/T_1) \right] \right. \\ \left. + (1-f) e^{-\gamma_r E/T_2} \left[\left(\gamma_r + \frac{T_2}{E} \right) \frac{\sinh(\beta_r \gamma_r \sqrt{E^2 - m^2}/T_2)}{\beta_r \gamma_r \sqrt{E^2 - m^2}/T_2} - \frac{T_2}{E} \cosh(\beta_r \gamma_r \sqrt{E^2 - m^2}/T_2) \right] \right\}, \quad (5.1)$$

where β_r is the radial expansion velocity also called blast velocity which is also used to calculate $\gamma_r = 1/\sqrt{1-\beta_r^2}$. To set the parameters for the particles realistically, the results from the experimental data are used. There the Siemens Rasmussen ansatz gives very precise results to describe the transverse mass spectra of the different particles species [Sch16]. Applying this fit simultaneously to all particles, a common blast velocity β_r and the so-called freeze-out temperatures can be extracted. The values are used as input parameters to setup the particle fireball in the Pluto simulation. The results are summarized in Tab. 5.1. For most of the particles the transverse mass spectra can be fit with one single slope, only for the pions two slopes have to

be used [Ada20b]. This results in two different temperatures extracted from the fit with the corresponding fraction f and $1 - f$. To crosscheck the results the transverse mass spectra of charged pions, protons and Λ hyperons are compared. A reasonable agreement between the simulated particles and the experimental data is achieved which can be seen from Fig. 5.1.

Particle species	Average multiplicity	Temperature T_1 [MeV]	Temperature T_2 [MeV]	Fraction $f(T_1)$	Blast velocity β_r
π^+	7	49	89	98 %	0.34
π^0	9	49	89	98 %	0.34
π^-	12	49	89	98 %	0.34
p	75	80	-	100 %	0.34
Λ	1 (fixed)	60	-	100 %	0.34
K_S^0	1 (fixed)	80	-	100 %	0.34

Table 5.1: Particle species used in the event generator Pluto with the corresponding settings: multiplicity, temperatures and fractions, blast velocity. Most particles are generated with a Poissonian distribution with an average multiplicity, while the Λ and K_S^0 are generated once in each event.

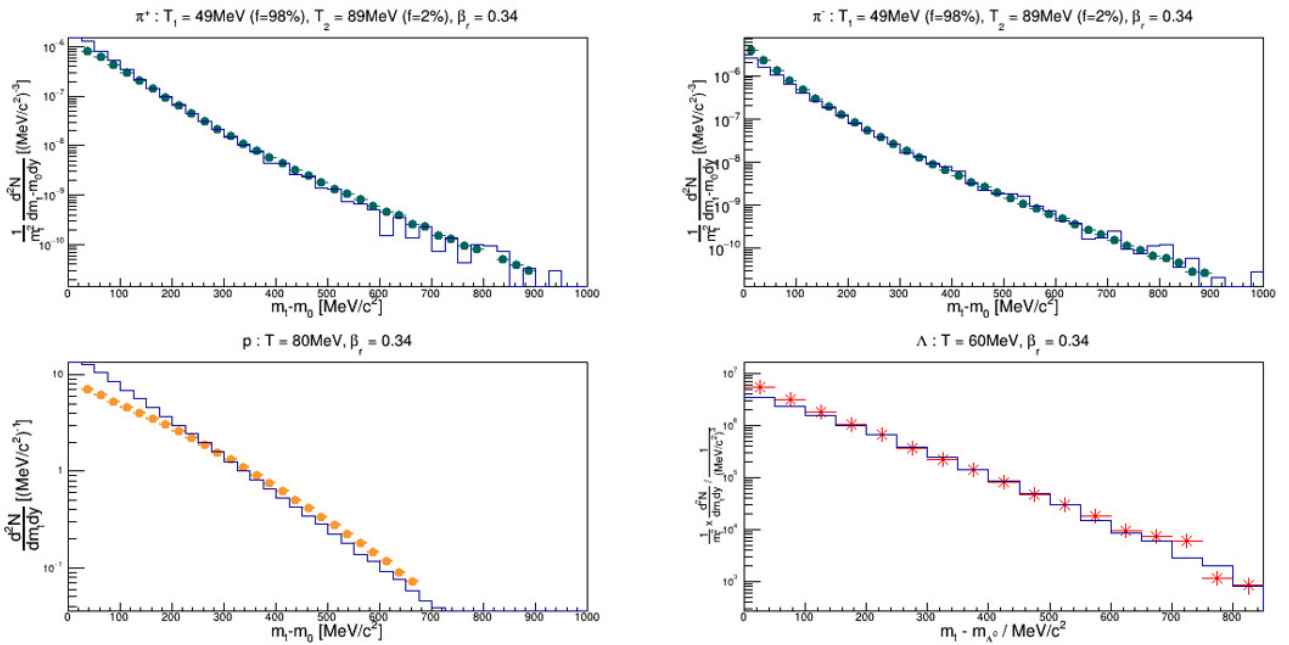


Figure 5.1: Transverse mass distributions for pions, protons and Λ hyperons in comparison. The data points represents the results from Au+Au collisions while the blue line depicts the results from a bunch of events generated with the Monte-Carlo event generator Pluto.

To generate a reasonable amount of combinatorial background, protons and pions are established to the simulated Pluto event. The multiplicities have been adjusted to their experimental multiplicities in the 10 – 20 % centrality bin to be closed to the experimental conditions. However, the multiplicities in the simulation have not been fixed but being generated randomly from a Poissonian distribution defined by the average multiplicity also summarized in Tab. 5.1. This

is to make sure that the relative appearance of the particles varies from event to event as in experimental data.

To study the effect on detector acceptance and reconstruction on the polarization measurement, the particle multiplicity of the Λ hyperon is fixed to one for each event to generate reasonable statistics without producing a large amount of data. Furthermore, to guarantee a good chance to reconstruct the Λ hyperon, its decay is forced to the channel $\Lambda \rightarrow p + \pi^-$, i.e. the branching ratio is set to 100 %. This decay is performed by Pluto taking into account all the kinematics and the mean lifetime of the Λ hyperon.

To also introduce a source of correlated background, the K_S^0 is introduced. The K_S^0 is the particle that is most often produced in the same collision with a Λ hyperon and therefore likely to appear in the experimental data. Its decay channel $K_S^0 \rightarrow \pi^+ + \pi^-$ includes two particles which might pass the daughter selection cuts of the Λ hyperon and thereby introduce a correlated source of background. Thus the K_S^0 is used to study correlated effects in more detail. If only the combinatorial background is of interest, all particles related to the K_S^0 can be removed easily in the last step of the analysis without influencing the uncorrelated result. As for the Λ hyperon, the decay channel is also fixed for the K_S^0 .

After all the quantities for the event and the corresponding particles have been generated, the results are stored in an ASCII format to feed the next step of the analysis which is typically the detector simulation done by HGEANT. The file starts with one line which contains the informations of the event. These are the event number followed by the number of particles, the center-of-mass rapidity and the impact parameter of the collision. Then this is followed by several lines containing all the particle informations. For each particle, the energy-momentum and the time-space components are stored together with its ID and several numbers to distinguish whether this particle is a primary or if not what particle species its mother particle corresponds to and so on.

For a primary particle, the space-time vector is $(\vec{x}, t) = (0, 0)$ while the secondary particles have a time off-set which is stored in ns and the space coordinates denote the vertex where the decay has happened. To get a realistic distribution of the event vertices overall, a list of reconstructed event vertex coordinates has been stored in a dedicated file from the experimental data. This guarantees that the distribution of the event vertices in X and Y is reproduced as well as the Z -distribution resulting from the 15 target segments. In the last stage of the Pluto simulation, these event vertices are read from the file and then all the particles of one event are set to the corresponding event vertex, while the secondary particles are shifted as if they would have been emitted from the new event vertex and then decayed some ns later.

5.2 Implementation of polarization and flow to the Pluto events

The next step is important to introduce the polarization to the Λ hyperons and the flow to all particles for the investigation of possible corrected detector effects. Neither Pluto nor HGEANT provide an option to do this and thus an intermediate step has been introduced for this purpose. The ASCII files from the Pluto output are taken, the properties inside are changed according to the requirements and then the same output format is written again, such that the input format of HGEANT is matched exactly.

For the implementation of both polarization and flow for each event, a corresponding reaction plane is needed. To avoid correlations to the fixed detector setup afterwards, the reaction plane is generated randomly for each event. Then the flow and polarization can be implemented with respect to the reaction plane angle Ψ_{RP} . Another problem is that in the typical Pluto output

format a storage of the reaction plane angle is not foreseen. However, since the storage of the impact parameter is not needed for this specific analysis, as no centrality selection will be used later on, this parameter is used to store the reaction plane angle in the intervall $[0, 2\pi]$. Later on in the analysis, for each event the corresponding reaction plane angle can be read from the file by using the function to get the impact parameter.

Having fixed the reaction plane angle for the event, the flow of the particles can be implemented. To mimic the situation in the experimental data as close as possible, the experimental results will be used to model the shape and magnitude of the signal. For the Au+Au beam time, the directed and elliptic flow have been measured multi-differentially as a function of transverse momentum and rapidity for protons [Ada20a], pions, kaons and Λ hyperons (this study). The idea is to model the dependencies of the first two flow components such that it can be applied to the simulations. As a first attempt, only the phase-space integrated values for the flow have been used, focussing on protons and Λ hyperons, resulting in $v_1 = -0.1$ and $v_2 = -0.06$. As a second attempt, the flow pattern has been implemented individually for the particle species depending on the phase-space region. Therefore, the experimentally measured v_1 and v_2 values including uncertainties have been extracted for several rapidity bins as a function of the transverse momentum. The midrapidity bin has been set to zero for all values of p_t . To describe the p_t -dependence for the directed flow for protons and Λ hyperons, the function

$$v_{1,p/\Lambda}^{\text{fit}}(p_t) = \frac{k_1}{x + k_2} + k_3, \quad (5.2)$$

is used while for the elliptic flow a third order polynom has been used, where k_0 to k_3 are the parameters to be adjusted. The fit has been performed for each rapidity bin and reasonable results over a large transverse momentum range are obtained, only for $p_t < 100 \text{ MeV}/c$ or $p_t > 1600 \text{ MeV}/c$ the fit does not follow the qualitative trend. However, the deviations are justified to be below 1% and in addition these particles will be removed mostly by the particle selection and will not be important for the final results.

For the pions, a reasonable description of the directed flow has been achieved using a third order polynom while for the elliptic flow the shape seems to favor the function

$$v_{2,\pi}^{\text{fit}}(p_t) = \frac{k_1}{x^3 + k_2} + k_3. \quad (5.3)$$

As a next step, the fit functions are used to determine the rapidity dependence in a very fine binning with respect to the transverse momentum. Then for each of these bins in p_t , the rapidity dependence is fit again to fill the gaps between the distinct data points. For the protons and the Λ hyperons, the fit function as expected is used:

$$v_{1,p/\Lambda}^{\text{fit}}(y_{CM}) = k_1 x + k_2 x^3. \quad (5.4)$$

This also makes sure that the directed flow at midrapidity vanishes. Even the trend of v_1 for pions is not similar to the protons and Λ hyperons, the same fit function is applied. For the description of the elliptic flow as a function of the rapidity, a second order polynom is used for protons and Λ hyperons. In case of the pions, there seems to be no dependence on the rapidity and thus a constant function is fit.

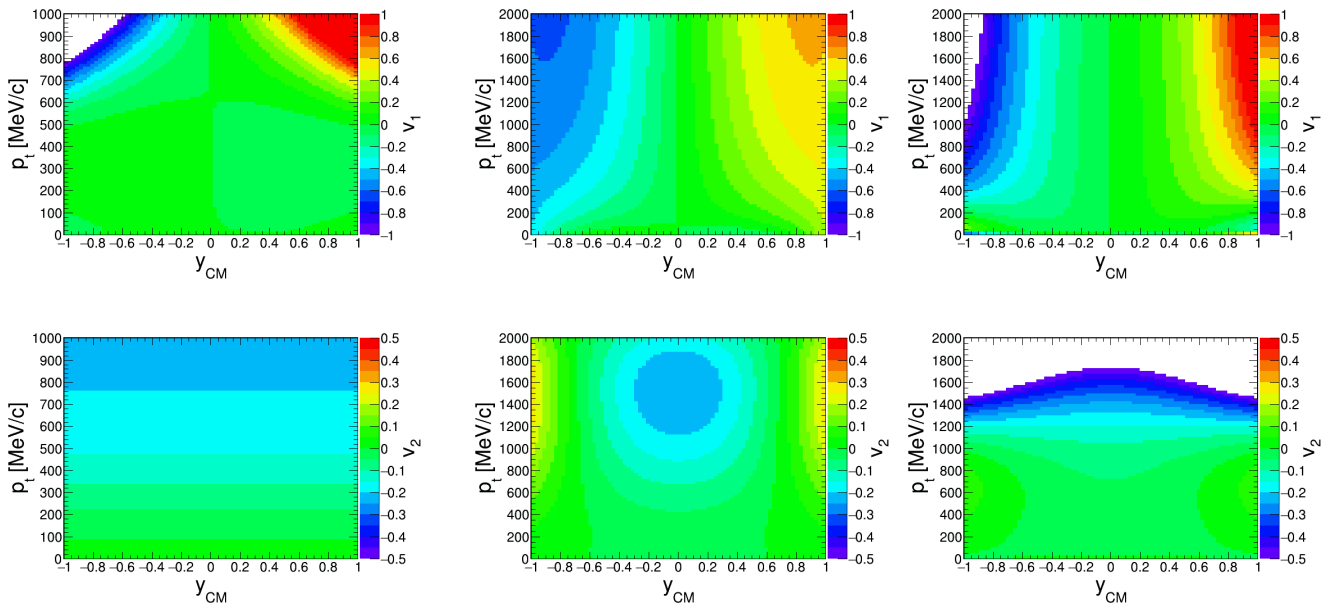


Figure 5.2: Two dimensional pattern of the directed (upper row) and elliptic flow (lower row) modeled from the experimental results of the Au+Au data for pions (left), protons (middle) and Λ hyperons (right). The pattern has been modeled over a large range in the transverse momentum and rapidity space to generate random flow values for the simulated particles which reproduce the situation in experimental data realistically.

The result of this procedure is a map in two dimensions which describes the flow components for the different particles in the full phase-space. The flow pattern of v_1 and v_2 for all these particles as modeled by the fit is shown in Fig. 5.2.

At the moment, the same procedure for the K_S^0 is implemented but the flow pattern of the pions is used. The reason is that the first studies with $v_1(p_t, y) = v_2(p_t, y) = 0$ showed that there is no significant impact on the final results with or without the $K_S^0 \rightarrow \pi^+ + \pi^-$ decay. More details will be explained in the following.

For the implementation of the flow for each simulated particle, the transverse momentum and its rapidity are calculated to get the corresponding v_1 and v_2 values from the histogram in Fig. 5.2. These values are used in the function

$$\frac{dN}{d\Delta\phi} = N_0(1 + 2\nu_1\cos(\Delta\phi) + 2\nu_2\cos(2\Delta\phi)) + N_{\text{cor}} \quad (5.5)$$

to mimic the angular dependence $\Delta\phi$ taking into account the first two flow components. N_{cor} is used to shift the function just above zero such that it can be used as a probability density distribution to generate a new angle $\Delta\phi^{\text{new}}$ randomly from the histogram. Since in reality the flow components are fit from a number distribution, it cannot have entries smaller than zero. The occurrence of negative values originates from the corrections applied to the experimental results, most importantly the correction for the event plane resolution R_{EP} , but also from regions where the fit function diverges since no more data points are available. In the former case, the shift by N_{cor} will be small and thus both flow components will be reduced slightly. In the latter case, there will be only a negligible amount of particles striking the detector and passing all selection cuts which again will not influence this systematic study at all.

Having the reaction plane angle from the corresponding event at hand, the new azimuthal angle of the particle can be calculated as $\phi^{\text{new}} = \Delta\phi^{\text{new}} + \Psi_{EP}$. If the particle under consideration is a primary particle and hence its space-time vector is $(\vec{x}, t) = (\vec{x}_{\text{EvtVertex}}, t)$ the momentum of the particle can be rotated in the plane perpendicular to the beam axis leaving the z-component of the momentum unchanged and setting the other components to:

$$p_x^{\text{new}} = p_t \cos(\phi^{\text{new}}), \quad (5.6)$$

$$p_y^{\text{new}} = p_t \sin(\phi^{\text{new}}), \quad (5.7)$$

$$p_z^{\text{new}} = p_z^{\text{old}}. \quad (5.8)$$

Applying this procedure for millions of particles will reproduce the overall flow pattern in the full phase-space.

For the secondary particle, i.e. the Λ hyperon and the K_S^0 , first the two daughter particles are combined to the mother track by a direct sum of their energy-momentum four-vector. Since the mother particles are also emitted from the primary vertex, the same procedure can be applied: calculating p_t and y to get the flow components, setting up the $\Delta\phi$ distribution accordingly, generate a new azimuthal angle. However, the rotation has not to be applied to the mother itself but to their daughter particles which are stored in the output file. To keep the kinematics of the decay as generated by Pluto unchanged, the relative azimuthal angles from the daughters to the mother are conserved and the rotation can be written as:

$$p_{x,D}^{\text{new}} = p_{t,D} \cos(\phi_M^{\text{new}} + \phi_M^{\text{old}} - \phi_D), \quad (5.9)$$

$$p_{y,D}^{\text{new}} = p_{t,D} \sin(\phi_M^{\text{new}} + \phi_M^{\text{old}} - \phi_D), \quad (5.10)$$

$$p_{z,D}^{\text{new}} = p_{z,D}^{\text{old}}, \quad (5.11)$$

where the index D represents the values from one of the daughters and M the mother particle. Since the daughters are not produced at the primary vertex, i.e. $(t_D, \vec{x}_D) \neq (0, \vec{x}_{\text{EvtVertex}})$, the decay vertex position has to be rotated accordingly by:

$$x_D^{\text{new}} = \sqrt{(x_D^{\text{old}} - x_{\text{EvtVertex}})^2 + (y_D^{\text{old}} - y_{\text{EvtVertex}})^2} \cdot \cos(\phi_M^{\text{new}}), \quad (5.12)$$

$$y_D^{\text{new}} = \sqrt{(x_D^{\text{old}} - x_{\text{EvtVertex}})^2 + (y_D^{\text{old}} - y_{\text{EvtVertex}})^2} \cdot \sin(\phi_M^{\text{new}}), \quad (5.13)$$

$$z_D^{\text{new}} = z_D^{\text{old}}, \quad (5.14)$$

keeping the absolute distance from the event to the decay vertex unchanged.

After the procedure has been applied, the simulated data can be analyzed to reconstruct the flow of the particles. The results are shown in Fig. 5.3. As can be seen in comparison to Fig. 5.2, the shape and magnitude of the flow as a function of rapidity and transverse momentum is reproduced. For the protons and Λ hyperons the kinematical restrictions can be seen by the sharp edge in the upper part of the distribution. Therefore, the phase-space region where the distribution of the extrapolated flow pattern starts to diverge from the experimental data does not contribute. Further, the detector acceptance and the particle selection cuts will even stronger

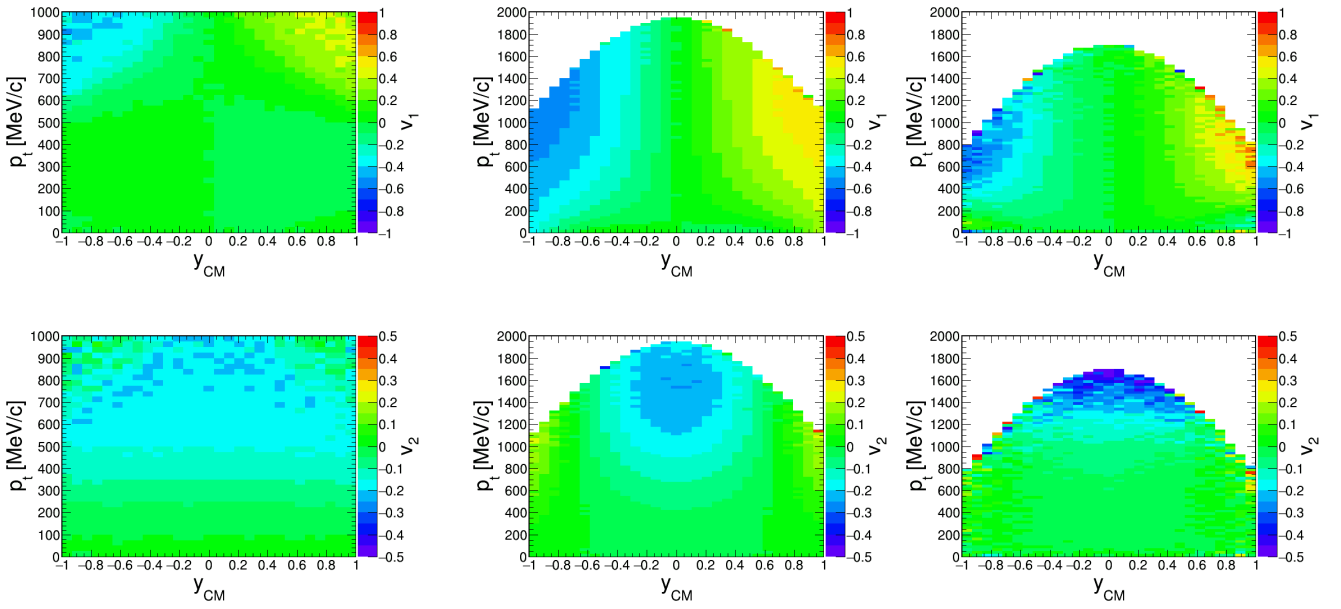


Figure 5.3: Two dimensional pattern of the directed (upper row) and elliptic flow (lower row) from the simulated Pluto events for pions (left), protons (middle) and Λ hyperons (right). Within the kinematical restrictions, the flow pattern that is implemented can be reproduced for both magnitude and shape of the distribution which can be seen in comparison to Fig. 5.2.

cut on the phase-space such that the remaining part is well in agreement with the experimental flow pattern.

The method for the implementation of the polarization is similar. First a degree of polarization $P_{\Lambda}^{\text{input}}$ for the Λ hyperons has to be set as an input value. From this value the magnitude of the first odd component b_1 (see Eq. 4.5) is calculated by reversing Eq. 1.28, i.e. $b_1^{\text{input}} = \pi \alpha_{\Lambda} P_{\Lambda}^{\text{input}} / 8$. Then a histogram is filled with the distribution following

$$\frac{dN}{d\Delta\phi_p^*} = N_0 \left(1 + 2b_1^{\text{input}} \sin(\Delta\phi_p^*) \right) \quad (5.15)$$

which is again used as a probability distribution from which a random angle $\Delta\phi_p^{*,\text{new}}$ is generated. An example for an input polarization of $P_{\Lambda}^{\text{input}} = 6\%$ is displayed in the left panel of Fig. 5.4. An overall shift of the distribution as in Eq. 5.5 is not necessary since $b_1^{\text{new}} \ll 0.5$ and thus the distribution cannot have unphysical negative values.

As the polarization of the Λ hyperons is given by the momentum direction of the proton in the rest frame of the Λ hyperon, both daughter particles have to be boosted according to Eq. 4.2. Then the rotation is performed in the rest frame of the Λ hyperon. The new momentum components of the proton are calculated using:

$$p_x^{*,\text{new}} = |\vec{p}_p^*| \cdot \cos(\Psi_{RP} - \Delta\phi_p^{*,\text{new}}) \cdot \sin(\theta_p^*), \quad (5.16)$$

$$p_y^{*,\text{new}} = |\vec{p}_p^*| \cdot \sin(\Psi_{RP} - \Delta\phi_p^{*,\text{new}}) \cdot \sin(\theta_p^*), \quad (5.17)$$

$$p_z^{*,\text{new}} = |\vec{p}_p^*| \cdot \cos(\theta_p^*). \quad (5.18)$$

In order to fulfill the momentum conservation, the momentum of the pion is set to $\vec{p}_{\pi^-}^{*,\text{new}} = -\vec{p}_p^{*,\text{new}}$. To get the corresponding energy and momentum values in the laboratory frame, the new energy-momentum four-vectors of both daughters have to be transformed back which can be done by using again Eq. 4.2 and replacing $\vec{\beta}_\Lambda \rightarrow -\vec{\beta}_\Lambda$. Afterwards the values for the energy and momentum are updated and written to the output file.

These files can directly be analyzed to check that the implementation has been done properly. In the right panel of Fig. 5.4, the results for the polarization analysis are shown making use of the $\Delta\phi$ -extraction method as described in Sec. 4.2. A determination of signal and background by the invariant mass distribution is not necessary since for the simulation the Λ hyperons can be identified by asking for the PID directly. The result shows that the input polarization can indeed be reconstructed from the files.

With the possibility to switch the flow of the particles on and off while implementing a varying amount of polarization to the Λ hyperons, the data is ready to be handed to the next step of the simulation where the detector acceptance and the reconstruction procedure are applied.

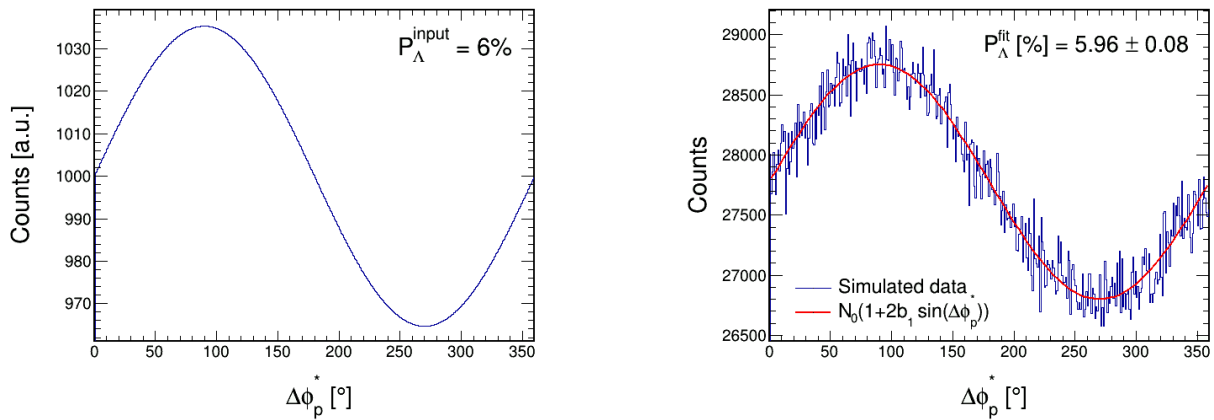


Figure 5.4: Implementation of the polarization to the events simulated with Pluto. Left panel: distribution of the azimuthal angle of the proton in the rest frame of the Λ hyperon for an input polarization of $P_\Lambda^{\text{input}} = 6\%$ which is used as a probability distribution to randomly generate the proton direction. Right panel: the same distribution as analyzed from the simulated Pluto files. Within statistical uncertainties the input polarization can be reproduced by making use of the $\Delta\phi$ -extraction method as described in Sec. 4.2.

5.3 Detector response and track reconstruction

As a next step of the simulation, the ASCII files are handed to the software HGEANT which is based on the software GEANT 3.21 [Bru87] developed at CERN. HGEANT contains the geometrical structure of the HADES detector with is defined from the technical drawings to match the real setup as close as possible. The START detector is not included since the collision time is taken from the Pluto event directly.

The software propagates all the particles from their initial positions to the detector. Thereby, all physical effects are taken into account. This includes not only possible decays of unstable particles, but also interactions with the detector material and deflections inside the magnetic field. This leads to a large amount of secondary particles being produced. All particles are

tracked until all possible detector hits have been generated. This results in a data set of particle hits in the different detector subsystems, containing the hit positions of the particle with the corresponding time, the momentum and the deposite energy.

This data must be converted into the digital response of the detector. This is done by the digitizer which is a software package to simulate the electronic response of the different detector subsystems. The signals have to be generated according to the measured detector response to reflect the finite resolution in the experiment, but also electronical noises and other effects concerning the analog to digital conversion are included. The parameters are set to reproduce the findings in the experimental data and mimic the raw electronic distributions recorded. After this steps are done, the resulting ROOT files can be treated as the files recorded in the experiment. Therefore, all the steps to reconstruct the particle tracks and the corresponding properties are just the same as for the experimental data as described in Ch. 3.

In summary, the simulated events are converted into the DST file format which can be analyzed in the same way as the experimental data. This allows to study the effects of the detector acceptance and the track reconstruction to the observables of interest, while all initial properties can be fully controlled.

5.4 Null hypothesis check

The simulated Pluto events with the possibility to implement a realistic flow pattern and different amount of polarization can be used for several studies. A proof of principle is to check how much of the input polarization can be reconstructed when the HADES acceptance and all reconstruction as well as the selections cuts have been applied. Besides this, the study is also important to understand the background correlation appearing in the polarization measurement as determined in Fig. 4.5 and 4.6. It is of special interest to check for possible correlations between the particle flow and the detector acceptance which might potentially influence the polarization measurement.

For a final comparison to the experimental data, sufficient statistics is needed such that even after all the selection criteria are applied, the analysis can still be performed with reasonable uncertainty. It turned out that a set of 40.000 events is sufficient. The events have been simulated and prepared according to the requirements described in Sec. 5.1 and 5.2. Then the detector response has been simulated as described in Sec. 5.3. The resulting DST files can directly be used for the default analysis, since they are in the same format as the experimental data. However, the additional information in the simulated files allows to check the overall amount of Λ candidates and to disentangle the origin of the proton and pion candidate. The relative appearance of the possible combination is summarized in Tab. 5.2. The table has been generated after all the selection cuts also used in the experimental data have been applied, except for a cut on the MVA.

Tab. 5.2 shows that the main source of background originates from primary protons, which are combined with the different sources of π^- candidates. The possibility, that a π^+ from a K_S^0 is mistaken as a proton, and survives all selection cuts, is negligible. The number has to be taken with some care, since the appearance of one Λ hyperon per event is much larger then in the experimental data. Since this argument holds also for the K_S^0 it can be expected that the main background in experiment arises from combinations of two primary particles.

The azimuthal angular distribution of the proton in the rest frame of the Λ hyperon is shown in Fig. 5.5. The left panel shows the distribution in case all six sectors are considered while in the right panel the same distribution is displayed when all particles reconstructed in sector 2 are

Origin of the proton candidate	Origin of the pion candidate		
	Primary	K_S^0 decay	Λ decay
Primary	29 %	11 %	22 %
K_S^0 decay	$\ll 1$ %	$\ll 1$ %	$\ll 1$ %
Λ decay	1 %	0.6 %	36 %

Table 5.2: Percentage of the particle combination to a Λ candidate in the simulated Pluto events after all selection cuts have been applied.

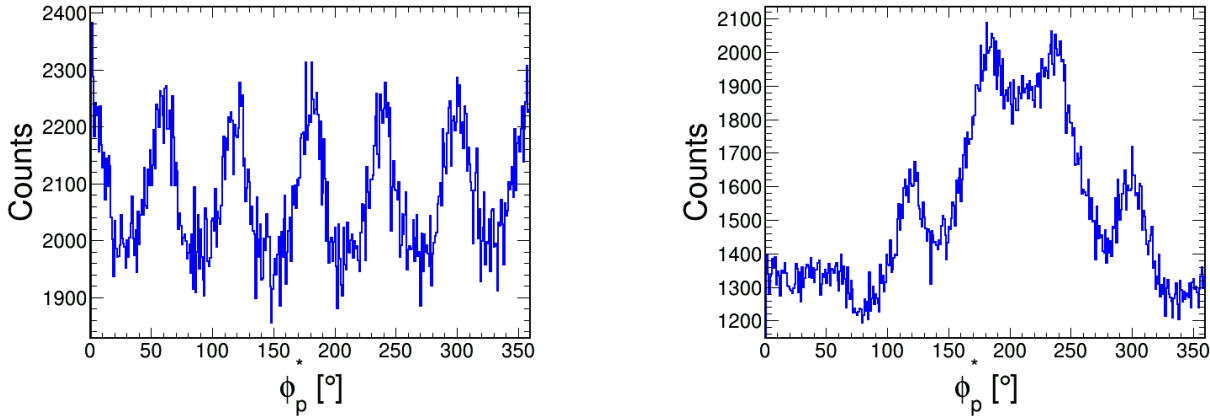


Figure 5.5: Distribution of the azimuthal angle of the proton in the rest frame of the Λ hyperon calculated from simulated Pluto events after all particle selections applied except for the discriminant. After the boost to the rest frame of the Λ the shape of the six sectors is still visible: all six sectors (left) and without the sector 2 (right). The distributions match the behavior of the experimental data (compare to Fig. 4.10).

removed. The structure originating from the HADES setup, i.e. the six sectors of MDCs, are still visible after the proton has been boosted to the rest frame of the Λ hyperon. In comparison to the experimental data (see Fig. 4.10) the distribution shows similar behavior. This will allow to investigate a possible influence of this shape to the final observables, also in case of an inactive sector as in the Au+Au data. Not only the influence of the anisotropic shape but also a coupled effect to the flow can be studied. It has been checked that the shape of the distribution does not depend neither on the flow pattern nor on the amount of polarization introduced.

For simplicity the first samples have been generated only with an integrated flow value, not depending neither on the phase space nor on the particle species. The values for the directed and elliptic flow have been chosen to match the integrated results of the Λ hyperons, i.e. $v_1 = -0.1$ and $v_2 = -0.06$. The resulting distribution of the azimuthal angle of the Λ hyperons is shown in Fig. 5.6 again for all six sectors active (left panel) and without sector 2 (right panel). The distribution has been fit with a Fourier expansion up to the second order only containing the even components representing the flow pattern. The removal of sector 2 reduces the overall amount of entries roughly by 30 %, however, the reconstructed flow components are not affected. This confirms that an anisotropy in the initial azimuthal distribution is randomized when the particles are correlated to the reaction plane, which is orientated randomly with respect to the detector.

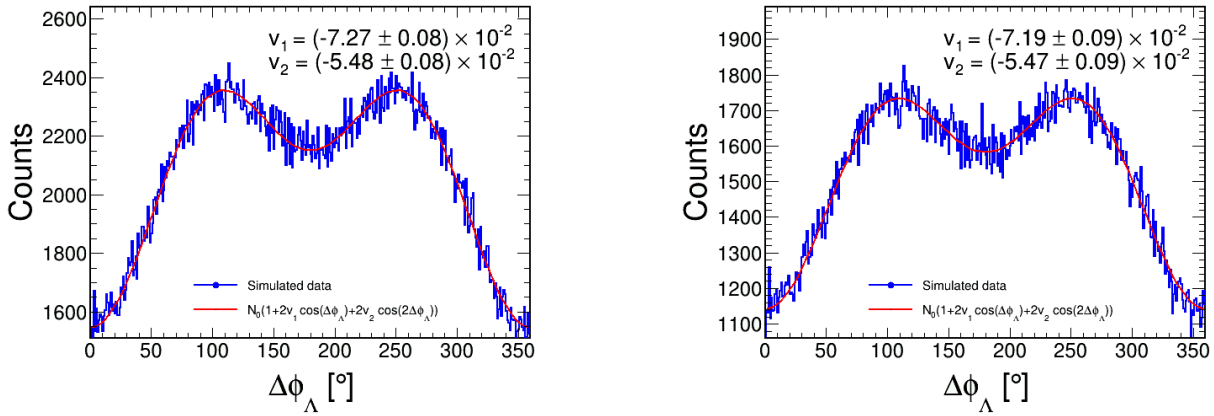


Figure 5.6: Distribution of the azimuthal angle of Λ hyperons calculated from simulated Pluto events after all particle selections applied. The events have been simulated with an integrated flow of $v_1 = -0.1$ and $v_2 = -0.06$ for all particles. The reconstructed values are slightly lower but in principle the pattern is reproduced. The reconstructed components do not depend on the amount of sectors used in the analysis: all six sectors (left) vs. sector 2 removed (right).

Comparing the absolute values of the directed and elliptic flow as reconstructed from the simulated data, both components are slightly reduced with respect to their input values. For the directed flow, the effect is of the order of 30% while for the second component v_2 the effect is smaller, i.e. roughly 8%. However, the general pattern is reproduced even within the acceptance and including all selection cuts.

Regarding the polarization measurement, the angular distribution of $\Delta\phi_p^*$ has to be considered. When no flow and no polarization is implemented the distribution is found to be flat and consistent with the input values. If only the polarization is implemented, the distribution shows the expected asymmetric shape which can be seen in Fig. 5.7. To reconstruct the value of the polarization in the distribution, it can be fit with a Fourier expansion. Clearly, the shape is perfectly described using only the first odd component, excluding for statistical fluctuations which do not have physical meaning. The determined component b_1 can be transformed to the actual polarization of the Λ hyperons according to Eq. 4.5. The event plane resolution correction R_{EP} therein can be dropped, since in the simulation the true reaction plane is known and used to measure flow and polarization, i.e. $R_{EP} \equiv 1$. Within statistical uncertainties, the input polarization is reconstructed which demonstrates that a global polarization measurement is possible. Another important finding is the consistency between the results when one sector of the distribution is removed. However, this effect has to be studied in more detail, taking into account different flow pattern of the particles which might have non-trivial correlations with the detector acceptance.

First the distribution of $\Delta\phi_p^*$ can be plotted for the simulated data sample with the integrated flow values of $v_1 = -0.1$ and $v_2 = -0.06$. The results for different input polarizations of $P_\Lambda = 0\%$ and $P_\Lambda = 6\%$ are displayed in Fig. 5.8. In both cases, a clear modification of the shape can be seen in comparison to the non-flowing data. The shape can be described by a Fourier expansion while only the first odd and the second even components are considerably non-zero. It seems that the elliptic flow pattern also introduces a similar pattern to the polarization angle,

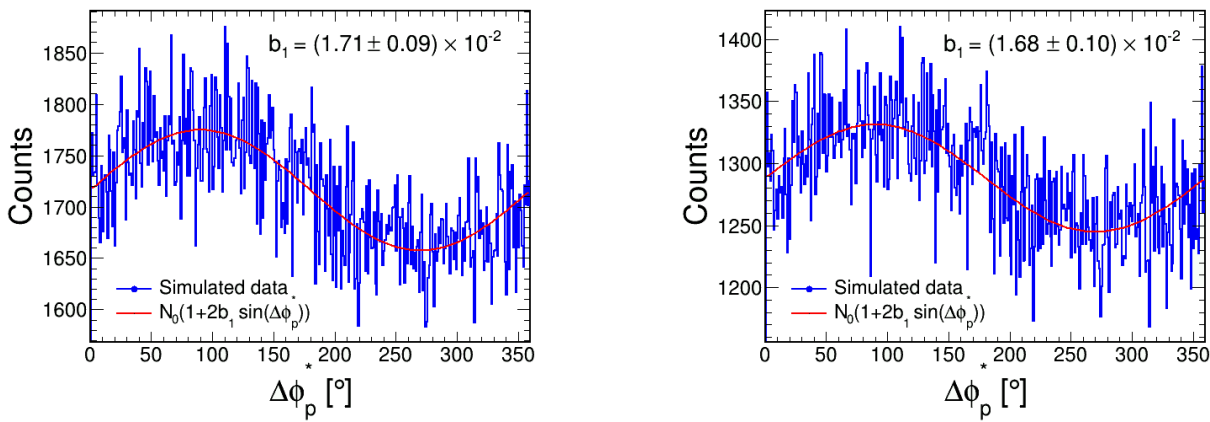


Figure 5.7: Distribution of the polarization angle calculated from simulated Pluto events after all particle selections applied. The distribution is fit with a Fourier expansion containing only the first odd component. The measured value for all six sectors active is $P_\Lambda = (5.95 \pm 0.31)\%$ and $P_\Lambda = (5.84 \pm 0.35)\%$ without sector 2 which confirms the input polarization for this sample of $P_\Lambda = 6\%$ within statistical uncertainties. This sample was generated without any flow pattern, i.e. $v_1 = v_2 = 0$.

however, of much smaller magnitude and opposite sign than v_2 . It has been checked that when no directed flow was implemented, the results do not change. However, this introduced pattern does not influence the reconstruction of the polarization as in all cases the reconstructed values match the input polarization.

The Pluto events can also be analyzed using the invariant mass fit method. In this case, no distinction between signal and background is made when the observables are calculated. The results of this method with the extracted values are displayed in Fig. 5.9. Two different samples are shown here: $P_\Lambda = 0\%$ and 6% as an input polarization of the Λ hyperons. Clearly, the input polarization is successfully reconstructed as within statistical uncertainties the results are consistent. An interesting effect can be observed as a function of the invariant mass: in the right panel of Fig. 5.9 the averaged component $\langle \sin(\Delta\phi_p^*) \rangle_{\text{TOT}}$ is not fluctuating around zero at regions of the invariant mass where the background is dominating. Instead, a non-zero background correlation appears which is approximately half as large as the signal value. This background correlation is not present when no input polarization was implemented as shown in the left panel of Fig. 5.9. This leads to the conclusion that the background correlation observed in the experimental data is related to the initial polarization of the Λ hyperons.

Several sets of simulated data have been generated with varying initial polarization. In the left panel of Fig. 5.10, the outcome of the polarization analysis, after all cuts applied, is displayed. Plotting only the true reconstructed Λ hyperons as a function of $\Delta\phi_p^*$ always yields the input polarization with is confirmed by the blue points. The red points show the results extracted by the invariant mass fit method which are also consistent with the input polarization taking into account statistical uncertainties. There is a small offset at very high polarization of $P = 12\%$ but this is not significant. Interesting is the trend indicated by the green points which represent the background correlation again extracted from the invariant mass fit method. The correlation to the polarized Λ hyperons is clearly visible as the increase follows the increasing input polarization, however with a smaller magnitude.

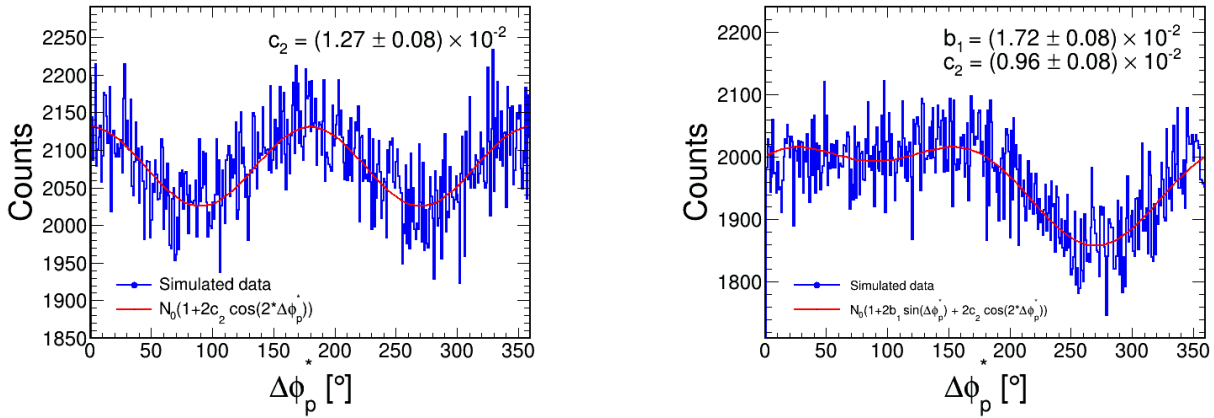


Figure 5.8: Distribution of the polarization angle for different input polarization implemented to Pluto events and after all particle selections applied. For both samples an integrated flow pattern of $\nu_1 = -0.1$ and $\nu_2 = -0.06$ has been implemented for all particles. An input polarization of $P_\Lambda = 0\%$ (left) and $P_\Lambda = 6\%$ (right) has been used. In both cases the reconstructed values are consistent with the input.

To check the origin of the background correlation the different daughter combinations can be removed from the sample. The remaining distribution of $\langle \sin(\Delta\phi_p^*) \rangle_{\text{TOT}}$ as a function of the invariant mass quantifies the contribution to the background correlation in comparison to the complete data sample. Referring to Tab. 5.2, the main contributions to the background are pure combinations of primary particles and primary protons combined with negatively charged pions originating from a Λ decay. Fig. 5.11 shows two reduced samples for an input polarization of $P = 6\%$: once all protons related to a Λ hyperon are removed (left panel) and once all pions related to a Λ hyperon are removed. Since in both cases all true Λ s are also removed, the signal is removed and thus only the linear background shape is fit to extract the background polarization. In the former case, this correlation is slightly reduced, but still significantly non-zero. However, if all the pions originating from a Λ hyperon are removed, the remaining background correlation vanishes. Therefore, the conclusion is that the background correlation found in the experimental data can be attributed to a correlated background source, when pions from a polarized Λ hyperon are paired with primary protons, which are among the most abandoned particles and therefore the chance of such a combination is high. In that case the contribution to $\langle \sin(\Delta\phi_p^*) \rangle_{\text{TOT}}$ is comparable to the true signal value, but since there is no real physical correlation between the two daughters, their invariant mass will not be restricted to the nominal Λ mass, but instead populated over a large range.

To check for possible influence of the missing sector in the Au+Au data, the invariant mass fit method has been used to extract the polarization from a sample with reduced signal-to-background ratio. The results are displayed in the right panel of Fig. 5.10. Starting from the overall sample of simulated Λ hyperons, again with an input polarization of $P = 6\%$, a certain percentage of correctly reconstructed Λ hyperons is removed from the sample. This reduces the amount of signal in the sample, while keeping the background correlation unaffected. Indeed the background correlation does not change, however, as the signal-to-background ratio decreases, the signal extracted from the fit starts to drop to the background value, while the statistical uncertainty is increasing. This goes in the direction of the polarization measurement

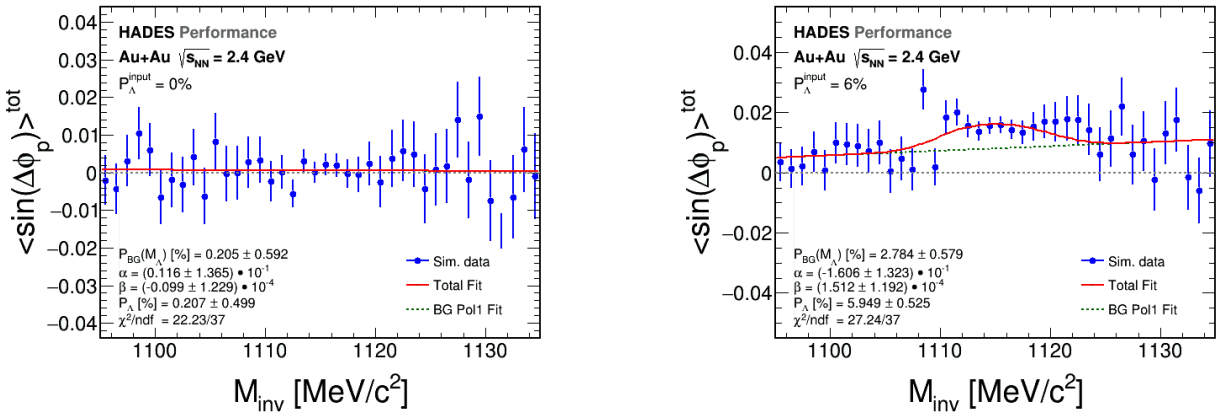


Figure 5.9: Global polarization measurement of simulated Pluto events using the invariant mass fit method for signal extraction after the same selection cuts as in the experimental data have been applied, except for the cut on the discriminant. Different values for the input polarization have been used: $P_\Lambda = 0\%$ (left panel) and $P_\Lambda = 6\%$ (right panel). In both cases the reconstructed signal matches the input polarization within statistical uncertainties.

as extracted from the Au+Au data (see Fig. 4.5). However, the signal-to-background ratio in the experimental data is around $S/B \sim 3 - 5$ which is well in the region where the output polarization matches the input.

The results from the study with multi-differential flow pattern are similar. The left panel of Fig. 5.12 displays the $\Delta\phi_p^*$ distribution of the reconstructed true Λ hyperons. Again, the input polarization is reconstructed within uncertainties and the only other component present is the second even term. Hence the results are qualitatively consistent. This is also underlined from the invariant mass fit method, shown in the right panel of Fig. 5.12. Here again the input polarization is precisely reconstructed. Also the presence of the background correlation could be verified, however, with a smaller magnitude in comparison to the integrated flow results.

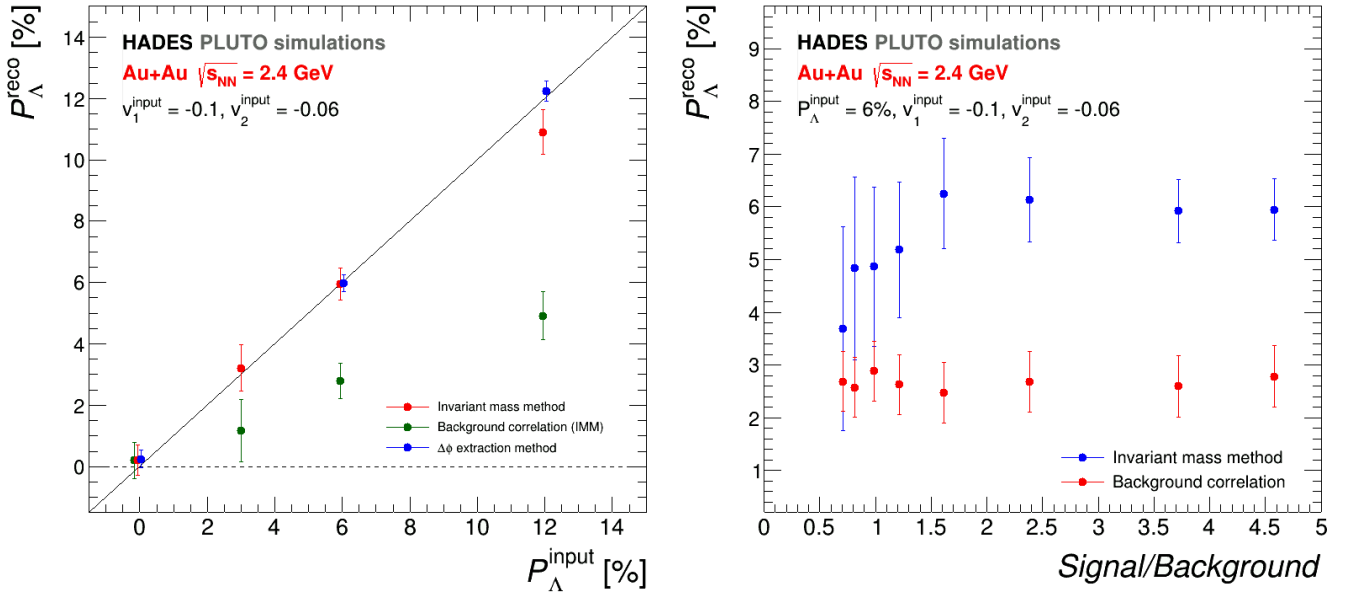


Figure 5.10: Correlation plot of the reconstructed polarization of the Λ hyperons after all selection cuts as in the experimental data have been applied. The analysis has been performed using Pluto events with different input polarization and integrated flow $v_1 = -0.1$ and $v_2 = -0.06$. Left panel: Reconstructed polarization and background correlation for different values of the input polarization. Right panel: Dependence of the extracted signal and background correlation using the invariant mass fit method on the signal-to-background ratio of the sample for a fixed input polarization of $P_\Lambda = 6\%$. The signal-to-background ratio has been changed by skipping only true Λ hyperons, where both daughters have been identified correctly.

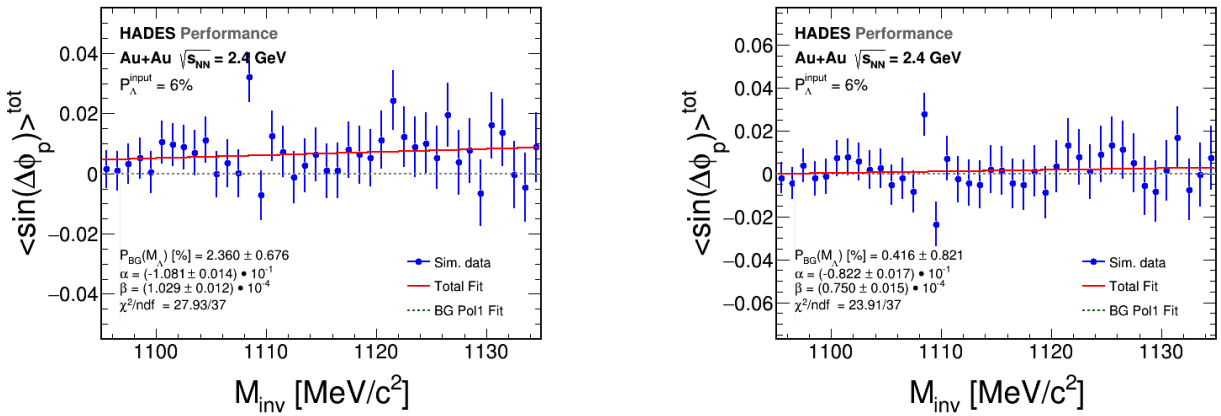


Figure 5.11: Background correlation in simulated Pluto events with input polarization of $P_\Lambda = 6\%$ as determined by the invariant mass fit method. Left panel: all protons originating from a true Λ hyperon have been removed from the sample before the analysis is performed. Right panel: same study but here all pions from a true Λ hyperon have been removed.

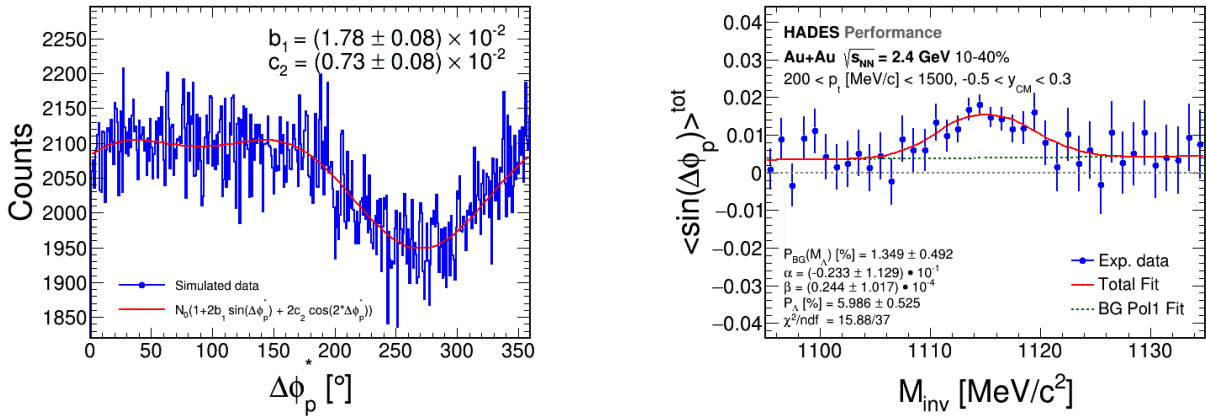


Figure 5.12: Global polarization measurement of simulated Pluto events with an input polarization of $P_\Lambda = 6\%$ and multi-differential flow pattern $v_1(p_t, y)$ and $v_2(p_t, y)$. Left panel: The distribution of $\Delta\phi_p^*$ for true Λ hyperons fit with a Fourier expansion containing only the first odd component and the second even component. From the fit the polarization can be determined to $P_\Lambda = (6.19 \pm 0.28)\%$. Right panel: Results from the invariant mass fit method for signal extraction and background correlation.

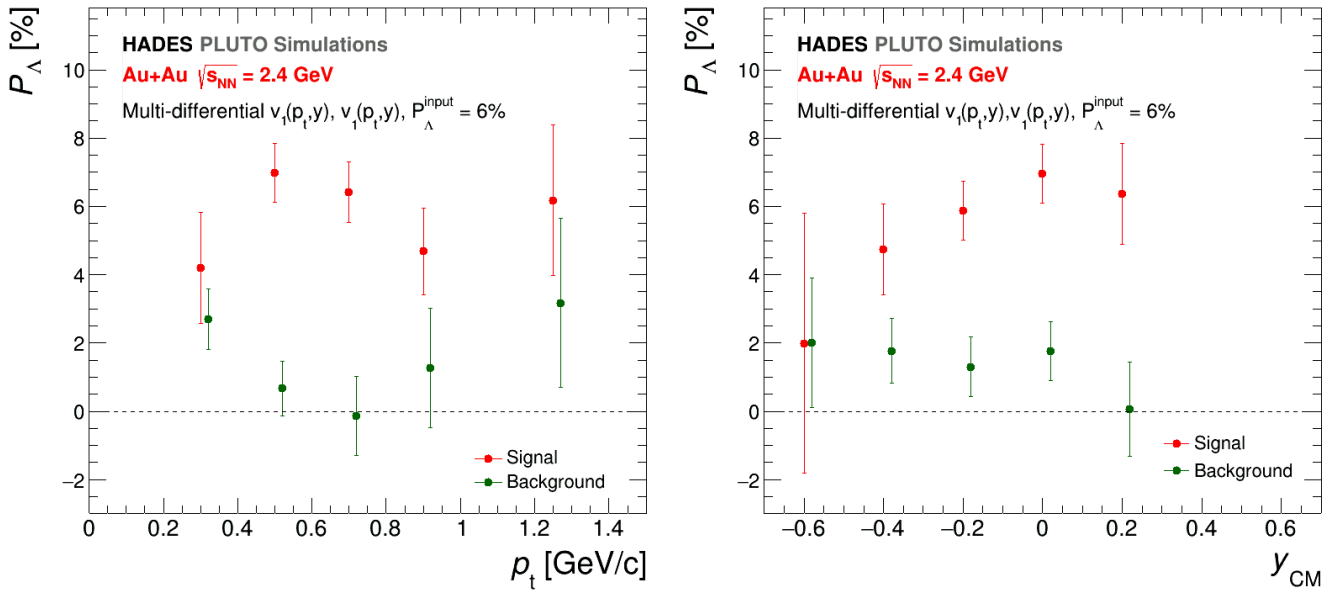


Figure 5.13: Transverse momentum (left) and rapidity (right) dependence of the reconstructed polarization of the Λ hyperons after all selection cuts as in the experimental data have been applied. The analysis has been performed using Pluto events with input polarization $P_\Lambda = 6\%$ and realistic flow pattern $v_1(p_t, y)$ and $v_2(p_t, y)$. The polarization has been extracted using the invariant mass fit method. The signal (red) and the background correlation (green) are shown.

In Fig. 5.13 the results of the invariant mass fit method as a function of the transverse momentum and rapidity are shown. Since the input polarization does not depend on the phase-space region, a possible trend might be related to a correlation to the flow pattern. Concerning the extracted signal, there are some variations from bin to bin, however, they are related to statistical fluctuation. Within the current statistical uncertainties, there is no significant deviation from a constant polarization signal. Concerning the background correlation, the same argument holds. The correlation is nearly constant over the rapidity range. For the transverse momentum dependence, there is a slightly decreasing trend as the combinatorial background fades towards higher p_t , however, this would have to be confirmed for the high momentum range with higher statistics. The important finding is that there is no significant trend introduced to the polarization of the Λ hyperons, which gives the confidence, that within the HADES acceptance, it will be possible to investigate a possible phase-space dependence of the Λ polarization.

Concerning the RDA discussed in Sec. 4.7, the same analysis can be performed using the Pluto setup including flow and polarization. The results are displayed in Fig. 5.14 for two data set with input polarization $P_\Lambda = 6\%$. The difference is that once the flow has been switched off and once the multi-differential flow pattern is introduced. In the former case, the is no significant effect with respect to the R'_V dependence as signal and background correlations are consistent within uncertainties. The situation changes completely if a realistic flow pattern is applied. The background shape as a function of the invariant mass matches qualitatively the measurement from the experimental data, however, the slope is underestimated. More interesting is the effect related to the signal extraction. Similar to the experimental data, the Λ polarization is enhanced in the region of negative R'_V while it is reduced and even reversed for positive values of R'_V .

In comparison to the experimental Au+Au data, both signal values are slightly lower. The difference of the absolute values in the two measurements for $R'_V < 3$ mm and $R'_V > 3$ mm can be calculated to:

$$\delta_{\text{SIM}} = |P_\Lambda^{R'_V < 3} - P_\Lambda^{R'_V > 3}| \approx 11\%. \quad (5.19)$$

This is close to the experimental Au+Au data where the difference is about $\delta_{\text{EXP}} \approx 9\%$ (see Fig. 4.18). For vanishing polarization of the Λ hyperons, the difference is statistically not significant. This suggests that the effect on the polarization signal with respect to R'_V is caused by a global polarization. If this is assumed, one might expect a value measured in the experimental data to be $\sim 20\%$ smaller than in the Pluto simulation. Rescaling the input polarization according to the difference found in the measurement of the Λ polarization with respect to R'_V one finds:

$$P_\Lambda^{\text{input}} \cdot \frac{\delta_{\text{EXP}}}{\delta_{\text{SIM}}} = 6\% \cdot \frac{0.09}{0.11} \approx 4.9\%. \quad (5.20)$$

This is close to the extracted signal in the Au+Au system. However, as the polarization of the Λ hyperons is simulated to be constant over the full phase-space, more differential correlations of polarization and flow are not taken into account.

The most important finding is that even with the strong dependency of the extracted polarization of the Λ hyperons with respect to R'_V , the overall value is well in agreement with the input polarization.

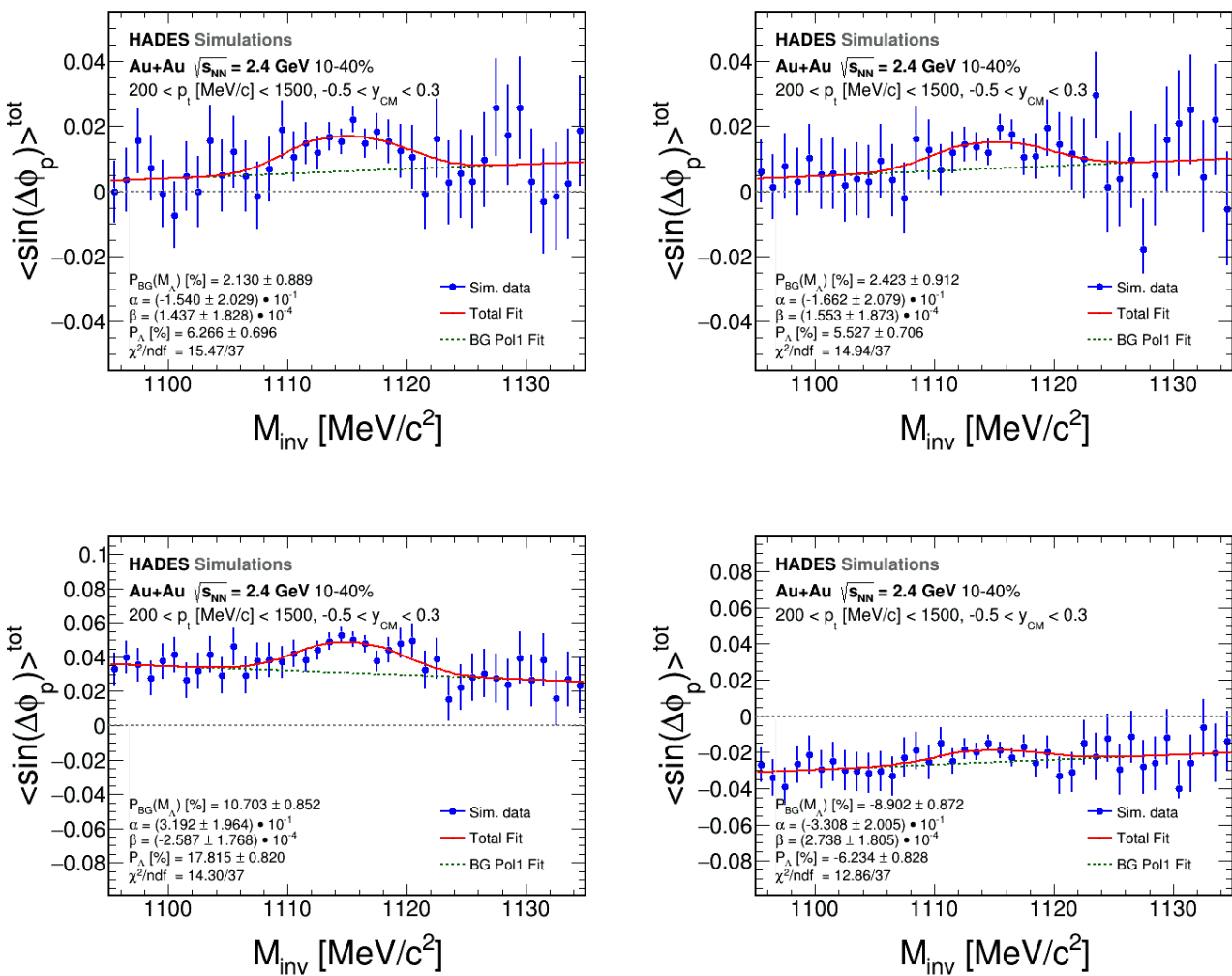


Figure 5.14: Polarization measurement extracted using the invariant mass fit method and depending on the radial distance from the event vertex line of $R'_V < -3$ mm (left column) and $R'_V > 3$ mm (right column). Different Pluto simulations including $P_{\Lambda} = 6\%$ are analyzed with (upper row) and without flow (lower row).

6 Determination of the systematic uncertainties

In this chapter the systematic investigations of the polarization and directed flow measurement will be discussed. In Sec. 6.1, the sources of systematic uncertainties are described as well as the differences for the integrated and differential results. Sec. 6.2 discusses the strategy of how the systematic uncertainties are evaluated including a more detailed discussion on the RDA correction. Sec. 6.3 includes summary tables and a review of the main sources of systematics.

6.1 Sources of systematic uncertainties

The measurement of the observables result in a final value together with a statistical uncertainty. This statistical uncertainty is extracted from a fit to the data and determined from a minimization procedure as described in Ap. 9.3. This procedure takes into account the statistical variations of the individual data points that are fit and thus returns the best fit parameters with their corresponding uncertainties, which are statistical in nature.

Yet there are also other effects that might influence an observable. There might be effects that systematically shift the extracted signal. In this case, the only way to deal with it is to do a careful analysis, identify these effects and apply corrections to get the unaffected result. The correction that fall into this category are:

- **Efficiency correction:**

This correction is applied to account for phase-space dependent reconstruction efficiency (see Sec. 4.6) as the measured observables might also depend on phase-space and when integrating this could be a potential bias. However, there are different approaches to correct for the efficiency and thus this might lead to systematic variation of the result.

- **Radial distance asymmetry correction:**

This correction was derived from the experimental data (see Sec. 4.7) to account for the asymmetric distribution of R'_V and the strong dependence of the polarization measurement on this particular parameter. However, there are several ways to define appropriate corrections and thus systematic variations of the final observables have to be evaluated.

Further systematics that can influence the measurement of the observables are the specific selection criteria which have been applied. As the selection of the decay daughter particles of the Λ hyperon, i.e. the identification of p and π^- , does not include a strong cut in the sample of these particles, the effect is not considered as a systematic. The following selection criteria are evaluated:

- **Pre-selection criteria on the decay topology of the Λ hyperon candidates:**

A specific set of topology parameters is determined for each combination of p and π^- as discussed in Sec. 3.9.4. These parameters are used to distinguish the random combinations from the decay products. As the distribution for signal and background overlap, the topology criteria always reject part of the signal distribution, which might involve a bias to the extracted observables.

- **Selection on the multi-variate analysis (MVA):**

The MVA defines a multi-dimensional map in the space of the topology parameters and the

masses of the particles and is used to select the Λ hyperon candidates used in the analysis (see Sec. 3.9.5). The informations of the MVA are brought into a single parameter, the discriminant $D_{\min}(\text{MVA})$ which is used for the selection.

- **Reduction of multiple counting:**

For the combinations of p and π^- within an event, it is possible that some particles appear in multiple Λ hyperon candidates. This is clearly unphysical and a decision has to be taken which combination is preferred (see Sec. 3.9.6). This can be done using the invariant mass of the MVA and the results obtained with these two approaches are compared.

Another potential bias to the measurement is the method that is used to extract the signal from the data sample used in the analysis, which contains background too. There are several option for the signal extraction with the invariant mass fit method (see Sec. 4.3) which have to be considered:

- **Signal and background determination:**

The signal and background fractions are needed as an input to the invariant mass fit method. They are determined by a fit to the invariant mass distribution. This can be done in two ways, either using the mixed-event technique or applying a direct fit to the same-event data (see Sec. 3.9.7).

- **Invariant mass range of the signal extraction:**

In the invariant mass fit method, the fit to extract the polarization signal (see Eq. 4.11) has to be applied in a wider invariant mass range in order to determine the background correlation in the region where the background fraction is $f_{\text{BG}} \approx 1$. As a linear dependency on the invariant mass is assumed, the background shape can depend on the range used for the fit.

- **Constant background assumption:**

The linear background shape used for the signal extraction in the invariant mass fit method is only motivated from the experimental data. However, as the data points are associated with statistical uncertainties, also different dependence of the background on the invariant mass is possible. Consequently, a constant dependency is tested too.

There is also a second method which can be used to extract the signal:

- **$\Delta\phi$ -extraction method:**

As the method itself might influence the extraction of the signal in a systematic way, the second method is used as a reference to the invariant mass fit method.

Then there are uncertainties in the calculation of the Λ hyperon polarization defined in Eq. 4.5. These are scaling errors that are included into the systematic uncertainty:

- **Event plane resolution correction:**

The determination of the event plane resolution correction R_{EP} (see Sec. 3.6) has a finite resolution which has to be taken into account.

- **Decay parameter:**

The measurement of the decay parameter α_Λ has a statistical uncertainty [Zyl20] which results in a scaling bias of the polarization measurement.

Systematic uncertainties in the differential analysis

For the differential analysis, the data sample is divided into smaller sub-samples resulting in lower statistical significance of the individual subsets. This leads to larger statistical fluctuation as the systematics are evaluated. To avoid an overestimation of the systematic uncertainties, the uncertainties found for the integrated results are taken. Only the sources, that are expected to depend on the differential parameter are re-evaluated in the particular analysis:

- **Efficiency correction:**

The efficiency correction is different for different regions of the phase-space and for different collision centralities. Consequently, the effect for the differential analysis is evaluated in each differential bin separately.

- **Radial distance asymmetry correction:**

The correction for the asymmetry in R'_V might be correlated to the collision centrality but also to the phase-space as different regions have varying signal-to-background ratio.

- **$\Delta\phi$ -extraction method:**

The application of the second method involves a decomposition of the data sample in bins of $\Delta\phi$ for which the amount of signal is determined from the invariant mass distribution. As the determination of the signal depends on the shape of the distribution and the background shape strongly depends on the phase-space region, it is evaluated separately for each bin.

- **Constant background assumption:**

Similar to the $\Delta\phi$ -extraction method, the background shape is important in the invariant mass fit method to determine the background.

- **Event plane resolution correction:**

The event plane resolution R_{EP} has larger uncertainty in the most central events as only few particles reach the Forward Wall and can be used for event plane reconstruction. Consequently, the associated scaling error will be different as a function of the centrality.

6.2 Evaluation of the final systematic uncertainties

The systematic uncertainty can be estimated by varying all possible selections that have been applied and check for the variation of the final observable. These variations can be treated similar to the statistical uncertainties and are combined by a quadratic sum. However, this is not the appropriate procedure as in principle the samples of different settings are highly correlated. To avoid this, one may divide the overall sample into different, independent subsamples and apply the analysis separately. Yet this is not possible for the polarization analysis due to the immense requirement of statistics.

If a cut is tightened, this set of data is completely included in the default sample and thus they are strongly correlated. This also holds in case of more relaxed cuts, just the other way round. A possible variation of the result might be due to a statistical variations only and not related to a systematic effect. In this case, this is already covered by the statistical uncertainty. To identify, whether a variation in the observable is most probably of statistical nature or due to a systematic variation, one can apply the so-called Barlow criterion [Bar02]:

$$B_{\text{crit}} = \frac{|x_{\text{var}} - x_{\text{def}}|}{\sqrt{\sigma_{\text{var}}^2 - \sigma_{\text{def}}^2}}, \quad (6.1)$$

where $x_{\text{def}} \pm \sigma_{\text{def}}$ is the result extracted from the default sample and $x_{\text{var}} \pm \sigma_{\text{var}}$ the result with the variation of a certain cut. Using this criterion allows to decide on a variation taking into account the statistics in the two samples which reflect in the corresponding uncertainties. If $B_{\text{crit}} < 1$, the variation is below the statistical variation and in this case, the corresponding variation is not included into the systematic uncertainty.

The next question arises to: what is a reasonable variation to a specific cut parameter? In this analysis, the variations to the different cut parameters will be applied in a symmetric range around the default value. The maximum variation is determined from the amount of Λ hyperons extracted from the invariant mass distribution. The cuts have been varied until N_{Λ} exceeds a variation of 15 % with respect to the default setting, i.e.

$$\frac{|N_{\Lambda}^{\text{var}} - N_{\Lambda}^{\text{def}}|}{N_{\Lambda}^{\text{def}}} \approx 15\%. \quad (6.2)$$

This ensures a consistent treatment of all the cut parameters and the resulting variations can be compared directly. Within the defined range of variation, a reasonable amount of bins have been set and then the analysis has been performed. By this, one can identify possible correlations or trends of the extracted signal which might give a hint for a further study. If the results just fluctuated around the default value, the Barlow criterion is applied to decide whether this variation is negligible or must be included into the systematic uncertainty.

The variation of cut parameters includes in principle also the PID of the daughter particles. However, the mass cuts used to identify the negatively charged pion and the proton are very widened (see Sec. 3.8) and thus all the systematics are covered by the Λ identification via its decay topology (see Sec. 3.9.4) and the neural network (see Sec. 3.9.5).

Then there are also different systematics related to the method applied to determine the combinatorial background and to extract the signal. In this case, the sample under consideration is identical, however, the results may differ as their corresponding uncertainty. Consequently, the Barlow criterion can be used again to identify the relevant contributions to the systematic uncertainty. The total systematic uncertainty is then calculated by:

$$\Delta_{\text{sys}} = \sqrt{\sum_i \Delta_i^2}, \quad (6.3)$$

where i runs over all the checks that have been performed and that pass the Barlow criterion B_{crit} . For sure there are parameters that are correlated, as the topology parameters, however, the correlation is not taken into account and the contributions are considered uncorrelated in Eq. 6.3.

Systematics on the radial distance asymmetry correction

Instead of the 3 bins weighting that is used to obtain the final results of the Λ polarization, different approaches have been tested to correct for the RDA. One approach was to restrict the values of R'_V to a finite range a and reweight the R'_V distribution to be flat afterwards. In the left panel of Fig. 6.1 the results of this procedure are shown together with an example distribution of the corresponding weights for a range of $a = 12$ mm in the right panel. The distribution of the weights show the necessity to cut on a finite range, as on the boundary they diverge. Together with the polarization measurements, the mean value with the default deviation are plotted by the grey lines. The result of the procedure is very stable, resulting in a small default deviation of the set of data points. The mean value of $\bar{P}_\Lambda \approx 3.2\%$ is larger than the uncorrected, full range value of $P_\Lambda \approx 2.8\%$ (see Fig. 4.7). Hence, the application of this weighting procedure to flatten the distribution of R'_V in an invariant mass range of $1110 \leq M_{\text{inv}}[\text{MeV}/c^2] \leq 1120$ results in a shift of $\Delta P_\Lambda \sim 0.4\%$ consistently for different ranges.

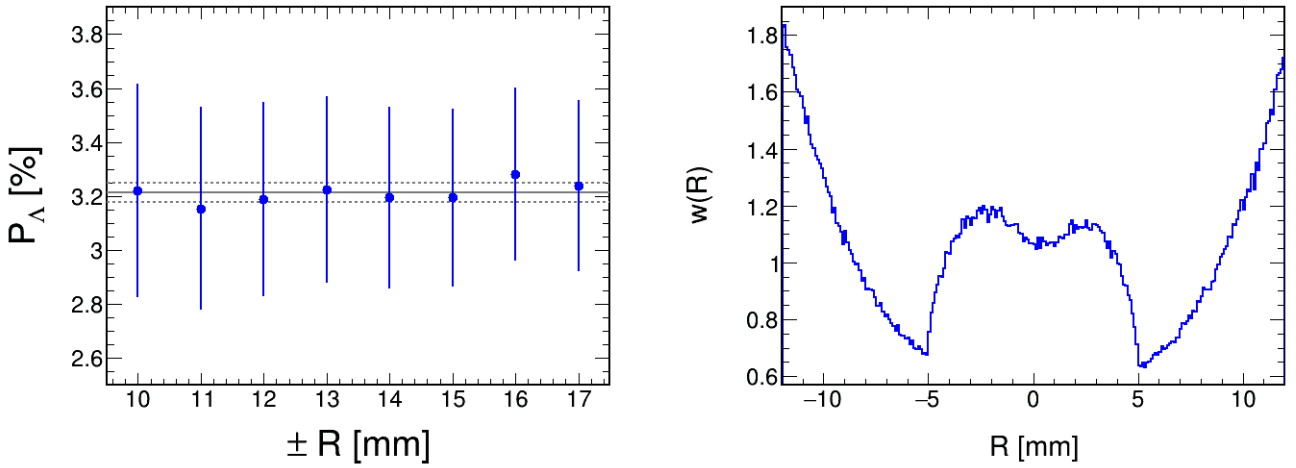


Figure 6.1: Left panel: Results of the extracted polarization signal for different ranges after the R-weighting defined within $1110 \leq M_{\text{inv}}[\text{MeV}/c^2] \leq 1120$ has been applied. The data set has a mean value of $\bar{P}_\Lambda[\%] = 3.212 \pm 0.036$ (grey lines). Right panel: The distribution of the calculated weights for a defined range of $a = 12$ mm.

As a second attempt, the distribution of R'_V can be scanned in small bins, for which the invariant mass distribution is plotted. Then the amount of signal can be determined and plotted again as a function of R'_V . This distribution is shown in the right panel of Fig. 6.2. Then the procedure above can be applied, however, in a more discrete way, since the amount of bins is limited. Since most of the background is sitting close to the event vertex line, i.e. R'_V is small, the shape of the distribution of net Λ hyperons is broadend. Therefore, the range of the weighting procedure can be shifted slightly to higher values. The results for this study are shown in the left panel of Fig. 6.2. In comparison to the first attempt, the fluctuations for different ranges are larger, however, the results are consistent and the mean value is basically unchanged. Hence, also with this solely signal driven correction, the effect to the final result is again a shift of $\Delta P_\Lambda \sim 0.4\%$. There are some disadvantages using such a correction procedure as described above. First, due to the necessity of a finite range to keep the weights in a reasonable range of the order

$w(R'_V) \sim 1$, the statistical significance of the sample is reduced. To give some number for the largest range, the signal sums up to $\sim 90\%$ of the overall Λ hyperons, while for the lowest range the sample is reduced to $\sim 60\%$. This is solely due to the range cut applied. It has been checked that the range cut itself does not influence the polarization measurement, but the signal reduction is significant and should be avoided.

Second, the aim of this approach is to correct the polarization measurement from the bias that is introduced due to the asymmetry in R'_V . Thus the corrected distribution should be symmetric, but the actual procedure is flattening the distribution completely. This might potentially cause some effect at the boundaries, especially for high $|R'_V|$ where the polarization magnitude is largest. These regions have the largest weights (see right panel of Fig. 6.1) and small statistical fluctuations might artificially influence the final result. This applies even more to the differential study of the polarization analysis, where the overall statistics is subdivided into much smaller samples.

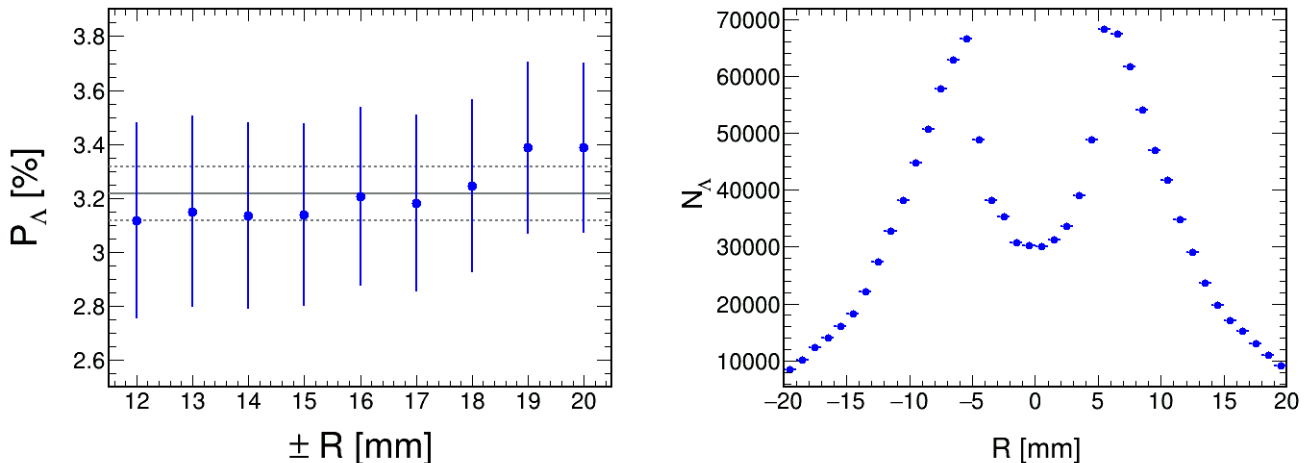


Figure 6.2: Left panel: Results of the extracted polarization signal for different ranges after the R -weighting defined only from true Λ hyperons has been applied. The data set has a mean value of $\bar{P}_\Lambda[\%] = 3.216 \pm 0.099$ (grey lines). Right panel: Signal distribution as extracted from the invariant mass distribution as a function of the radial distance to the event vertex line.

Therefore, the procedure of the 3 bin weighting according to the extracted amount of signal is used. As all the different approaches lead to consistent results, the strategy to estimate the systematic uncertainty introduced by the correction is as follows: the 3 bin signal weighting is restricted to ranges a similar to the left panel of Fig. 6.2. Then the 3 bin weights are updated within a given range and the procedure described in Sec. 4.7 is applied. This has the advantage, that it can be consistently applied also to the differential analysis where some bins have limited statistics. The variation found with varying range a with respect to the full range result are taken as systematic uncertainties and treated as described above.

For the extraction of the directed flow of the Λ hyperons, the same study has been performed. In Fig. 6.3 the results of the invariant mass fit method for $-0.35 < y_{CM} < -0.25$ are shown in two different regions of R'_V . In contrast to the polarization, the directed flow is an even function of R'_V and the extracted signal values are comparable in magnitude and have the same sign. The

difference between the two results is small and as they are combined to the overall result, the effect of applying the RDA correction is negligible. Consequently, the RDA correction is not used in the flow measurement.

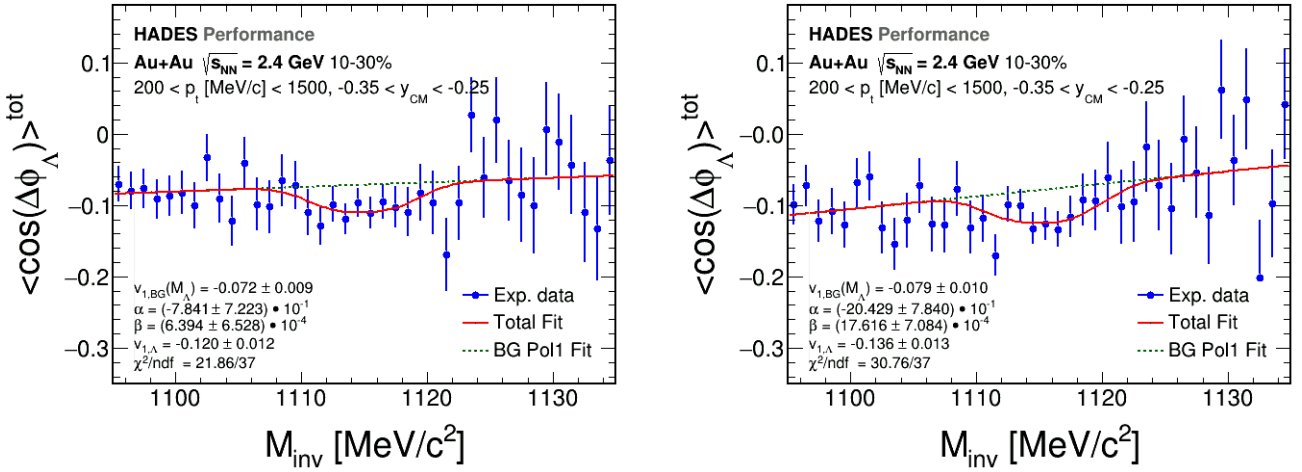


Figure 6.3: Measurement of the directed flow using the invariant mass fit method as a function of the radial distance asymmetry in Au+Au collisions at $\sqrt{s_{\text{NN}}} = 2.4 \text{ GeV}$ for $-0.35 < y_{\text{CM}} < -0.25$. Two different regions of $R'_V > 3 \text{ mm}$ and $R'_V < -3 \text{ mm}$ are shown.

6.3 Evaluation of the systematic uncertainties and summary tables

In this section, the summary tables and a discussion of the main sources of the systematic uncertainties will be discussed.

6.3.1 Global polarization measurement in Ag+Ag

The variations with the decay topology parameters are shown in Fig. 6.4. For $D_{\text{min}}(\text{MVA})$ and d_3 the Barlow criterion is consistently below unity such that both do not contribute to the overall systematic uncertainty. For d_ν , d_1 and d_t the variations are statistically significant, but the deviation from the default result is small. The main contribution to the systematic uncertainty comes from the variation of d_2 . For d_2 (and also d_3), the RDA weights are updated for each specific value of the cut (see Sec. 4.7 for details). For d_2 the value of the extracted polarization decreases slightly as the cut is relaxed, i.e. if d_2 is smaller. The maximum deviation from the default result is found to be $\Delta_{\text{sys}}^{d_2} = \pm 0.237$ which corresponds to a relative uncertainty of $\Delta_{\text{sys}}^{d_2}/P_\Lambda = 7.5\%$.

Further studies as the determination of the signal and background using the same-event fit to the invariant mass distribution, varying the fit range for the signal extraction and changing the selection of the best pair according to the discriminant (see Sec. 3.9.6) are not passing the Barlow criterion and are rejected. This also holds for the effect of the efficiency correction which is negligible. The polarization fit assuming constant background passes the Barlow criterion, however, the contribution to the overall systematics is small compared to the main sources.

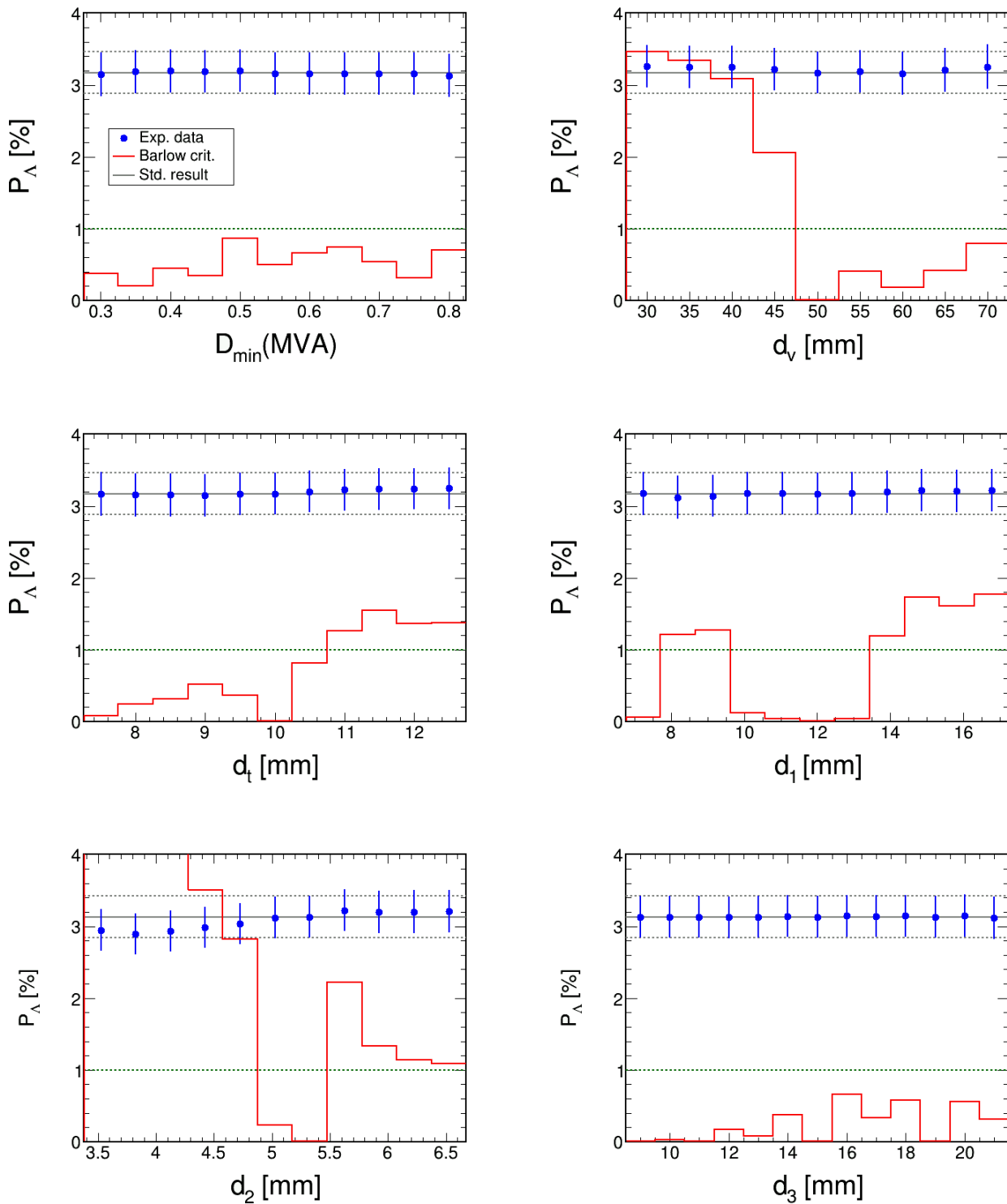


Figure 6.4: Λ polarization in $\text{Ag}+\text{Ag}$ collisions at $\sqrt{s_{NN}} = 2.55 \text{ GeV}$ depending on the individual topology parameters (blue points). The default result is shown too (grey line). The ranges have been adjusted to a maximum variation of 15 % in the Λ yield. A variation is considered relevant and enters the systematic uncertainty if the Barlow criterion [Bar02] is beyond $B_{\text{crit}} = 1$ (red line).

Two scaling uncertainties are also included, the 2% variation of the decay parameter α_Λ and the event plane resolution uncertainty of $\Delta R_{EP} = 5\%$ as estimated in [Mam20a].

Using the $\Delta\phi$ -extraction method for comparison, the polarization value is well in agreement within statistical uncertainties. Fig. 6.5 displays the results for 30 bins in $\Delta\phi_p^*$. In the left panel, only the first order harmonics have been fit while in the right panel, the fit is performed up to the third order. As can be seen, the impact on the parameter b_1 , used to calculate the polarization, is not significant. The only non-vanishing components are the first odd, i.e. b_1 , and the first and second even harmonics, i.e. c_1 and c_2 . Higher order harmonics in the distribution are found to be consistent with zero, as long as the period of the harmonic is larger than the bin width of the distribution. In the latter case, the fit would start to pick up the bin-to-bin fluctuations and thus the extracted values will not have any physical meaning.

The comparison of the two methods using different amount of bins for the $\Delta\phi$ -extraction method is shown in the left panel of Fig. 6.6. As discussed in Sec. 4.2 and 6.3.2, the results of both methods are not corrected for the finite resolution of the event plane reconstruction for this particular comparison. Again, both methods deliver consistent results, except for the statistical uncertainty, which is notably smaller in the $\Delta\phi$ -extraction method. Since there the statistical uncertainty is not significantly affected, neither by a change in the amount of bins, nor by a change in the fit order of the Fourier decomposition, the invariant mass fit method will be taken as a reference for the final results. Another consequence of the difference of the statistical uncertainties in the two methods is that the Barlow criterion is scaled down. Nevertheless, as the variations of the value itself are small, the difference between the methods does not enter the total systematic uncertainty.

The systematic effect of the RDA correction is shown in the right panel of Fig. 6.6. The polarization decreases slowly as the range of R'_V is restricted, even when the weights are always updated to the current setting. The Barlow criterion is consistently below one, meaning that the variations are not significant beyond statistical uncertainties.

A summary of all the systematic checks that have been performed together with the maximum variation with respect to the default result can be found in Tab. 6.1. All contributions, that pass the Barlow criterion are added quadratically to result in the overall systematic uncertainty for the polarization measurement in Ag+Ag to be $\Delta_{sys}^{total} = 0.319$, which is of the same order as the statistical uncertainty.

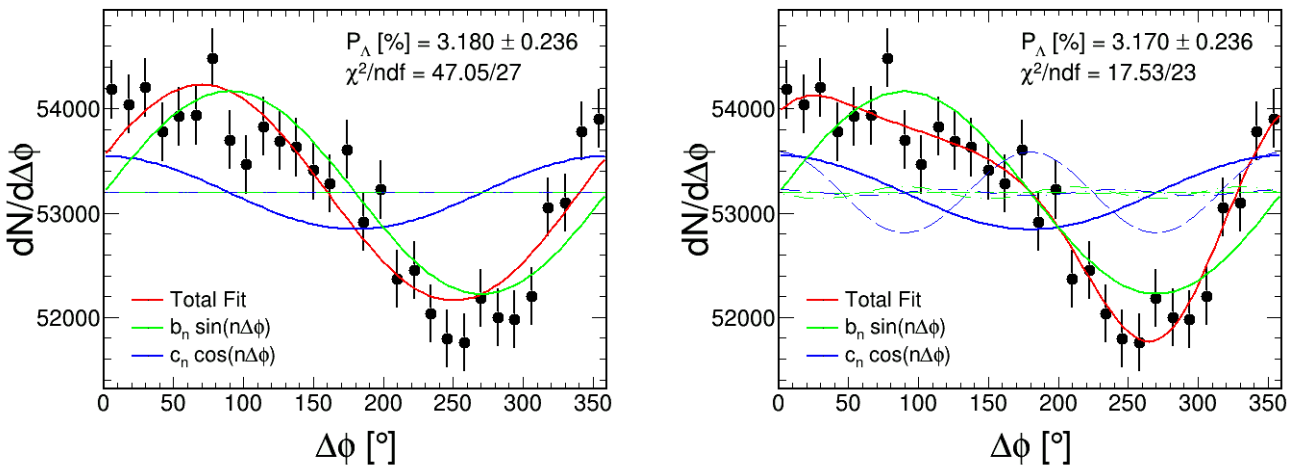


Figure 6.5: Distribution of the net Λ counts as a function of $\Delta\phi_p^*$ in Ag+Ag collisions at $\sqrt{s_{NN}} = 2.55$ GeV. The distributions have been fit with a Fourier decomposition of first (left) and third order (right) to extract the first odd harmonic coefficient b_1 from which the polarization is calculated. The solid lines represent the first harmonics, the dashed lines the second and the dashed and dotted lines indicate the strength of the third harmonics.

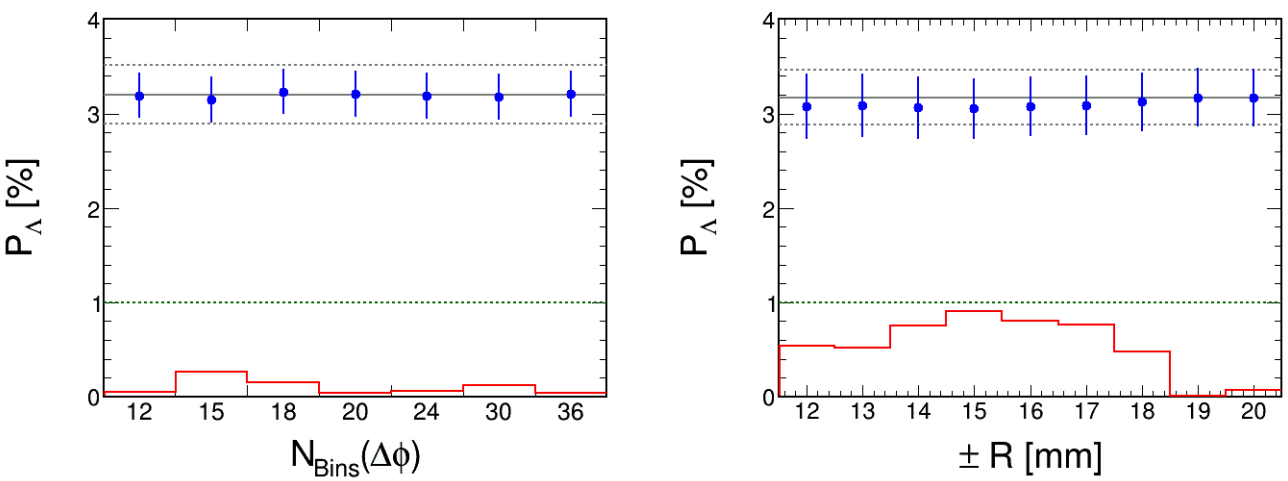


Figure 6.6: Systematic investigation of the $\Delta\phi$ -extraction method with different amount of bins in $\Delta\phi$ (left) and the radial distance asymmetry for different ranges (right) in the Λ polarization measurement in Ag+Ag collisions at $\sqrt{s_{NN}} = 2.55$ GeV. The red line displays the Barlow criterion which is found to be $B_{\text{crit}} < 1$ in all cases such that the variations are neglected and not included to the overall systematics. The grey solid line indicates the value extracted from the invariant mass fit method while the grey dashed lines mark the statistical uncertainty.

Systematic on P_Λ [%]	Au+Au@1.23 AGeV			Ag+Ag@1.58 AGeV		
	Absolute	Relative	B_{crit}	Absolute	Relative	B_{crit}
D_{\min} (MVA)	± 0.553	$\pm 11.9\%$	✓	± 0.042	$\pm 1.3\%$	✗
d_ν	± 0.301	$\pm 6.5\%$	✓	± 0.084	$\pm 2.6\%$	✓
d_1	± 0.263	$\pm 5.7\%$	✓	± 0.051	$\pm 1.6\%$	✓
d_2	± 0.672	$\pm 14.6\%$	✓	± 0.237	$\pm 7.5\%$	✓
d_3	± 0.233	$\pm 5.0\%$	✓	± 0.019	$\pm 0.6\%$	✗
d_t	± 0.341	$\pm 7.4\%$	✓	± 0.074	$\pm 2.3\%$	✓
Best D_{\min} (MVA)	± 0.005	$\pm 0.1\%$	✗	± 0.013	$\pm 0.4\%$	✗
Same-event mass fit	± 0.000	$\pm 0.0\%$	✗	± 0.023	$\pm 0.7\%$	✗
Fit range	± 0.102	$\pm 2.2\%$	✗	± 0.032	$\pm 1.0\%$	✗
Pol0 BG fit	± 0.088	$\pm 1.9\%$	✗	± 0.035	$\pm 1.1\%$	✓
Efficiency	± 0.611	$\pm 13.3\%$	✓	± 0.053	$\pm 1.7\%$	✗
$\Delta\phi$ method	± 0.253	$\pm 5.5\%$	✗	± 0.053	$\pm 1.7\%$	✗
R_{EP}	± 0.138	$\pm 3.0\%$	✓	± 0.159	$\pm 5.0\%$	✓
α_Λ	± 0.094	$\pm 2.0\%$	✓	± 0.063	$\pm 2.0\%$	✓
RDA	± 0.686	$\pm 14.9\%$	✗	± 0.121	$\pm 3.8\%$	✗
$\Delta_{\text{sys}}^{\text{total}}$	± 1.220	$\pm 26.5\%$	-	± 0.319	$\pm 10.1\%$	-

Table 6.1: Summary of the systematic uncertainties in the polarization measurement for Au+Au and Ag+Ag. The Barlow criterion [Bar02] has been applied to decide whether a variation is beyond statistical fluctuations. Only in this particular case, the variation is included in the quadratic sum resulting in the overall systematic uncertainty $\Delta_{\text{sys}}^{\text{total}}$.

Centrality dependence

The high statistics data sample collected in Ag+Ag collisions at $\sqrt{s_{NN}} = 2.55$ GeV allows to perform a differential analysis of the global polarization of the Λ hyperons. For the centrality dependent analysis, the results are shown in Fig. 6.7 and 6.8. They have been obtained by applying the same procedure as for the integrated result.

In the differential analysis, the sample is subdivided such that the statistical significance of each subsample is reduced compared to the complete data set. The subdivision is usually not uniform. To estimate the systematic uncertainty for the individual bins, most of the systematic uncertainties are propagated from the measurement of the integrated value, i.e. the results in Tab. 6.1. This is to avoid an overestimation of the systematic uncertainty by fluctuations under variation of a certain cut parameter which are expected to be larger, but statistical in nature. This holds for all the parameters, which are not expected to show a specific dependence on the collision centrality. Then the relative variations are taken and applied to each different centrality bin. To complete the systematics, there are also some checks that have been performed separately for each centrality bin. One is the effect of the efficiency correction. As it is applied phase-space dependent for the integrated centrality range, the efficiency map will be the same for each centrality bin. However, the polarization as a function of the phase-space might be varying for different centrality and thus the relative correction might be different. To take such an effect into account, the effect of the efficiency correction has been studied in each centrality bin and found to be statistically important only in the 10 – 20 % and 30 – 40 % centrality bin.

As the signal-to-background ratio changes significantly with the collision centrality as shown in Fig. 6.7 and 6.8, the comparison to the $\Delta\phi$ -extraction method has been performed for each individual centrality bin but found to be below statistical fluctuations and consequently, it is neglected.

Another important check to be done differentially, is the systematic of the RDA correction, as a correlation to physical variables cannot be excluded. Hence the range R'_V has been varied and the polarization measurement has been performed with updated weights. The effect has been found to be beyond statistical variations only in the 0 – 10% and 20 – 30% centrality bin.

Finally, the precision of the event plane reconstruction procedure depends on the amount of spectators reaching the Forward Wall. As in the central collisions, most particles are participants while for peripheral collisions there are more spectators, the accuracy of the event plane reconstruction is much higher in peripheral events. To take this effect into account, the uncertainty in the event plane resolution is estimated separately for each centrality bin. From the study presented in [Mam20a], the uncertainty has been estimated to be 15 % in the most central bin while decreasing to 3 % in the most peripheral bin. The precise values are displayed in Tab. 6.2 together with the other centrality dependent systematic studies. The overall uncertainties are determined from a quadratic sum, explicitly including the variations from the integrated polarization measurement that have been considered independent on the collision centrality.

Systematics on P_Λ [%] Centrality	0 – 10 %		10 – 20 %		20 – 30 %		30 – 40 %	
	ΔP_Λ [%]	B_{crit}						
Efficiency	± 0.012	✗	± 0.159	✓	± 0.023	✗	± 0.474	✓
$\Delta\phi$ method	± 0.176	✗	± 0.070	✗	± 0.096	✗	± 0.319	✗
R_{EP}	± 0.129	✓	± 0.151	✓	± 0.196	✓	± 0.167	✓
RDA	± 0.364	✓	± 0.058	✗	± 0.280	✓	± 0.268	✗
$\Delta_{\text{sys}}^{\text{total}}$	± 0.393	-	± 0.256	-	± 0.484	-	± 0.698	-

Table 6.2: Summary of the systematic uncertainties in the polarization measurement for Ag+Ag as a function of the collision centrality. The Barlow criterion [Bar02] has been applied to decide whether a variation is beyond statistical fluctuations. Only in this particular case, the variation is included in the quadratic sum resulting in the overall systematic uncertainty $\Delta_{\text{sys}}^{\text{total}}$. The dependence on other parameters not listed here are taken from Tab. 6.1. For the event plane resolution correction, the uncertainties vary from the central to the peripheral bin by: 15 %, 10 %, 5 %, 3 %.

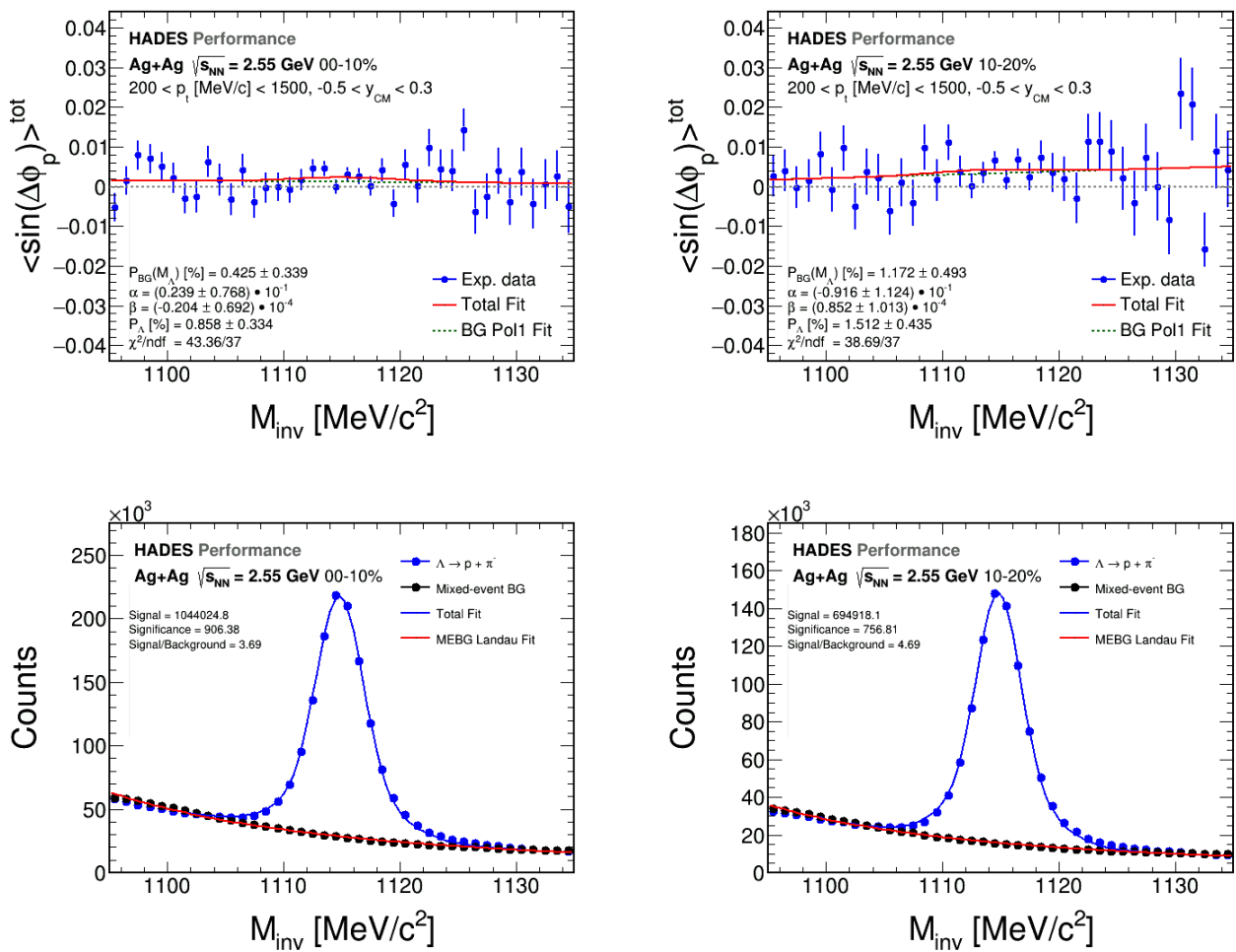


Figure 6.7: Centrality dependent polarization measurement for 0 – 20 % centrality. Upper row: signal extraction using the invariant mass fit method. Lower row: corresponding distribution of the invariant mass.

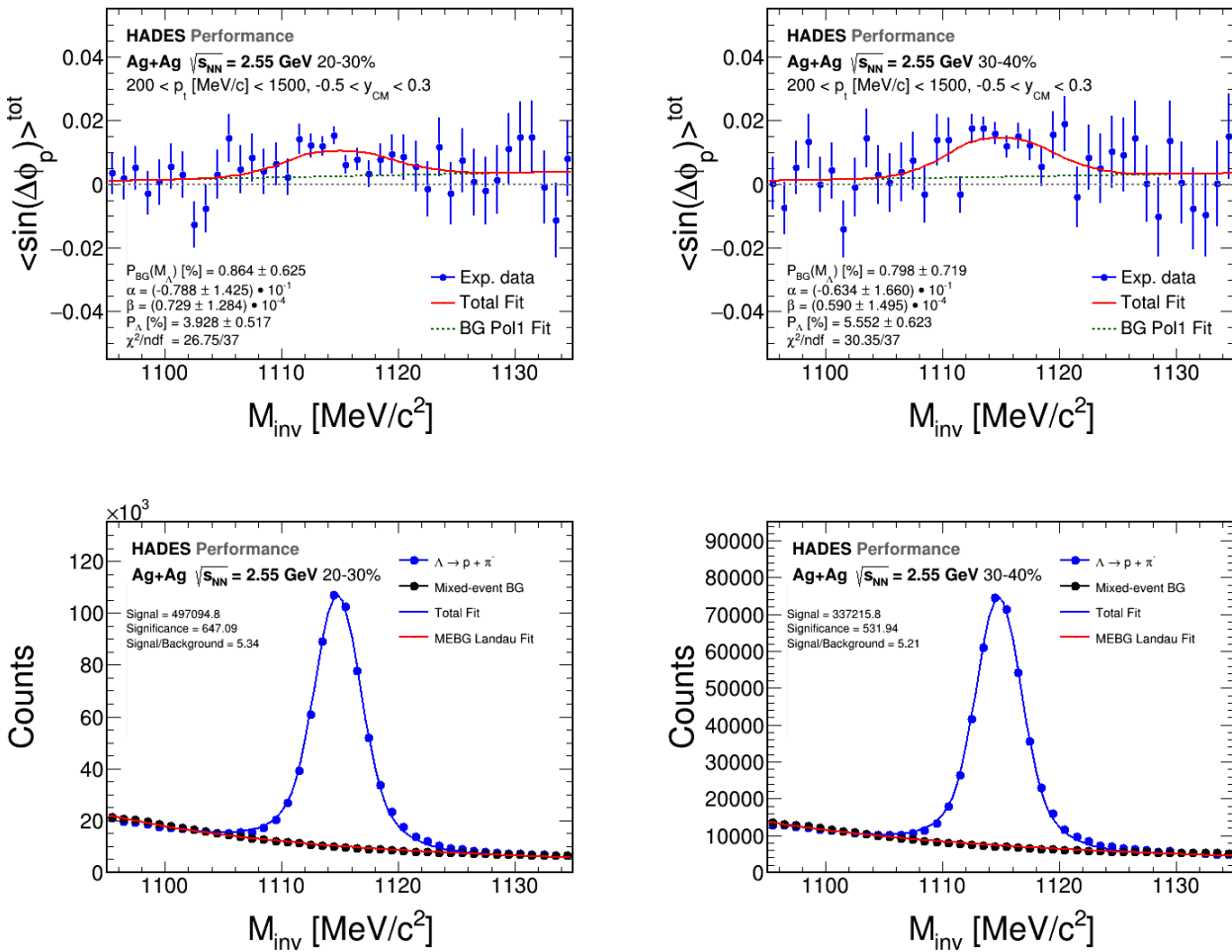


Figure 6.8: Centrality dependent polarization measurement for 20–40 % centrality. Upper row: signal extraction using the invariant mass fit method. Lower row: corresponding distribution of the invariant mass.

Phase-space dependence

Similarly to the centrality dependent study, the procedure is applied also for the phase-space dependent polarization measurement. Due to the high statistics requirement, the analysis will only be done for Ag+Ag collisions at $\sqrt{s_{NN}} = 2.55$ GeV and only differentially in one parameter. Hence for the rapidity dependence, the results are integrated in transverse momentum and vice versa. Additionally, for each of the corresponding region in the phase-space, the efficiency matrix is recalculated as described in Sec. 4.6 to ensure a relative weighting within each bin separately.

The results of the invariant mass fit method as a function of rapidity are shown in Fig. 6.9 and 6.10. Looking to the invariant mass distributions, the background is populating mostly at the backward rapidities. The Λ hyperons are mainly produced at slightly backward rapidities and spread symmetrically over the whole range. As a consequence, the signal-to-background ratio is poor in the backward region while the mid- and forward bins are clearly dominated by the signal. In addition, the shape of the background changes significantly, since the backward region is populated by a lot of combinatorial background, while the forward regions show more

correlated background of Λ decay products wrongly matched to primary particles and therefore the main background contribution to the invariant mass distributions in Fig. 6.10 shifts towards the nominal Λ mass.

The different behavior of the background also reflects in the polarization measurement displayed in Fig. 6.9. At the most backward rapidities, where the combinatorial background is dominating, the background correlation is found to be consistent with zero or even slightly negative within statistical uncertainties. The more the signal starts to dominate the distribution, the background correlation enhances. The maximum value is found in the most forward rapidity bin, consistent with the measured value of the signal itself. This supports the conclusion drawn in Ch. 5 that the non-zero background correlation is caused by a source correlated with the polarized Λ hyperons themselves, i.e. from mismatched decay products from polarized Λ hyperons with uncorrelated particles, mostly primaries.

The polarization measurement has been performed also as a function of the transverse momentum, integrated over rapidity. The results from the invariant mass fit method are shown in Fig. 6.11 and the corresponding distributions of the invariant mass in Fig. 6.12. In principle, the same conclusions as for the rapidity differential results can be drawn, however, the differences between low to high p_t are not as prominent as for backward to forward rapidities (see Fig. 4.12). At the low transverse momentum, there is the largest contribution from the background, i.e. mostly of combinatorial origin. Consequently, the background correlation is found consistent with zero and clearly distinguishable from the signal contribution which is found significantly non-zero for all the different transverse momentum bins. Towards higher transverse momenta, the background correlation increases up to $p_t \sim 1 \text{ GeV}/c$ where the magnitude actually matches the signal value. At the very high transverse momenta, the statistics gets very small, making it necessary to extend the bin width to get an analyzable distribution. Due to this, the bin-to-bin fluctuations are larger, resulting in a larger statistical uncertainty extracted from the fit.

For the estimation of the systematic uncertainties, the event plane resolution, which is now constant for all phase-space bins, is taken from the integrated result. Instead, the fit assuming a constant polarization of the background in $\langle \sin(\Delta\phi_p^*) \rangle_{\text{TOT}}$ is performed for each phase-space bin separately. This is due to the fact that the background shape strongly depends on the phase-space region (see Fig. 6.10) and therefore the variation with respect to the linear background assumption might differ from bin-to-bin. As it turned out, none of the results extracted using the constant background assumption passes the Barlow criterion and consequently it is neglected for the determination of the systematic uncertainties. The systematic uncertainties are of similar magnitude, comparable to the statistical uncertainties. The largest systematic is observed in the most backward rapidity, i.e. $-0.7 < y_{CM} < -0.5$, and the low transverse momentum bin, i.e. $200 < p_t [\text{MeV}/c] < 400$. These are the bins which are dominated by background which seem to have a strong influence on the RDA correction. The summary of all the systematic investigations and the overall uncertainty is given in Tab. 6.3 for the rapidity and in Tab. 6.4 dependent results.

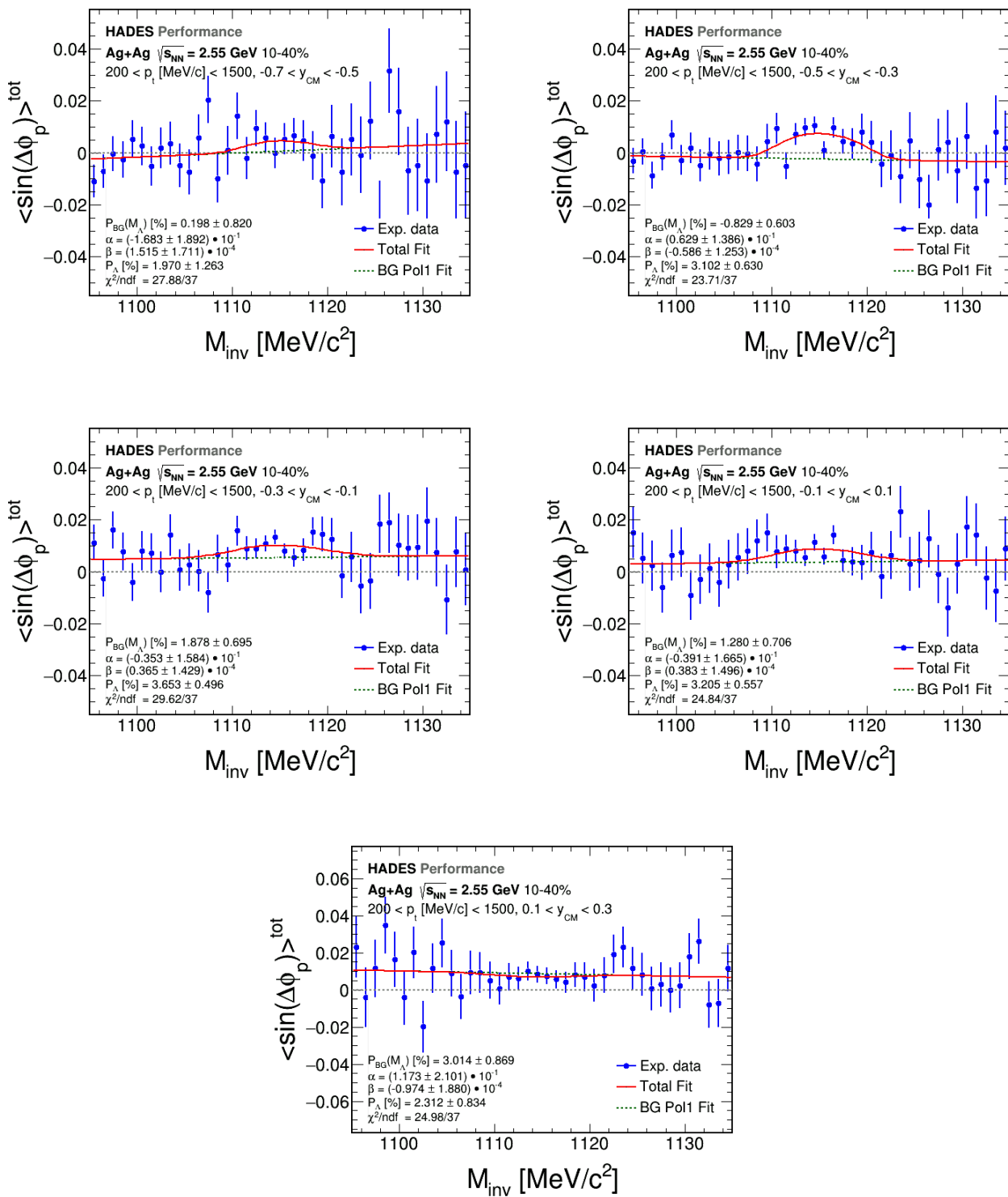


Figure 6.9: Polarization measurement in Ag+Ag collisions at $\sqrt{s_{NN}} = 2.55 \text{ GeV}$ for different bins in rapidity integrated in transverse momentum.

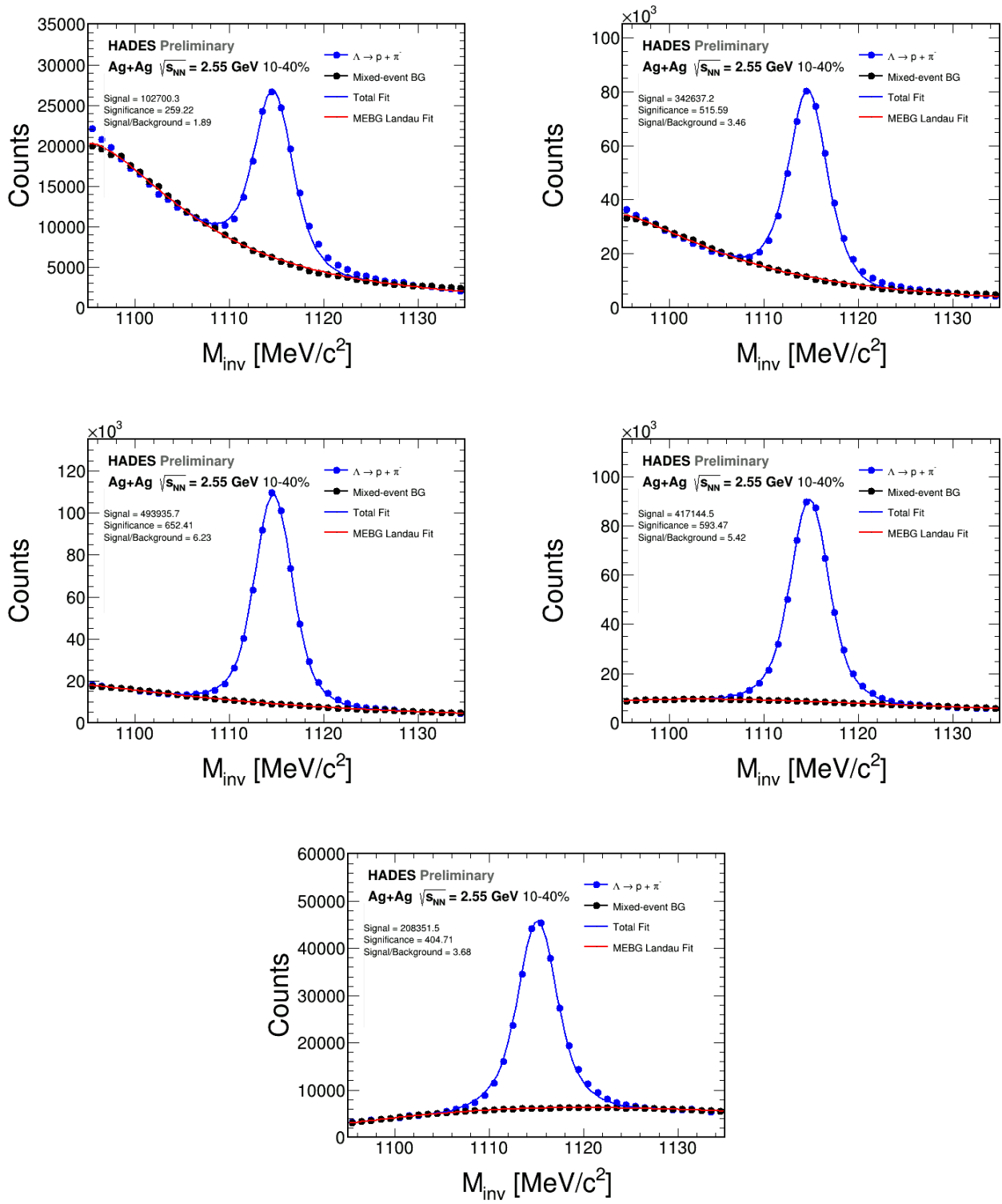


Figure 6.10: Invariant mass distributions in $\text{Ag} + \text{Ag}$ collisions at $\sqrt{s_{\text{NN}}} = 2.55 \text{ GeV}$ for different bins in rapidity integrated in the transverse momentum. From left to right and top to bottom: $-0.7 < y_{\text{CM}} < -0.5$, $-0.5 < y_{\text{CM}} < -0.3$, $-0.3 < y_{\text{CM}} < -0.1$, $-0.1 < y_{\text{CM}} < 0.1$, $0.1 < y_{\text{CM}} < 0.3$.

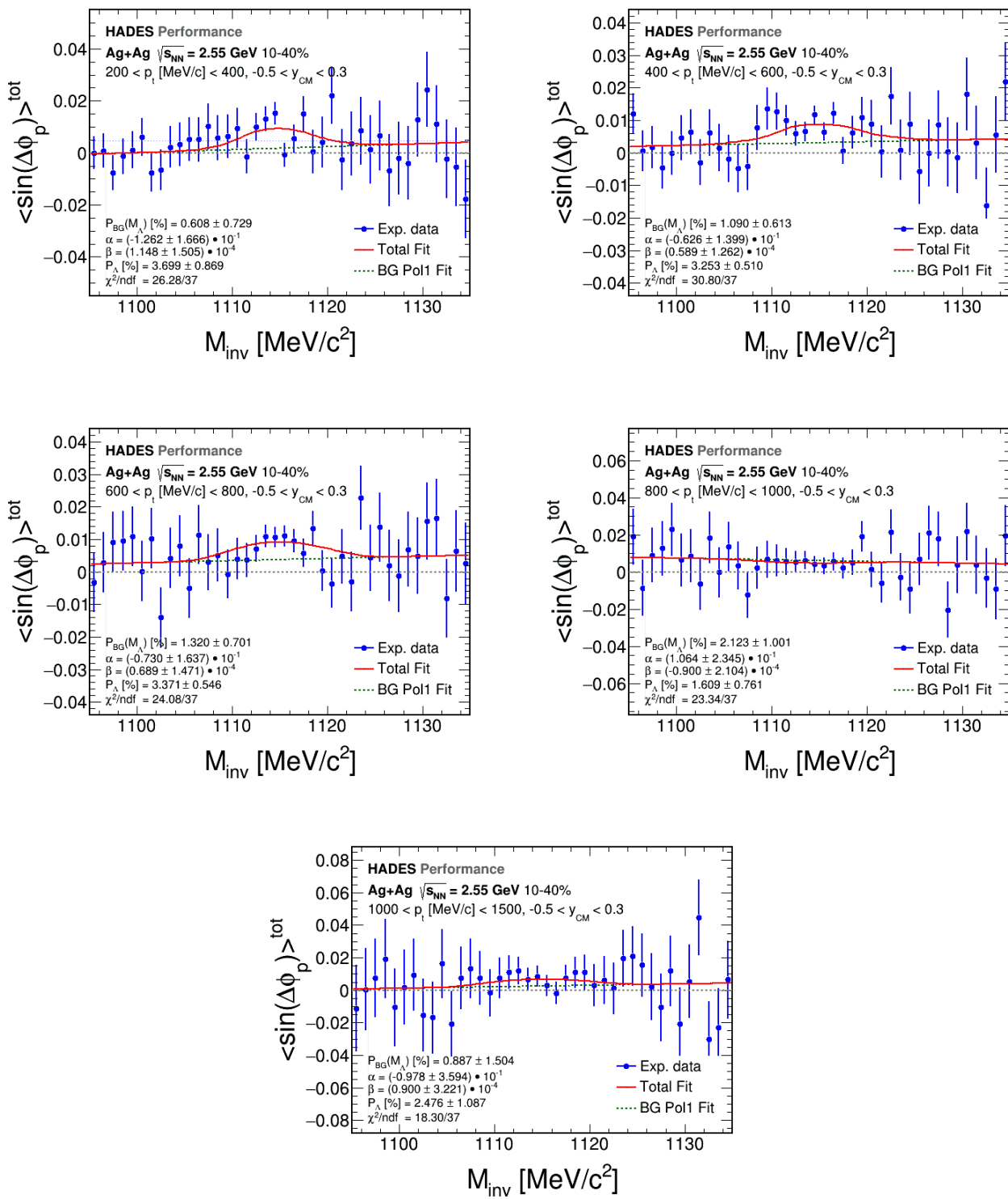


Figure 6.11: Polarization measurement in Ag+Ag collisions at $\sqrt{s_{\text{NN}}} = 2.55 \text{ GeV}$ for different bins in transverse momentum integrated over rapidity.

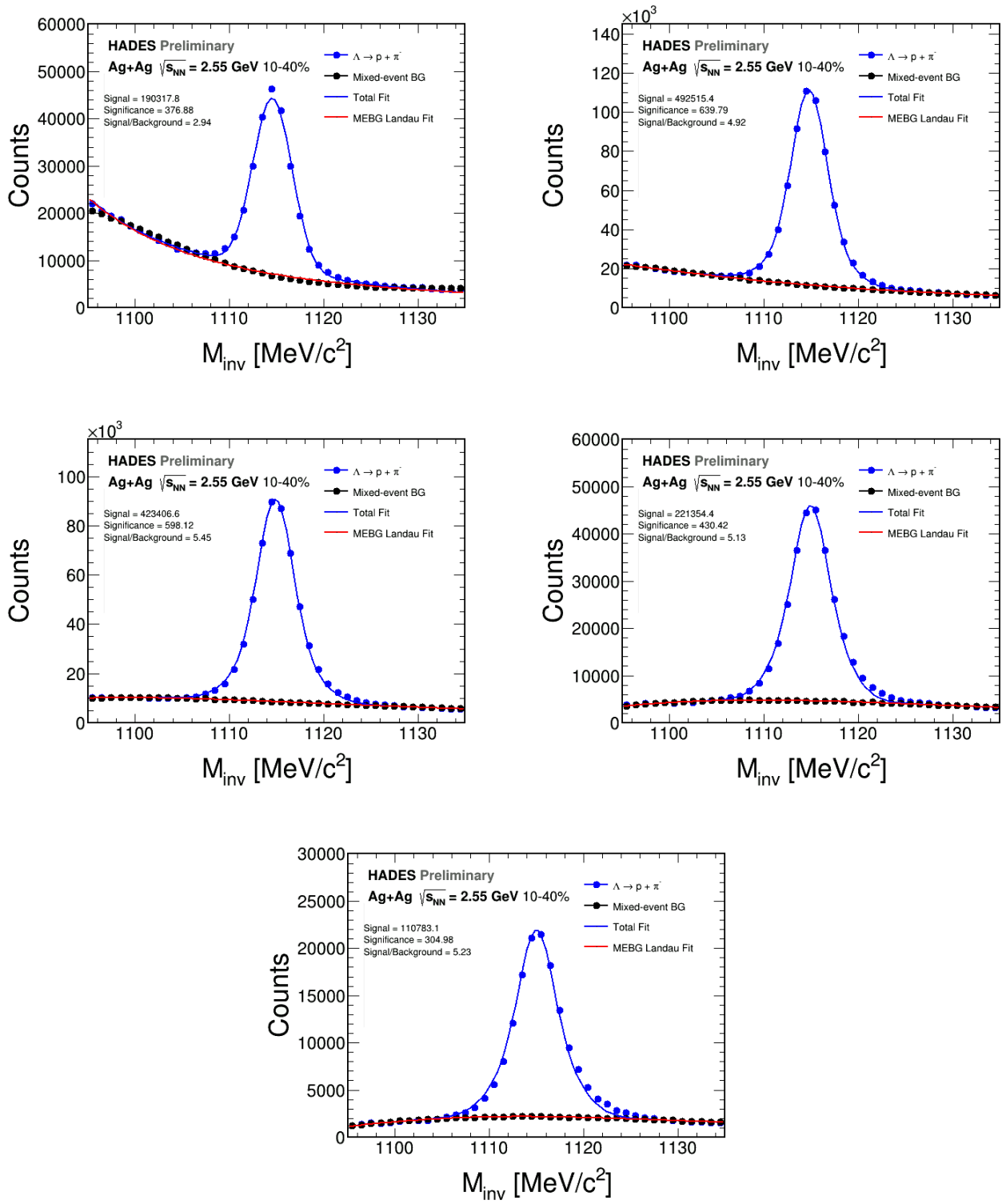


Figure 6.12: Invariant mass distributions in $\text{Ag} + \text{Ag}$ collisions at $\sqrt{s_{\text{NN}}} = 2.55 \text{ GeV}$ for different bins in the transverse momentum integrated over rapidity. From left to right and top to bottom (in units $[p_t] = \text{MeV}/c$): $200 < p_t < 400$, $400 < p_t < 600$, $600 < p_t < 800$, $800 < p_t < 1000$, $1000 < p_t < 1500$.

Systematics on P_Λ [%] Rapidity	$-0.7 < y_{CM} < -0.5$	$-0.5 < y_{CM} < -0.3$	$-0.3 < y_{CM} < -0.1$	$-0.1 < y_{CM} < 0.1$	$0.1 < y_{CM} < 0.3$			
	ΔP_Λ [%]	B_{crit}	ΔP_Λ [%]	B_{crit}	ΔP_Λ [%]	B_{crit}	ΔP_Λ [%]	B_{crit}
Efficiency	± 0.311	\times	± 0.249	\checkmark	± 0.261	\checkmark	± 0.007	\times
$\Delta\phi$ method	± 0.188	\times	± 0.302	\times	± 0.225	\times	± 0.105	\times
Pol0 BG fit	± 0.241	\checkmark	± 0.051	\times	± 0.015	\times	± 0.006	\times
RDA	± 1.349	\checkmark	± 0.199	\times	± 0.358	\checkmark	± 0.331	\checkmark
$\Delta_{\text{sys}}^{\text{total}}$	± 1.384	-	± 0.392	-	± 0.569	-	± 0.456	-

Table 6.3: Summary of the systematic uncertainties in the polarization measurement for Ag+Ag as a function of the rapidity. The Barlow criterion [Bar02] has been applied to decide whether a variation is beyond statistical fluctuations. Only in this particular case, the variation is included in the quadratic sum resulting in the overall systematic uncertainty $\Delta_{\text{sys}}^{\text{total}}$. The dependence on other parameters not listed here are taken from Tab. 6.1.

Systematics on P_Λ [%] Transverse momentum [MeV/c]	$200 < p_t < 400$	$400 < p_t < 600$	$600 < p_t < 800$	$800 < p_t < 1000$	$1000 < p_t < 1500$	
	ΔP_Λ [%]	B_{crit}	ΔP_Λ [%]	B_{crit}	ΔP_Λ [%]	B_{crit}
Efficiency	± 0.500	\checkmark	± 0.050	\times	± 0.155	\checkmark
$\Delta\phi$ method	± 0.453	\times	± 0.138	\times	0.352	\times
Pol0 BG fit	± 0.105	\times	± 0.029	\times	± 0.014	\times
RDA	± 0.863	\checkmark	± 0.290	\times	± 0.407	\checkmark
$\Delta_{\text{sys}}^{\text{total}}$	± 1.061	-	± 0.318	-	± 0.546	-

Table 6.4: Summary of the systematic uncertainties in the polarization measurement for Ag+Ag as a function of the transverse momentum. The Barlow criterion [Bar02] has been applied to decide whether a variation is beyond statistical fluctuations. Only in this particular case, the variation is included in the quadratic sum resulting in the overall systematic uncertainty $\Delta_{\text{sys}}^{\text{total}}$. The dependence on other parameters not listed here are taken from Tab. 6.1.

6.3.2 Global polarization measurement in Au+Au

The Λ polarization as extracted from the invariant mass fit method for varying topology parameters, including the discriminant, is shown in Fig. 6.4 for the Au+Au data. The corrections to reweight the radial distance asymmetry have been assumed to be constant for the change of the parameters except for d_2 and d_3 (see Sec. 4.7). For the latter two, the weights have been updated each time the cut value has been changed. In general, the systematic variations are consistent with the default result, but the variations are significant beyond statistical uncertainties as for all of them the Barlow criterion is found to be $B_{\text{crit}} > 1$. For d_2 and $D_{\min}(\text{MVA})$ particularly, the changes are largest. For the former, the divergence from the default results starts to increase as the d_2 cut is tightened.

The contribution to the overall systematic uncertainty is extracted by taking the maximum deviation from the default result within the range that has been investigated. The relative deviations are found to be of the order of $\Delta_{\text{sys}}/P_{\Lambda} \sim 5 - 15\%$, which is smaller compared to the statistical uncertainty of $\Delta P_{\Lambda}/P_{\Lambda} \approx 21\%$.

Further systematics that have been checked are the determination of the signal and background using the same-event fit to the invariant mass distribution, varying the fit range for the signal extraction and assuming constant background instead of linear shape (Eq. 4.11) as well as to change the selection of the best pair according to the discriminant (see Sec. 3.9.6). For all the different settings, the variations are of the order of $\Delta_{\text{sys}}/P_{\Lambda} \sim 1\%$ at maximum and mostly not even passing the Barlow criterion. Hence their contribution to the overall systematic is negligible.

In the left panel of Fig. 6.13, the results of the polarization measurement using the $\Delta\phi$ -extraction method are shown. Thereby, the amount of bins in $\Delta\phi_p^*$ have been varied to get a handle on the effect of bin-to-bin fluctuations to the signal extraction. For the comparison to the invariant mass fit method, the results are compared after efficiency and RDA corrections, but without correcting for the event plane resolution. This has the reason that this particular correction cannot be applied on a particle-by-particle basis, but only as in integrated value over the whole centrality range of 10 – 40 %. To apply this value correctly, one would have to subdivide the sample into smaller bins in centrality which is not possible due to the limited statistics (see Sec. 4.2). To avoid the propagation of this methodical problem to the systematic uncertainties, the methods are compared forcing $R_{EP} \equiv 1$.

In general, the results shown in Fig. 6.13 are in agreement with each other and also with the value from the invariant mass fit method. However, the statistical uncertainty extracted using the $\Delta\phi$ -extraction method is around $\sim 25\%$ smaller. In addition, it is almost unaffected when the amount of bins in $\Delta\phi_p^*$ is varied from 12 – 36. This does not even change when the fit order is varied and reduced to first order only (see Eq. 4.4). This is remarkable taking into account the fact that the number of free parameters using a fit function up to the third order and 12 bins in $\Delta\phi_p^*$ is only $f_{\text{ndf}} = 12 - 7 = 5$. Therefore, the method seems to underestimate a bit the bin-to-bin fluctuations. The systematical variations are not significant in terms of the Barlow criterion, but it has to be mentioned that this is mainly driven by the difference in the statistical uncertainty appearing in the denominator of Eq. 6.1.

For the systematic uncertainty associated with the RDA correction, the three bin weighting according to the signal distribution is applied in a finite range of R'_V . For each range, the weights are updated. The motivation to choose the specific range was given by the other method to reweight the RDA, i.e. applying continuous weights in a finite range to flatten the distribution

in R'_V (see Sec. 4.7 for details). In principle, even for the finite range the updated weights should account for the losses in the tails and thus this study returns an estimate for the systematic variation of the RDA correction. The investigation is compared to the full range result in the right panel of Fig. 6.13. The values are in agreement, only for the very small ranges the extracted signal is reduced slightly, however, this is not significant in comparison to statistical uncertainties and therefore dropped from the overall systematic.

To complete the systematic uncertainty determination, there are three more sources that are taken into account. The first is a scaling error in the decay parameter of $\Delta\alpha_\Lambda = 2\%$ which is added to the systematics. Second, there is also an uncertainty in the determination of the event plane resolution R_{EP} which also occurs as a scaling error. A detailed study has been performed using different set of subevents based on specific region of the Forward Wall and also the MDC detector [Mam20a] and from this the uncertainty has been estimated to be $\Delta R_{EP} = 3\%$.

As a last contribution, the variation introduced from the efficiency correction is also included to the systematic uncertainty. The variation is found to be one of the most important sources. This is related to the fact that in the Au+Au data there is not really a well-defined peak structure that restricts the polarization fit in the region of the Λ mass. Consequently, the fluctuations are larger and might even be amplified when corrections are applied. Hence, the signal extraction is sensitive to single bin fluctuations, resulting in larger uncertainties.

All the contributions that pass the Barlow criterion are finally added in quadrature resulting in an overall systematic uncertainty for the polarization measurement to be $\Delta_{sys}^{total} = \pm 1.220$ which corresponds to a relative variation of 26.5 %. A detailed summary of the different sources and the overall systematic is given in Tab. 6.1.

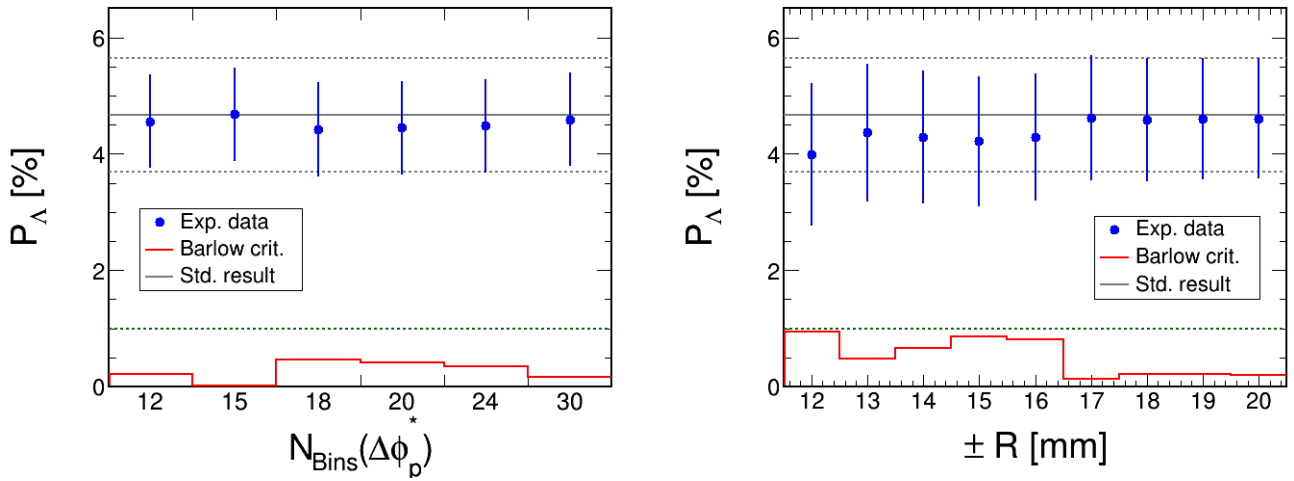


Figure 6.13: Systematic investigation of the $\Delta\phi$ -extraction method with different amount of bins in $\Delta\phi$ (left) and the radial distance asymmetry for different ranges (right) in the Λ polarization measurement in Au+Au collisions at $\sqrt{s_{NN}} = 2.4\text{ GeV}$. The red line displays the Barlow criterion which is found to be $B_{crit} < 1$ in all cases such that the variations are neglected and not included to the overall systematics. The grey solid line indicates the value extracted from the invariant mass fit method while the grey dashed lines mark the statistical uncertainty.

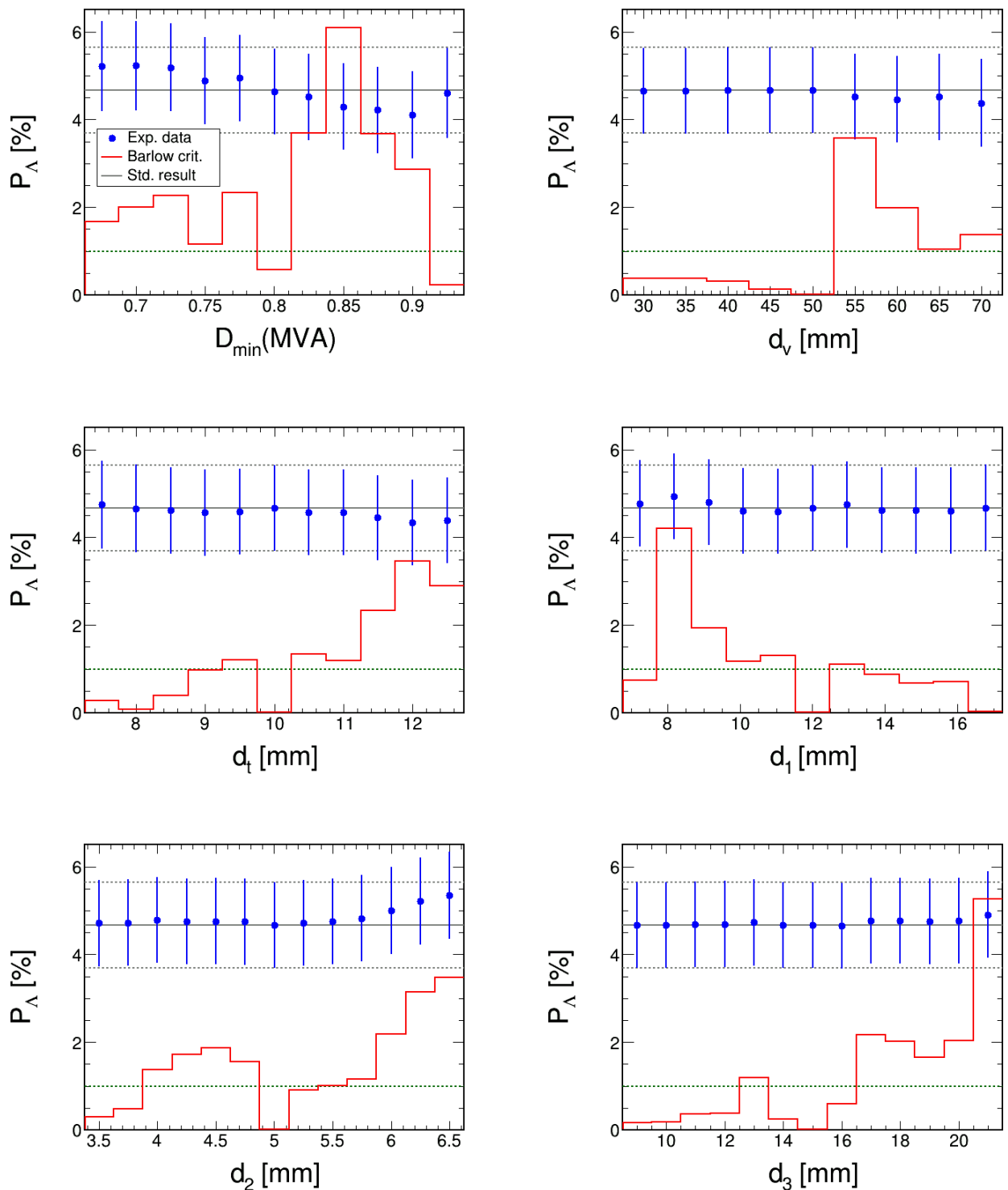


Figure 6.14: Λ polarization in Au+Au collisions at $\sqrt{s_{NN}} = 2.4$ GeV depending on the individual topology parameters (blue points). The default result is shown too (grey line). The range has been adjusted to a maximum variation of 15 % in the Λ yield. A variation is considered relevant and enters the systematic uncertainty if the Barlow criterion [Bar02] is beyond $B_{\text{crit}} = 1$ (red line).

6.3.3 Directed flow slope at midrapidity in Au+Au

Following the same procedure as for the polarization measurement, the systematic uncertainty of the directed flow slope at midrapidity can be extracted in the same way. Yet this time, the variations affect the observable only in an indirect way. For example, as a cut parameter is varied, this will change the overall sample by some amount of statistics either put on top or being removed. However, this difference distributes over several bins in rapidity for which the flow analysis is performed separately (see Sec. 4.2 and 4.3 for details). This applies explicitly to the comparison of the two different methods to extract v_1 which are found to be well in agreement showing only small variations and are therefore neglected for the overall systematic.

The systematic studies for the extraction of the directed flow slope at midrapidity, as the topology parameters are varied, is displayed in Fig. 6.15. The Barlow criterion is not shown for better visibility, however, in all cases it excels one and thus all of the variations are taken into account for the systematic uncertainty. The dominant contribution is related to the discriminant.

Other checks are found to have only small contributions, if they pass the Barlow criterion at all. Two other important sources are the effect of the efficiency correction and the event plane resolution uncertainty estimated in the same way as for the polarization measurement in Sec. 6.3.2. The overall systematic uncertainty is found to be of the order of 10% and thereby exceeding the statistical uncertainty by about 60%. However, in comparison to the extracted slope the uncertainties are reasonable. A detailed summary of all the determined systematic uncertainties can be found in Tab. 6.5.

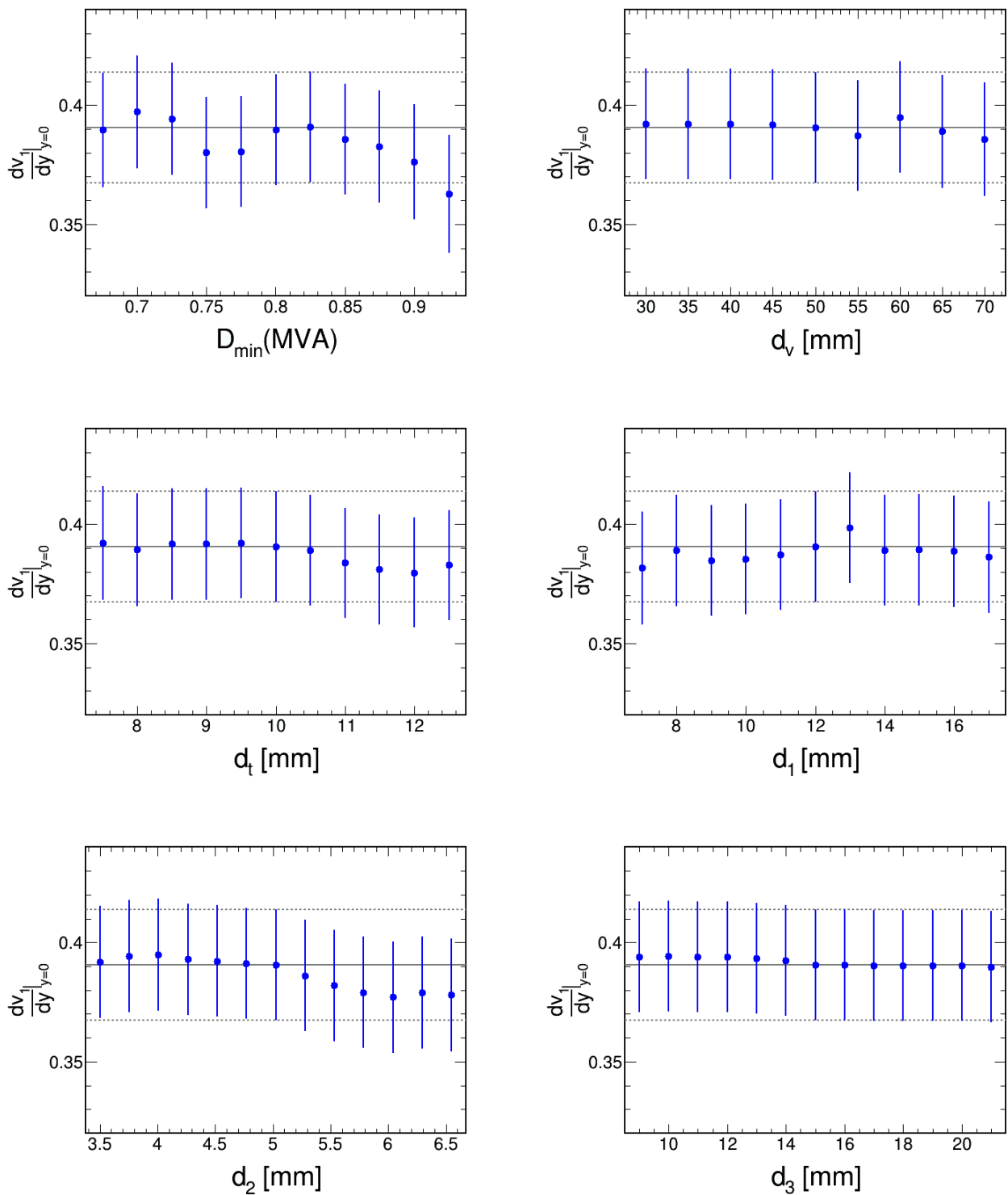


Figure 6.15: Systematic investigation of the directed flow slope at midrapidity (blue points) for the individual variation of the different topology parameters in Au+Au collisions at $\sqrt{s_{NN}} = 2.4$ GeV. The default result is shown too (grey line).

6.3.4 Directed flow slope at midrapidity in Ag+Ag at $\sqrt{s_{NN}} = 2.55 \text{ GeV}$

The same study performed for the Au+Au data (see Sec. 6.3.3) is also applied to extract the directed flow in Ag+Ag. The directed flow can be extracted precisely for different rapidity bins. Two examples are shown in Fig. 4.25. There is a small deviation from the anti-symmetry of the directed flow, however, it does not have a considerable influence on the extraction of the slope at midrapidity. Considering the two rapidity bins, the difference in the background correlation is remarkable, showing again the impact from several different sources contributing.

The systematic variation of the directed flow slope as a function of all the topology parameters is shown in Fig. 6.16. The Barlow criterion is not plotted, however, in all cases the variations are significant and have to be included to the final systematics. An overview of the results of the systematic checks in comparison to Au+Au is shown in Tab. 6.5. For Ag+Ag, the variations with the topology parameters are generally smaller. The main contributions arise from the event plane resolution and the efficiency correction. Also for the application of the $\Delta\phi$ -extraction method, a deviation beyond statistical fluctuations has been found and included to the final systematics. Overall, the uncertainty has been found to be of the order of 10% similar to Au+Au. Due to the high statistics sample, the statistical uncertainty in Ag+Ag is roughly 2.5% such that the systematic uncertainty exceeds by a factor 3 – 4. This could be partially related to the fact that all relevant contributions to $\Delta_{\text{sys}}^{\text{total}}$ are added quadratically, without taking into account for possible correlations, especially for the topology parameters which are known to be strongly correlated. However, the systematic uncertainty is still reasonable with respect to the measured value.

Systematic on $\frac{d\nu_1}{dy} \Big _{y=0}$	Au+Au@1.23AGeV			Ag+Ag@1.58AGeV		
	Absolute	Relative	B_{crit}	Absolute	Relative	B_{crit}
D_{\min} (MVA)	± 0.028	$\pm 7.2\%$	✓	± 0.004	$\pm 1.4\%$	✓
d_ν	± 0.005	$\pm 1.3\%$	✓	± 0.005	$\pm 1.7\%$	✓
d_1	± 0.009	$\pm 2.3\%$	✓	± 0.007	$\pm 2.4\%$	✓
d_2	± 0.013	$\pm 3.3\%$	✓	± 0.005	$\pm 1.7\%$	✓
d_3	± 0.004	$\pm 1.0\%$	✓	± 0.002	$\pm 0.7\%$	✓
d_t	± 0.011	$\pm 2.8\%$	✓	± 0.004	$\pm 1.4\%$	✓
Best D_{\min} (MVA)	± 0.001	$\pm 0.3\%$	✗	± 0.000	$\pm 0.0\%$	✗
Same-event mass fit	± 0.000	$\pm 0.0\%$	✗	± 0.000	$\pm 0.0\%$	✗
Fit range	± 0.004	$\pm 1.0\%$	✓	± 0.001	$\pm 0.3\%$	✗
Efficiency	± 0.011	$\pm 2.8\%$	✓	± 0.014	$\pm 4.9\%$	✓
$\Delta\phi$ method	± 0.002	$\pm 0.5\%$	✗	± 0.009	$\pm 3.1\%$	✓
R_{EP}	± 0.012	$\pm 3.0\%$	✓	± 0.014	$\pm 5.0\%$	✓
$\Delta_{\text{sys}}^{\text{total}}$	± 0.038	$\pm 9.9\%$	-	± 0.025	$\pm 8.7\%$	-

Table 6.5: Summary of the systematic uncertainties in the directed flow slope at midrapidity measurement for Au+Au and Ag+Ag. The Barlow criterion [Bar02] has been applied to decide whether a variation is beyond statistical fluctuations. Only in this particular case, the variation is included in the quadratic sum resulting in the overall systematic uncertainty $\Delta_{\text{sys}}^{\text{total}}$.

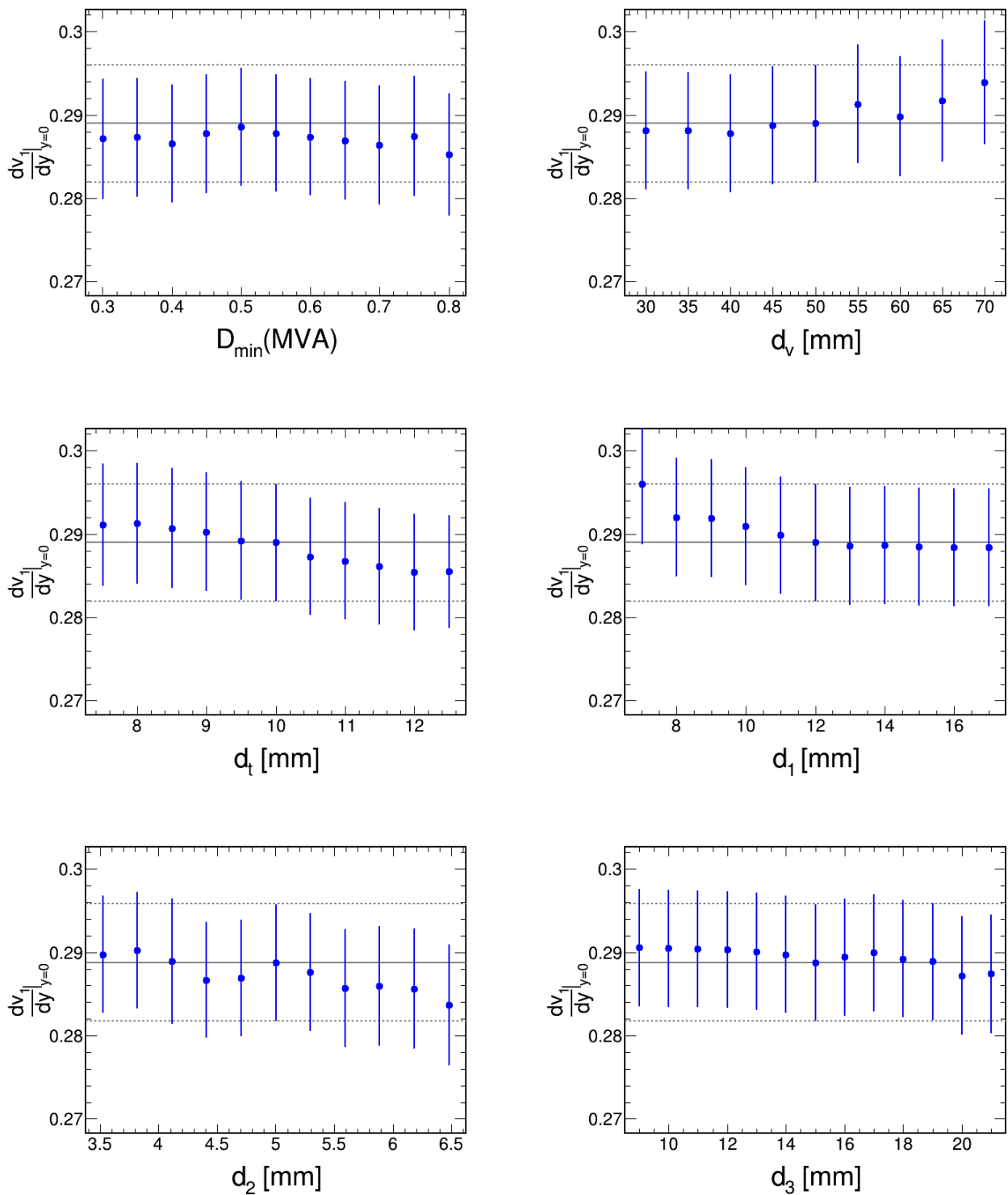


Figure 6.16: Systematic investigation of the directed flow slope at midrapidity (blue points) for the individual variation of the different topology parameters in $\text{Ag}+\text{Ag}$ collisions at $\sqrt{s_{NN}} = 2.55 \text{ GeV}$. The default result is shown too (grey line).

6.4 Hard-cut analysis

Another cross-check to be performed is the comparison of the results to a default hard-cut analysis. Here, the selection of the Λ candidates is solely determined by the topology cuts without any neural network trained afterwards. This has the clear disadvantage, that the selection criteria have to be enhanced (see Tab. 3.5) which removes a significant part of the signal.

However, the comparison to the hard-cut analysis may indicate if there is a correlation between the discriminant returned from the neural network and the actual polarization measurement. At least in the simulations, as shown in Sec. 5.4, this could be ruled out since all the patterns found in the experimental data have been reproduced qualitatively. However, not all possible effects are covered by the simulations and consequently it is required to test as much as possible on the experimental data only.

The result of the invariant mass fit method for the hard-cut analysis in Ag+Ag at $\sqrt{s_{NN}} = 2.55$ GeV are shown in Fig. 6.17. The same analysis procedure as in Fig. 4.19 has been applied except for the selection on the decay topology. Comparing the distributions of the invariant mass, the hard-cut sample is much cleaner, as there is fewer background in the sample and the signal-to-background ratio is twice as large. However, this is at the cost of a reduction of the reconstructed Λ hyperons by more than 50 %. This propagates to the statistical uncertainty extracted from the fit to the $\langle \sin(\Delta\phi_p^*) \rangle_{TOT}$ which increases by roughly $\sim 1/3$. The strong reduction of the background in the hard-cut sample results in a large fluctuation of the background correlation in peak region of the nominal Λ mass. Therefore, the clear peak structure at the nominal Λ mass disappears, however, the data points are still consistently following a trend for the signal correlation significantly different from zero. Concerning the RDA correction, the same procedure as in Fig. 4.19 has been applied and the effect of the correction has been found comparable. Overall, the value of the hard-cut analysis is well in agreement with the default result using the neural network. Hence, there is no significant bias from the neural network to the polarization measurement.

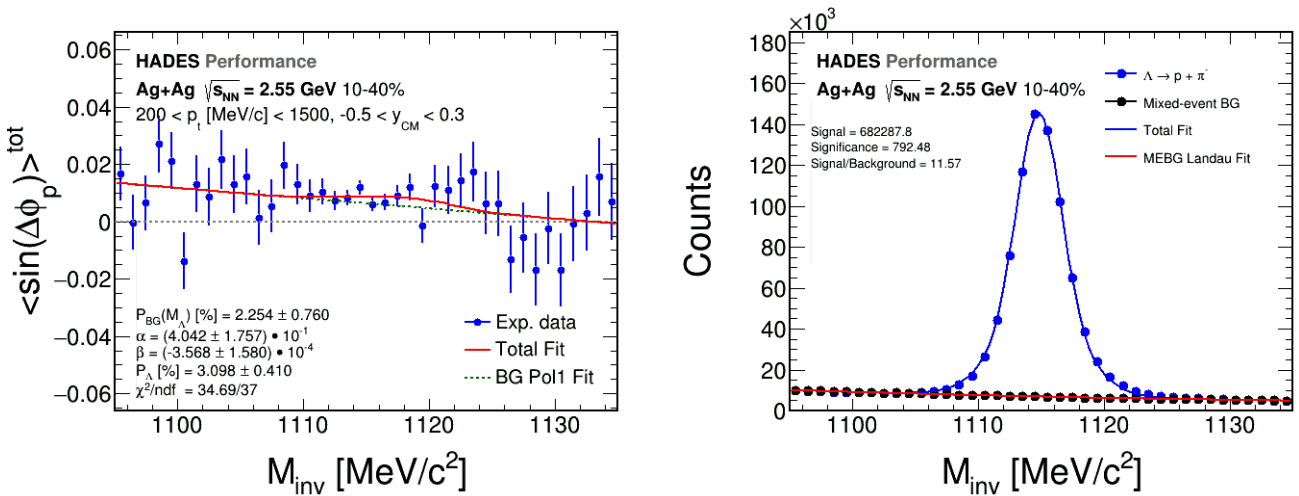


Figure 6.17: Polarization measurement in Ag+Ag collisions at $\sqrt{s_{NN}} = 2.55$ GeV extracted from a sample determined by hard-cuts on the decay topology using the invariant mass fit method. Efficiency and RDA correction have been recalculated for this particular sample. The results are consistent with the multi-variate analysis.

Similar conclusions can be drawn for the Au+Au data. The results of the hard-cut analysis are shown in Fig. 6.18. In comparison to Fig. 4.20, the extracted polarization is larger, however, due to the reduced statistics this can be attributed to statistical fluctuations of single bins that drive the polarization fit resulting in stronger variations of the final value. However, the results is at least qualitatively consistent as also for the hard-cut analysis a non-zero polarization has been measured. The larger fluctuations for the Au+Au data have been discussed in detail in Sec. 6.3.2 and result in a larger systematic uncertainty that covers the behavior.

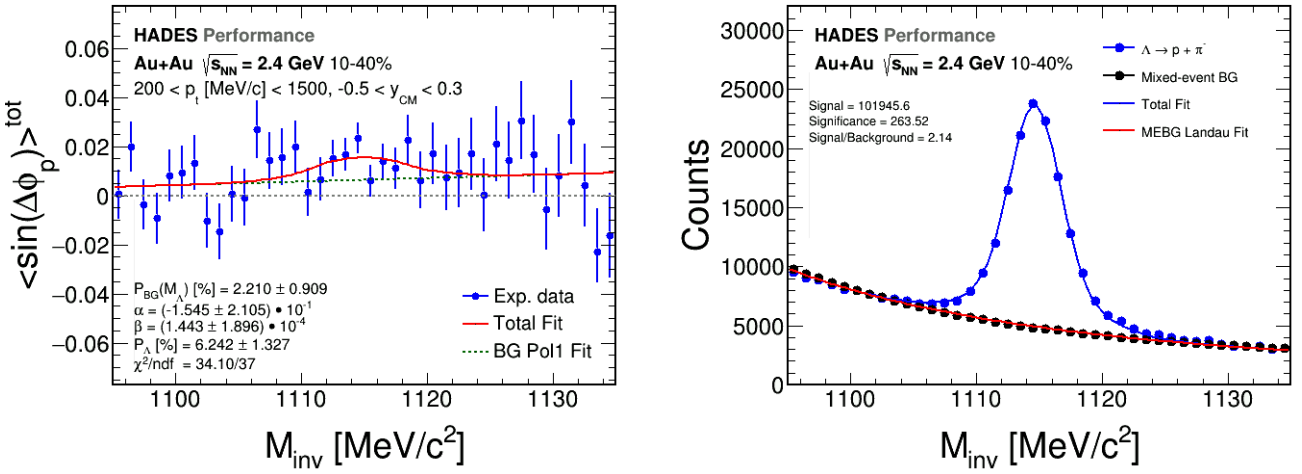


Figure 6.18: Polarization measurement in Au+Au collisions at $\sqrt{s_{NN}} = 2.4 \text{ GeV}$ extracted from a sample determined by hard-cuts on the decay topology using the invariant mass fit method. Efficiency and RDA correction have been recalculated for this particular sample. The results are consistent with the multi-variate analysis.



7 Results and discussion

In the chapter, the results of the multi-differential global polarization and flow measurement of Λ hyperons in Au+Au collisions at $\sqrt{s_{NN}} = 2.4$ GeV and Ag+Ag collisions at $\sqrt{s_{NN}} = 2.55$ GeV will be discussed. The results are obtained using the invariant mass fit method (see Sec. 4.3) for the extraction of the signal value. As both directed flow and polarization are averaged observables, they have been corrected for the relative efficiency which depends on the phase-space region in transverse momentum and rapidity (see Sec. 4.6). To determine the effect of the finite detector acceptance, detailed simulations have been performed (see Ch. 5). As a result, the effect of the detector acceptance on the polarization measurement can be neglected. Another correction that has been found important for the polarization analysis of the Λ hyperon is the radial distance asymmetry (RDA). An experimental driven approach has been developed to correct for the effect on the polarization (see Sec. 4.7) by the asymmetry of the reconstructed tracks with respect to a straight line through the collision vertex and parallel to the z-axis. Applying RDA correction to the data leads to a slight enhancement of the extracted signal. For the directed flow the RDA correction is not used, as for v_1 no significant dependence is observed.

The results are discussed in this chapter. Sec. 7.1 is dedicated to the directed flow of the Λ hyperons presented as a function of rapidity and the extraction of its slope at midrapidity. This will be compared to the slope of the proton directed flow extracted from the same HADES data sets and put in the context of other experiments. In Sec. 7.2, the measurement of the global polarization is presented, also multi-differentially as a function of collision centrality, rapidity and transverse momentum. Final remarks and an outlook will be given in Sec. 7.3.

7.1 Directed flow measurement of the Λ hyperons

Fig. 7.1 shows the results of the directed flow measurement as a function of rapidity in the center-of-mass frame for Λ hyperons in Au+Au collisions at $\sqrt{s_{NN}} = 2.4$ GeV (left panel) and Ag+Ag collisions at $\sqrt{s_{NN}} = 2.55$ GeV (right panel). The results are integrated in a transverse momentum range of $200 \leq p_t[\text{MeV}/c] \leq 1500$ and a range of 10 – 30 % in the collision centrality. As the directed flow is anti-symmetric with respect to midrapidity, there are two features to be notified. First, at midrapidity, i.e. $y_{CM} = 0$, the directed flow vanishes, i.e. $v_1|_{y_{CM}=0} = 0$. Second, the reflected data points must overlap, i.e. $v_1|_{y_{CM}} = -v_1|_{-y_{CM}}$. For the latter, the reflected data points are also shown in Fig. 7.1. For both collision systems, the flow anti-symmetry is clearly observed. Only around midrapidity, there is a small difference between measured and reflected points. For the Au+Au system, this only affected one bin at $y_{CM} = 0.1$ which fluctuates above the general trend of the data points. For the Ag+Ag system, there is a consistent trend in the range of $-0.2 \leq y_{CM} \leq 0.2$ that reduces the extracted value of v_1 and is included to the systematic uncertainty of the measurement.

To determine the offset of the directed flow at midrapidity, the rapidity dependence is fit with a third order polynomial function:

$$v_1(y_{CM}) = F_0 + F_1 \cdot y_{CM} + F_3 \cdot y_{CM}^3, \quad (7.1)$$

while the quadratic term is fixed to zero, $F_2 \equiv 0$, due to the expected anti-symmetry of v_1 with respect to y_{CM} . The parameter F_0 is the measure for the offset at midrapidity, F_1 is the slope at

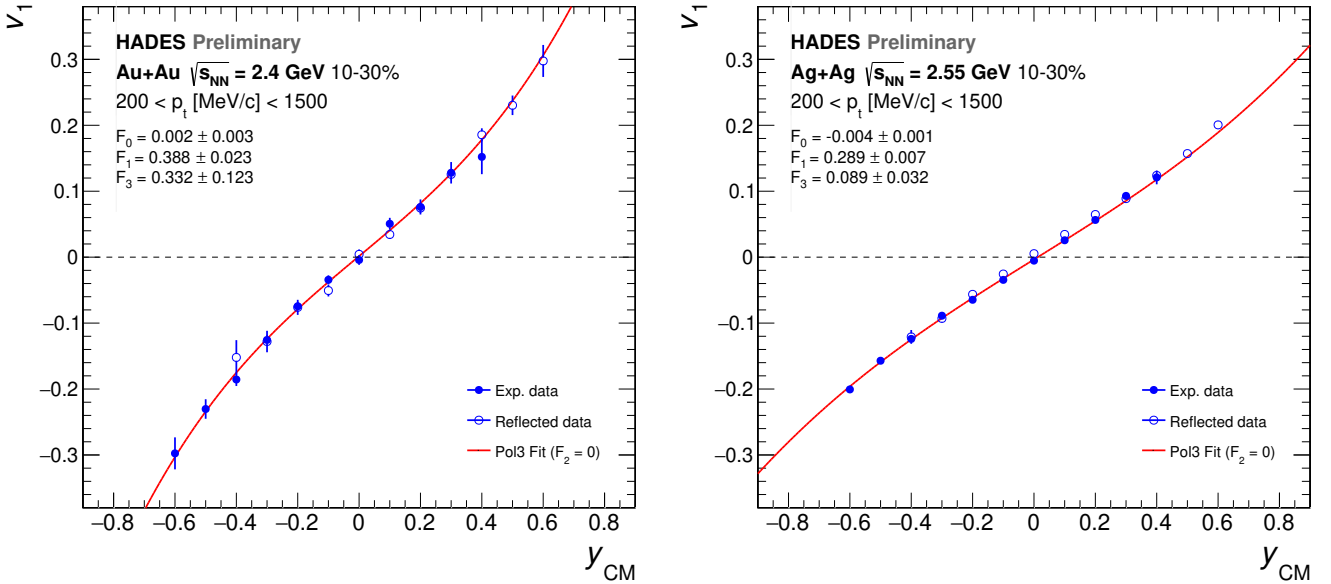


Figure 7.1: Measurement of the directed flow as a function of the rapidity for Au+Au collisions at $\sqrt{s_{NN}} = 2.4 \text{ GeV}$ (left panel) and Ag+Ag collisions at $\sqrt{s_{NN}} = 2.55 \text{ GeV}$ (right panel). Reflected points are shown as the directed flow should be anti-symmetric with respect to midrapidity. A third order polynom with $F_2 \equiv 0$ is fit to extract the slope at midrapidity.

midrapidity and F_3 the parameter that defines the curvature. All three parameters are extracted from the fit. For the Au+Au run, the offset at midrapidity is extracted to be $F_0 = (1.514 \pm 3.331) \cdot 10^{-3}$. Within statistical uncertainties, the value is consistent with zero. The same study for the Ag+Ag run returns F_0 shifted slightly to the negative values as expected from the trend observed for the data points around midrapidity. The value is measured to be $F_0 = (-3.513 \pm 1.114) \cdot 10^{-3}$.

A good measure for v_1 is the slope at midrapidity. This is due to the fact that its sign encodes the general trend, i.e. in which direction the particles are deflected while its absolute value defines the strength of this effect. In case of a positive slope, the particles sitting at higher rapidities are pushed outwards, away from the collision center. If the slope is negative, its exactly the opposite effect and the particle at high rapidity are deflected inwards due to an attractive interaction. Both scenarios are possible, depending on the energy of the colliding system.

From the polynomial fit in Fig. 7.1, the slope at midrapidity could be determined to be $F_1 = 0.388 \pm 0.023(\text{stat.}) \pm 0.038(\text{sys.})$ in Au+Au and $F_1 = 0.289 \pm 0.007(\text{stat.}) \pm 0.025(\text{sys.})$ in Ag+Ag collisions. For the estimation of the systematic uncertainties see Ch. 6 for more details. At the HADES energies, the driving force of the directed flow as a function of rapidity is the coulomb repulsion leading to a strong outwards deflection reflecting in a positive slope at midrapidity. For a lower collision energy, the coulomb repulsion is expected to be larger and thus the same applies also to the v_1 slope at midrapidity. This trend is confirmed by the two measurements at $\sqrt{s_{NN}} = 2.4 \text{ GeV}$ and $\sqrt{s_{NN}} = 2.55 \text{ GeV}$ as for the lower beam energy, the value is significantly larger.

In Fig. 7.2, the results are displayed as a function of the collision energy and compared to the world data. An important point has to be made in the comparison of the different measure-

ments. The directed flow depends strongly on the centrality and transverse momentum range, which is used to determine the rapidity dependence. For the results of the directed flow slope

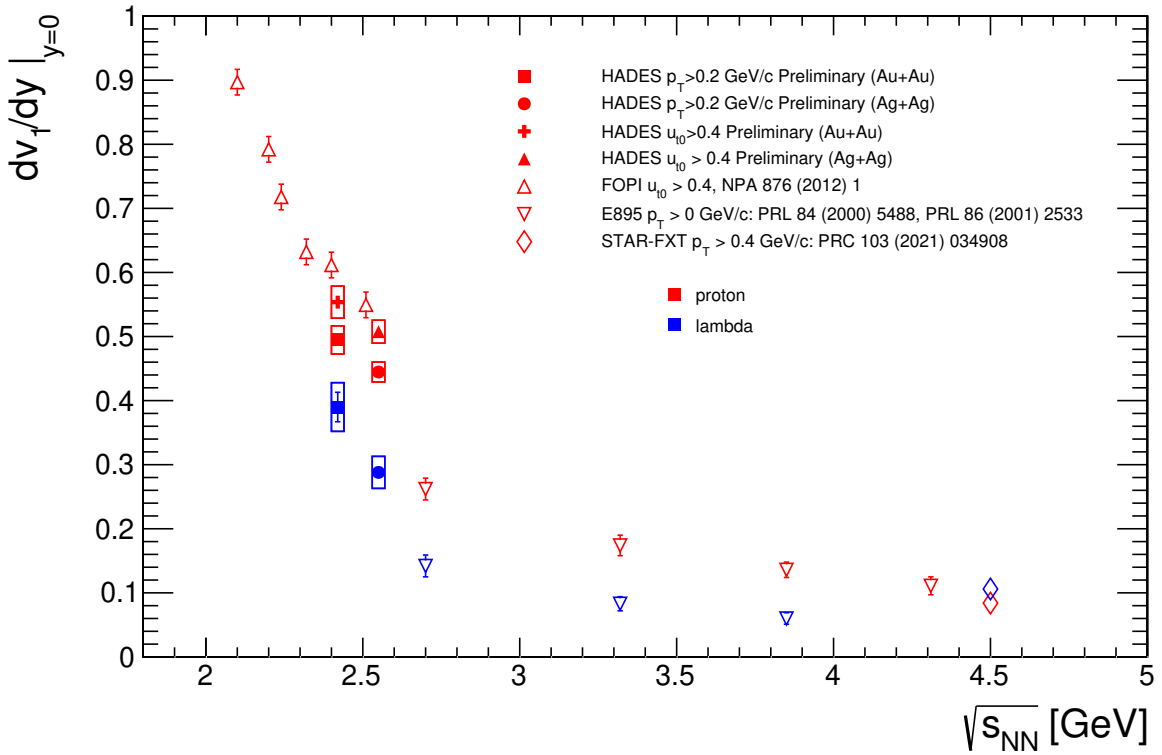


Figure 7.2: Directed flow slope at midrapidity as a function of the collision energy for protons (red) and Λ hyperons (blue) measured by HADES (this study and [Mam20b, Mam20c]), E895 [Liu00, Chu01], FOPI [Rei12] and STAR [Ada21].

of the protons published by the FOPI collaboration [Rei12], they used a low momentum cut of the dimensionless quantity u_{t0} defined as:

$$u_{t0} = \frac{p_t}{p_{CM, \text{projectile}}} > 0.4, \quad (7.2)$$

where $p_{CM, \text{projectile}}$ is the beam momentum. For $\sqrt{s_{NN}} = 2.4 \text{ GeV}$ this corresponds to a low transverse momentum cut of $p_t > 300 \text{ MeV/c}$ while for $\sqrt{s_{NN}} = 2.55 \text{ GeV}$ it is $p_t > 344 \text{ MeV/c}$. For comparison, the same cuts have been used for the protons measured with HADES [Mam20b, Mam20c] shown by the open squares and circles in Fig. 7.2. The HADES results are well in agreement with the FOPI measurements of the proton directed flow slope at midrapidity. When the cut on the transverse momentum is lowered to $p_t > 200 \text{ MeV/c}$, $d v_1/d y |_{y_{CM}=0}$ decreases by approximately $\sim 20\%$ as can be seen by the filled HADES data points. Consequently, the specific phase-space cuts have to be taken into account when experimental results are compared. This also holds for the comparison to the results obtained by the E895 collaboration. As no lower p_t has been applied, a lower value of the slopes is extracted. This can be clearly seen in the comparison to the HADES points in Fig. 7.2, as both protons and Λ hyperons are consistently shifted with respect to the HADES results with a lower momentum cut of $p_t > 200 \text{ MeV/c}$. Comparing the results of the HADES measurements for protons and Λ hyper-

ons, a significant difference in the slope of these two particles is observed similar to the findings by E895 collaboration. Also the relative difference is of the same order:

$$\frac{d v_1}{d y_{CM}} \bigg|_{y_{CM}=0,\Lambda} \sim \frac{2}{3} \cdot \frac{d v_1}{d y_{CM}} \bigg|_{y_{CM}=0,p}, \quad (7.3)$$

while for the HADES Au+Au run the difference is slightly smaller, but also associated with larger uncertainties. In contrast, the recent measurements by the STAR collaboration at $\sqrt{s_{NN}} = 4.5 \text{ GeV}$ show no difference in the v_1 slope at midrapidity between protons and Λ hyperons within uncertainties [Ada21]. This poses the question about the origin of the splitting between protons and Λ hyperons at lower energies which is still to be understood.

7.2 Global polarization measurement of the Λ hyperons

The main aim of this work was to measure for the first time the global polarization in heavy-ion collisions at lower beam energy at $\sqrt{s_{NN}} \sim 2$ GeV. So far, no other measurements have been performed in this energy regime. The measurement of the global polarization has been performed using the Λ hyperon. Its weak decay channel $\Lambda \rightarrow p + \pi^-$ offers a great possibility to measure the spin orientation of the Λ hyperon as due to the parity violation, the proton is predominantly emitted in the spin direction of the Λ hyperon. Thus the measure of the proton direction in the rest frame of the Λ hyperon allows to reconstruct a possible polarization with respect to the orbital angular momentum.

The global polarization signal of the Λ hyperons has been extracted using the invariant mass fit method (see Sec. 4.3) for Au+Au collisions at $\sqrt{s_{NN}} = 2.4$ GeV and Ag+Ag collisions at $\sqrt{s_{NN}} = 2.55$ GeV. The analysis is performed in 10 – 40 % collision centrality while the phase-space has been restricted to $-0.5 < y_{CM} < 0.3$ in rapidity and $200 < p_t[\text{MeV}/c] < 1500$ in the transverse momentum. The Λ polarization is found to be $P_\Lambda[\%] = 4.609 \pm 0.966(\text{stat.}) \pm 1.220(\text{sys.})$ in the Au+Au system and $P_\Lambda[\%] = 3.174 \pm 0.294(\text{stat.}) \pm 0.319(\text{sys.})$ in the Ag+Ag system. The smaller uncertainties in the Ag+Ag run reflect the high amount of statistics that have been collected.

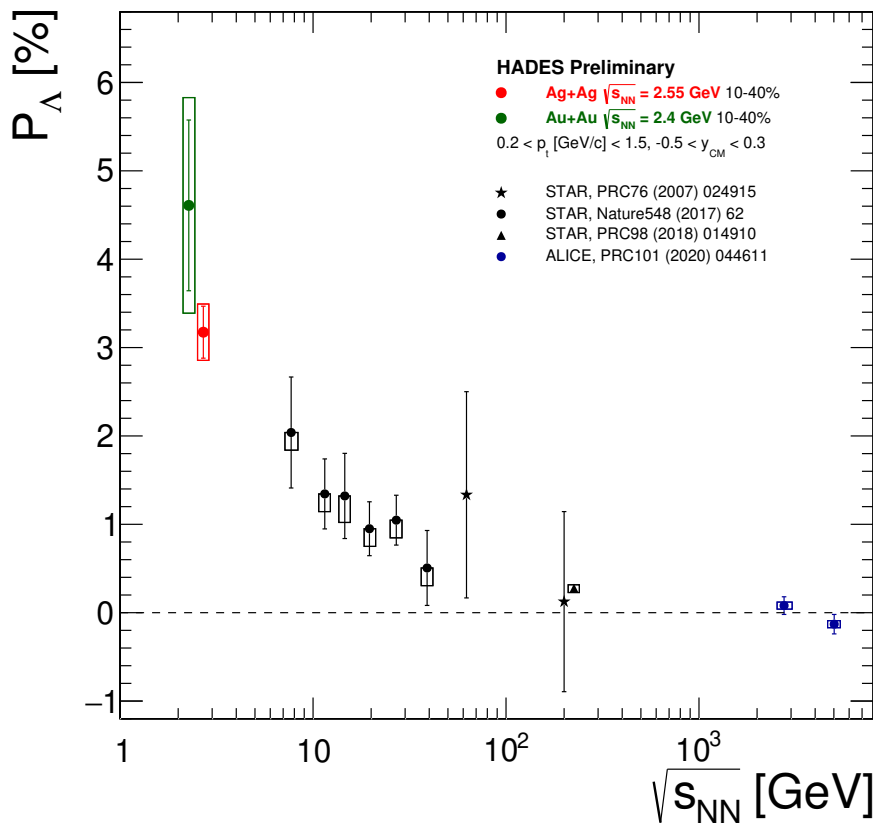


Figure 7.3: Beam energy dependence of the global polarization of the Λ hyperons measured by HADES (this study), STAR [Abe07, Ada17, Ada18a] and ALICE [Ach20]. The HADES results and the STAR results at $\sqrt{s_{NN}} = 200$ GeV have been shifted slightly for better visibility.

The results are displayed as a function of the beam energy in Fig. 7.3 and compared to previous measurements of the Λ global polarization. The HADES results have been shifted slightly in

$\sqrt{s_{NN}}$ for better visibility. Both measurements continue the increasing trend of the global Λ polarization towards lower collision energies measured by the STAR collaboration at the beam energy scan phase I [Ada17]. Consequently, the largest polarization of the Λ hyperons has been measured by HADES. Especially the Ag+Ag analysis provides a precise measurement with a 10σ confidence interval. For the Au+Au run the confidence interval is found to be 3.8σ . The latter is caused by the physical condition that the production of the Λ hyperons at $\sqrt{s_{NN}} = 2.4\text{ GeV}$ is subthreshold and the one, i.e. technical occurrence of an inactive sector during most of the beam time. Both these effects reduce the signal-to-background ratio and together with the larger combinatorial background due to the larger system size of Au in comparison to Ag, the precision of the measurement is reduced. Still the result is consistent with the Ag+Ag system, as for the larger Au+Au system, larger orbital angular momenta are generated and therefore an enhancement of the global Λ polarization can be expected. This is well in line with the measurements presented in this analysis.

Centrality dependence of the global polarization

The high statistics collected in the Ag+Ag run allows for a multi-differential analysis of the global polarization measurement. According to Eq. 1.17 the orbital angular momentum is in first approximation proportional to the impact parameter of the collision. Thus the global polarization is expected to increase towards peripheral events. However, it is not fully clear, how much of the orbital angular momentum remains in the fireball and how much is carried away by the spectators. Investigations showed that at $\sqrt{s_{NN}} = 200\text{ GeV}$ only a fraction of 10 – 20 % of the orbital angular momentum stays in the system [Jia16]. They also found a strong dependence of this fraction as a function of the impact parameter b while the maximum value was reached at $b = 4\text{ fm}$, corresponding to $\sim 7\%$ centrality in Au+Au and $\sim 11\%$ centrality in Ag+Ag. Towards more peripheral events, the fraction of the orbital momentum inherent to the fireball slowly decreases. However, at the much lower collision energies measured with HADES, the colliding nuclei are much slower and additionally less Lorentz-contracted. Therefore, they play a more important role for the fireball and thus the fraction of orbital angular momentum might be larger and show different behavior as a function of the collision centrality.

Fig. 7.4 shows the results of the global polarization measurement of the Λ hyperons for Ag+Ag collisions at $\sqrt{s_{NN}} = 2.55\text{ GeV}$ measured within $-0.5 < y_{CM} < 0.3$ and $200 < p_t[\text{MeV}/c] < 1500$. The values are summarized in Tab. 7.1. The most-central bin has also been analyzed although it is excluded in the analysis of the integrated polarization discussed above. As expected, the extracted Λ polarization shows only small deviation from zero. For the 10 – 20 % centrality bin, the observed signal increases slightly, but the main rise start in the more peripheral collisions reaching values of more than 5 % of the Λ polarization in the most peripheral collisions analyzed in this work. This strong enhancement goes in line with the expectation of the larger orbital angular momentum in the peripheral collisions.

For comparison, the theoretical predictions of the centrality dependence of the global polarization of the Λ hyperons (see Sec. 1.4 for details) is shown by the blue band [Vit20]. Although the theoretical calculations does not represent the same phase-space region, they are consistent with the measured values and reproduce the centrality dependence observed in the experimental data.

As long and the Au+Au and the Ag+Ag system are analyzed within the same centrality range, the centrality dependence of the global polarization should reveal the same behavior in both systems. Due to the larger system size in Au+Au, the magnitude of the polarization is expected

to be larger. In [Iva06] the global polarization of the Λ hyperons has been calculated for varying impact parameter of $b = 2, 4, 6$ and 8 fm in Au+Au collisions and shows an increasing trend towards peripheral collisions. In Ag+Ag collisions, the impact parameter $b = 4\text{--}8$ fm corresponds approximately to the 10–40% centrality range. Hence, the increasing trend predicted for the Au+Au system as a function of the impact parameter, is at least qualitatively consistent with the experimental findings in the Ag+Ag system.

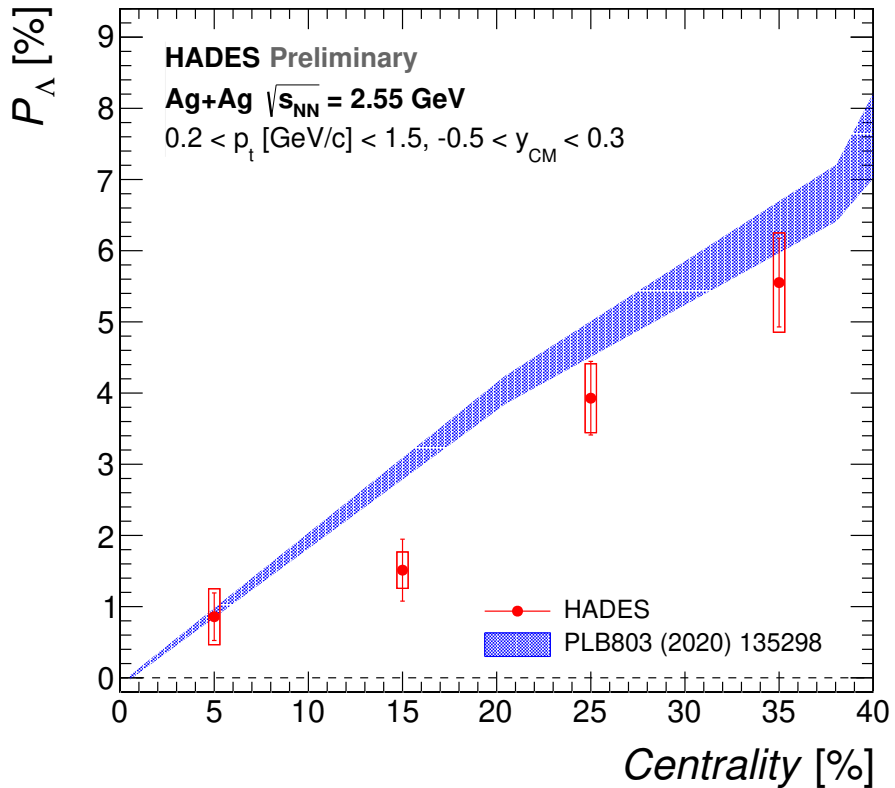


Figure 7.4: Centrality dependence of the global polarization of the Λ hyperons in Ag+Ag collisions at $\sqrt{s_{NN}} = 2.55$ GeV. The theoretical calculations are based on a connection of the thermal vorticity with the mean spin vector of the Λ hyperon, while the initial state is simulated using the UrQMD model [Vit20]. The theoretical predictions are calculated for $p_t > 200$ MeV/c and $-0.7 < y_{CM} < 0.6$ and not yet fully adjusted to the experimental data.

Centrality	P_Λ [%]	$\Delta^{\text{stat.}}$ [%]	$\Delta^{\text{sys.}}$ [%]
0 – 10 %	0.858	0.334	0.393
10 – 20 %	1.512	0.435	0.256
20 – 30 %	3.928	0.517	0.484
30 – 40 %	5.552	0.623	0.698

Table 7.1: Centrality dependent global polarization measurement of the Λ hyperons in Ag+Ag collisions at $\sqrt{s_{NN}} = 2.55 \text{ GeV}$ for $-0.5 < y_{CM} < 0.3$ in rapidity and $200 < p_t [\text{MeV}/c] < 1500$ in transverse momentum. The results including statistical and systematic uncertainties are summarized.

Phase-space dependence of the global polarization

Similar to the centrality dependence, the global Λ polarization has been measured as a function of the phase-space region for 10 – 40 % collision centrality. Due to the high amount of statistics needed to perform a multi-differential precision measurement, the rapidity dependent results are integrated over transverse momentum for $200 < p_t [\text{MeV}/c] < 1500$ while the transverse momentum differential results are shown within $-0.5 < y_{CM} < 0.3$.

The results for the rapidity dependence of the global polarization are displayed in Fig. 7.5 and the values are summarized in Tab. 7.2. In the figure, the two most backward data points have been reflected to the forward rapidity (open symbols) to indicated a possible trend of the Λ polarization. In contrast to the directed flow, the global polarization for symmetric collision systems is an even function of the rapidity and therefore it should be backward-forward symmetric. Within the uncertainties of the measurement, no significant dependency on the rapidity is observed. This is consistent with the theoretical predictions [Vit20] taken from Fig. 1.17 (see Sec. 1.4.6). For comparison, the results for an impact parameter of $b = 5.5 \text{ fm}$ have been used. This corresponds to approximately 20 % collision centrality in the Ag+Ag system. As the experimental results are integrated over 10 – 40 % centrality but more Λ hyperons are produced in the more central events, the theoretical predictions at $b = 5.5 \text{ fm}$ should give a good estimation of the expectations for the integrated results. Besides the consistent trend of approximately constant polarization as a function of rapidity, the predictions agree well also quantitatively, although the average value is slightly above the measured one.

Another comparison to the theoretical predictions of [Iva06] discussed in Sec. 1.4.6 has been performed for Au+Au collisions at different collision energies. In Fig. 1.15 the beam energy dependence of the global polarization of the Λ hyperons is shown for different ranges in rapidity (always symmetric around midrapidity) down to $\sqrt{s_{NN}} = 2.4 \text{ GeV}$. As the rapidity window is lowered from $|y_{CM}| < 0.6$ to $|y_{CM}| < 0.35$, the predicted polarization decreases by $\sim 1\%$ depending on the equation of state used for the calculation. Consequently, a minimum of the global Λ polarization at midrapidity is expected, increasing slowly and symmetric towards the outer regions. Such a trend is not observed in the Ag+Ag data in Fig. 7.5, however, the associated uncertainties of the measurement does not allow for a final conclusion as they are of similar magnitude as the predicted effect of the rapidity dependence.

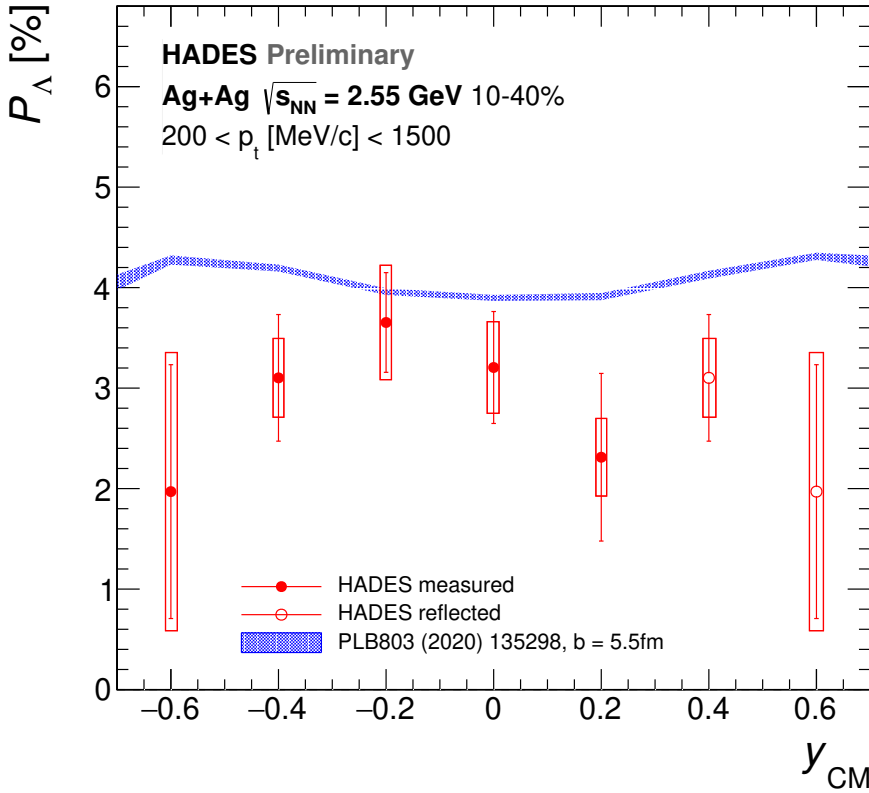


Figure 7.5: Rapidity dependence of the global polarization of the Λ hyperons in Ag+Ag collisions at $\sqrt{s_{NN}} = 2.55$ GeV. The theoretical calculations are based on a connection of the thermal vorticity with the mean spin vector of the Λ hyperon, while the initial state is simulated using the UrQMD model [Vit20]. The theoretical predictions are shown for $p_t > 200$ MeV/c which matches the lower p_t cut applied to the experimental data.

Rapidity	P_Λ [%]	$\Delta^{\text{stat.}}$ [%]	$\Delta^{\text{sys.}}$ [%]
$-0.7 < y_{CM} < -0.5$	1.970	1.263	1.384
$-0.5 < y_{CM} < -0.3$	3.102	0.630	0.392
$-0.3 < y_{CM} < -0.1$	3.653	0.496	0.569
$-0.1 < y_{CM} < 0.1$	3.205	0.557	0.456
$0.1 < y_{CM} < 0.3$	2.312	0.834	0.386

Table 7.2: Rapidity dependent global polarization measurement of the Λ hyperons in Ag+Ag collisions at $\sqrt{s_{NN}} = 2.55$ GeV for 10 – 40 % collision centrality and $200 < p_t$ [MeV/c] < 1500 in transverse momentum. The results including statistical and systematic uncertainties are summarized.

Fig. 7.6 displayed the transverse momentum dependence measured in the Ag+Ag system. The extracted Λ polarization values can be found in Tab. 7.3. Within uncertainties of the measurement, no significant dependence on the transverse momentum is observed. Potentially, there could be a slow decrease of the polarization towards high transverse momenta of $p_t > 800$ MeV/c, but this is also the region with the fewest statistics (see Sec. 4.6) and therefore fluctuations are expected to be larger.

Again the experimental results are shown in Fig. 1.16 with the theoretical predictions calculated according to [Vit20]. The theoretical data points corresponding to Ag+Ag collisions at $b = 5.5\%$ have been taken for comparison. The calculations have been performed in a rapidity range of $-0.7 < y_{CM} < 0.6$ as shown in Fig. 1.17. This is larger than the experimental coverage of $-0.5 < y_{CM} < 0.3$, however, since no significant rapidity dependence is predicted, the influence on the transverse momentum dependence can be neglected. For the transverse momentum of $200 < p_t[\text{MeV}/c] < 800$ the theoretical prediction matches the experimental results. At the higher p_t , the predicted polarization continues to slowly increase, while the experimental data point more in the direction of a slow decrease. However, within the measured uncertainty, no final conclusions can be drawn so far.

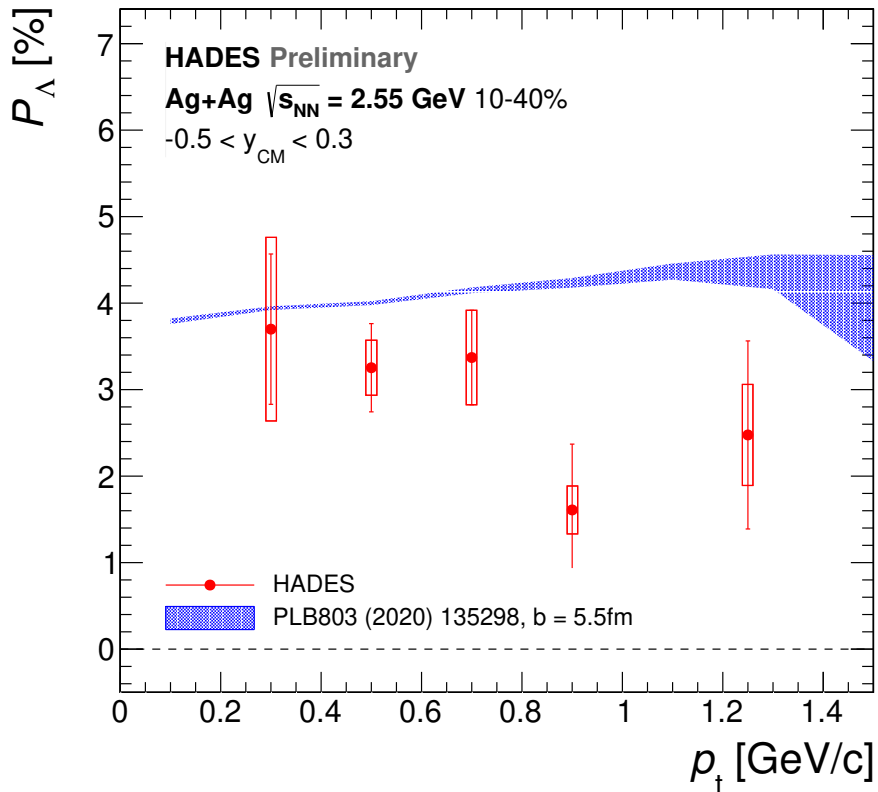


Figure 7.6: Transverse momentum dependence of the global polarization of the Λ hyperons in Ag+Ag collisions at $\sqrt{s_{NN}} = 2.55$ GeV. Note that the last transverse momentum bin covers a larger range of $1000 < p_t[\text{MeV}/c] < 1500$. The theoretical calculations are based on a connection of the thermal vorticity with the mean spin vector of the Λ hyperon, while the initial state is simulated using the UrQMD model [Vit20]. The theoretical predictions are integrated over $-0.7 < y_{CM} < 0.6$, thus cover a larger range in rapidity compared to the experimental results.

Transverse momentum	P_Λ [%]	$\Delta^{\text{stat.}}$ [%]	$\Delta^{\text{sys.}}$ [%]
$200 < p_t [\text{MeV}/c] < 400$	3.699	0.869	1.061
$400 < p_t [\text{MeV}/c] < 600$	3.253	0.510	0.318
$600 < p_t [\text{MeV}/c] < 800$	3.371	0.546	0.546
$800 < p_t [\text{MeV}/c] < 1000$	1.609	0.761	0.277
$1000 < p_t [\text{MeV}/c] < 1500$	2.476	1.087	0.584

Table 7.3: Transverse momentum dependent global polarization measurement of the Λ hyperons in Ag+Ag collisions at $\sqrt{s_{NN}} = 2.55 \text{ GeV}$ for 10 – 40% collision centrality and $-0.5 < y_{CM} < 0.3$ in rapidity. The results including statistical and systematic uncertainties are summarized.

7.3 Conclusions and outlook

The global polarization of the system using the polarization of the Λ hyperons as an observable has been performed in Au+Au and Ag+Ag collisions. The Λ polarization is observed to continue the increasing trend measured by the STAR collaboration [Ada17] down to collision energies of $\sqrt{s_{NN}} = 2.4 \text{ GeV}$. The theoretical calculations are mostly based on relativistic hydrodynamics, assuming at least local thermodynamic equilibrium to be present through all the stages of the collision. Under this assumption, also extending to the spin degrees of freedom, a relation of the thermal vorticity (see Eq. 1.21) and the mean spin vector of spin-1/2 particle could be developed (see Eq. 1.20). Then, any model providing the initial conditions of the heavy-ion collision as the temperature and velocity fields can be used to calculate the vorticity and consequently the spin polarization of the spin-1/2 particles.

While the local thermodynamic equilibrium is a good approximation at higher collision energies where the QGP is formed, its application to the low energy regime around $\sqrt{s_{NN}} \sim 2 \text{ GeV}$ where baryons are the dominant degrees of freedom is questionable. If local thermodynamic equilibrium is not achieved, the temperatures are not well defined and the applicability of the thermal vorticity is not reasonable in this case. Still the calculations can be performed using the kinematical vorticity [Bec15] as it has been done in [Den20]. They found the global polarization to be peaking around $\sqrt{s_{NN}} = 3 - 5 \text{ GeV}$, depending on the collision centrality, and then dropping down quickly to yield zero at $\sqrt{s_{NN}} = 1.9 \text{ GeV}$. As the increasing trend from higher energies down to the maximum is limited to be consistent with the data from the beam energy scan phase I program measure by STAR [Ada17], the calculation does not fit with the experimental results extracted in this work. However, further investigations are necessary in order to include a non-equilibrium treatment of the Λ polarization [Den20].

Similar calculations have been performed in [Jia16] and found the global Λ polarization to peak at $\sqrt{s_{NN}} = 7.7 \text{ GeV}$ and decreasing towards HADES energies to $P_\Lambda \sim 1\%$. Clearly, this is not consistent with the measurements presented in this analysis.

In contrast, predictions based on 3-fluid hydrodynamical model [Iva06, Iva21] suggest a strong enhancement of the global polarization down to $\sqrt{s_{NN}} \sim 2.5 \text{ GeV}$ up to $P_\Lambda = 5 - 7\%$ in peripheral Au+Au collisions, while the results differ about $\Delta P_\Lambda \approx 1\%$ depending on the choice of the equation of state. Consequently, a precise global polarization measurement of the Λ hyperons can also be used to restrict the EoS in the lower energy range, as the Λ polarization for $\sqrt{s_{NN}} > 3 \text{ GeV}$ is found not sensitive to the choice of EoS [Iva21]. For the comparison to the HADES results, the Λ polarization for the example of the crossover EoS has been plotted

in Fig. 7.7 together with the measured data points for collision energies $\sqrt{s_{NN}} < 12$ GeV. The lower boundary of the theoretical band is defined from the calculations at $b = 6$ fm, while the upper boundary corresponds to $b = 8$ fm. This can be converted to the collision centrality to yield $\sim 15 - 30\%$ for the Au+Au and $\sim 25 - 45\%$ for the Ag+Ag system. The Λ polarization measured in the Au+Au system fits well in the trend predicted by 3D-fluid dynamics. The Λ polarization in Ag+Ag is lower, however, as the experimental value is calculated for 10 – 40% centrality, this is more central compared to the theory band and thus expected to be lower. In addition, the effects of the smaller system size might also result in a reduction of the global Λ polarization in Ag+Ag compared to the Au+Au system, as in the later there are more spectators due to the larger mass number.

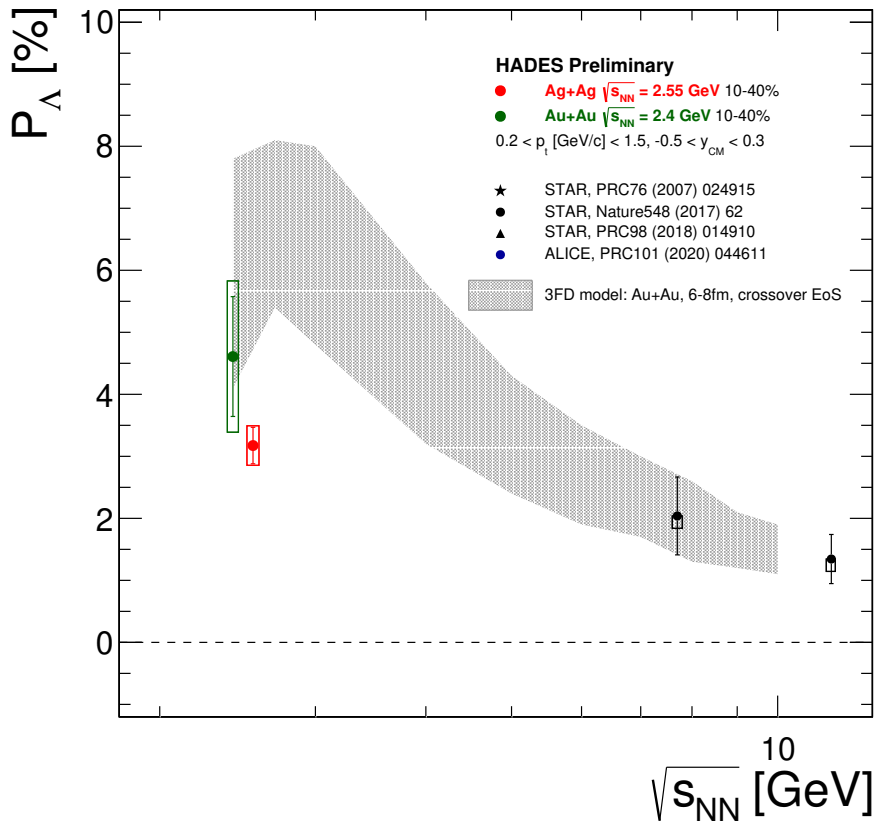


Figure 7.7: Beam energy dependence of the global polarization of the Λ hyperons in the low energy regime (STAR [Ada17], HADES (this study)) in comparison to the theoretical predictions from 3-fluid hydrodynamic models [Iva06, Iva21]. The HADES results have been shifted slightly for better visibility.

The experimental results have also been compared to theoretical calculations based on the local equilibrium hydrodynamic ansatz discussed above [Vit20]. For the determination of the thermal vorticity, i.e. the temperature and velocity fields, the UrQMD transport model has been used [Bas98]. The predictions are in agreement with the experimental findings for the differential global Λ polarization analysis for the centrality, rapidity and transverse momentum dependence.

In summary, it is very interesting that the hydrodynamical approach based on local thermodynamic equilibrium and the calculations from 3D-fluid dynamics are consistent with the ex-

periemtal data, while the non-equilibrium approach based on kinematical vorticity significantly underestimates the measured polarization. Further theoretical studies and new measurements will provide more data to clarify the situation at the lower beam energies. As the hydrodynamical approaches have been successful to describe the beam energy dependence of the global Λ polarization, but had problems at the same time to correctly predict the longitudinal polarization along the beamline discussed in Sec. 1.4.5 which is related to the elliptic flow. However, new theoretical studies advertise the importance of the spin polarization induced by thermal shear to resolve this problem [Fu21, Bec21]. As the elliptic flow changes at HADES energies to be negative, in contrast to the positive elliptic flow at higher energies (see Fig. 1.8), the sign of the longitudinal polarization in the different region of the azimuthal angle can be expected to swap the sign. The large statistics sample of the Ag+Ag data offers a possibility to perform conjoined measurements of elliptic flow and longitudinal polarization to provide new data to further constrain the model calculations.

8 Summary

The first measurements of the global polarization using the Λ hyperon have been performed multi-differentially at low collision energies of $\sqrt{s_{NN}} = 2.4 \text{ GeV}$ in Au+Au and $\sqrt{s_{NN}} = 2.55 \text{ GeV}$ in Ag+Ag collisions, together with a measurement of the azimuthal anisotropy (directed flow). For the reconstruction of the Λ hyperons, a multi-variate analysis (MVA) has been introduced to increase the performance of the selection cuts based on the ROOT package [Hoe07]. The neural network has been trained on Λ hyperons generated with Pluto [Frö09] and embedded to experimental data for the signal, while the mixed-event technique was used to model the combinatorial background. Furthermore, the masses of the identified decay daughters, i.e. p and π^- , are fed to the MVA as it significantly improves the distinction between π^- and μ . The selection on the MVA has been optimized for the maximum significance of the signal in the experimental data. Overall, an increase in the amount of reconstructed Λ hyperons of $\sim 30\%$ has been achieved in comparison to the hard-cut analysis [Sch17].

Two methods for the analysis of both, polarization and flow have been implemented: the $\Delta\phi$ -extraction method and the invariant mass fit method. While the invariant mass fit method has been used to extract the final results, the $\Delta\phi$ method contributes to the systematic uncertainty. During the analysis of the global polarization, a strong dependence on the radial distance of the proton track to a straight line through the collision vertex and parallel to the beamline has been identified. The distribution was not symmetric as in the simulations, consequently an experimental driven approach has been developed to correct for this effect. Consistently, in the Au+Au and Ag+Ag system the radial distance asymmetry (RDA) correction resulted in a slight increase of the Λ polarization measurement. The results proved robust against variations of the correction procedure as the range of application, the number of bins and the choice of signal or total distribution used to calculate the weights.

Based on the event generator Pluto, a simulation framework has been developed to investigate the effect of the HADES detector acceptance on the global polarization measurement. This framework allowed to generate particles with their experimentally measured flow pattern in the directed, i.e. v_1 and elliptic flow, i.e. v_2 , multi-differentially in rapidity and transverse momentum. Additionally, the Λ hyperons have been generated with different amount of polarization. Then the detector acceptance effects have been studied and no significant effect on the polarization measurement has been observed which proved the possibility to measure the global polarization of the Λ hyperons with HADES.

The global polarization measurements using Λ hyperon polarization have been performed. A signal of $P_\Lambda[\%] = 4.609 \pm 0.966(\text{stat.}) \pm 1.220(\text{sys.})$ has been extracted from the Au+Au system, while $P_\Lambda[\%] = 3.174 \pm 0.294(\text{stat.}) \pm 0.319(\text{sys.})$ for the Ag+Ag system has been measured. This is the highest Λ polarization ever measured in heavy-ion collisions. The HADES measurements fit in the increasing trend measured by the STAR collaboration in the beam energy scan phase I down to $\sqrt{s_{NN}} = 7.7 \text{ GeV}$ [Ada17]. As a "turning point" is expected where the polarization is supposed to decrease and yield zero at low collision energies, theoretical predictions for HADES have been diverse.

In [Jia16] the global Λ polarization is predicted to peak at $\sqrt{s_{NN}} = 7.7 \text{ GeV}$ and decreasing towards HADES energies to $P_\Lambda \sim 1\%$. Another theoretical calculation suggests the maximum polarization at around $\sqrt{s_{NN}} = 3\text{--}5 \text{ GeV}$, depending on the collision centrality [Den20]. At lower energies they predicted the global Λ polarization to drop down to zero at $\sqrt{s_{NN}} = 1.9 \text{ GeV}$. Both

these scenarios are not consistent with our measurements.

Other calculations based on 3-fluid hydrodynamical model [Iva06, Iva21] predict a strong enhancement of the global polarization down to $\sqrt{s_{NN}} \sim 2.5$ GeV up to $P_\Lambda = 5 - 7\%$ in peripheral Au+Au collisions, while the results differ about $\Delta P_\Lambda \approx 1\%$ depending on the choice of the equation of state. The Λ polarization measured in the Au+Au system fits well in the trend predicted by 3D-fluid dynamics, while for Ag+Ag system the effect of the different system size would have to be quantified in this theory for a comparison.

Another approach to calculate the global Λ polarization at lower energies has been performed by [Vit20] based on local thermodynamic equilibrium also applying to the spin degrees of freedom. Although this assumption is questionable at the HADES energies, the results are consistent with the measurement. The predicted behavior as a function of the rapidity, transverse momentum and centrality is consistent with the differential measurement in the Ag+Ag system with HADES.

In addition, the directed flow of the Λ hyperon has been measured as a function of the rapidity. From a third order polynomial fit the slope at midrapidity has been extracted and found to be $d v_1/dy|_{y_{CM}=0} = 0.388 \pm 0.023(\text{stat.}) \pm 0.038(\text{sys.})$ in Au+Au collisions, while in Ag+Ag a value $d v_1/dy|_{y_{CM}=0} = 0.289 \pm 0.007(\text{stat.}) \pm 0.025(\text{sys.})$ has been extracted, following the increasing trend of $d v_1/dy|_{y_{CM}=0}$ measured by the E895 and STAR collaborations [Chu01, Ada21]. In comparison to the protons measured with HADES for the same collision systems and energy [Mam20b, Mam20c], the slope of the Λ hyperons is observed to be approximately $\sim 2/3$ of the proton slope, consistent with the measurements from E895 collaboration, but in contrast to the recent measurement from the STAR fixed target run at $\sqrt{s_{NN}} = 4.5$ GeV, where no significant difference has been observed. The simultaneous description of both polarization and directed flow provides challenges to the theory calculations. Thus, the HADES measurements provide important input to constrain the models to identify the underlying nature of the effect.

Bibliography

[Aad12] G. Aad et al. (ATLAS Collaboration), "Observation of a new particle in the search for the Standard Model Higgs boson with the ATLAS detector at the LHC", Phys. Rev. Lett. B716 (2012) 1-29, arXiv:1207.7214 [hep-ex].

[Abb17] B.P. Abbott et al. (LIGO and VIRGO Collaboration), "GW170817: Observation of Gravitational Waves from a Binary Neutron Star Inspiral", Phys. Rev. Lett. 119 (2017) 16, 161101, arXiv:1710.05832 [gr-qc].

[Abe07] B.I. Abelev et al. (STAR Collaboration), "Global polarization measurement in Au+Au collisions", Phys. Rev. C 76 (2007) 024915, arXiv:0705.1691 [nucl-ex].

[Ach20] S. Acharya et al. (ALICE Collaboration), "Global polarization of $\Lambda\bar{\Lambda}$ hyperons in Pb+Pb collisions at $\sqrt{s_{NN}} = 2.76$ and 5.02 TeV", Phys. Rev. C101 (2020) 4, 044611, arXiv:1909.01281 [nucl-ex].

[Ada05] J. Adams et al. (STAR Collaboration), "Experimental and theoretical challenges in the search for the quark gluon plasma: The STAR Collaboration's critical assessment of the evidence from RHIC collisions", Nucl. Phys. A757 (2005) 102-183, arXiv:nucl-ex/0501009 [nucl-ex].

[Ada12] A. Adams et al., "Strongly correlated quantum fluids", New J. Phys. 14 (2012), arXiv:1205.5180 [hep-th].

[Ada13] L. Adamczyk et al., "Elliptic flow of identified hadrons in Au+Au collisions at $\sqrt{s_{NN}} = 7.7 - 62.4$ GeV", Phys. Rev. C88 (2013) 014902, arXiv:1301.2348 [nucl-ex].

[Ada14] L. Adamczyk et al. (STAR Collaboration), "Beam-Energy Dependence of the Directed Flow on Protons, Antiprotons, and Pions in Au+Au Collisions", Phys. Rev. Lett. 112 (2014) 16, 162301, arXiv:1401.3043 [nucl-ex].

[Ada17] L. Adamczyk et al. (STAR Collaboration), "Global Λ hyperon polarization in nuclear collisions: evidence for the most vortical fluid", Nature 548 (2017) 62-65, arXiv:1701.06657 [nucl-ex].

[Ada18a] J. Adam et al. (STAR Collaboration), "Global polarization of Λ hyperons in Au+Au collisions at $\sqrt{s_{NN}} = 200$ GeV", Phys. Rev. C 98 (2018) 014910, arXiv:1805.04400 [nucl-ex].

[Ada18b] L. Adamczyk et al. (STAR Collaboration), "Beam-Energy Dependence of the Directed Flow of Λ , $\bar{\Lambda}$, K^\pm , K_s^0 and ϕ in Au+Au Collisions", Phys. Rev. Lett. 120 (2018) 6, 062301, arXiv:1708.07132 [hep-ex].

[Ada18c] J. Adamczewski-Musch et al., "Centrality determination of Au+Au collisions at 1.23 AGeV with HADES", Eur. Phys. J. A 54 (2018) 85, arXiv:1712.07993 [nucl-ex].

[Ada19a] J. Adamczewski-Musch et al. (HADES Collaboration), "Probing dense baryon-rich matter with virtual photons", Nature Phys. 15 (2019) 10, 1040-1045.

[Ada19b] J. Adamczewski-Musch et al. (HADES Collaboration), "Sub-threshold production of K_S^0 mesons and Λ hyperons in Au+Au collisions at $\sqrt{s_{NN}} = 2.4$ GeV", Phys. Lett. B793 (2019) 457-463, arXiv:1812.07304 [nucl-ex].

[Ada20a] J. Adamczewski-Musch et al. (HADES Collaboration), "Directed, elliptic and higher order flow harmonics of protons, deuterons and tritons in Au+Au collisions at $\sqrt{s_{NN}} = 2.4$ GeV", Phys. Rev. Lett. 125 (2020) 262301, arXiv:2005.12217 [nucl-ex].

[Ada20b] J. Adamczewski-Musch et al. (HADES Collaboration), "Charged-pion production in Au+Au collisions at $\sqrt{s_{NN}} = 2.4$ GeV: HADES Collaboration", Eur. Phys. J. A56 (2020) 10, 259, arXiv:2005.08774 [nucl-ex].

[Ada20c] J. Adam et al. (STAR Collaboration), "Global polarization of Ξ and Ω hyperons in Au+Au collisions at $\sqrt{s_{NN}} = 200$ GeV", arXiv:2012.13601 [nucl-ex] (2020).

[Ada21] J. Adam et al. (STAR Collaboration), "Flow and interferometry results from Au+Au collisions at $\sqrt{s_{NN}} = 4.5$ GeV", Phys. Rev. C103 (2021) 3, 034908, arXiv:2007.14005 [nucl-ex].

[Adc05] K. Adcox et al. (PHENIX Collaboration), "Formation of dense matter in relativistic nucleus-nucleus collisions at RHIC: Experimental evaluation by the PHENIX collaboration", Nucl. Phys. A757 (2005) 184-283, arXiv:nucl-ex/0410003 [nucl-ex].

[And05] A. Andronic et al. (FOPI Collaboration), "Excitation function of elliptic flow in Au+Au collisions and the nuclear matter equation of state", Phys. Lett. B612 (2005) 173-180, arXiv:nucl-ex/0411024 [nucl-ex].

[Aga09] G. Agakishiev et al., "The High-Acceptance Dielectron Spectrometer HADES", Eur.Phys.J. A41, 243-277 (2009).

[Ago02] C. Agodi et al., "The HADES time-of-flight wall", Nucl. Instrum. Meth. A, 492 (2002) 14-25.

[And37] C. Anderson et al., "Note on the Nature of Cosmic Ray Particles", Phys. Rev. 51 (1937) 884-886.

[And14] O. Andreeva et al., "Forward scintillation hodoscope for nuclear fragment detection at the high acceptance dielectron spectrometer (HADES) setup", Instrum. and Exp. Tech. 57 (2014) 103-119.

[Ant13] J. Antoniadis et al., "A Massive Pulsar in a Compact Relativistic Binary", Science 340 (2013) 6131, arXiv:1304.6875 [astro-ph.HE].

[Ars05] I. Arsene et al. (BRAHMS Collaboration), "Quark gluon plasma and color glass condensate at RHIC? The Perspective from the BRAHMS experiment", Nucl. Phys. A757 (2005) 1-27, arXiv:nucl-ex/0410020 [nucl-ex].

[Bac05] B.B. Back et al. (PHOBOS Collaboration), "The PHOBOS perspective on discoveries at RHIC", Nucl. Phys. A757 (2005) 28-101, arXiv:nucl-ex/0410022 [nucl-ex].

[Bal04] A. Balanda et al., "The HADES Pre-Shower detector", Nucl. Instrum. Meth. A, 531 (2004) 445-458.

[Bar02] R. Barlow, "Systematic errors: Facts and fictions", Advanced Statistical Techniques in Particle Physics (2002) 134-144, arXiv:hep-ex/0207026 [hep-ex].

[Bar15] S.J. Barnett, "Magnetization by rotation", Phys. Rev. 6 (1915) 239-270.

[Bar97] J. Barrette et al., "Proton and Pion Production Relative to the Reaction Plane in Au+Au Collisions at AGS Energies", Phys. Rev. C 56 (1997) 3254-3264, arXiv:nucl-ex/9707002.

[Bar08] Jr. CdC Barros and Y. Hama, "Antihyperon polarization in high-energy inclusive reactions", Int. J. Mod. Phys. E17 (2008) 371-392, arXiv:hep-ph/0507013 [hep-ph].

[Bar11] Jr. CdC Barros and Y. Hama, " Λ and $\bar{\Lambda}$ polarization in Au-Au collisions at RHIC", Phys. Lett. B699 (2011) 74-77, arXiv:0712.3447 [hep-ph].

[Bas98] S. Bass et al., "Microscopic models for ultrarelativistic heavy ion collisions", Prog. Part. Nucl. Phys. 41 (1998) 255-370.

[Baz18] M. Baznat et al., "Hyperon polarization in heavy-ion collisions and holographic gravitational anomaly", Phys. Rev. C97 (2018) 4, 041902, arXiv:1701.00923 [nucl-th].

[Bec08] F. Becattini et al., "Angular momentum conservation in heavy-ion collisions at very high energies", Phys. Rev. C77 (2008) 024906, arXiv:0711.1253 [nucl-th].

[Bec13] F. Becattini et al., "Relativistic distribution function for particles with spin at local thermodynamical equilibrium", Ann. Phys. 338 (2013) 32-49, arXiv:1303.3431 [nucl-th].

[Bec15] F. Becattini et al., "A study of vorticity formation in high energy nuclear collisions", Eur. Phys. J. C75 (2015) 9, 406, arXiv:1501.04468 [nucl-th].

[Bec17] F. Becattini et al., "Global hyperon polarization at local thermodynamic equilibrium with vorticity, magnetic field and feed-down", Phys. Rev. C95 (2017) 5, 054902, arXiv:1610.02506 [nucl-th].

[Bec18a] F. Becattini et al., "Spin tensor and its role in non-equilibrium thermodynamics", Phys. Lett. B789 (2019) 419-425, arXiv:1807.10994 [hep-th].

[Bec18b] F. Becattini and I. Karpenko, "Collective Longitudinal Polarization in Relativistic Heavy-Ion collisions at Very High Energy", Phys. Rev. Lett. 120 (2018) 1, 012302, arXiv:1707.07984 [nucl-th].

[Bec19] F. Becattini et al., "Polarization transfer in hyperon decays and its effect in relativistic nuclear collisions", Eur. Phys. J. C79 (2019) 9, 741, arXiv:1905.03123 [nucl-th].

[Bec20] F. Becattini and M.A. Lisa, "Polarization and vorticity in the Quark-Gluon Plasma", Ann. Rev. Nucl. Part. Sci. 70 (2020) 395-423, arXiv:2003.03640 [nucl-ex].

[Bec21] F. Becattini et al., "Local polarization and isothermal local equilibrium in relativistic heavy ion collisions", arXiv:2103.14621 [nucl-th].

[Bel09] D. Belver et al., "The HADES RPC inner TOF wall", Nucl. Instrum. Meth. A, 602 (2009) 687-690.

[Ber81] G. Bertsch and J. Cugnon, "Entropy production in high energy collisions", Phys. Rev. C24 (1981) 2514-2520.

[Bor04] N. Borghini and J.Y. Ollitrault, "Azimuthally sensitive correlations in nucleus-nucleus collisions", Phys. Rev. C70 (2004) 064905, arXiv:nucl-th/0407041 [nucl-th].

[Bro90] F.R. Brown et al., "On the existence of a phase transition for QCD with three light quarks", Phys. Rev. Lett. 65 (1990) 2491-2494.

[Bru87] R. Brun et al., "GEANT3" (1987).

[Bru97] R. Brun and F. Rademakers, "ROOT, an object-oriented data analysis framework", Nucl. Instr. Meth. A389 (1997) 81.

[Cab09] P. Cabanelas et al., "Performance of multi-gap timing RPCs for relativistic ions in the range $Z=1-6$ ", Rev. Mod. Phys. 75, p. 1243-1286 (2009), arXiv:0905.0682 [nucl-ex].

[Cha32] J. Chadwick, "The Existence of a neutron", Proc. Roy. Soc. A, 136 (1932) 692-708.

[Cha08] D.J. Champion et al., "An Eccentric Binary Millisecond Pulsar in the Galactic Plane", Science 320 (2008) 1309-1312, arXiv:0805.2396 [astro-ph].

[Che07] J.H. Chen (STAR Collaboration), "Spin alignment of $K^{*0}(892)$ and $\phi(1020)$ mesons in Au+Au and p+p collisions at $\sqrt{s_{NN}} = 200$ GeV, J. Phys. G 34 (2007) 331-336.

[Chu01] P. Chung et al. (E895 Collaboration), "Directed flow of Lambda hyperons in 2-AGeV to 6-AGeV Au+Au collisions", Phys. Rev. Lett. 86 (2001) 2533-2536, arXiv:nucl-ex/0101002 [nucl-ex].

[Cse13] L.P. Csernai et al., "Flow Vorticity in Peripheral High Energy Heavy Ion Collisions", Phys. Rev. C87 (2013) 3, 034906, arXiv:1302.5310 [nucl-th].

[Czy11] W. Czyzycki et al., "Electromagnetic Calorimeter for HADES", arXiv:1109.5550 [nucl-ex] (2011).

[Dan01] P. Danielewicz, "Nuclear equation of state", AIP Conf. Proc. 597 (2001) 1, 24-42, arXiv:nucl-th/0112006 [nucl-th].

[Dan02] P. Danielewicz et al., "Determination of the equation of state of dense matter", Science 298 (2002) 1592-1596, arXiv:nucl-th/0208016.

[Dem10] P. Demorest et al., "Shapiro Delay Measurement of A Two Solar Mass Neutron Star", Nature 467 (2010) 1081-1083, arXiv:1010.5788 [astro-ph.HE].

[Den20] X.-G. Deng et al., "Vorticity in low-energy heavy-ion collisions", Phys. Rev. C101 (2020) 6, 064908, arXiv:2001.01371 [nucl-th].

[Ein15] A. Einstein et al., "Experimenteller Nachweis der Ampereschen Molekularströme", Verh. Dtsch. Phys. Ges. 17 (1915) 152-170.

[Eng64] F. Englert and R. Brout, "Broken Symmetry and the Mass of Gauge Vector Mesons", Phys. Rev. Lett. 13 (1964) 321-323.

[Fev16] A. Le Fèvre et al., "Constraining the nuclear matter equation of state around twice saturation density", Nucl. Phys. A945 (2016) 112-133, arXiv:1501.05246 [nucl-ex].

[Flo18] W. Florkowski et al., "Thermodynamic versus kinetic approach to polarization-vorticity coupling", Phys. Rev. C98 (2018) 4, 044906, arXiv:1806.02616 [hep-ph].

[Flo19a] W. Florkowski et al., "Relativistic hydrodynamics with spin", Nucl. Phys. A982 (2019) 523-526, arXiv:1807.04946 [nucl-th].

[Flo19b] W. Florkowski et al., "Relativistic hydrodynamics with spin-polarized fluids", Prog. Part. Nucl. Phys. 108 (2019) 103709, arXiv:1811.04409 [nucl-th].

[Fod04] Z. Fodor and S.D. Katz, "Critical point of QCD at finite T and mu, lattice results for physical quark masses", JHEP 04 (2004) 050, arXiv:hep-lat/0402006 [hep-lat].

[Frö08] I. Fröhlich et al., "A General Purpose Trigger and Readout Board for HADES and FAIR-Experiments", IEEE Trans. Nucl. Sci., Vol. 55 (2008) 59-66.

[Frö09] I. Fröhlich et al., "Design of the Pluto Event Generator", arXiv:0905.2568v1 (2009).

[Fu21] B. Fu et al., "Shear-induced spin polarization in heavy-ion collisions", arXiv:2103.10403 [hep-ph].

[Gal18] T. Galatyuk et al., "Tests of the Electromagnetic Calorimeter for HADES Experiment at GSI", KnE Energ.Phys. 3 (2018) 162-169.

[Gal21] A.D. Gallegos et al., "Hydrodynamics of spin currents", arXiv:2101.04759 [hep-th].

[Goy17] V.A. Goy et al., "Sign problem in finite density lattice QCD", PTEP 2017 (2017) 3, 031D01, arXiv:1611.08093 [hep-lat].

[Hat19] K. Hattori et al., "Fate of spin polarization in a relativistic fluid: An entropy-current analysis", Phys. Lett. B795 (2019) 100-106, arXiv:1901.06615 [hep-th].

[Hei13] U. Heinz and R. Snellings, "Collective flow and viscosity in relativistic heavy-ion collisions", Ann. Rev. Nucl. Part. Sci. 63 (2013) 123-151, arXiv:1301.2826 [nucl-th].

[Hig64] PW. Higgs, "Broken Symmetries and the Masses of Gauge Bosons", Phys. Rev. Lett. 13 (1964) 508-509.

[Hoe07] A. Hoecker et al., "TMVA: Toolkit for Multivariate Data Analysis", PoS A CAT 040 (2007).

[Hua20] X.-G. Huang et al., "Vorticity and Spin Polarization in Heavy Ion Collisions: Transport Models", arXiv:2010.08937 [nucl-th].

[Iva06] Y.B. Ivanov et al., "Relativistic heavy-ion collisions within 3-fluid hydrodynamics: Hadronic scenario", Phys. Rev. C73 (2006) 044904, arXiv:nucl-th/0503088 [nucl-th].

[Iva19] Y.B. Ivanov et al., "Estimates of hyperon polarization in heavy-ion collisions at collisions energies $\sqrt{s_{NN}} = 4-40$ GeV, Phys. Rev. C100 (2019) 1, 014908, arXiv:1903.05455 [nucl-th].

[Iva20] Y.B. Ivanov et al., "Correlation between global polarization, angular momentum, and flow in heavy-ion collisions", Phys. Rev. C102 (2020) 2, 024916, arXiv:2004.05166 [nucl-th].

[Iva21] Y.B. Ivanov, "Global Λ polarization in moderately relativistic nuclear collisions", Phys. Rev. C103 (2021) 3, L031903, arXiv:2012.07597 [nucl-th].

[Jia16] Y. Jiang et al., "Rotating quark-gluon plasma in relativistic heavy-ion collisions", Phys. Rev. C94 (2016) 4, 044910, arXiv:1602.06580 [hep-ph].

[Kar15a] I. Karpenko et al., "Estimation of the shear viscosity at finite net-baryon density from A+A collision data at $\sqrt{s_{NN}} = 7.7 - 200 \text{ GeV}$ ", Phys. Rev. C91 (2015) 6, 064901, arXiv:1502.01978 [nucl-th].

[Kar15b] B. Kardan, "Centrality Determination at 1.23AGeV Gold-Gold Collision and Readout-Electronics for the HADES Electromagnetic Calorimeter", Diploma thesis, Goethe Universität Frankfurt (2015).

[Kar17] I. Karpenko and F. Becattini, "Study of Λ polarization in relativistic nuclear collisions at $\sqrt{s_{NN}} = 7.7 - 200 \text{ GeV}$ ", Eur. Phys. J. C77 (2017) 4, 213, arXiv:1610.04717 [nucl-th].

[Kar18] B. Kardan, "Flow of protons and light nuclei", Talk at the HADES Collaboration meeting XXXV (2018).

[Kar21] I. Karpenko, "Vorticity and Polarization in Heavy Ion Collisions: Hydrodynamics Models", arXiv:2101.04963.

[Kin11] B. Kindler et al., "Targets for the electron-positron pair spectrometer HADES", Nucl. Instrum. Meth. A, 655 (2011) 95-99.

[Kor14] G. Kornakov et al., "Time of flight measurement in heavy-ion collisions with the HADES RPC TOF wall", JINST 9 (2014) 11, C11015.

[Kor17] F. Kornas, "Hunting for the chiral magnetic effect", Master thesis, Technische Universität Darmstadt (2017).

[Lat47] C. Lattes et al., "Processes involving Charged Mesons", Nature 159 (1947) 694-697.

[Li17] H. Li et al., "Global Λ polarization in heavy-ion collisions from a transport model", Phys. Rev. C96 (2017), 5, 054908, arXiv:1704.01507 [nucl-th].

[Lia04] Z.-T. Liang et al., "Globally polarized quark-gluon plasma in non-central A+A collisions", Phys. Rev. Lett. 94 (2005) 102301, arXiv:nucl-th/0410079 [nucl-th].

[Lia05] Z.-T. Liang et al., "Spin Alignment of Vector Mesons in Non-central A+A Collisions", Phys. Lett. B629 (2005) 20.

[Lia21] J. Liao, "Hyperon Global Polarization in Nucleus-Nucleus Collisions at sub-10-GeV Beam Energy", Talk at the 19th Conference on Strangeness in Quark Matter (2021).

[Lin05] Z.-W. Lin et al., "A Multi-phase transport model for relativistic heavy ion collisions", Phys. Rev. C72 (2005) 064901, arXiv:nucl-th/0411110 [nucl-th].

[Liu00] H. Liu et al. (E895 Collaboratio), Sideward flow in Au+Au collisions between 2-A-GeV and 8-A-GeV", Phys. Rev. Lett. 84 (2000) 5488-5492, arXiv:nucl-ex/0005005 [nucl-ex].

[Liu21] S.Y.F. Liu and Y. Yin, "Spin polarization induced by the hydrodynamic gradient", arXiv:2103.09200 [hep-ph].

[Lon15] D. Lonardoni et al., "Hyperon puzzle: Hints from Quantum Monte Carlo Calculations", Phys. Rev. Lett. 114 (2015) 9, 092301, arXiv:1407.4448 [nucl-th].

[Mam20a] M. Mamaev, "Studies on proton flow systematics", Talk at the HADES Collaboration Meeting XXXIX (2020).

[Mam20b] M. Mamaev (HADES Collaboration), "Directed flow of protons with the event plane and scalar product methods in the HADES experiment at SIS18", *J. Phys. Conf. Ser.* 1690 (2020) 1, 012122.

[Mam20c] M. Mamaev (HADES Collaboration), "Estimating non-flow effects in measurements of directed flow of protons with the HADES experiment at GSI", arXiv:2012.04433 [nucl-ex].

[Mar15] J. Markert, "Software and DST status", Talk at the HADES Collaboration Meeting XXX (2015).

[Mar16] J. Markert, "Software and DST status", Talk at the HADES Collaboration Meeting XXXI (2016).

[Mas16] H. Masui et al., "Event plane resolution correction for azimuthal anisotropy in wide centrality bins", *Nucl. Instrum. Meth. A* 833 (2016), 181-185.

[Mic12] J. Michel, "Development and Implementation of a New Trigger and Data Acquisition System for the HADES Detector", PhD thesis, Goethe Universität Frankfurt (2012).

[Mil07] M. L. Miller et al., "Glauber modeling in high energy nuclear collisions", *Ann. Rev. Nucl. Part. Sci.* 57 (2007) 205-243, arXiv:nucl-ex/0701025 [nucl-ex].

[Moh21] B. Mohanty (ALICE Collaboration), "Spin alignment of vector mesons with ALICE at the LHC", *PoS ICHEP2020* (2021) 555, arXiv:2012.04167 [nucl-ex].

[Mue04] C. Müntz et al., "The HADES Tracking System", *Nucl. Instrum. Meth. A*, 535 (2004) 242-246.

[Nii19] T. Niida (STAR Collaboration), "Global and local polarization of Λ hyperons in Au+Au collisions at 200 GeV from STAR", *Nucl. Phys. A* 982 (2019) 511-514, arXiv:1808.10482 [nucl-ex].

[Oll96] J.-Y. Ollitrault, "A method of reconstructing azimuthal distributions in heavy ion collisions", Proceedings of the XXV International Symposium on Multiparticle Dynamics (1996) 290-296, arXiv:nucl-ex/9711003.

[Oll98] J.-Y. Ollitrault, "Flow systematics from SIS to SPS energies", *Nucl. Phys. A* 638 (1998) 195-206, arXiv:nucl-ex/9802005.

[Pie10] J. Pietraszko et al., "Diamonds as timing detectors for minimum-ionizing particles: The HADES proton-beam monitor and START signal detector for time of flight measurements", *Nucl. Instrum. Meth. A*, 618 (2010) 121-123.

[Pie13] J. Pietraszko, "Beam detectors in Au+Au run and future developments", Talk in the HADES Collaboration Meeting XXVI, Prague, Czech Republic (2013).

[Pie14] J. Pietraszko et al., "Radiation damage in single crystal CVD diamond material investigated with a high current relativistic ^{197}Au beam", *Nucl. Instrum. Meth. A*, 763 (2014) 1-5.

[Pos98] A.M. Poskanzer et al., "Methods for analyzing anisotropic flow in relativistic nuclear collisions", Phys. Rev. C 58 (1998) 1671-1678, arXiv:nucl-ex/9805001 [nucl-ex].

[Pov14] B. Povh et al., "Teilchen und Kerne - Eine Einführung in die physikalischen Konzepte", Springer Verlag (2014) 9. Auflage.

[Pro18] G.Y. Prokhorov et al., "Rotation and spin dynamics in heavy-ion collisions", EPJ Web Conf. 191 (2018) 05006.

[Rei12] W. Reisdorf et al. (FOPI Collaboration), "Systematics of azimuthal asymmetries in heavy ion collisions in the 1 A GeV regime", Nucl. Phys. A876 (2012) 1-60, arXiv:1112.3180 [nucl-ex].

[Rus06] A. Rustamov, "Exclusive η Meson Reconstruction in Proton-Proton Collisions at 2.2 GeV with the HADES Spectrometer and High Resolution Tracking", PhD thesis, Technische Universität Darmstadt (2006).

[Rut11] E. Rutherford, "The Scattering of α and β Particles by Matter and the Structure of the Atom", Philosophical Magazine Series 6, 21 (1911) 669-688.

[Sad07] A. Sadovsky, "Investigation of K^+ meson production in C+C collisions at 2 AGeV with HADES", PhD thesis, Technische Universität Dresden (2007).

[Sal94] P. Salabura et al. (HADES Collaboration), "Proposal for a High-Acceptance Di-Electron Spectrometer", GSI (1994).

[Sav64] A. Savitzky and M.J.E. Golay, "Smoothing and Differentiation of Data by Simplified Least Squares Procedures", Analytical Chemistry 36 (1964) 8, 1627-1639.

[Sch93] E. Schnedermann et al., "Thermal phenomenology of hadrons from 200-A/GeV S+S collisions", Phys. Rev. C48 (1993) 2462-2475, arXiv:nucl-th/9307020 [nucl-th].

[Sch07] B.-J. Schäfer et al., "The Phase Structure of the Polyakov–Quark-Meson Model", Phys. Rev. D 76 (2007) 074023, arXiv:0704.3234 [hep-ph].

[Sch08] A. Schmah, "Produktion von Seltsamkeit in Ar+KCl Reaktionen bei 1.756 AGeV mit HADES", PhD thesis, Technische Universität Darmstadt (2008).

[Sch16] H. Schuldes, "Charged kaon and phi reconstruction in Au+Au collisions at 1.23 AGeV", PhD thesis, Goethe Universität Frankfurt (2016).

[Sch17] T. Scheib, " Λ and K_S^0 production in Au+Au collisions at 1.23 AGeV", PhD thesis, Goethe Universität Frankfurt (2017).

[Sel06] Ilya Selyuzhenkov (STAR Collaboration), "Global polarization measurement in Au+Au collisions", J. Phys. G 32 (2006) 557-562, arXiv:nucl-ex/0605035 [nucl-ex].

[Sel07a] Ilya Selyuzhenkov (STAR Collaboration), "Centrality dependence of hyperon global polarization in Au+Au collisions at RHIC", J. Phys. G 34 (2007) 1099-1102, arXiv:nucl-ex/0701034 [nucl-ex].

[Sel07b] Ilya Selyuzhenkov (STAR Collaboration), "Anti-Lambda hyperon global polarization in Au+Au collisions at RHIC", arXiv:nucl-ex/0702001 [nucl-ex] (2007).

[Sel17] P. Sellheim, "Reconstruction of the low-mass dielectron signal in 1.23AGeV Au+Au collisions", PhD thesis, Goethe Universität Frankfurt (2017).

[She21] D. She et al., "Relativistic Viscous Hydrodynamics with Angular Momentum", arXiv:2105.04060 [nucl-th].

[Shi20] S. Shi et al., "From chiral kinetic theory to relativistic viscous spin hydrodynamics", Phys. Rev. C103 (2021) 4, 044906, arXiv:2008.08618 [nucl-th].

[Sie79] P.J. Siemens and J.O. Rasmussen, "Evidence for a blast wave from compress nuclear matter", Phys. Rev. Lett. 42 (1979) 880-887.

[Sin21] S. Singha (STAR Collaboration), "Measurement of global spin alignment of K^{*0} and ϕ vector mesons using the STAR detector at RHIC", Nucl. Phys. A1005 (2021) 121733, arXiv:2002.07427 [nucl-ex].

[Sor17] A. Sorin and O. Teryaev, "Axial anomaly and energy dependence of hyperon polarization in heavy-ion collisions", Phys. Rev. C95 (2017) 1, 011902, arXiv:1606.08398 [nucl-th].

[Spi18] S. Spies, "Rekonstruktion schwacher Zerfälle in Au+Au Kollisionen bei 1.23AGeV", Master thesis, Goethe Universität Frankfurt (2018).

[Spi20] S. Spies, "Weak decays in Ag+Ag", Talk at the HADES Collaboration Meeting XXXIX (2020).

[Ste09] M.A. Stephanov, "Non-Gaussian fluctuations near the QCD critical point", Phys. Rev. Lett. 102 (2009) 032301, arXiv:0809.3450 [hep-ph].

[Ste11] M.A. Stephanov, "On the sign of kurtosis near the QCD critical point", Phys. Rev. Lett. 107 (2011) 052301, arXiv:1104.1627 [hep-ph].

[Svo14] O. Svoboda et al., "Electromagnetic calorimeter for the HADES@FAIR experiment", JINST 9 (2014) C05002.

[Tak16] M. Takahashi el al., "Spin hydrodynamic generation", Nature Phys. 12 (2016) 52-56.

[Tho97] J. Thomson, "Cathode Rays", The London, Edinburgh and Dublin Philosophical Magazine and Journal of Science, 44:269 (1897) 293-316.

[Tlu17] P. Tlusty, M. Gumberidze, HADES Internal Reports.

[Vit20] O. Vitiuk et al., "Is different Λ and $\bar{\Lambda}$ polarization caused by different spatio-temporal freeze-out picture?", Phys. Lett. B803 (2020) 135298, arXiv:1910.06292 [hep-ph].

[Vit21] O. Vitiuk, private communication.

[Vol96] S. Voloshin and Y. Zhang, "Flow Study in Relativistic Nuclear Collisions by Fourier Expansion of Azimuthal Particle Distributions", Z. Phys. C70 (1996) 665, arXiv:hep-ph/9407282 [hep-ph].

[Vol04] S.A. Voloshin, "Polarized secondary particles in unpolarized high energy hadron-hadron collisions?", arXiv:nucl-th/0410089 [nucl-th] (2004).

[Vol10] S.A. Voloshin et al., "Collective phenomena in non-central nuclear collisions", Landolt-Bornstein 23 (2010) 293-333, arXiv:0809.2949 [nucl-ex].

[Vol17] S.A. Voloshin, "Vorticity and particle polarization in heavy-ion collisions (experimental perspective)", EPJ Web Conf. 171 (2018) 07002, arXiv:1710.08934 [nucl-ex].

[Wig32] E.P. Wigner, "On the quantum correction for thermodynamic equilibrium", Phys. Rev. 40 (1932) 749-759.

[Wil74] K.G. Wilson, "Confinement of Quarks", Phys. Rev. D10 (1974) 2445-2459.

[Win74] H. Wind, "Momentum analysis by using a quintic spline model for the track", Nucl. Instr. Meth. 115 (1974) 431.

[Wu57] C.S. Wu et al., "Experimental Test of Parity Conservation in β Decay", Phys. Rev. 105 (1957) 1413-1414.

[Wu19] H.-Z. Wu et al., "Local spin polarization in high energy heavy ion collisions", Phys. Rev. Research 1 (2019) 033058, arXiv:1906.09385 [nucl-th].

[Xia19] X.-L. Xia et al., "Feed-down effect on Λ spin polarization", Phys. Rev. C100 (2019) 1, 014913, arXiv:1905.03120 [nucl.th].

[Xie17] Y. Xie et al., "Global Λ polarization in high energy collisions", Phys. Rev. C95 (2017) 3, 031901, arXiv:1703.03770.

[Yuk35] Hideki Yukawa, "On the Interaction of Elementary Particles I", Proc. Phys. Math. Soc. Jap. 17 (1935) 48-57.

[Zyl20] P. A. Zyla et al. (Particle Data Group), Prog. Theor. Exp. Phys. 2020, 083C01 (2020).

9 Appendix

9.1 Natural units

Usually in relativistic quantum mechanics the natural units are used. The unit of length is defined as the distance, the light travels in vacuum in one second. This sets the value for the velocity of light $c = 1$. Due to this, c is usually omitted when appearing in an equation. The same can be done for the reduced Planck's constant \hbar which also appears very often in quantum mechanical relations. By redefining the electric charge e , the reduced Planck's constant can be set to $\hbar = 1$. This gives a lot more simplicity to the equations used, however, it has to be taken into account when physical dimensions are determined.

9.2 Kinematical Quantities

The data analyzed in this work was collected from Au+Au collisions with a beam energy of $E_{\text{Beam}} = 1.23 \text{ GeV}$. This means that each nucleon of the incoming Au ion has a kinetic energy of $E_{\text{kin}} = 1.23 \text{ GeV}$. Hence, their total energy is $E_0 = E_{\text{kin}} + m_N$, where m_N is the mass of a nucleon, i.e. the average of the proton and neutron mass $m_N = (m_p + m_n)/2 = 0.94 \text{ GeV}$.

An invariant quantity, which has the same value in each system, is the square of the mass of a system of particles defined as

$$s = \left(\sum_i P_i^\mu \right) \left(\sum_i P_{i,\mu} \right). \quad (9.1)$$

Here, i is the index for the particle and P^μ is the corresponding 4-momentum vector. In our case we consider a collision of two nucleons, align the z-Axis along the beam direction and hence the momentum in x- and y-direction is $p_x = p_y = 0$. Therefore, these two dimensions can be omitted from the calculation and the 4-momentum for the incoming particle reduces to $P_1^\mu = (E, p_z)$ in the laboratory frame. Then the target particle is at rest and $P_2^\mu = (m_N, 0)$. Inserting this into equation 9.1 and using $m^2 = E^2 - p^2$ leads to:

$$s_{NN} = 2m_N (E_0 + m_N). \quad (9.2)$$

If we insert the values from above, we can calculate the so-called nucleon-nucleon collision energy which is $\sqrt{s}_{NN} = 2.4 \text{ GeV}$. This is the mean energy in a nucleon-nucleon collision which can be used to produce particles. This approach is very useful in order to investigate to which extend a heavy-ion collision can be described by the sum of single nucleon-nucleon collisions or many-particle effects play a role.

Another important quantity in heavy-ion collisions is the rapidity y which is defined by:

$$y = \frac{1}{2} \ln \left(\frac{E + p_L}{E - p_L} \right). \quad (9.3)$$

Here E is the total energy and p_L is the longitudinal momentum component. Hence the rapidity is a measure for the longitudinal velocity. The advantage of this quantity is that rapidities are additive quantities. This means that the rapidity distribution dN/dy as well as rapidity

differences $|y_1 - y_2|$ of different systems 1 and 2 are invariant under Lorentz transformations. Consequently, the rapidity in the laboratory frame can be transformed to the center-of-mass frame by subtracting the so-called midrapidity y_{mid} . The midrapidity is the rapidity of the center-of-mass frame itself. We can calculate the beam rapidity for a collision of two Au ions by:

$$y_{\text{Beam}} = \frac{1}{2} \ln \left(\frac{E_{\text{Au}} + p_{\text{Au}}}{E_{\text{Au}} - p_{\text{Au}}} \right), \quad (9.4)$$

where $p_{\text{Au}} = \sqrt{E_{\text{Au}}^2 - m_{\text{Au}}^2}$ and $E_{\text{Au}} = E_{\text{Beam}} \cdot A_{\text{Au}} + m_{\text{Au}}$ with the mass number of Au $A_{\text{Au}} = 197$ and its mass $m_{\text{Au}} = 183.51 \text{ GeV}$. Using the beam energy from above this results in $y_{\text{Beam}} = 1.48$. The midrapidity is simply the half of the beam rapidity, hence $y_{\text{mid}} = y_{\text{Beam}}/2 = 0.74$.

Most of the particles produced in a heavy-ion collision will be located at midrapidity. Particles which are faster, i.e. $y_{\text{CM}} > 0$ are called forward-flying particles and must have gained some energy from the system. In contrast, backward-flying particles, i.e. $y_{\text{CM}} < 0$ lost some of their energy in the system. Thus looking to the rapidity distribution allows to inside the system created in heavy-ion collisions.

As the rapidity is a measure for the longitudinal velocity, one needs to have also a quantity for the transverse components. Usually, the transverse momentum $p_t = \sqrt{p_x^2 + p_y^2}$ is used.

9.3 χ^2 minimization

To quantify if a physical model describes a set of data points, the χ^2 -minimization procedure is used. Changing a quantity x and measuring a physical observable y with the precision Δy one results in a set of data points which can be sampled $(x_i | y_i | \Delta y_i)$ while $i = 1, \dots, N$ and N the number of measurements. It is assumed that the observable y is only statistically distributed, i.e. there are no systematical errors or they are corrected for. Then one can test the quality of physical model $f(x)$ to describe the data sample by

$$\chi^2 = \sum_{i=1}^N \left(\frac{y_i - f(x_i)}{\Delta y_i} \right)^2. \quad (9.5)$$

The smaller χ^2 , the better the model fits to the data. The square effectuates that large deviations are contributing stronger to the sum and the normalization to the uncertainty is useful in order to weight more the data points which have smaller uncertainties.

If the physical model $f(x)$ contains parameters p_k , the best choice for a parameter can be defined by the partial derivative of χ^2 with respect to this particular parameter and finding the minimum, hence determine $p_{k,0}$ by

$$\frac{\partial \chi^2}{\partial p_k} (p_{k,0}) = 0. \quad (9.6)$$

How well a data sample is described by a certain model can be determined from the χ^2 distribution. Having more than one data set of the same observable, which are assumed to be stochastically independent, quadratic, standard-normal distributed random variables one can determine the distribution of the χ^2 and finds

$$p_f(x) = \begin{cases} \frac{x^{f/2} e^{-x/2}}{2^{f/2} \Gamma(f/2)}, & x > 0 \\ 0, & x \leq 0 \end{cases}. \quad (9.7)$$

Therefore, the distribution of χ^2 depends on one single parameter $f = N - N_p$, which is the number of degrees of freedom, i.e. the number of parameters subtracted from the number of data points. The expectation value of this distribution is $E(p_f(x)) = f$ and hence the fit describes the data very well in case the reduced χ^2 is closed to one: $\chi_{\text{red}}^2 = \chi^2/f \approx 1$. One can also calculate the probability to find a χ^2 larger then the measured one in order to decide whether a model must be rejected.

9.4 Decay Topology

The first step to calculate the decay topology parameters is to parametrize the two daughter tracks. From the HYDRA class, HParticleCand, the following quantities are used: the z components along the beamline, the radial distance R in the plane perpendicular to the beamline, the azimuthal angle ϕ and the polar angle θ . Using these quantities one can define two vectors that parametrize the particle track in the region surrounded by the tracking system. The base \vec{b} is defined by:

$$\vec{b} = (R \cos(\phi), R \sin(\phi), z). \quad (9.8)$$

The direction \vec{d} of the track can be defined as:

$$\vec{d} = (\sin(\theta) \cos(\phi), \sin(\theta) \sin(\phi), \cos(\theta)), \quad (9.9)$$

being the usual definition in spherical coordinates.

As a next step, an estimate for the possible decay vertex has to be calculated. If the two daughter tracks have an intersection point, it can be calculated directly and defined as the decay vertex. Otherwise the point of closest approach (DCA) is calculated. Therefore, two planes are calculated from the daughter tracks reading:

$$E_1 : \vec{x} = \vec{b}_1 + \lambda \vec{d}_1 + \mu (\vec{d}_1 \times \vec{d}_2) \quad (9.10)$$

$$E_2 : \vec{x} = \vec{b}_2 + \nu \vec{d}_2 + \rho (\vec{d}_1 \times \vec{d}_2). \quad (9.11)$$

Then the intersection point \vec{P}_1 of E_1 with $g_2 : \vec{x} = \vec{b}_2 + \lambda \vec{d}_2$ and vice versa \vec{P}_2 can be calculated. The point of closest approach, which will be used as the decay vertex, is given by:

$$\vec{v}_{\text{Decay}} = \frac{1}{2} (\vec{P}_1 + \vec{P}_2). \quad (9.12)$$

As a measure for the quality of the possible decay vertex of two daughter candidates, the topology parameter d_t is introduced which is defined as the distance of closest approach between the two tracks. Following the calculation above this leads to:

$$d_t = |\vec{P}_1 - \vec{P}_2|. \quad (9.13)$$

However, in the analysis the determination of d_t is separated from the calculation of the decay vertex. Hence it is calculated using the following equation:

$$d_t = \left| \frac{(\vec{b}_1 - \vec{b}_2) \cdot (\vec{d}_1 \times \vec{d}_2)}{|\vec{d}_1 \times \vec{d}_2|} \right|. \quad (9.14)$$

The opening angle $\Delta\alpha$ can also be calculated directly as the angle between the two directions, i.e. $\Delta\alpha \ll (\vec{d}_1, \vec{d}_2)$.

The decay length d_v of the Λ hyperon candidate is calculated by taking the difference between the event vertex and the decay vertex, hence

$$d_v = |\vec{v}_{\text{Decay}} - \vec{v}_{\text{EventVertex}}|. \quad (9.15)$$

The DCA of the daughter tracks to the event vertex, d_2 and d_3 , are calculated as

$$d_{2,3} = |\vec{d} \times (\vec{b} - \vec{v}_{\text{EventVertex}})|, \quad (9.16)$$

with the respective base and direction for each daughter track. The same formula is also used for the calculation of the DCA of the mother track to the event vertex, d_1 , implementing the base and direction of the mother track. As a base, the decay vertex \vec{v}_{Decay} is taken. For the direction of the mother track, the two daughter momenta are added resulting in the momentum of the Λ candidate \vec{p}_Λ due to momentum conservation. Dividing it by the absolute value gives a unit vector with specifies the direction of the mother track.

After all the decay topology parameters have been calculated, they can be plotted for the experimental data before further cuts are applied. In Fig. 9.1, the distributions of all parameters are shown and compared to the same distributions calculated for the mixed-events. Since overall, the contribution of the Λ hyperons is negligible, the two samples show very similar behaviour, as there is no significant difference in their shapes. This legitimates the use of the mixed-event sample as an input for the neural network to be trained to distinguish the random combinations of two tracks from the real Λ hyperons present in the experimental data.

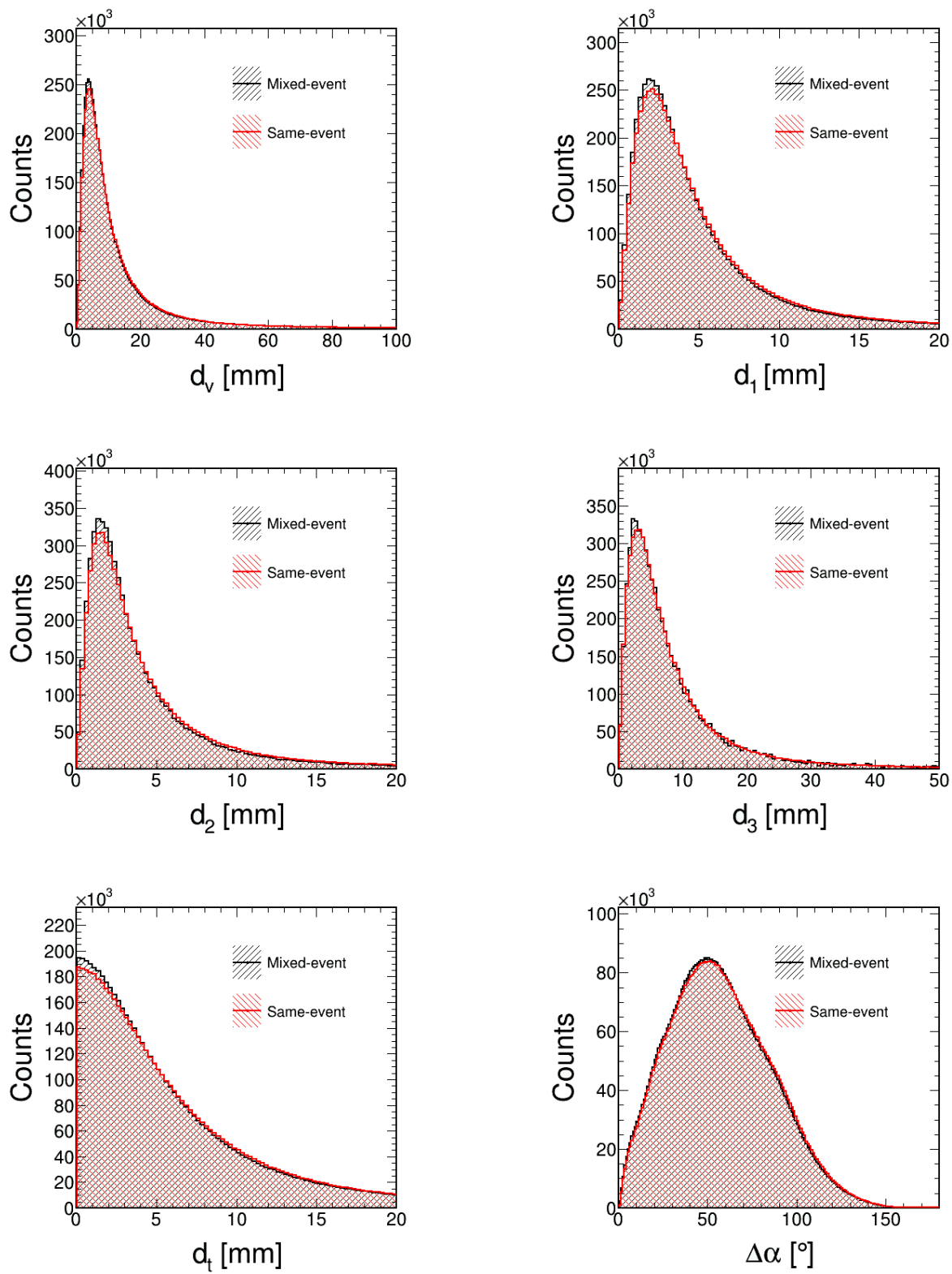


Figure 9.1: Distributions of the topology parameters from the mixed-event (black) and the same-event background (red). Since there are no cuts on the decay topology applied, the signal contribution in the same-event sample is negligible.

9.5 Why the momentum of the Λ hyperon is not used in the neural network

In principle, when the momentum of the Λ hyperon is used as an additional parameter in the neural network, the selection power can be increased further. Hence the neural network has been trained with and without the momentum. After all default selection of the Λ candidates, the overall distributions are plotted in the phase-space as a function of rapidity and transverse momentum. Fig. 9.2 shows the ratio of the sample including the momentum divided by the sample where the momentum is not used. As can be seen, a strong phase-space dependence is introduced when the momentum is included, hence otherwise the neural network does not know about the kinematics. Since a possible polarization might be phase-space dependent, the impact of this phase-space dependent selection from the neural network might have significant influence on the extracted signal. Therefore, the momentum of the Λ hyperon is not used as a parameter in the multi-variate analysis.

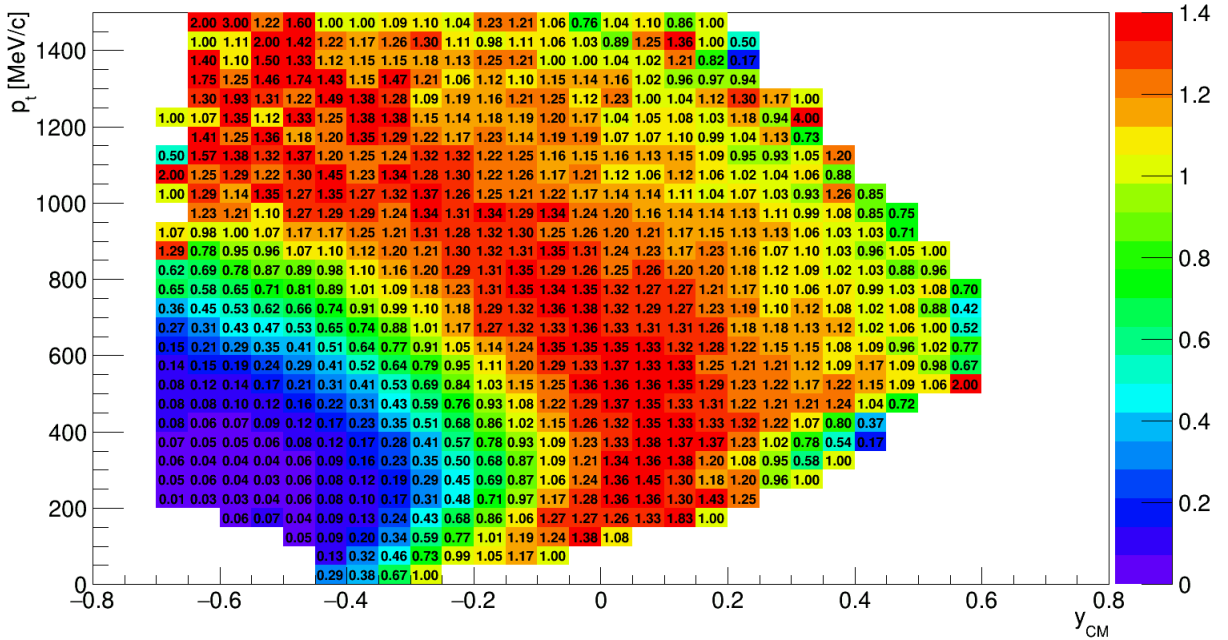


Figure 9.2: Ratio of the overall Λ candidates in Au+Au passing all selection criteria described in Ch. 3, when the momentum of the Λ hyperon is used in the multi-variate analysis divided by the sample where the momentum of the Λ hyperon is not used. A strong difference in the phase-space distributions is visible.

9.6 Invariant mass distribution for Ag+Ag at 1.23 AGeV

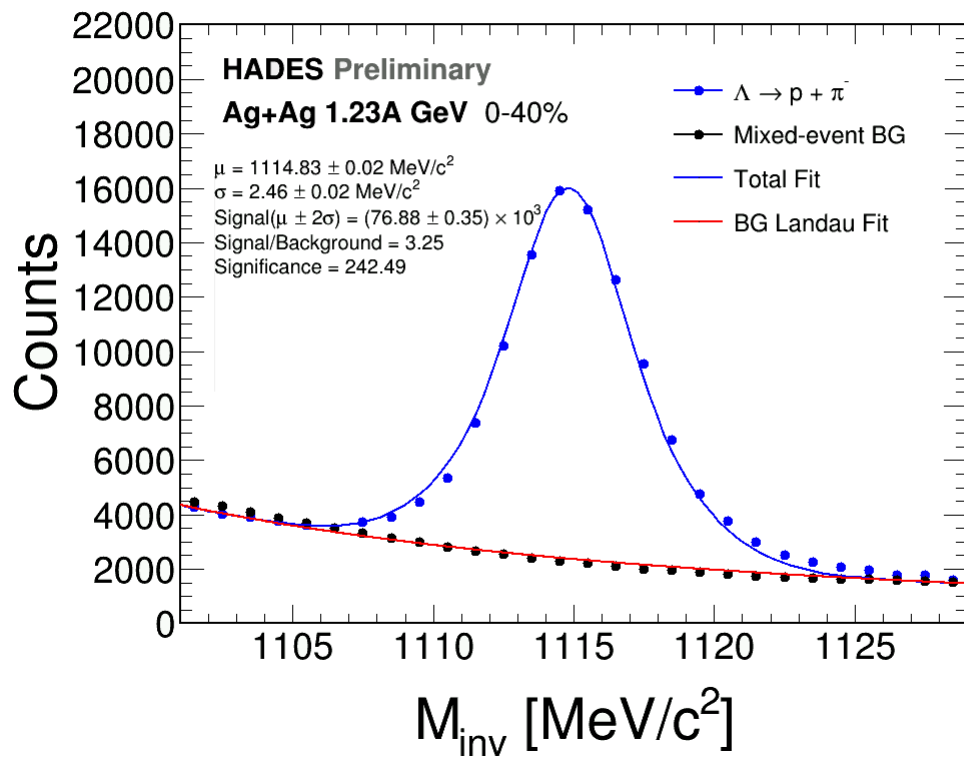


Figure 9.3: Invariant mass distribution in Ag+Ag at 1.23 AGeV for 0 – 40 % centrality.

9.7 Radial distance asymmetry - Supporting material

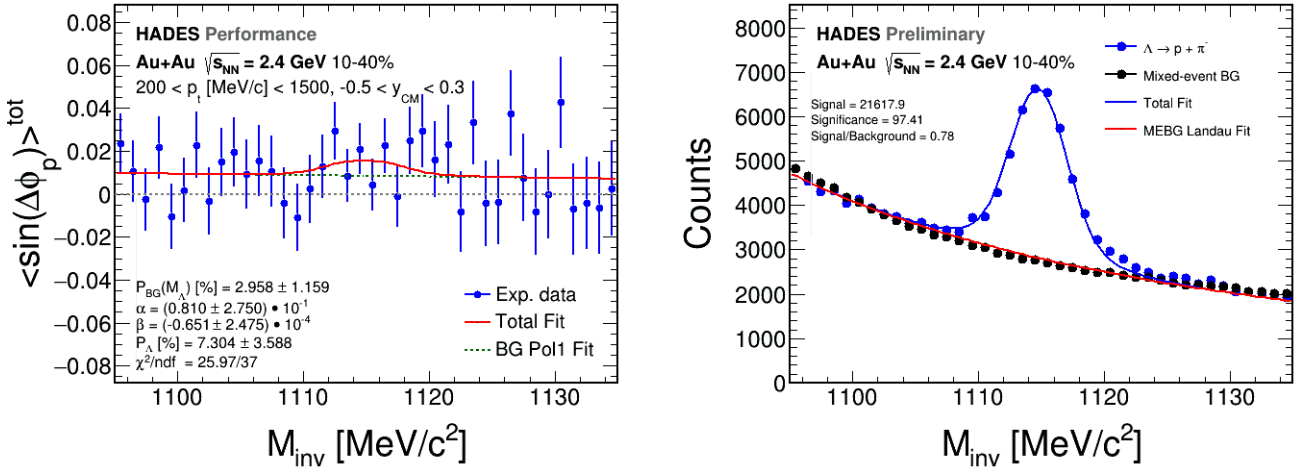


Figure 9.4: Polarization measurement in Au+Au collisions extracted using the invariant mass fit method depending for a radial distance to the event vertex line of $-3 \text{ mm} \leq R'_V \leq 3 \text{ mm}$ (left) and the corresponding invariant mass distribution (right).

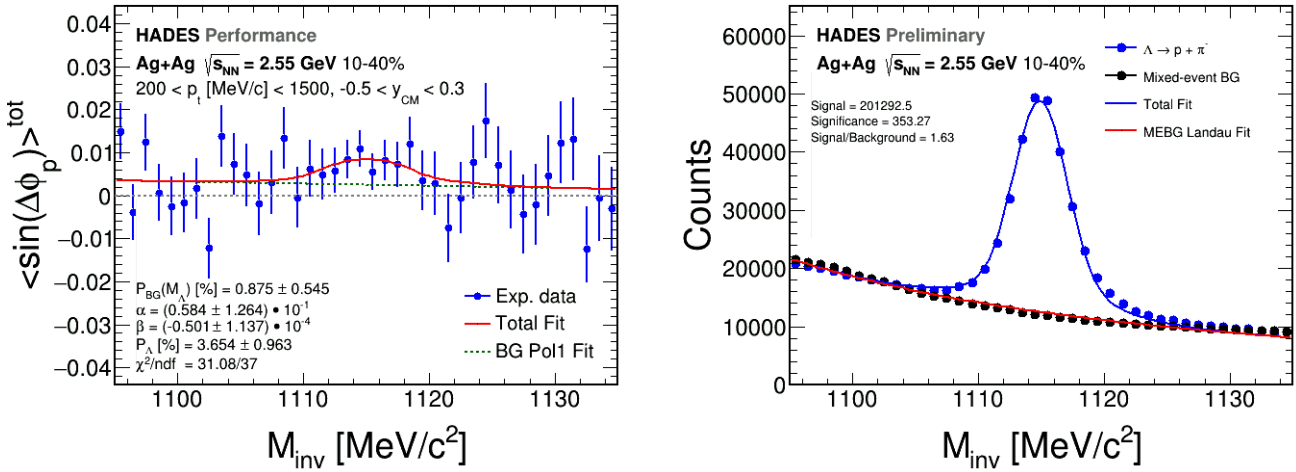


Figure 9.5: Polarization measurement in Ag+Ag collisions extracted using the invariant mass fit method depending for a radial distance to the event vertex line of $-3 \text{ mm} \leq R'_V \leq 3 \text{ mm}$ (left) and the corresponding invariant mass distribution (right).

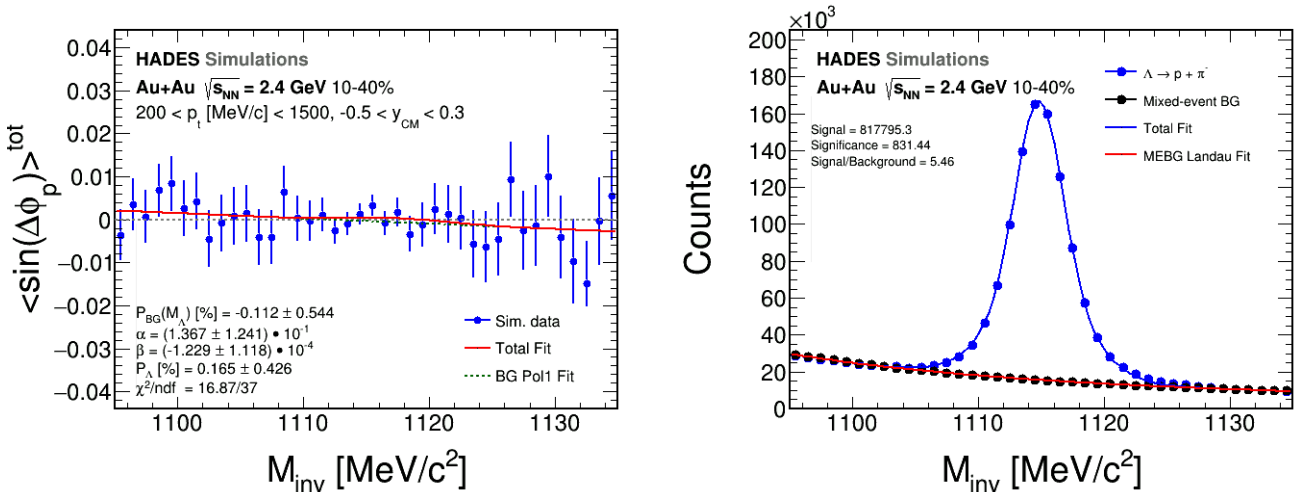


Figure 9.6: Polarization measurement in UrQMD Au+Au collisions with embedded Λ hyperons extracted using the invariant mass fit method (left) and the corresponding invariant mass distribution (right).

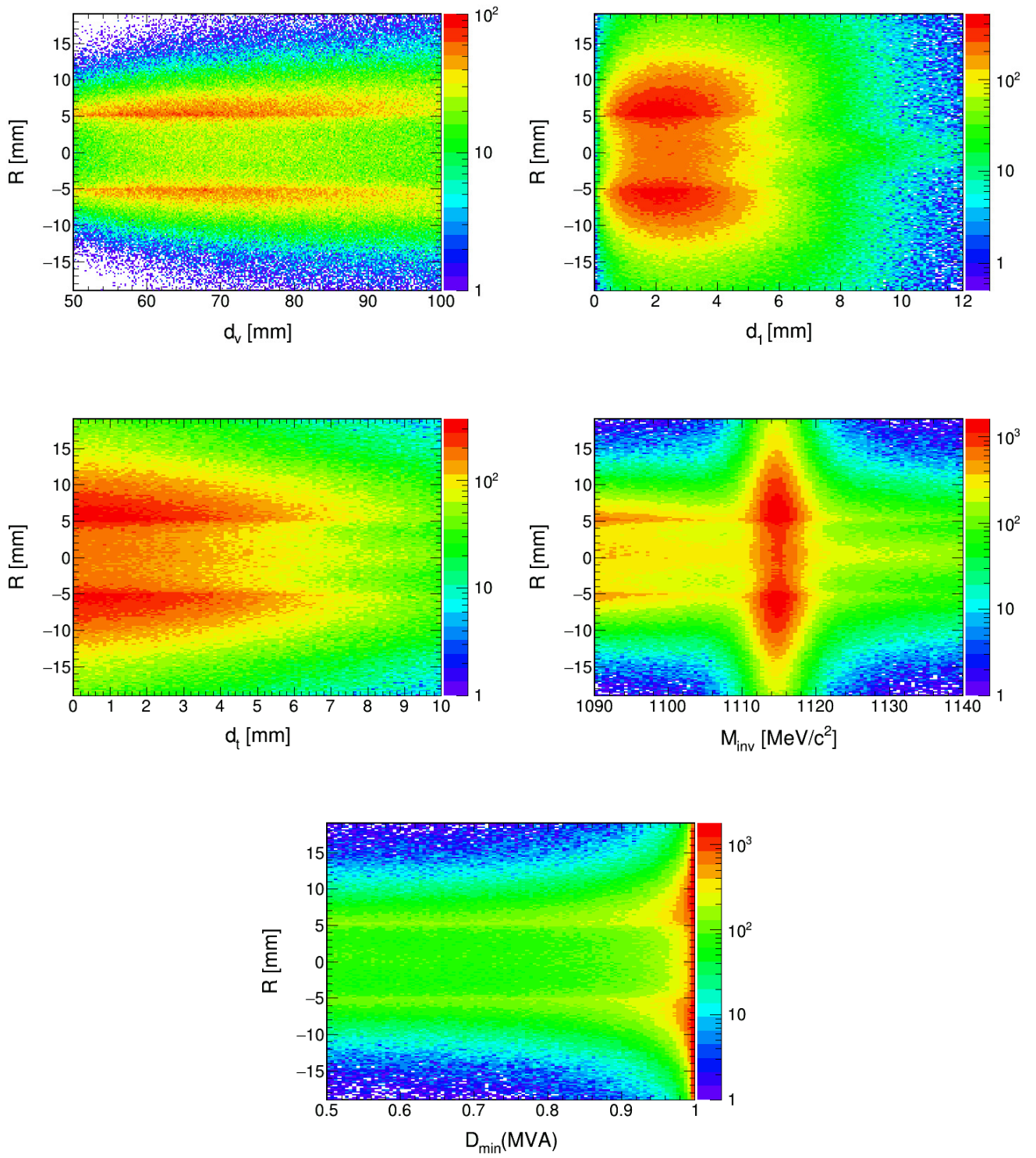


Figure 9.7: Two-dimensional distribution of the radial distance to the event vertex line with respect to different parameters for $1110 \leq M_{\text{inv}}[\text{MeV}/c] \leq 1120$ to match the signal region. The d_2 cut reflects in the sharp edge at $R'_V = 5 \text{ mm}$ visible in all plots. Otherwise there is no clear dependence on any of the parameters plotted on the x -axis.

Curriculum Vitae

Personal information

Name: Frédéric Julian Kornas

Date of birth: 19. June 1991

City of birth: Wiesbaden, Germany

University education

PhD in experimental physics (05/2017-today)

- **place:**
Technische Universität Darmstadt
- **title:**
Global polarization of Λ hyperons as a probe for vortical effects in A+A collisions at HADES
- **supervisor:**
Prof. Dr. Tetyana Galatyuk, Dr. Ilya Selyuzhenkov

Master of science (04/2014-04/2017)

- **place:**
Technische Universität Darmstadt
- **title:**
Hunting for the chiral magnetic effect
- **supervisor:**
Prof. Dr. Tetyana Galatyuk, Dr. Ilya Selyuzhenkov

Bachelor of science (10/2010-03/2014)

- **place:**
Technische Universität Darmstadt
- **title:**
Inelastische Elektronenstreuung am Vibratorkern ^{70}Zn
- **supervisor:**
Prof. Dr. Dr. Norbert Pietralla